ABSTRACT

Title of dissertation: FUNDAMENTAL ROTORCRAFT ACOUSTIC MODELING FROM EXPERIMENTS (FRAME)

Eric Greenwood, Doctor of Philosophy, 2011

Dissertation directed by: Professor Fredric H. Schmitz
Department of Aerospace Engineering

A new methodology is developed for the construction of helicopter source noise models for use in mission planning tools from experimental measurements of helicopter external noise radiation. The models are constructed by employing a parameter identification method to an assumed analytical model of the rotor harmonic noise sources. This new method allows for the identification of individual rotor harmonic noise sources and allows them to be characterized in terms of their individual non-dimensional governing parameters. The method is applied to both wind tunnel measurements and ground noise measurements of two-bladed rotors. The method is shown to match the parametric trends of main rotor harmonic noise, allowing accurate estimates of the dominant rotorcraft noise sources to be made for operating conditions based on a small number of measurements taken at different operating conditions. The ability of this method to estimate changes in noise radiation due to changes in ambient conditions is also demonstrated.

FUNDAMENTAL ROTORCRAFT ACOUSTIC MODELING FROM EXPERIMENTS (FRAME)

by

Eric Greenwood II

Dissertation submitted to the Faculty of the Graduate School of the
University of Maryland, College Park in partial fulfillment
of the requirements for the degree of
Doctor of Philosophy
2011

Advisory Committee:
Professor James E. Hubbard, Jr., Chair/Advisor
Professor Fredric H. Schmitz, Advisor
Professor James Baeder
Professor Christopher Cadou
Professor Inderjit Chopra
Professor Ramani Duraiswami

Acknowledgments

There are many people to whom I owe my gratitude for their support in the preparation of this dissertation. First, I would like to thank all of the members of my dissertation committee for their advice and encouragement. I especially thank Dr. James E. Hubbard for agreeing to chair my dissertation committee and advocating for me from the National Institute of Aerospace here in Hampton, Virginia. Thanks to the last minute heroics of Drs. Duraiswami and Cadou, my scheduled dissertation defense was rescued from a confluence of unusual circumstances. Committee members Drs. Chopra and Baeder have helped me many times over the years, in addition to serving on my dissertation committee. I would also like the thank Dr. Roberto Celi for several helpful discussions on optimization and parameter identification, which helped me develop the modeling method described in this dissertation.

I would like to sincerely thank my colleagues at NASA Langley Research Center and NASA's Subsonic Rotary Wing project for their support throughout this process. I am indebted to the management of the Aeroacoustics Branch, Dr. Charlotte Whitfield and Michael A. Marcolini, for exceeding my expectations and putting forth every effort to make this work a success. A number of my Langley colleagues have helped me throughout the course of this research, including Michael E. Watts, David A. Conner, Charlie Smith, Casey Burley, and Chris Kilzer.

My experience at the University of Maryland has been a great one, and my work on this dissertation and related research would not have been possible without the help of some of my UMD compatriots. I must especially thank Cal Sargent, Rick

Sickenberger, Dr. Sudarshan Koushik, and Dr. Gaurav Gopalan, who have offered me substantial advice and encouragement and all of whom I number among my friends. Thanks to Dr. Ben Wel-C Sim of the US Army Aeroflightdynamics Directorate for his help and friendship, as well.

I also must thank my wife, Carrie E. Greenwood. I'm not sure how she puts up with me and my helicopter obsession, but she does so without second thought. I know this process hasn't been easy for her, but her support has been unwavering. Likewise, my parents have always supported me in the pursuit of my dreams, and I thank them for making me who I am today.

Lastly, I cannot fully express the depth of my gratitude for my advisor Dr. Fredric H. Schmitz. In these last six years I have learned much from him. He has pushed me to succeed; while it's sometimes been a struggle, both my work and myself have been better for it. His passion and drive for excellence in his own work are an inspiration to me. I am very fortunate to have been his student and cannot imagine a better mentor.

Table of Contents

List of Tables

List of Figures

Nomenclature

A	Rotor disk area, ft^2 (m^2)
a	Wavelet scale
A,B,C	Assumed inflow distribution parameters
a,b_1,b_2	Particle swarm control weights
a_0	Ambient speed of sound, ft/s (m/s)
A_1,A_2,b_1,b_2	Empirical indicial aerodynamics constants
a_x	Longitudinal acceleration, ft/s^2 (m/s^2)
b	Number of blades
c	Rotor blade chord, ft (m)
c_i	Radial basis function center location
C_T	Thrust coefficient, $\frac{T}{\rho A(\Omega R)^2}$
C_v	Empirical vortex core growth parameter
$C_{p'}$	Acoustic pressure coefficient
C_p	Surface pressure coefficient
c_{d0}	Rotor airfoil section profile drag coefficient
D	Assumed wake contraction parameter
d	Longitudinal distance between assumed and actual sources, ft (m)
$d\bar{S}$	Non-dimensional elemental area
D_f	Parasitic drag force, lbf (N)
D_{nC}, D_{nS}	Drag distribution Fourier coefficients
dS	Surface elemental area, ft^2 (m^2)
e	Integrated error
$F(X)$	Objective (error) function
$f(x)$	Generic function
f_e	Effective flat plate drag area, ft^2(m^2)
g	Gravitational acceleration, ft/s^2 (m/s^2)

i,j,k	Index variables
M	Mach number
M_H	Hover tip Mach number, $\frac{\Omega R}{a_0}$
M_o	Observer Mach number
M_r	Mach number in propagation direction
M_{AT}	Advancing tip Mach number, $\frac{\Omega R+V}{a_0}$
N	Generic integer quantity
n	Surface normal
N_{obs}	Number of observers
p	Power of generalized norm
P	Surface pressure, lbf/ft^2 (Pa)
p'	Acoustic pressure, lbf/ft^2 (Pa)
p_{RMS}	Root mean squared acoustic pressure, lbf/ft^2 (Pa)
p'_X	Simulated acoustic pressure, lbf/ft^2 (Pa)
p'_{meas}	Measured acoustic pressure, lbf/ft^2 (Pa)
Q	Lighthill stress tensor, lbf/ft^2 (Pa)
$Q(x,\tau)$	Acoustic point source strength
$\bar{r}$	Non-dimensional propagation distance
$\bar{r}_0$	Non-dimensional initial vortex core size
$\bar{r}_c$	Non-dimensional vortex core size
$\mathcal{R}_1$, $\mathcal{R}_2$	Random variables
R	Rotor radius, ft (m)
r	Propagation distance, ft (m)
r_c	Vortex core size, ft (m)
r_r	Non-dimensional tip vortex rollup radius
r_v	Non-dimensional radial location of vortex element
$q(x,\tau)$	Acoustic source strength

s	Non-dimensional reduced time
$\bar{t}$	Non-dimensional time of observation
T	Length of time period, s
T	Rotor thrust, lbf (N)
t	Time, s
t/c	Thickness-to-chord ratio
T_{nC}, T_{nS}	Thrust distribution Fourier coefficients
U	Elemental velocity, ft/s (m/s)
$U(a,t)$	Signal in continuos wavelet domain
$u(t')$	Signal in time domain
V	Vehicle airspeed, ft/s (m/s)
v_θ	Vortex tangential velocity, ft/s (m/s)
v_i	Particle velocity
v_n	Velocity normal to the surface, ft/s (m/s)
W	Vehicle weight, lbf (N)
w_k	Error weights
$\bar{x}$	Non-dimensional position vector
$\bar{x}$,$\bar{y}$,$\bar{z}$	Non-dimensionalized hub-centric rotor coordinates
$\bar{x}_n$	Moving average at point n
X	Vector of dependent parameters
x	Cartesian position vector, ft (m)
x,y,z	Cartesian blade element coordinates, ft (m)
$X(s)$, $Y(s)$	Indicial exponential functions
X_i	Particle position
x_s	Source location vector, ft (m)
α_{TPP}	Rotor tip-path-plane angle of attack, rad
β	Regularization performance ratio

$\bar{\Gamma}_0$	Nominal non-dimensional tip vortex strength
$\bar{\gamma}_v$	Non-dimensional vortex strength
γ	Flight path angle, rad
γ_0,γ_{1C},γ_{1S}	Vortex strength distribution Fourier coefficients
γ_v	Vortex strength, ft^2/s (m^2/s)
δ	Dirac delta function
ϵ	Multi-quadric shape factor
θ	Angle between observer and rotor disk
H	Rotor in-plane "hub-force, lbf (N)
λ	Mean inflow ratio, $\frac{\bar{v}_i - V \sin \alpha_{TPP}}{\Omega R}$
λ_1	Landgrebe wake contraction rate
λ_i	Local induced inflow ratio
λ_{i_0}	Mean induced inflow ratio
μ	Advance ratio, $\frac{V}{\Omega R}$
μ_x	Advance ratio component parallel to tip-path-plane
μ_z	Advance ratio component perpendicular to tip-path-plane
ν_i	Radial basis function weight
ξ	Airfoil surface element slope
$\xi(x)$	Wavelet basis function
ρ_0	Ambient density, slug/ft^3 (kg/m^3)
σ	Ricker basis shape parameter
σ_k	Moving standard deviation at point k
$\bar{\tau}$	Non-dimensional time of emission
τ	Time of emission, s
Φ	Basis function
ϕ	Wake age, rad
χ	Wake skew angle, rad

ψ	Rotor azimuth, rad
ψ_b	Azimuthal location of rotor blade, rad
ψ_v	Azimuthal location of vortex element, rad
Ω	Rotor rotational speed, rad/s
ω	Frequency, rad/s
ω'	Observed frequency, rad/s

Chapter 1

Introduction

1.1 Background

Noise is an inevitable consequence of rotary wing flight, and can severely constrain helicopter operations. Civil helicopter operations are frequently limited by the public acceptance of aircraft noise, as well as local and national regulations on permissible noise levels. These noise criteria restrict the use of helicopters for passenger transport, sightseeing, electronic news gathering, and aerial law enforcement. Noise criteria also restrict the construction of heliports, preventing the adoption of point-to-point vertical lift commuter aircraft, often touted as a solution to the overcrowding of airspace worldwide. Military operations are likewise adversely affected by rotorcraft noise. While rotorcraft frequently evade detection by visual, infrared, or radar means by flying nap-of-the-earth, low to the ground and amongst terrain features, the lower frequency acoustic waves produced by rotorcraft carry over long distances and can refract around terrain. Consequently, rotorcraft are often first detected by acoustic means. Acoustic detection can be achieved using anything from elaborate arrays of electronic detectors to the unaugmented human ear, and can greatly decrease the survivability of helicopter missions. In both civil and military cases, the acoustic impact of helicopter operations can be reduced through either the design or the operation of the rotorcraft. However, changing the

design of the helicopter to reduce noise typically results in a reduction in other key performance parameters, such as payload or maximum speed. In addition, design changes offer no remedy for rotorcraft which have already been produced and are currently in widespread service. Designing helicopter operations for reduced acoustic impact is a realistic and promising avenue for increasing the number and variety of helicopter operations without exceeding existing limits on community annoyance or survivability.[2][3] Designing helicopter operations for reduced noise requires an accurate method of assessing the acoustic impact of individual helicopter operations.

1.2 Ground Noise Contours

The acoustic impact of helicopter operations is typically quantified using ground noise contours. (Figure 1.1 on the following page.) For community noise, ground noise contours are used in order to plan helicopter operations so as to minimize annoyance in noise sensitive areas, to ensure compliance with community noise regulations, and to plan the location and design of heliports. Ground noise contours are also an increasingly valuable tool for military mission planning—designing flight paths that minimize the chance of aural or electronic detection, thereby improving the survivability of the helicopter.

The process of generating ground noise contours requires three models: a helicopter noise source model, an atmospheric propagation model, and a receiver model. (Figure 1.2 on page 4.) The helicopter noise source model describes the external noise radiation of the helicopter as it moves along the desired flight trajectory.

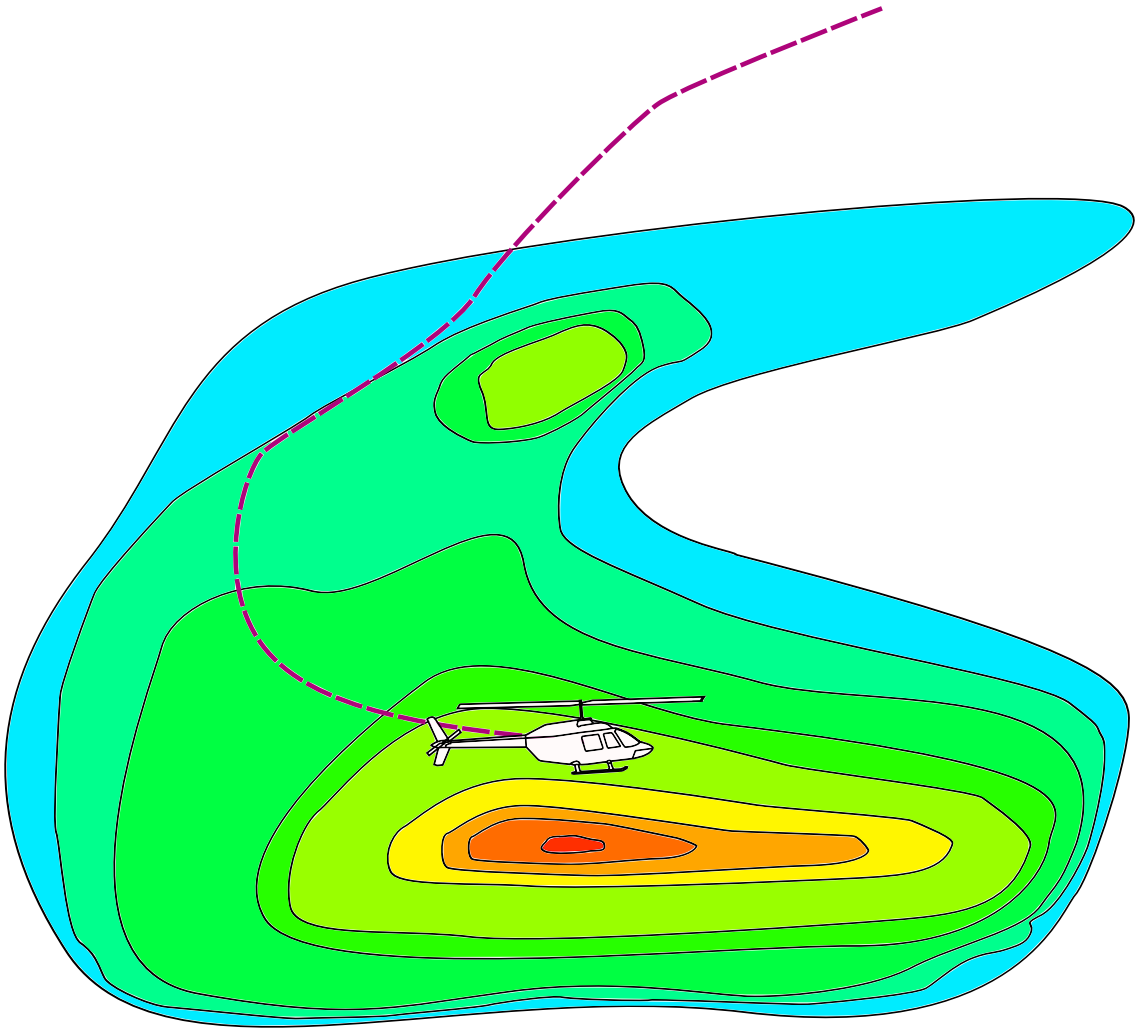

Figure 1.1: A notional ground noise contour for a helicopter on an approach trajectory.

The atmospheric propagation model describes how the noise radiated by the helicopter is transmitted from the helicopter through the atmosphere and to observers on the ground. The receiver model describes how the noise heard on the ground impacts the observer. Atmospheric propagation models have received much attention recently with high-fidelity physics-based models being incorporated into the current generation of ground noise contour estimation tools.[4] While most current aural receiver models

are based on empirically generated descriptions of the frequency response of the human auditory system,[5] some recent research has suggested that these models may be inadequate for harmonic noise sources and that time-domain models, which capture both the magnitude and phase of the noise as a function of frequency, may be required.[6] The focus of this dissertation is on helicopter noise source modeling: accurate noise contour estimation is only possible with an accurate model of the noise at the source, no matter the quality and sophistication of the propagation and receiver models.

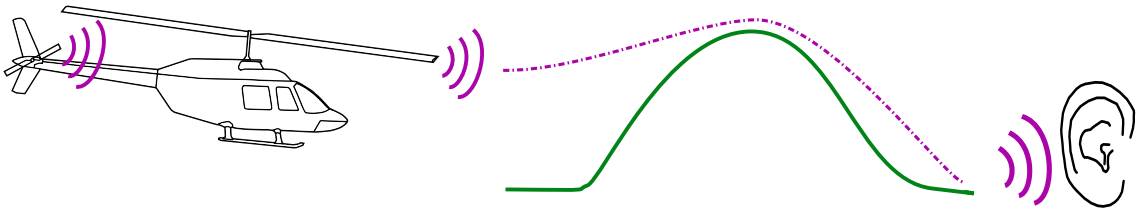

Figure 1.2: The three components of ground noise contour modeling. From left to right: the helicopter source noise model, the atmospheric propagation model, and the receiver model.

1.3 Helicopter Noise Source Modeling

Helicopter noise source modeling can be broadly divided into two approaches, theoretical models that develop estimates of helicopter external noise radiation from first principles and empirical models which incorporate measurements of helicopter noise in the construction of the model. The state-of-the-art in theoretical modeling is still very time consuming and requires validation for new configurations and operating conditions; routine theoretical modeling of helicopter noise for specific

configurations over a wide range of operating conditions is not yet practical. On the other hand, numerous empirical modeling schemes are currently in use. The two types of empirical models in general use are integrated models and source hemisphere models.

1.3.1 Integrated Noise Models

Integrated models have been used in the Federal Aviation Administrations Heliport Noise Model (HNM),[7] Integrated Noise Model (INM),[8] and the upcoming Aviation Environmental Design Tool (AEDT).[9] Integrated noise models are developed from measurements of noise on the ground captured during aircraft flyovers. Integrated models provide a representation of the time-averaged noise radiated to points on the ground for an aircraft flying along a theoretically infinite flight track. The variations of the integrated noise levels with respect to the distance between the source and receiver are described by empirically developed Noise-Power-Distance (NPD) curves.[10] NPD curves are developed for three standardized flight conditions, also used for noise certification: level flight, takeoff, and approach. The distribution of noise levels by frequency is handled by assigning a spectral class to the NPD curves where the "spectral class" describes a normalized frequency spectrum that is assigned to the noise radiated by the noise source model in all directions for all flight conditions.

In an extension to the modeling method for helicopter noise, some measure of the lateral variation in noise levels is achieved through the use of separate NPD

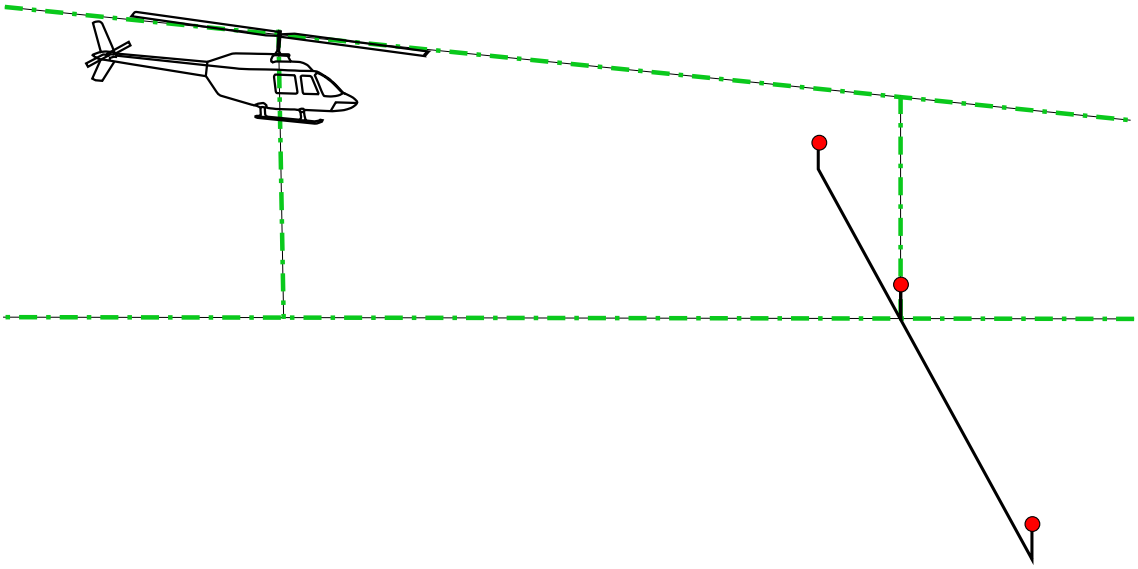

Figure 1.3: A diagram of the Integrated Noise Model three microphone measurement standard.

curves for the left and right sides of the helicopter. These NPD curves are developed from measurements of the helicopter using three above-ground microphone locations for each of the three standardized flight conditions, as shown in Figure 1.3. However, integrated modeling does not explicitly model the overall directivity of the noise radiated from the helicopter. Lateral directivity is coarsely modeled by differentiation in the left, right, and center NPD curves as well as an empirically determined sideline correction, which extrapolates the left or right NPD values for observers far from the flight path of the helicopter. Longitudinal directivity is not directly captured by the model, but is implicit in the distance dependence of the NPD. Similarly, variation in noise levels with changes in flight condition is coarsely modeled using data from only the three standardized noise certification flight conditions. Integrated modeling is suitable for estimating averaged noise levels over many repeated flights—and is

considered applicable over only a limited geographical area, such as an airport—but does not accurately capture the noise radiation from a single flyover event. Integrated Noise Model was initially developed for fixed-wing aircraft, where due to the large volume of air traffic, time averaged noise levels provide a useful measure of the noise impact of airport operations. However, due to the typically lower volume of rotorcraft flight operations, and the unique character, directionality, and sensitivity to operating condition of rotor noise sources, integrated noise modeling may not be well suited to assessing the noise impact of most rotorcraft operations.

1.3.2 Source Noise Hemisphere Modeling

In order to address these deficiencies in modeling the external noise radiation of rotorcraft, several more sophisticated simulation methods have been developed based on the concept of empirically constructed source noise hemispheres (Figure 1.4 on the next page). The fundamental assumption of these methods is that for far-field observers, the helicopter can be represented by a single compact noise source occupying a point in space, typically chosen to be the main rotor hub of the helicopter. As the helicopter flies over a ground-based array of microphones, the microphones measure the noise along the set of directions between the assumed source and the microphones. The noise can then be "de-propagated" along these directions, accounting for the time-delay between the emission of noise from the assumed source and the reception of noise at the microphone, to points a fixed distance away from the compact source by accounting for transmission losses due to spherical spreading

and atmospheric absorption. The result is a measurement of the noise levels on the surface of a hemisphere set a fixed distance away from the main rotor hub of the helicopter. Typically, the noise levels on the surface of the hemisphere are given in terms of 1/3-octave or narrowband frequency spectra. This provides a description of the noise radiated by the helicopter for a single measured flight condition in terms of amplitude, frequency and direction. By repeating the process for various flight conditions, a database of acoustic hemispheres can be generated for use in ground noise contour generation.

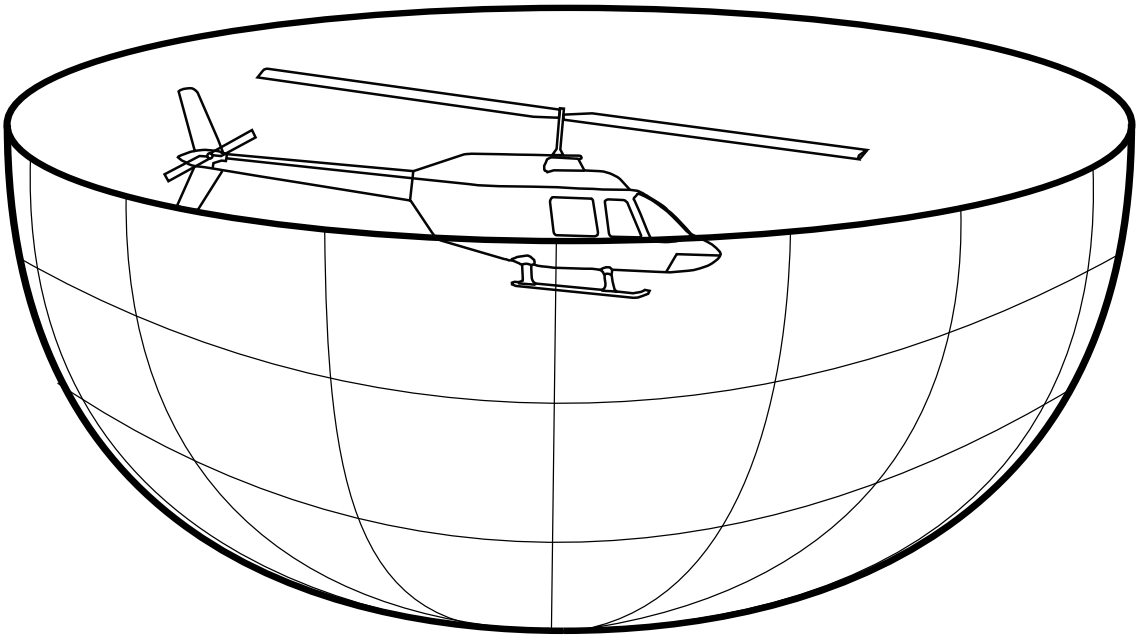

Figure 1.4: An source noise hemisphere centered about the main rotor hub.

1.3.2.1 Rotorcraft Noise Model

The most popular hemisphere-based helicopter noise-modeling tool in the United States is the Rotorcraft Noise Model (RNM)[11], developed by NASA, DoD, and Wyle Laboratories. RNM develops noise hemispheres from acoustic measurements of a helicopter in steady straight-line flight over a linear array of microphones, as shown in Figure 1.5 on the following page. As the helicopter passes over the array, each microphone captures a range of directivity angles over the duration of the measurement (Figure 1.6 on page 11). Since the acoustic state of the helicopter is assumed steady, these measurements are used to construct a single hemisphere representing one flight condition. Flight conditions are defined in RNM in terms of the airspeed of the helicopter and the flight path angle. In order to characterize the helicopter, numerous combinations of airspeed and flight path angle are tested, resulting in a large database of acoustic hemispheres for steady straight-line flight conditions (Figure 1.7 on page 12). These hemispheres may then be used to estimate noise levels on the ground by dividing the desired trajectory into a sequence of steady straight-line segments. Each segment is then associated with a measured hemisphere—if an exact match for a desired flight segment is not found in the database of hemispheres, a new hemisphere is generated by interpolating the noise levels on the surface of the hemisphere between known values of airspeed and flight path angle. For turning flight segments, RNM has the capability to rotate the noise source hemispheres by the bank angle of the helicopter, but makes no other adjustments to the noise source.[12]

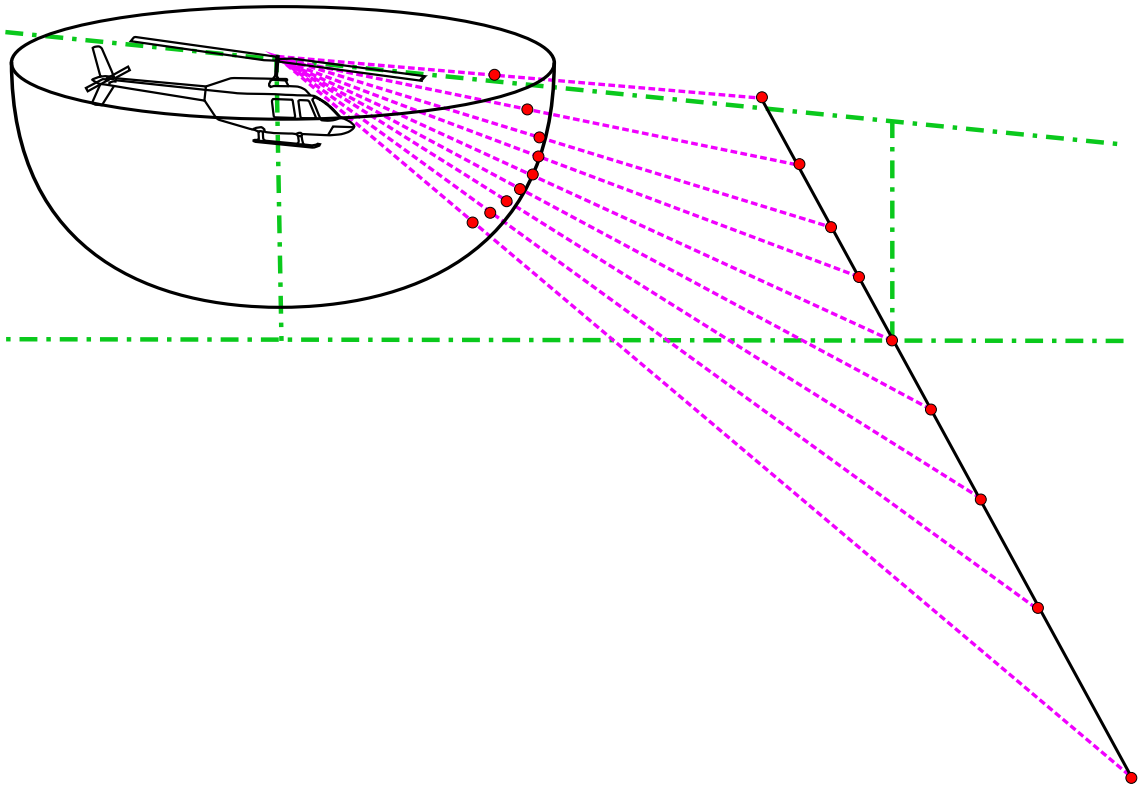

Figure 1.5: The Rotorcraft Noise Model (RNM) hemisphere measurement array.

1.3.2.2 RNM/Q-SAM

An extension to RNM enables it to model moderately accelerating or decelerating quasi-steady flight conditions using the Quasi-Static Acoustic Mapping (Q-SAM) method,[13] which provides an acoustic equivalence between steady and quasi-steady straight-line flight conditions, allowing a relation to be made between the effect of moderate accelerations and changes in flight path angle. However, RNM is otherwise incapable of modeling the noise produced by unsteady flight and operating conditions other than those directly measured. The principle behind RNM/Q-SAM is discussed in more detail later, in Section 2.2.2.2.

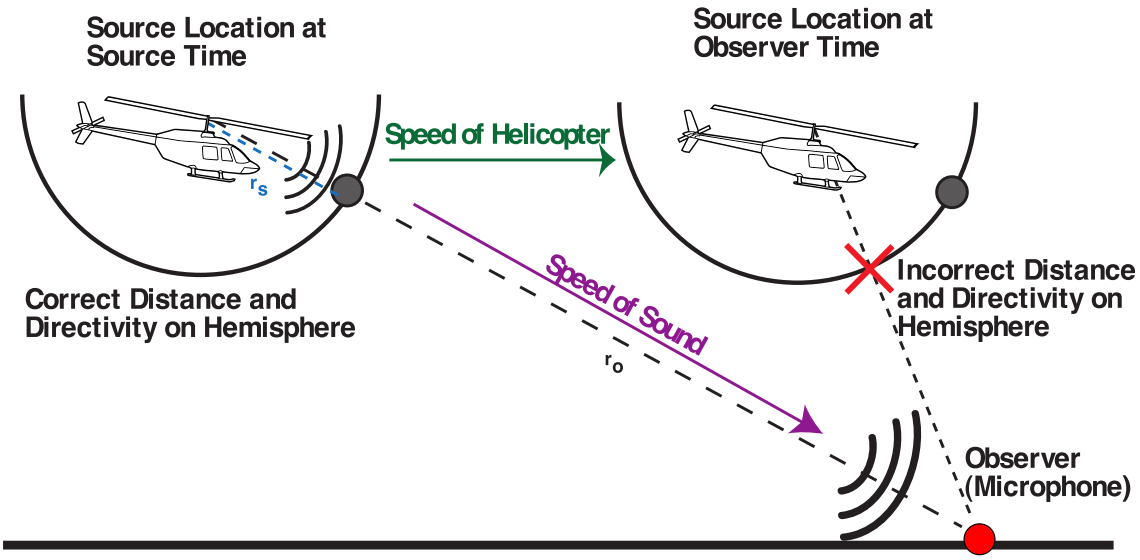

Figure 1.6: The process of building a noise source hemisphere from measured data.

1.3.2.3 HELENA and SELENE

The European HELicopter Environmental Noise Analysis (HELENA)[14] and Sound Exposure Level starting from the Emitted Noise Evaluation (SELENE)[15] tools developed under the Friendcopter program are similar to RNM, except that 2D ground microphone arrays may be used. This allows noise to be measured across a wide range of directivity angles simultaneously. (Figure 1.8 on page 13.) In concept, noise hemispheres could be developed from non-steady measurements, since the array covers nearly an entire hemisphere worth of directivity angles simultaneously. In practice, frequency spectra are generated at each microphone location from a finite time window of acoustic pressure data. Depending on the required frequency bandwidth, this time window may be quite large—significantly larger than the time scale of acoustic events associated with the transient maneuver. Flight conditions may

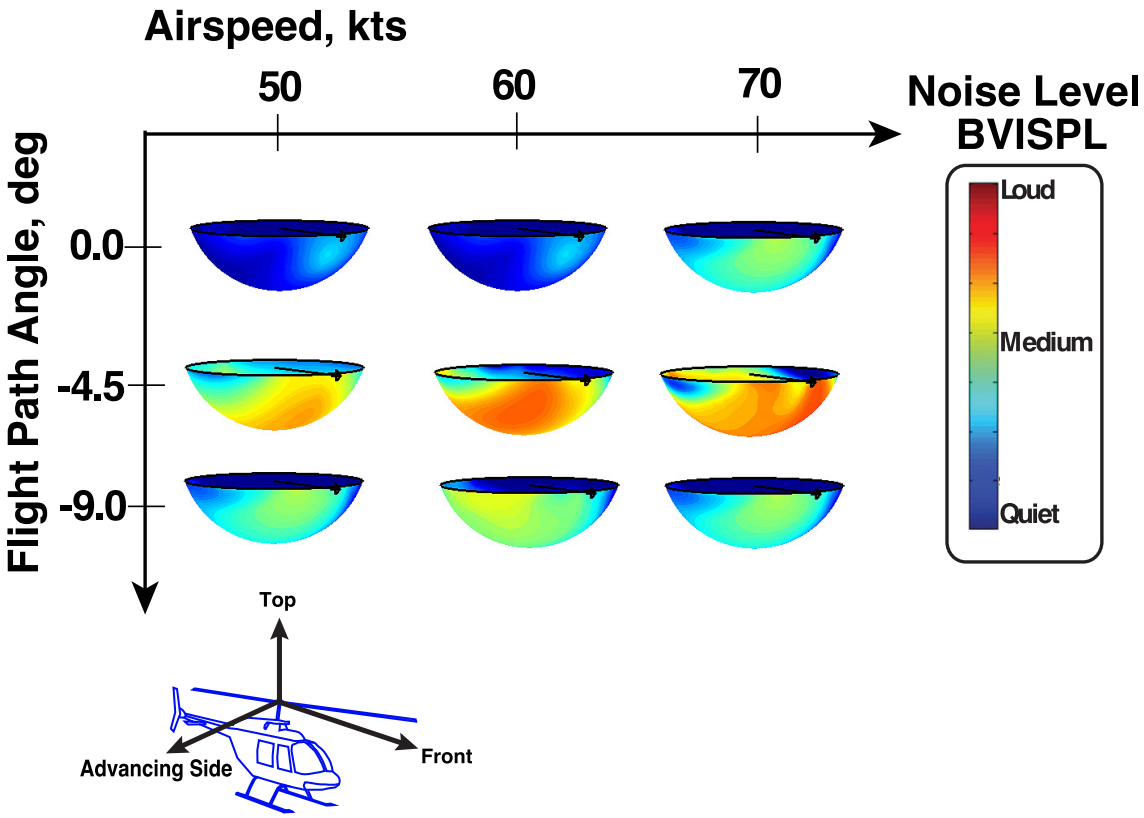

Figure 1.7: RNM database of source noise hemispheres.

be defined with respect to either dimensional or non-dimensional parameters. For instance, dimensional parameters airspeed and rotor torque,[15] and non-dimensional parameters advance ratio and tip path plane angle of attack,[14] have been used in prior research.

1.3.2.4 HAMSTER

Qinetiq's Helicopter Acoustic Measurement System for Trials and Experimental Reduction (HAMSTER)[4] technique is focused on developing models in order to assess the long-range detectability of helicopter operations. As such, an accurate

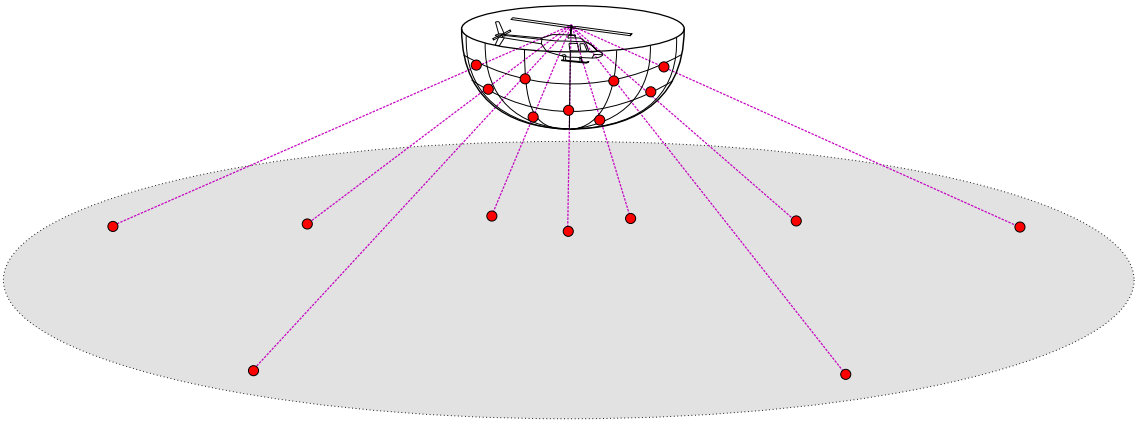

Figure 1.8: The HELicopter Environmental Noise Analysis (HELENA) measurement array.

description of the in-plane noise of the helicopter is desired. In addition to a ground-based array of microphones, HAMSTER uses tower-mounted beam forming arrays to measure noise in the plane of the horizon (Figure 1.9 on the following page). By directing the array towards the helicopter, the influence of interfering acoustic reflections off of the ground can be suppressed. However, because of the narrow angle of the beam, the helicopter must be flown across the array at several altitudes in order to construct a full hemisphere. The relatively sparse linear microphone arrays have a limited number of microphone distance pairs; consequently, data is processed with a coarse 1/3-octave frequency resolution; constructing an accurate pressure time-history representation of the in-plane noise radiation would require a more refined array. Due to the large amount of data required to construct a single model, hemispheres are typically only generated for several level flight speeds, and one climbing and one descending flight condition at a single moderate airspeed.

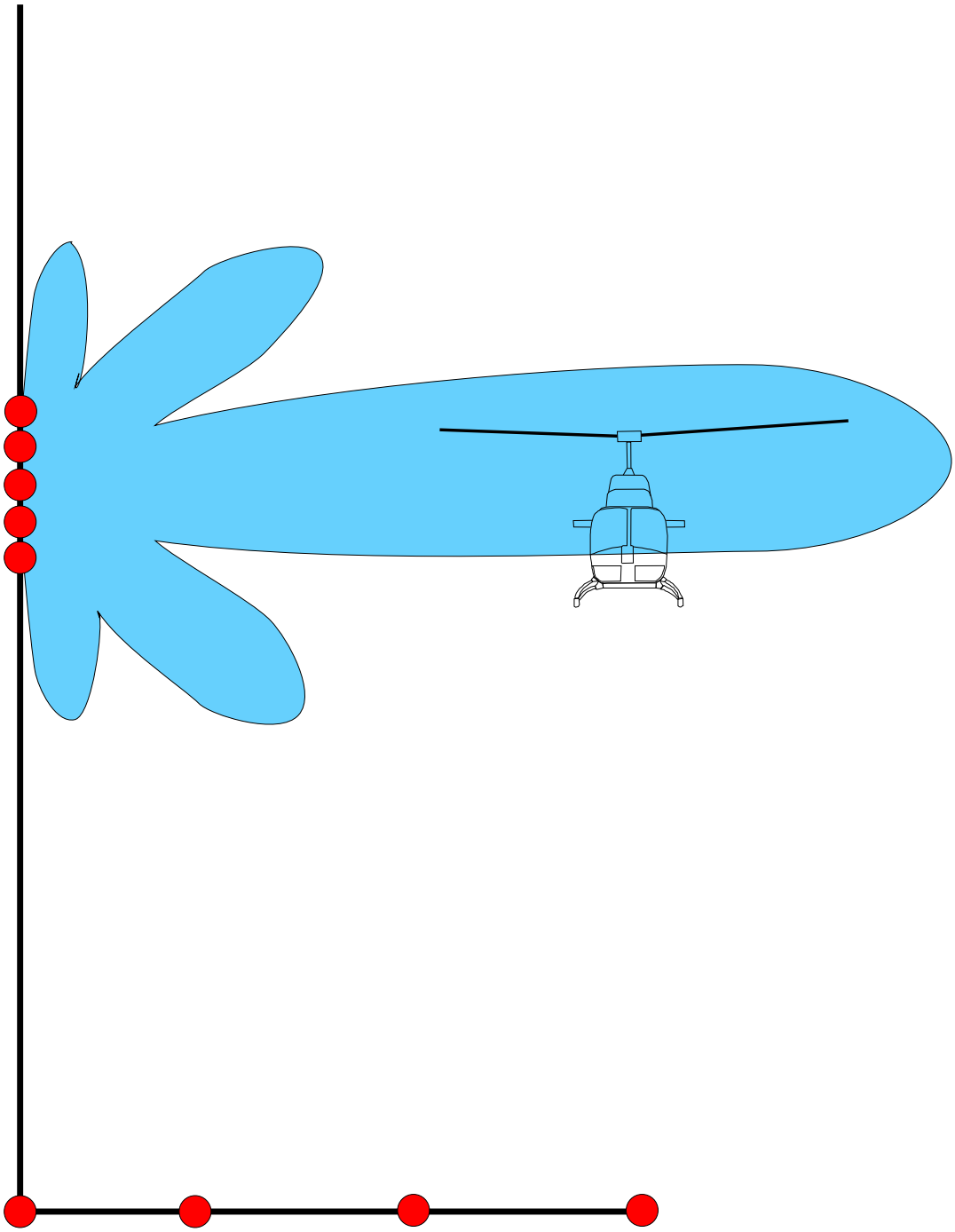

Figure 1.9: The Helicopter Acoustic Measurement System for Trials and Experimental Reduction (HAMSTER) beamforming array.

1.3.2.5 Deficiencies of Source Noise Hemisphere Modeling

While source noise hemisphere noise modeling is a major improvement over integrated noise modeling, there are still significant deficiencies. The noise hemispheres developed under the compact source assumption cannot easily be generalized to other flight conditions, since each hemisphere represents the totality of noise radiating from the helicopter for a particular flight condition. While the hemispheres may be classified in terms of some non-dimensional parameters, the acoustic hemispheres still represent a single unique flight condition. As the flight condition changes, the contributions of each individual noise source to the overall external noise radiation changes. Consequently, a large flight test program is required in order to produce accurate estimates of helicopter noise radiation for a wide range of flight conditions. In general, the full range of helicopter operating conditions is not accounted for, especially variations in the configuration of the helicopter, such as changes in gross weight, and variations in the operating environment, such as air density or temperature. Due to the expense of measuring the noise of the helicopter in all possible flight conditions, configurations, and atmospheric conditions, the effects of these variations are ignored in current helicopter noise source models.

1.4 Objective

It is the objective of this dissertation to develop a new phenomenological method of modeling helicopter noise sources from measurements which:

- *Generalizes noise models based on the non-dimensional governing parameters of the noise sources*

  In order to produce phenomenological models that describe the external noise radiation of the helicopter across a wide range of operating conditions, it is necessary to identify the governing parameters of the noise generation mechanisms. Multiple sources of noise contribute to the overall noise radiation of the helicopter; therefore, each source must be modeled individually with respect to its own governing parameters

- *Allows accurate noise estimates to be made at different operating conditions than those measured*

  An accurate estimation scheme allows a wider range of operating conditions to be modeled with a smaller set of measured data. Operating conditions include not only various flight conditions, but also atmospheric and configuration variations which affect the acoustic state of the vehicle. Current data-driven interpolation approaches are incapable of producing accurate noise estimates for operating conditions far from those measured. It is also impossible to accurately estimate noise radiation at operating conditions outside the measured range using interpolation techniques. Without the capability to estimate noise radiation at conditions not measured, general-purpose helicopter noise source

models will require an impractically large set of measured data to cover the full range of likely helicopter operating conditions.

- *Retains accuracy of noise estimates for measured flight conditions*

  The new modeling method should preserve the accuracy of existing methods for flight conditions where measured data exists. The new method should categorically improve the quality of helicopter noise source modeling for ground noise contour estimation.

1.5 Approach

To achieve these objectives, a new modeling scheme is proposed. For the greatest flexibility and accuracy, each noise source on the helicopter must be modeled separately in terms of its own set of non-dimensional governing parameters. Existing physical knowledge of the major noise source mechanisms of the helicopter should be incorporated in the modeling structure, in order to improve the accuracy of noise estimates made for conditions not measured. The phenomenological models of the noise sources are then fit to specific flight vehicles using measured test data. The approach to developing this new modeling method is:

1. Develop a method of separating the major noise sources of the helicopter.

2. Develop a phenomenological modeling framework for each noise source in terms of non-dimensional governing parameters as well as a set of dependent modeling parameters which are used to capture physics not explicitly included in the assumed modeling structure

3. Employ parameter identification techniques to determine the values of the dependent parameters which cause the model to match measured data for flight conditions defined in terms of the non-dimensional governing parameters

4. Validate the method using both wind tunnel and flight test measurements of rotor noise

A diagram of the method is shown in Figure 1.10 on the next page.

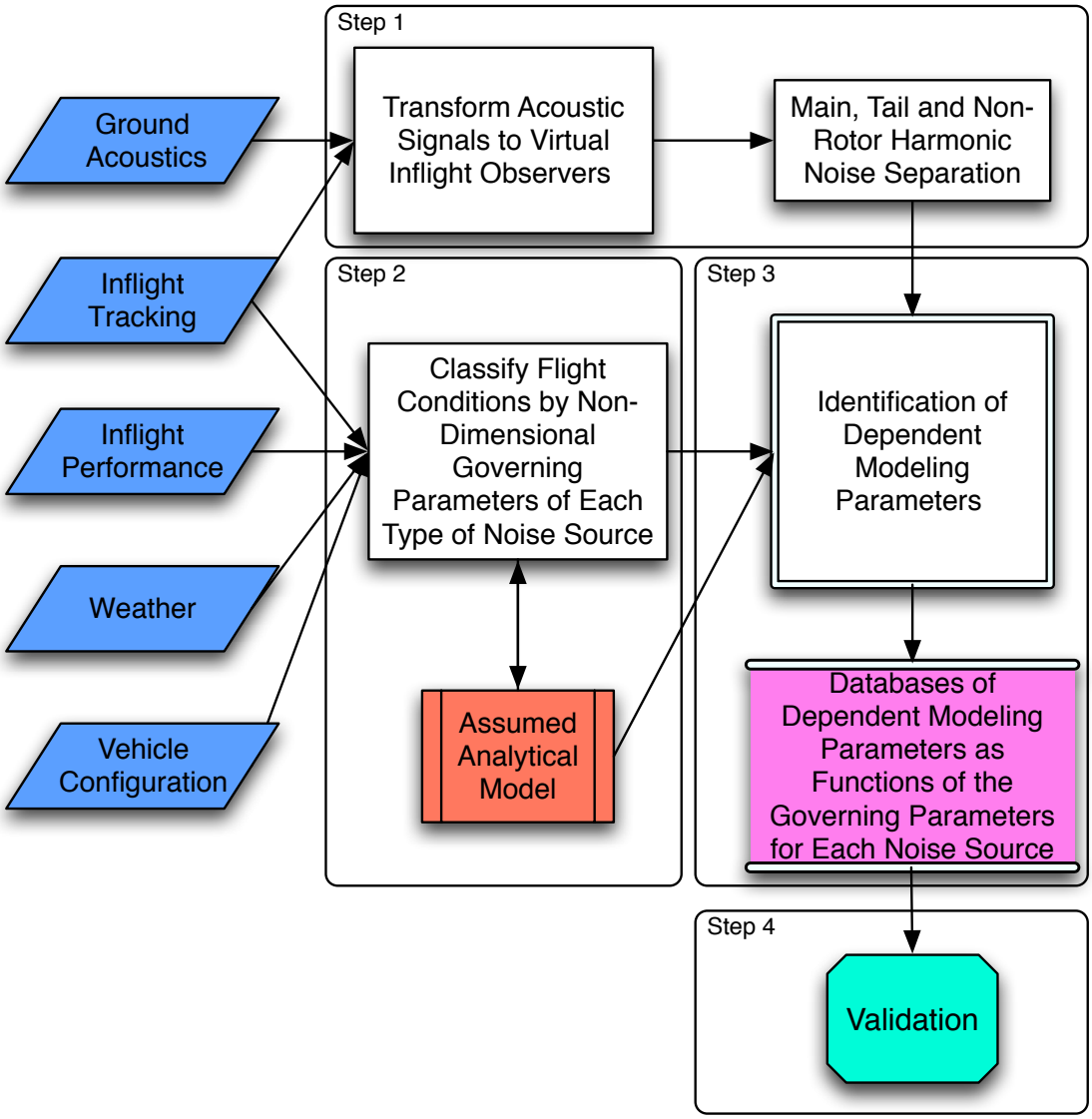

Figure 1.10: Flowchart of the modeling approach developed in this dissertation.

Chapter 2

Phenomenological Helicopter Noise Source Modeling

2.1 Helicopter Noise Sources

The comprehensive characterization of helicopter noise radiation is difficult. Helicopter noise is generated by many different sources. These sources can be broadly classified as rotor harmonic noise sources and non-rotor-harmonic noise sources. Rotor harmonic noise sources dominate the external noise radiation of helicopters.[16] Two types of rotor harmonic noise exist: lower harmonic noise sources and impulsive noise sources. The main and tail rotors continuously generate lower harmonic noise during all flight conditions. Impulsive noise only occurs during certain flight conditions, but is the dominant source of noise when it occurs.[17] These noise sources are illustrated in Figure 2.1 on the following page.

Lower harmonic noise is produced by two mechanisms termed steady loading noise and thickness noise. Steady loading noise is generated by periodic application of aerodynamic forces by the rotor to the fluid medium—the resulting noise occurs at the blade passing frequency and its integer harmonics. For two-bladed and large multi-bladed main rotors, the first two harmonics will typically occur at sub-audible frequencies (i.e. below 20 Hz), observed only by electronic detection equipment or felt by induced structural vibrations. The higher harmonics of steady loading are of lesser magnitude and are generally significant only in the absence of more powerful

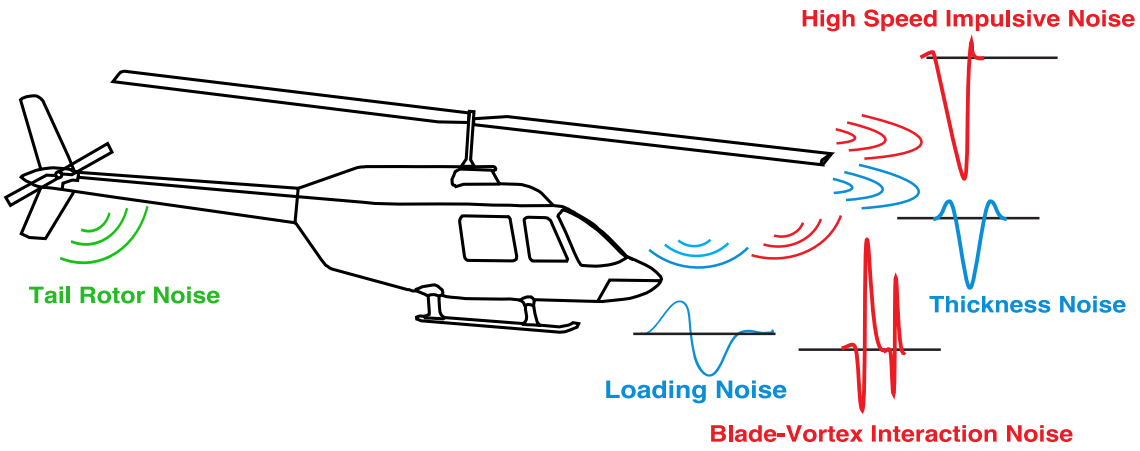

Figure 2.1: Helicopter rotor harmonic noise sources.

noise sources. Thickness noise is generated by the displacement of the air caused by the periodic passage of the rotor blade sections through space. This effect is dominant near the tips of the blades where the section free-stream Mach number is greatest. The resultant noise is observed as a series of low-frequency pulses occurring at the blade passage frequency of the rotor. As the tip Mach number is increased, the intensity of thickness noise increases rapidly. The shape and magnitude of the pulse changes significantly as the advancing tip Mach number enters the transonic regime and local shocks develop about the blades—at this point it becomes a dominant source of noise and is termed High Speed Impulsive (HSI) harmonic noise.[18] HSI noise is dependent not only on the shape of the blade section but also on the transonic flow field surrounding the surface of the airfoil near the blade tip. HSI noise is less important on modern helicopter designs featuring lower tip speeds and thinner blade sections.

The other impulsive noise source, termed Blade-Vortex Interaction (BVI) noise,

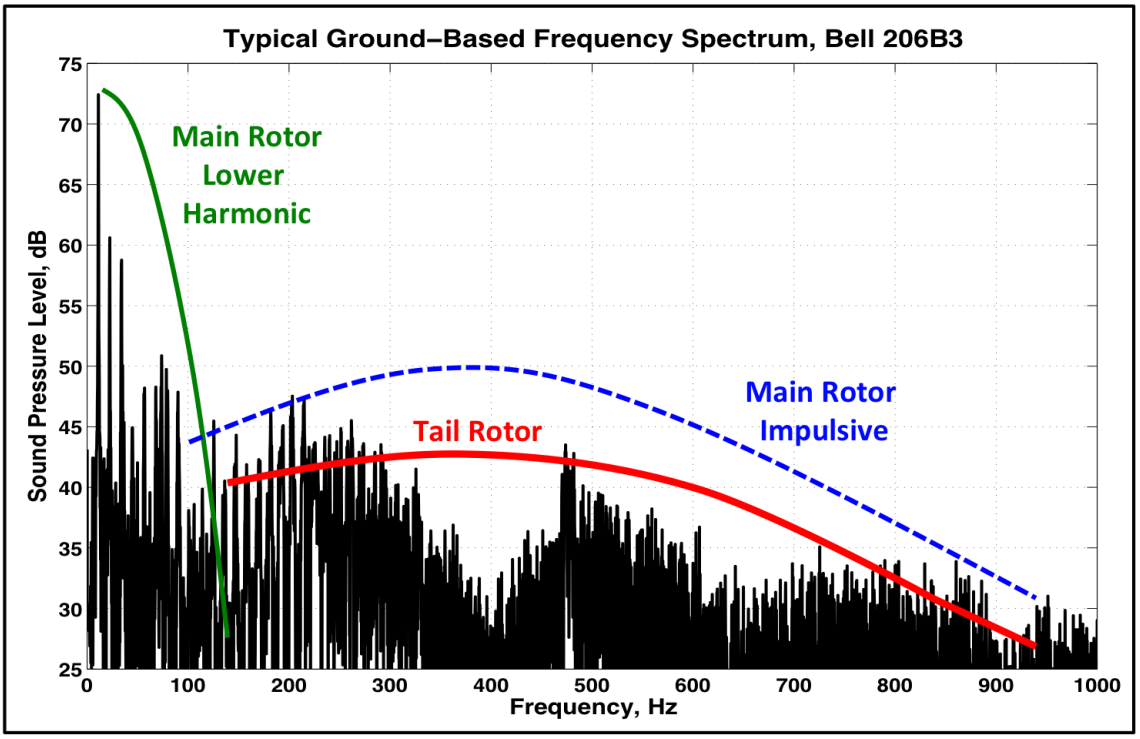

Figure 2.2: Typical frequency spectrum of helicopter noise. (Bell 206B3)

occurs when the rotor blades pass near the vortices created and trailed from the tips of preceding blades. These vortices induce rapid changes in the local angle of attack of the following blades causing rapid changes in rotor airloads. Since the magnitude of loading noise is related to the time-rate-of-change of the forces exerted by the blade on to the medium, a highly impulsive noise results. This condition commonly occurs during moderate speed shallow descents.[19] BVI noise is a particularly important consideration for community land use planning purposes because typical landing approach trajectories incorporate the same shallow descents which lead to high levels of BVI noise. Tail rotor harmonic noise sources are similar to main rotor harmonic noise sources and can be modeled in the same fashion. Typically, the tail rotor does

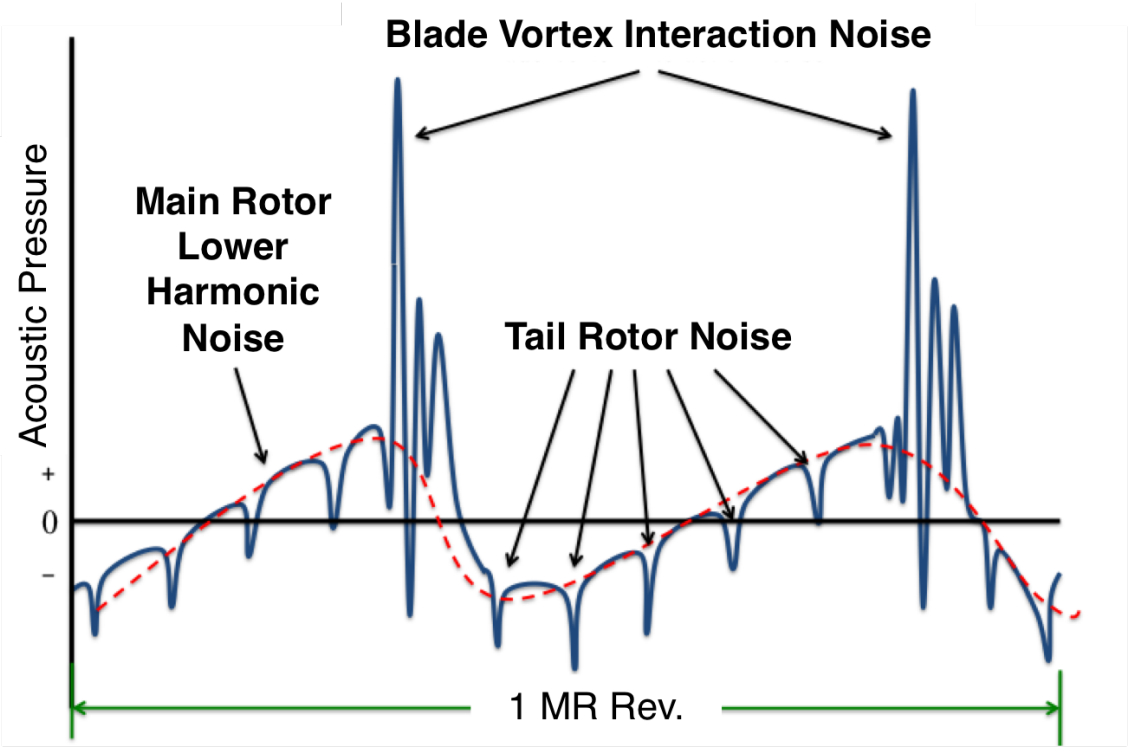

Figure 2.3: Notional acoustic pressure time history of helicopter noise.

not operate in conditions where significant impulsive noise occurs — however, due to the higher rotational rate of the tail rotor, typically six to seven times higher than the main rotor, tail rotor lower harmonic noise sources occur at higher frequencies than main rotor lower harmonic noise. (Figure 2.2) Since the human ear is more sensitive to these frequencies, tail rotor harmonic noise can be the dominant source of noise for annoyance.[20] A notional diagram of the acoustic pressure time-history produced by rotor harmonic noise sources is shown in Figure 2.3.

In addition to the rotor harmonic noise sources, there are several noise sources that are not harmonic with the rotor blade passage frequency. An aerodynamic source of non-rotor harmonic noise is rotor broadband noise. The rotor produces

broadband noise over the mid- to high-frequency range. Such noise is caused by random aerodynamic interactions with the rotor blades, due to turbulence generated by boundary layer effects, vortex shedding, flow separation, and re-ingestion of the rotor wake, as well as atmospheric turbulence.[21] This source of noise always exists on the rotor, but is usually only noticeable in operating regions where the other rotor noise sources are not dominant. While this noise source is generally not significant for helicopter rotors, it can be important for high thrust, low tip speed configurations, such as small unmanned vehicles or wind turbines. In addition to the aerodynamic noise sources, non-rotor harmonic noise is generated by the gearbox and engine of the helicopter. Engine noise has both tonal and broadband components, whereas gearbox noise is largely tonal. However, both sources of noise tend to be of much higher frequency than the other helicopter noise sources, and are much more readily absorbed by the atmosphere. As such, mechanical noise has little effect on ground noise contours except at very low altitudes where the distances between source and observer are small. This dissertation focuses on the modeling of rotor harmonic noise sources, since they are the dominant external noise sources of helicopters and consequently set the ground noise contours resulting from helicopter operations. Both main and tail rotor harmonic noise sources have the same mechanisms and can be modeled in the same fashion. One common way to model rotor harmonic noise sources is with the Ffowcs Williams – Hawkings (FW-H) equation,[22] which describes exactly how noise is generated by arbitrary surfaces in motion through a medium.

2.2 Harmonic Noise Source Modeling

2.2.1 Ffowcs Williams – Hawkings Equation

The FW-H equation (Equation 2.1) can be divided into three terms: monopole, dipole, and quadrupole (Figure 2.4 on the following page).

$$
\begin{aligned}
p'(x,t) = & \frac{1}{4\pi}\frac{\partial}{\partial t}\int_S \left[\frac{\rho_0 v_n}{r\,|1-M_r|}\right]_\tau dS - && \text{(monopole)} \\
& \frac{1}{4\pi}\frac{\partial}{\partial x_i}\int_S \left[\frac{P_{ij}n_j}{r\,|1-M_r|}\right]_\tau dS + && \text{(dipole)} \\
& \frac{1}{4\pi}\frac{\partial^2}{\partial x_i x_j}\int_S \left[\frac{Q_{ij}}{r\,|1-M_r|}\right]_\tau dS && \text{(quadrupole)}
\end{aligned}
\tag{2.1}
$$

The monopole term models thickness noise by considering the rotor blade as a set of monopole mass sources and sinks which describe how the blades displace the medium. The dipole term models the mechanisms of loading noise, including BVI, as a set of aerodynamic dipole sources on the surface of the blades that describe the forces the blades exert on the medium. The quadrupole term includes the effects of complex noise sources inside a fluid volume surrounding the rotor blades—this is how the effect of the transonic flow field that causes HSI noise is modeled. Since HSI noise is not a major consideration for the types of helicopters and operating conditions that are the focus of this dissertation, the quadrupole term will be neglected and only the on-surface monopole and dipole terms will be retained.

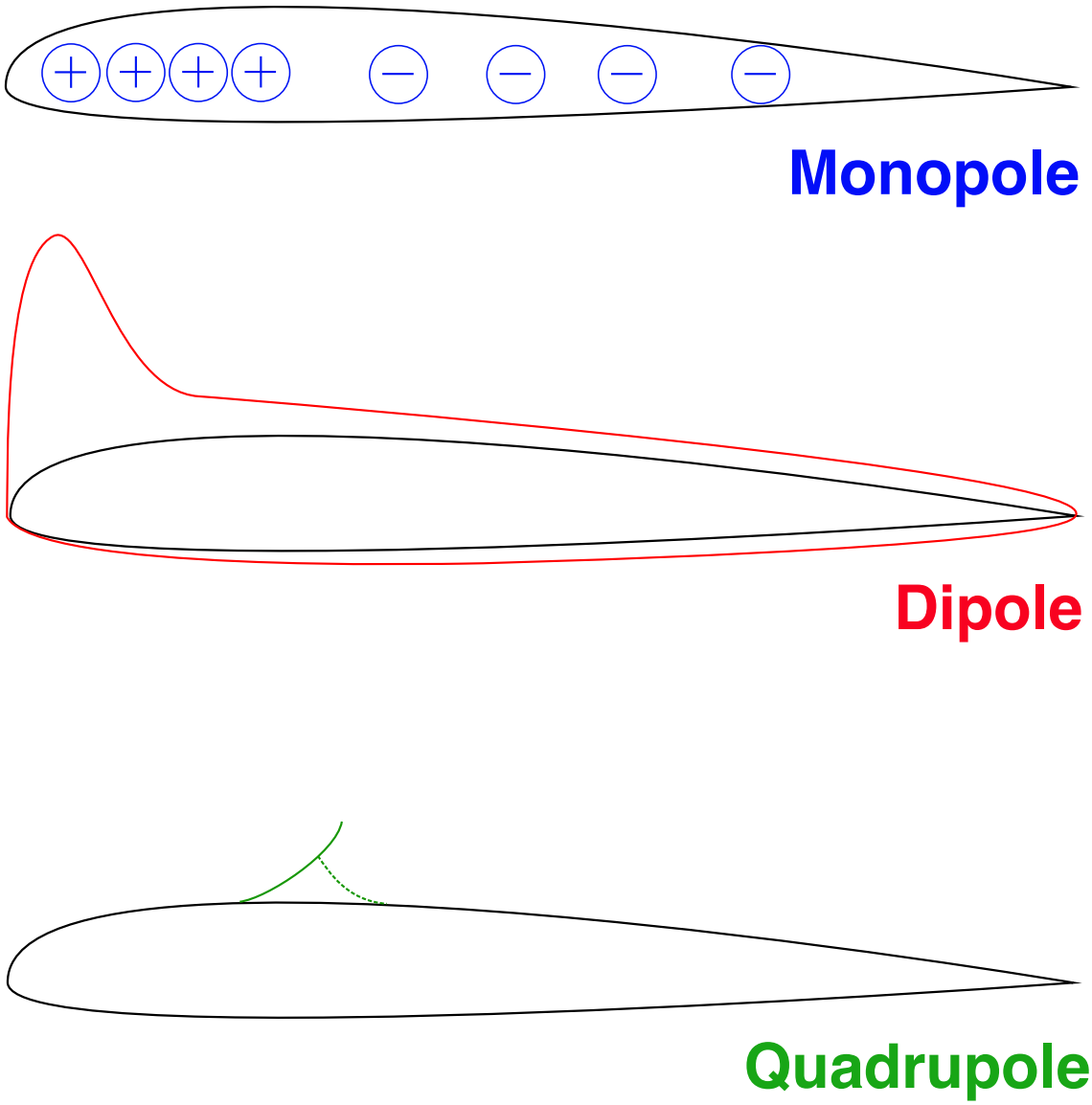

Figure 2.4: The aerodynamic origins of the three types of noise sources in the Ffowcs Williams – Hawkings equation.

2.2.2 Non-Dimensionalization

2.2.2.1 Non-Dimensional Governing Parameters

Previous research, both theoretical and experimental,[23] has shown that the external noise radiation of a particular rotor design in steady-state flight can be uniquely determined from a set of four non-dimensional governing parameters. In this dissertation, these parameters are non-dimensionalized as the rotor advance ratio (μ), hover tip Mach number (M_H), thrust coefficient (C_T), and mean inflow ratio (λ). The advance ratio and hover tip Mach number control the motion of the blade sections through the medium, and hence the free-stream Mach number seen by the blades over each rotor revolution. In addition, these parameters control the epicycloidal pattern of the wake (Figure 2.5), and hence the interaction geometry of individual blade vortex interactions. The interaction geometry controls how the acoustic effect of BVI accumulates in phase, and hence its magnitude and directivity, as shown in Figure 2.6 on page 29. The thrust coefficient and inflow ratio are important parameters in determining the magnitude and distribution of aerodynamic loads over the rotor disk. The inflow ratio influences the angle-of-attack of the rotating blade sections and hence lift coefficient. In addition, the inflow ratio controls the "miss-distance" between the rotor blades and the trailed wake during BVIs (Figure 2.7), and hence their strength. Lastly, the thrust coefficient controls the rotor blade loading as well as the strength of the trailed tip vortices, and hence the strength of BVI. Sometimes, different sets of four independent non-dimensional governing parameters are selected, but they are equivalent - for example, advancing

tip Mach number (M_{AT}) may be substituted for hover tip Mach number, as the two are related to each other by advance ratio. (See Equation 2.9) The selection of the set of parameters used in this dissertation will be shown analytically in Sections 2.2.2.3 and 2.2.3.

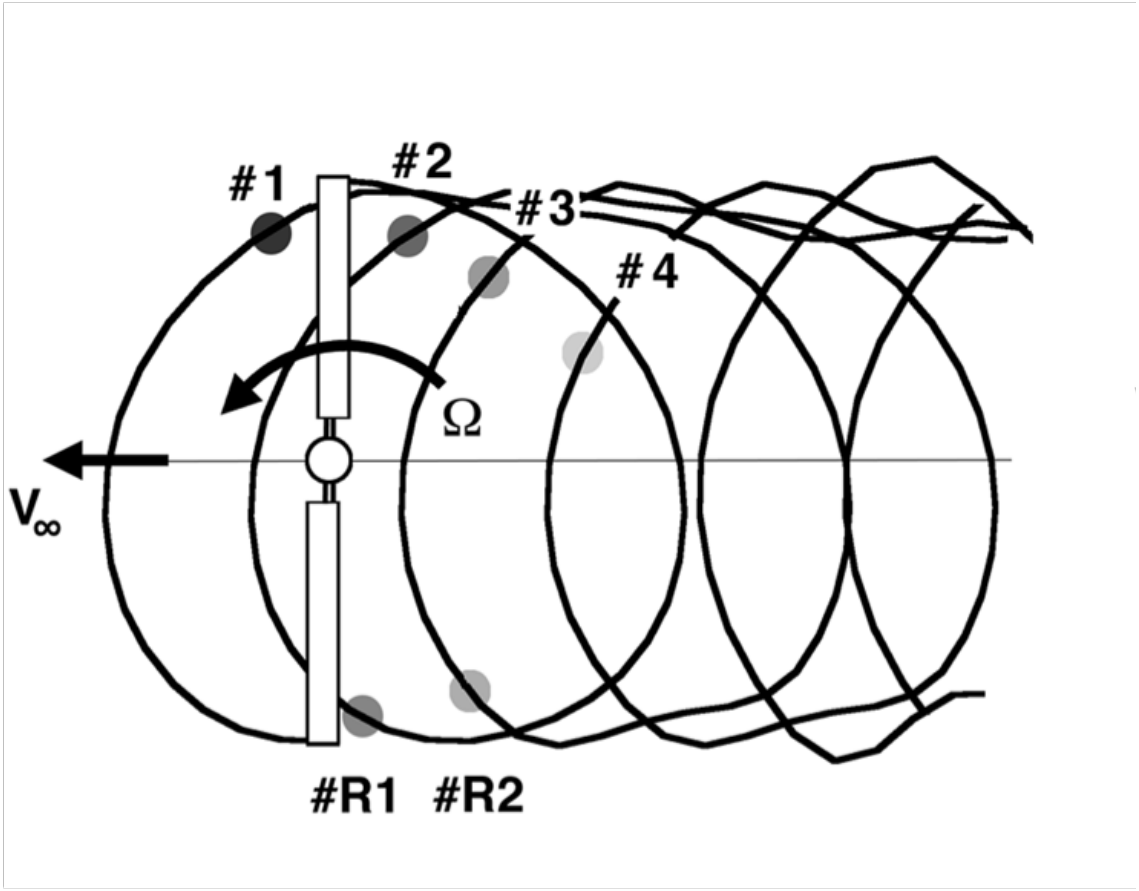

Figure 2.5: The "top-view" geometry of the wake, controlled by μ and M_H. The potential BVI locations on the advancing and retreating sides are label.

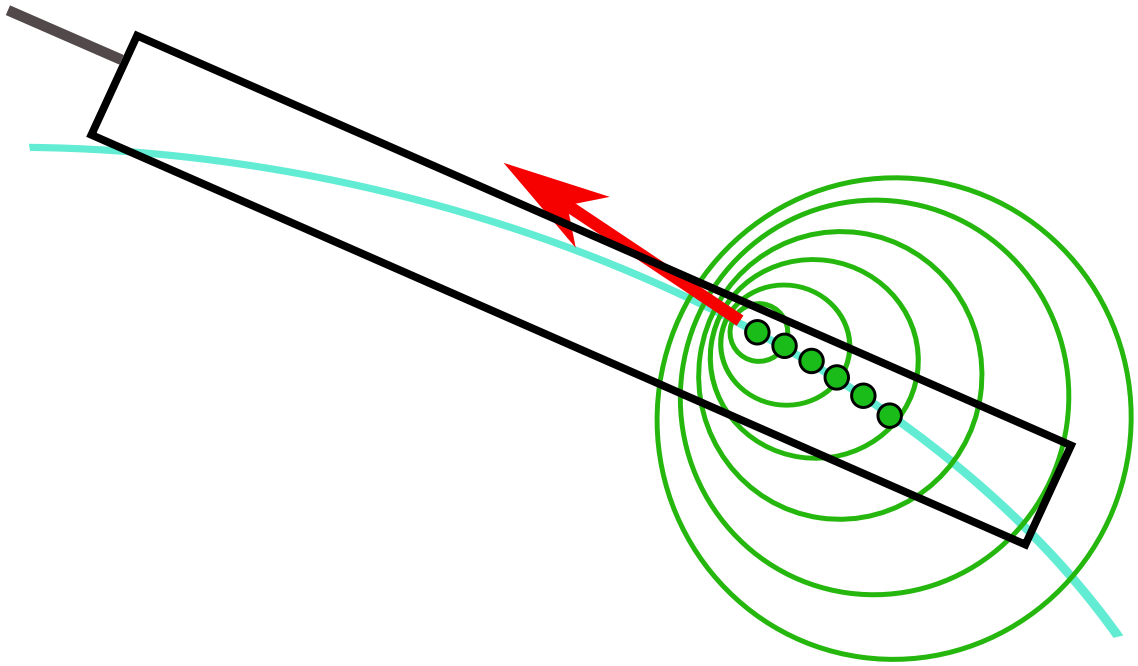

Figure 2.6: A diagram of the phase collection process of Blade-Vortex Interaction (BVI) noise.

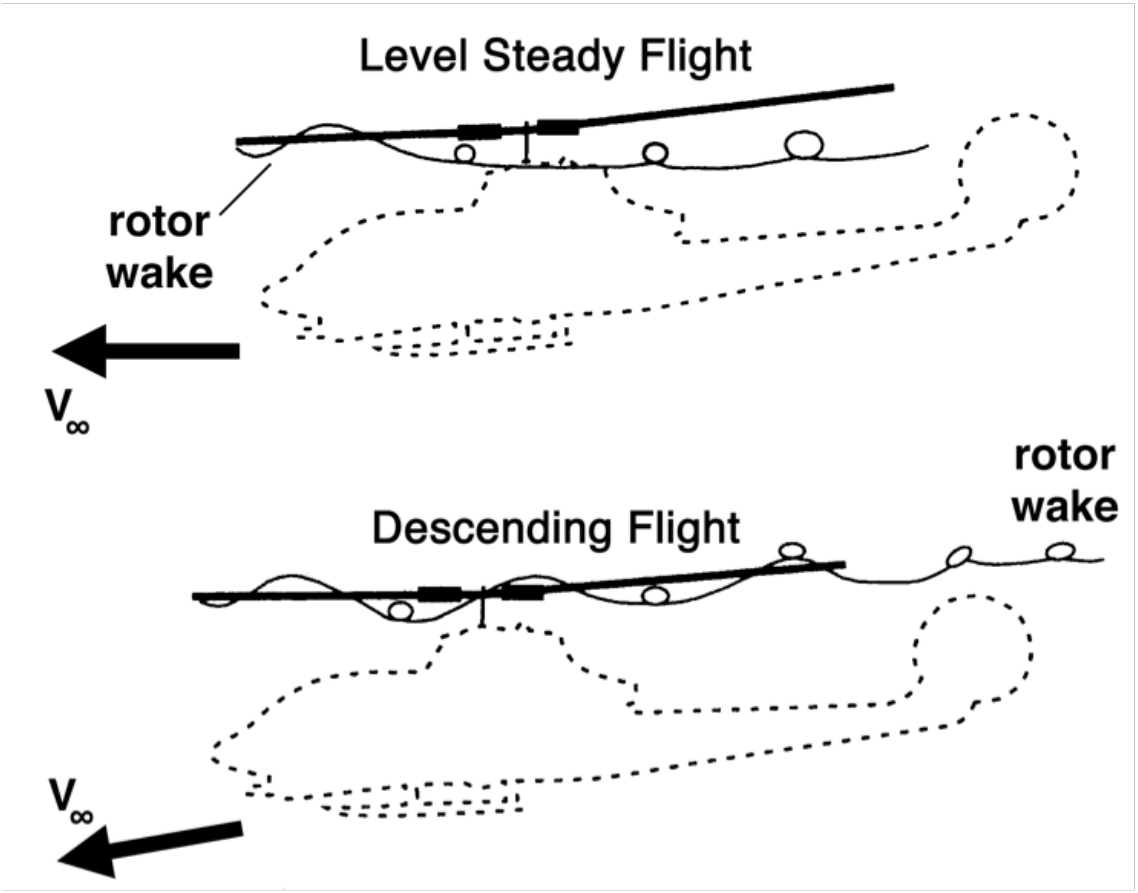

Figure 2.7: The "side-view" geometry of the rotor wake, controlled by λ.

2.2.2.2 Generalization

An important application of non-dimensionalization is that it allows noise models defined uniquely in terms of the governing non-dimensional parameters values to be generalized across a wide range of equivalent dimensionally-defined flight conditions. The Quasi-Static Acoustic Mapping method (Q-SAM)[19] is a prior application of this principle to helicopter noise, as mentioned in Section 1.3.2.2. Q-SAM allows an acoustic equivalence to be made between flight path angle and low to moderate longitudinal accelerations. The equivalence is derived from the non-dimensional governing parameters—under the assumption that gross weight, rotor RPM, and airspeed are held constant, three of the four non-dimensional governing parameters can be held fixed: thrust coefficient, hover tip Mach number, and advance ratio. Then, by applying a simple longitudinal force balance and simple momentum theory, it is shown that rotor inflow ratio and hence BVI "miss-distance," can be held constant for a constant rotor tip-path-plane angle of attack, which is itself defined by the constant helicopter drag-to-weight ratio and the variable helicopter flight path angle and longitudinal acceleration. (See Section 2.2.3.1 for more details.) Consequently, for moderate accelerations where the airspeed of the helicopter changes slowly, accelerations can be modeled by using measured data for steady-state flight conditions at a flight path angle resulting in an equivalent tip-path-plane angle of attack, and hence equivalent inflow ratio. When combined with RNM, the effect is the selection of acoustic hemisphere models based on main rotor advance ratio and inflow ratio, as opposed to airspeed and rate of descent, as shown in Figure 2.8 on

the following page.

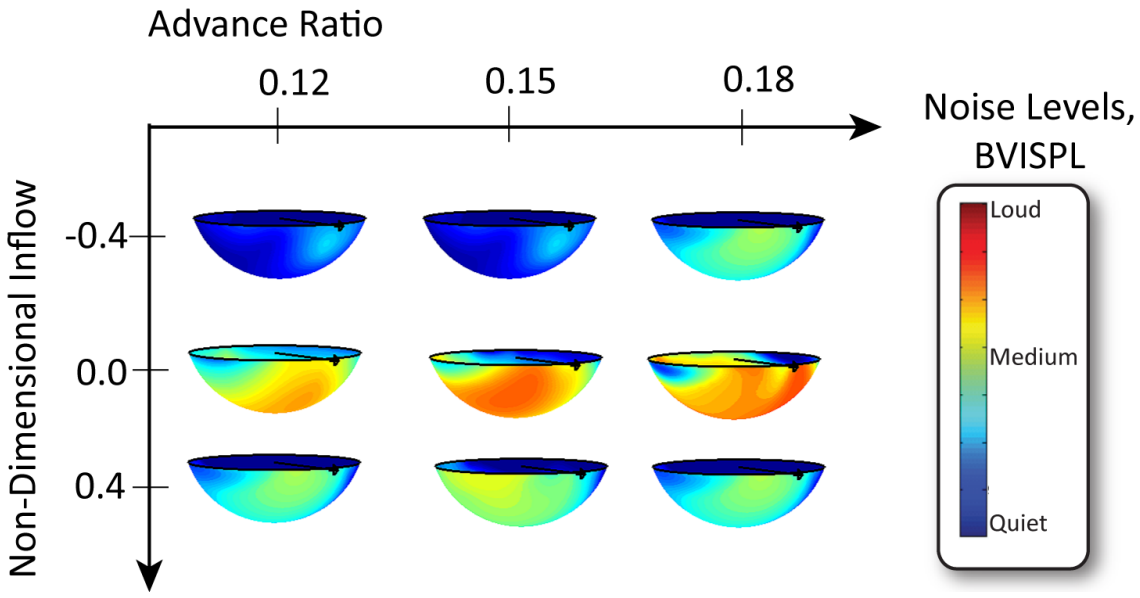

Figure 2.8: RNM/Q-SAM database of source noise hemispheres based on μ and λ.

This concept was further expanded to steady-turning flight conditions by the author,[24] allowing moderate accelerating, turning, and descending maneuvers to be modeled using steady straight-line flight data. However, under steady turning flight conditions, thrust must vary to counteract centripetal acceleration. Variation in thrust changes the inflow ratio, the amount of which can be determined from momentum theory, but also changes the vortex strength for which the effect on noise cannot be directly determined without the acquisition of helicopter noise data at several thrust levels. The result is a helicopter noise model defined in terms of main rotor thrust coefficient in addition to advance ratio and inflow ratio, as shown in Figure 2.9 on the next page.

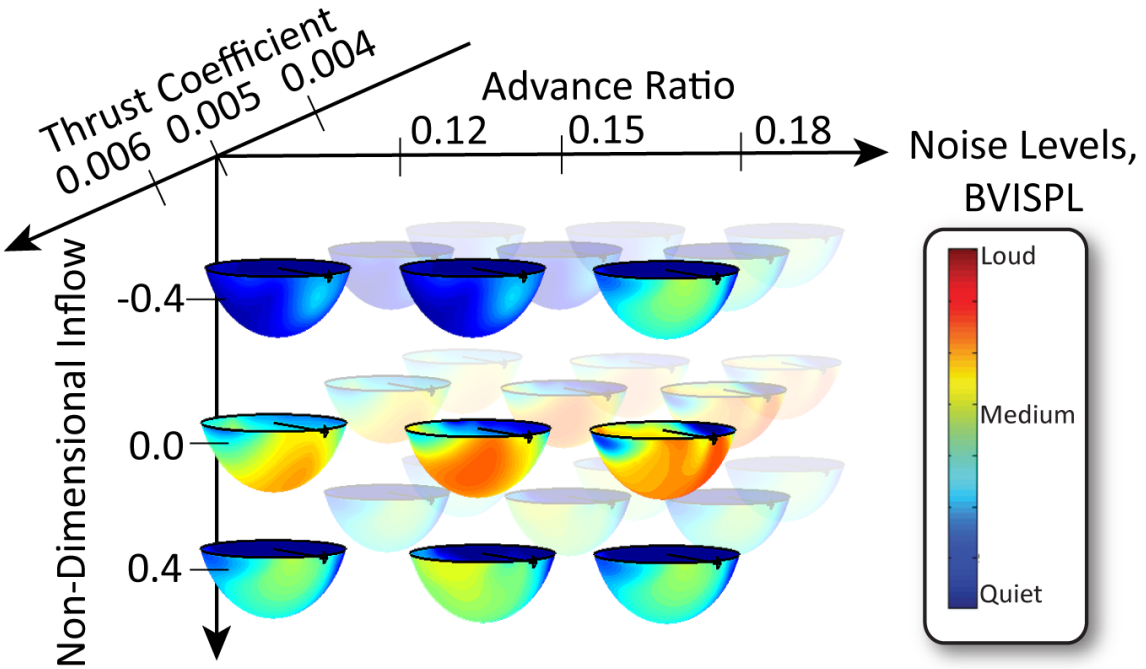

Figure 2.9: RNM/Q-SAM database of source noise hemispheres, extended to steady turning flight.

2.2.2.3 Non-Dimensional Ffowcs Williams – Hawkings

In order to facilitate comparisons between acoustically equivalent rotor operating conditions, it is beneficial to rearrange the FW-H equation in a non-dimensional form. This can be performed, based on the approach used in Reference [23], as follows:

First, the time of observation of the acoustic pressure is non-dimensionalized by the rotational rate of the rotor:

$$\bar{t} = \frac{t}{\Omega} \tag{2.2}$$

The time of emission is likewise non-dimensionalized:

$$\bar{\tau} = \frac{\tau}{\Omega} \tag{2.3}$$

The geometric parameters can be non-dimensionalized—following standard convention, these are non-dimensionalized by rotor radius:

$$\bar{r} = \frac{r}{R} \tag{2.4a}$$

$$\bar{x_i} = \frac{x_i}{R} \tag{2.4b}$$

$$d\bar{S} = \frac{dS}{R^2} \tag{2.4c}$$

The Mach number is defined as the ratio between the speed of the element with respect to the medium to the speed of sound:

$$M = \frac{U}{a_0} \tag{2.5}$$

The hover tip Mach number is defined as the relation between the rotor radius and the rotational rate:

$$M_H = \frac{\Omega R}{a_0} \tag{2.6}$$

The tip Mach number in forward flight can then be defined in terms of the advance ratio and related to hover tip Mach number:

$$M_T = \frac{U}{a_0} = \frac{\Omega R + V \sin\psi}{a_0} = M_{HT}\left(1 + \mu \sin\bar{\tau}\right) \tag{2.7}$$

where the advance ratio is the ratio between the aircraft velocity and hover tip velocity:

$$\mu = \frac{V}{\Omega R} \tag{2.8}$$

The advancing tip and hover tip Mach numbers are therefore related by advance ratio:

$$M_{AT} = M_{HT}\,(1+\mu) \tag{2.9}$$

By neglecting spanwise and perpendicular flow, the velocities normal to the rotor blade surfaces are assumed to have the form:

$$v_n = U\frac{dz}{dy} = U\xi = Ma_0\xi \tag{2.10}$$

where $\xi = \frac{dz}{dy}$ is the geometric slope of the airfoil surface.

The acoustic pressure is then non-dimensionalized as the acoustic pressure coefficient:

$$C_{p'}(\bar{x},\bar{t}) = \frac{p'(\bar{x},\bar{t})}{\rho_0 a_0^2} \tag{2.11}$$

Similarly, the on-surface blade pressures may be non-dimensionalized with respect to the dynamic pressure:

$$C_{p_{ij}} = \frac{p_{ij}}{\rho_0 U^2} \tag{2.12}$$

Substituting Equations 2.2 through 2.12 back into the FW-H equation (2.1), and neglecting the quadrupole term yields:

$$\begin{aligned} C_{p'}(\bar{x},\bar{t})\rho_0 a_0^2 = {} & \frac{1}{4\pi}\frac{M_{HT}a_0}{R}\frac{\partial}{\partial\bar{t}}\int_S\left[\frac{\rho_0\xi M a_0}{\bar{r}R(1-M_r)}d\bar{S}R^2\right]_{\bar{\tau}} \\ & -\frac{1}{4\pi}\frac{1}{R}\frac{\partial}{\partial\bar{x}_i}\int_S\left[\frac{C_{p_{ij}}n_j\rho_0\frac{U}{a_0}^2}{\bar{r}(1-M_r)}d\bar{S}R^2\right]_{\bar{\tau}} \end{aligned} \tag{2.13}$$

Simplifying this expression yields a non-dimensionalized version of the FW-H equation (2.1):

$$C_{p'}(\bar{x},\bar{t}) = \frac{1}{4\pi}\frac{\partial}{\partial\bar{t}}\int_S\frac{\xi M}{\bar{r}(1-M_r)}d\bar{S} - \frac{1}{4\pi}\frac{\partial}{\partial\bar{x}_i}\int_S\frac{C_{p_{ij}}n_j M^2}{\bar{r}(1-M_r)}d\bar{S} \tag{2.14}$$

Neglecting the spanwise and perpendicular flow components, and substituting for the resulting blade element Mach numbers:

$$C_{p'}(\bar{x},\bar{t}) = \frac{1}{4\pi}\frac{\partial}{\partial \bar{t}}\int_S \frac{\xi M_{HT}(1+\mu\sin\bar{\tau})\bar{r}}{\bar{r}(1-M_{HT}(1+\mu\sin\bar{\tau})\bar{r}\cos\theta)}d\bar{S} - \frac{1}{4\pi}\frac{\partial}{\partial \bar{x}_i}\int_S \frac{C_{p_{ij}}n_j {M^2}_{HT}(1+\mu\sin\bar{\tau})^2\bar{r}^2}{\bar{r}(1-M_{HT}(1+\mu\sin\bar{\tau})\bar{r}\cos\theta)}d\bar{S} \tag{2.15}$$

where θ is the angle between the assumed rotor plane and the observer.

From Equation 2.15 it is apparent that monopole thickness noise can be solved for directly with operating condition of the rotor defined by hover tip Mach number (M_H), advance ratio (μ), and the blade geometry. For higher tip Mach numbers, this formulation is known to underpredict the resulting noise levels due to additional off-surface aerodynamic effects which are included in the neglected quadrupole volumetric source term. However, for moderate tip Mach numbers, the monopole prediction provides a reasonable level of accuracy.

The dipole term is likewise dependent on hover tip Mach number (M_H) and advance ratio (μ); however, it is also a function of the non-dimensionalized on-surface blade pressures described by $C_{p_{ij}}$. Further assumptions about the aerodynamic loads must be introduced to identify the complete set of non-dimensional governing parameters for rotor harmonic noise.

2.2.3 Aerodynamic Loading Model

Solving for the dipole loading noise of the rotor is a more complex task than the monopole thickness noise calculation. While the monopole source strengths are known exactly from the geometry and motion of the rotor blades with respect to the

medium, the determination of the dipole source strengths is less straighforward. The four non-dimensional governing parameters of rotor harmonic noise (μ, C_T, λ, and M_H) specify a unique operating condition for the rotor, but there is no simple way of calculating the exact distribution of loads across the rotor in both space and time. Without restrictions on how loads can be distributed across the rotor disk, there are a theoretically infinite number of configurations that can yield the same far-field noise radiation. However, by introducing some reasonable engineering assumptions, a physical structure can be developed to limit the set of possible loading distributions to those that are practically realizable.

2.2.3.1 Trim

The first component to the assumed loading structure is a simple trim model. Given an estimate of the flat plate drag area and rotor "hub-force" (related to profile drag) of the helicopter, a longitudinal force balance (Figure 2.10 on the following page) can be established in order to estimate the angle of attack of the tip-path-plane for a given flight condition as follows:

$$\alpha_{TPP} = -\frac{D_f + H}{W} - \gamma - \frac{a_x}{g} \tag{2.16}$$

where the parasite drag-to-weight ratio can be estimated as:

$$\frac{D_f}{W} = \frac{f_e}{2AC_T}\mu^2 \tag{2.17}$$

For low flight speeds, H/W may be included in the parasite drag term, otherwise it may be estimated using a simple blade-element theory derived approximation, one

standard expression being:

$$\frac{H}{W} = \frac{\sigma c_{d0}}{8} \frac{1 + 4.6\mu^2}{\mu C_T} \tag{2.18}$$

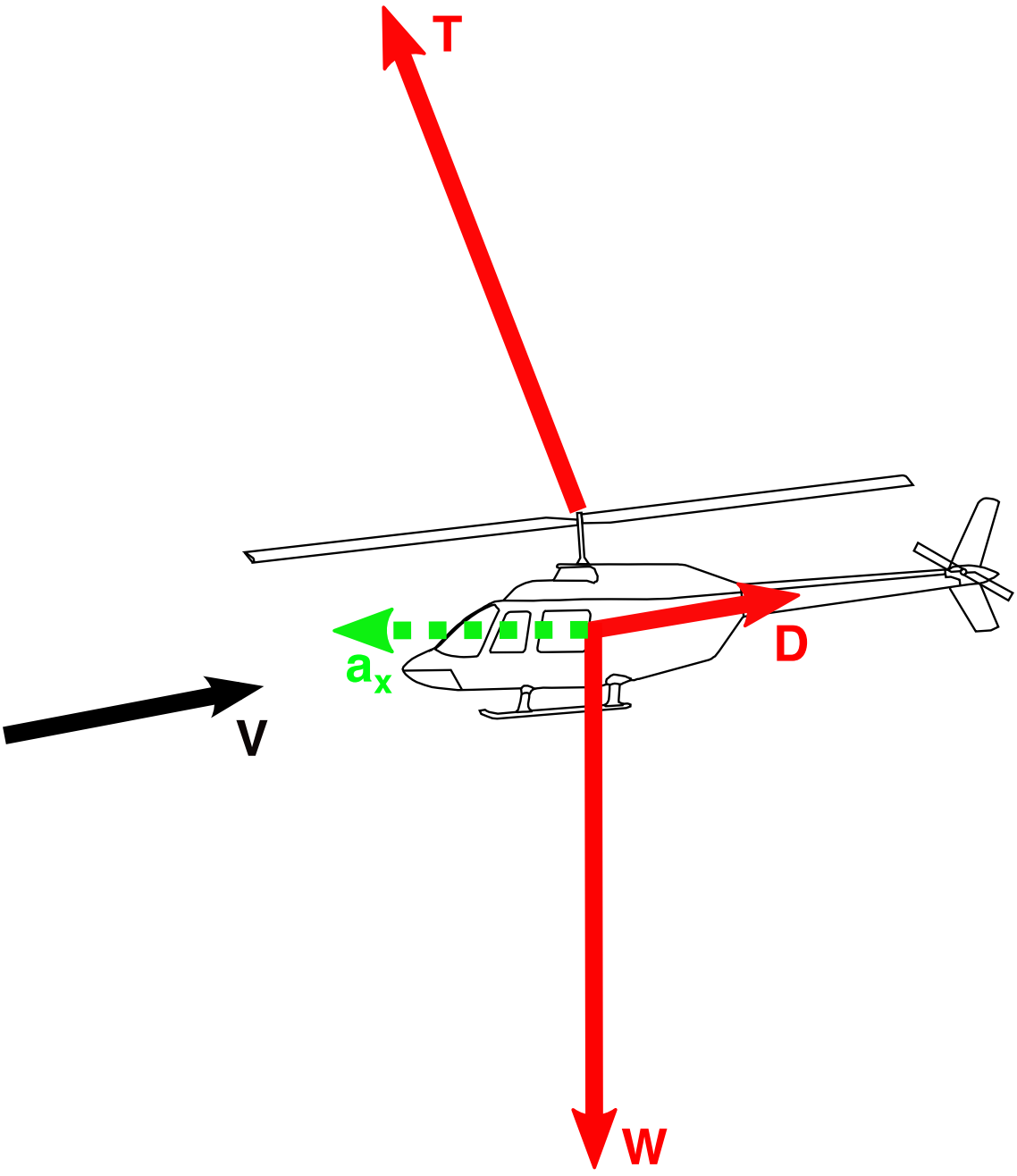

Figure 2.10: Longitudinal force balance.

From the angle of attack of the rotor disk and the required rotor thrust, the

non-dimensional inflow through the rotor can be calculated numerically using the equation:

$$\lambda = -\mu \tan \alpha_{TPP} + \frac{C_T}{2\sqrt{\lambda^2 + \mu^2}} \tag{2.19}$$

where the inflow ratio is defined in forward flight as:

$$\lambda = \frac{-V \sin \alpha_{TPP} + v_i}{\Omega R} \tag{2.20}$$

and the thrust is non-dimensionalized as thrust coefficient, which is defined as:

$$C_T = \frac{T}{\rho_0 A (\Omega R)^2} \tag{2.21}$$

2.2.3.2 Lower Harmonic Loading

Next, the lower harmonic loading can be given an assumed form. Under the assumption of uniform inflow and an ideally twisted rotor, blade element theory suggests that the spanwise distribution of rotor blade loads should be approximately triangular from the blade hub to the blade tip. In the chordwise direction, the load is concentrated at the quarter chord. The azimuthal distribution can be specified in rotor time for each individual lower harmonic using a truncated Fourier series:

$$T = T_0 + \sum_n^k T_{nC} \cos n\psi + T_{nS} \sin n\psi \tag{2.22a}$$

$$D = D_0 + \sum_n^k D_{nC} \cos n\psi + D_{nS} \sin n\psi \tag{2.22b}$$

A diagram of the T_{1C} contribution to the loading distribution is shown in Figure 2.11 on the next page.

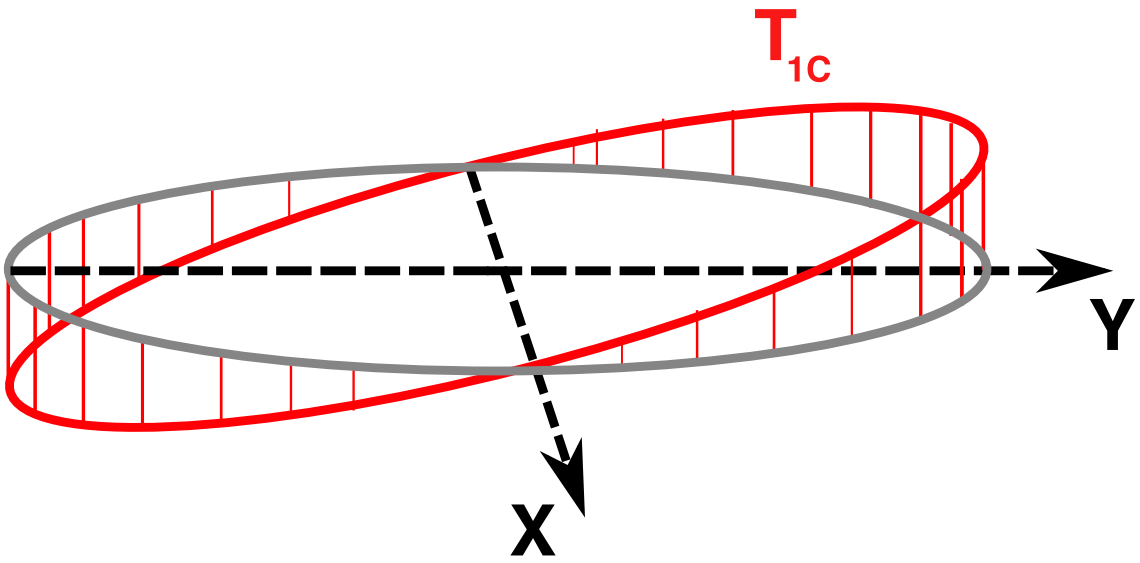

Figure 2.11: Contribution of Fourier coefficient T_{1C} to lower harmonic loading.

2.2.3.3 Rotor Wake Modeling

While suitable for the lower harmonic loads, a direct specification of the individual loading harmonics is tedious for impulsive noise sources, such as BVI, and does not include additional physical understanding of the problem. A better approach is to model the BVI noise process with a model of the vortex wake structure, providing a physical description of the blade-vortex interaction, including both the effects of the miss-distance between the vortex and the rotor blade, which determines the strength of individual interactions, as well as the phase collection process of the interactions, which determines the directivity of radiated noise.

Figure 2.12 on page 42 uses Hugens' wavelets to illustrate in two-dimensions how the interaction angle between the vortex and the blade causes the acoustic effect of the BVI to phase in the medium causing the noise to be radiated in different

directions. For instance, on the advancing side of the rotor the "α" interaction occurs further from the rear of the rotor and at an oblique angle; as the disturbance moves along the interaction through the medium, the waves collect in phase focusing the radiated noise ahead of and towards the retreating side of the rotor. As BVI occur farther back on the rotor disk, the interaction angle changes and directivity shifts towards the advancing side. Interaction "γ" is an example of a parallel BVI, where the blade and vortex are parallel at the time of the interaction so that the disturbance in the medium occurs near-simultaneously along its extent–the results in a large magnitude of BVI noise radiated towards the advancing side of the rotor. The same process occurs on the retreating side of the rotor, along these interactions contribute less to the overall noise radiation of the helicopter since the blade section Mach numbers are lower on this side.

The BVI noise process is dominated by the trailed rotor tip vortices; in order to simulate BVI, a physics-based description of the path of the trailed tip vortices through medium is desired. Undistorted rigid wake models lack the flexibility required to accurately model the miss-distance of the interactions. On the other hand, distorted prescribed wake models provide a realistic structure for describing the path of the trailed tip vortices through the medium for a given flight condition. There are two major prescribed wake models in use: the UTRC generalized wake model[25] and Beddoes wake model.[26] The generalized wake model defines a set of geometric distortions to a rigid wake. In practice, the values of these distortion parameters are determined from empirically measured data for specific flight conditions and rotor configurations. The distortions to the wake in this model have no direct

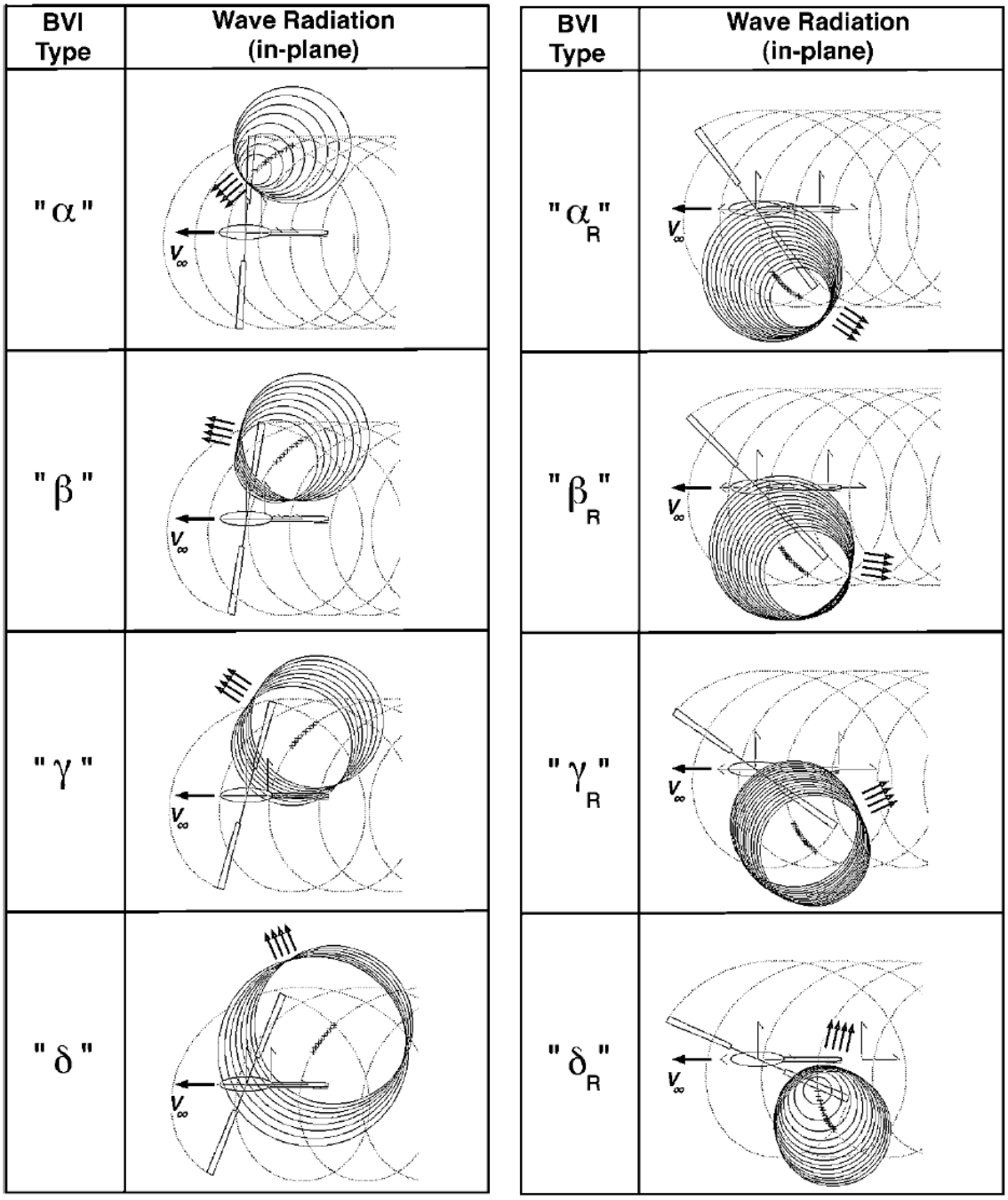

Figure 2.12: Acoustic phasing and corresponding in-plane directivity of different advancing and retreating side BVI. [1]

physical meaning and are simply a description of the measured wake geometry. The Beddoes wake model, on the other hand, defines tip vortex locations for steady

flight under some physical assumptions. In the original Beddoes wake model, the position of the tip vortices was determined by assuming a linear longitudinal inflow distribution superimposed with a lateral cubic downwash distribution to account for tip effects. The convection of the non-interacting vortices is then calculated based on the combined freestream flow and prescribed induced inflow distribution over the rotor. That is:

$$\bar{z} = \mu_z \phi - \int_{\psi_b}^{\psi_v} \lambda_i \, d\psi \tag{2.23}$$

where $\phi = \psi_b - \psi_v$ is the wake age and where the Glauert[27] longitudinal linear inflow distribution is combined with a lateral cubic downwash distribution to produce Beddoes' prescribed inflow over the rotor disk such that:

$$\lambda_i = \lambda_{i_0} \left(1 + \chi \cos\psi + \chi | \, r_v \sin\psi|^3\right) \tag{2.24}$$

The mean induced inflow ratio, λ_{i_0} can be solved for numerically from [28]:

$$\lambda_{i_0} = \frac{C_T}{2\sqrt{\left(\mu_z + \lambda_i\right)^2 + \mu_x^2}} \tag{2.25}$$

χ is the wake skew angle, defined as:

$$\chi = \left| \tan^{-1}\left(\frac{\mu_x}{\mu_z + \lambda_{i_0}}\right) \right| \tag{2.26}$$

The Beddoes wake method can be further extended by assuming alternate inflow distributions across the rotor disk. For instance, van der Wall[29] incorporated Drees' [30] lateral inflow model and increased the constant inflow ratio over the area swept by the rotor blades in order to account for the effect of the root cut-out:

$$\lambda_i = \lambda_{i_0} \left(1.2 + \chi \cos\psi + \chi | \, r_v \sin\psi|^3 - 2\mu_x \sin\psi\right) \tag{2.27}$$

In practice, the best coefficients of the linear inflow distribution are not known *a priori* for a given rotor configuration. For instance, the longitudinal inflow ratio

is sometimes taken as $\frac{\chi}{2}$ instead of χ, based on other experimental observations of rotor inflow. A more general way of expressing a range of possible assumed inflow distributions is:

$$\lambda_i = \lambda_{i_0} \left(A\chi \left(\cos\psi + | r_v \sin\psi |^3 \right) + 2B\mu_x \sin\psi + C \right) \tag{2.28}$$

where A, B, and C are parameters which control the respective longitudinal, lateral, and mean components of the prescribed linear distribution of inflow over the rotor.

Given this general form of the assumed inflow distribution, the vertical displacement of the rotor tip vortices can be solved for using Equation 2.23. Underneath the rotor disk, where BVI occur, the integration results in the following algebraic expression of the vertical wake geometry:

$$\bar{z} = \mu_z \phi - \lambda_{i_0} \left[A\chi \left(\cos\psi_v + \frac{\mu_x \phi}{2 r_v} - | r_v \sin\psi_v |^3 \right) + 2B\mu_x \sin\psi_v + C \right] \phi \tag{2.29}$$

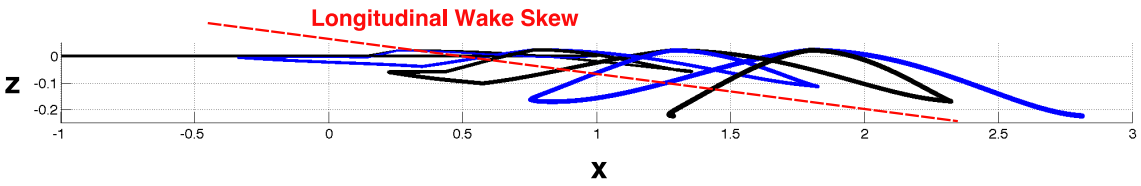

Figure 2.13: A side view of the Beddoes wake model.

In addition to the vertical displacement of the wake, the longitudinal and lateral motion of the wake affects the phase collection process of the BVI. Near the rotor disk, the "top-view" geometry of the wake is mostly epicyclodial, although the tip vortices roll-up somewhat inboard of the blade tips:

$$\bar{x} = r_v \cos\psi_v + \mu_x \phi \tag{2.30a}$$

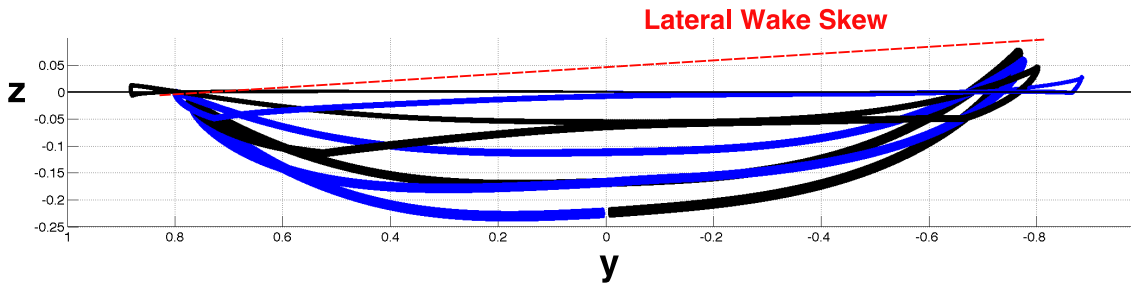

Figure 2.14: A head-on view of the Beddoes wake model.

$$\bar{y} = r_v \sin \psi_v \tag{2.30b}$$

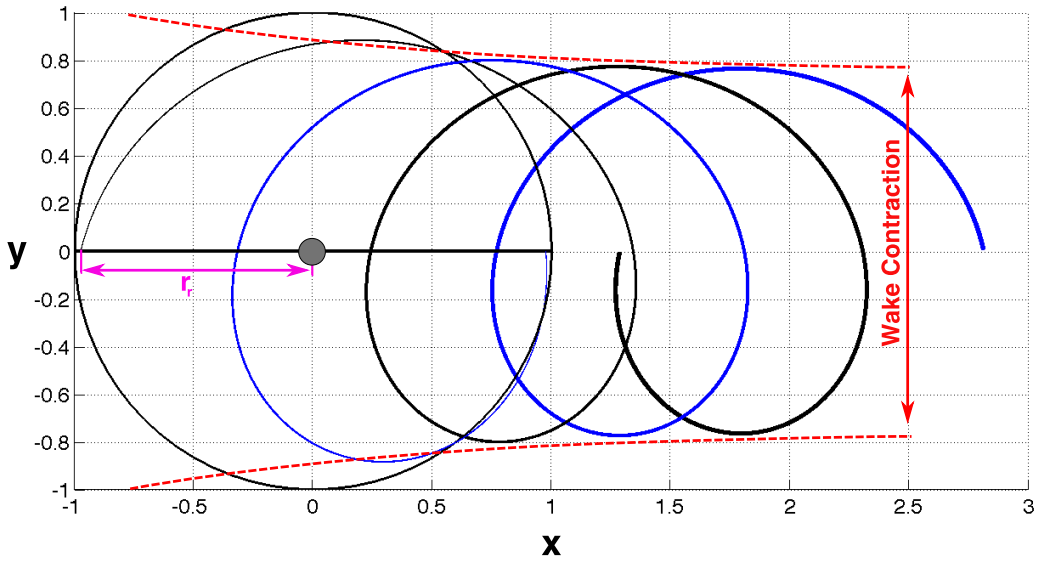

Figure 2.15: An overhead view of the Beddoes wake model.

Over time the rotor wake contracts slightly, which can change the phase of late BVI relative to the earlier BVI. This can be accounted for by incorporating a model

of the wake contraction, such as that identified by Landgrebe.[31]

$$r_v = r_r \left(D + (1 - D)e^{-\lambda_1 \phi}\right) \tag{2.31a}$$

$$\lambda_1 = 0.145 + 27C_T \tag{2.31b}$$

In addition to the wake geometry, the structure of the vortex has an effect on the magnitude and impulsiveness of the interaction. The Biot-Savart law describes the flow induced by an inviscid vortex, and accurately models the flow induced by real vortices at relatively far distances from the vortex. However, near the vortex, viscosity reduces the velocity induced by the vortex. The Vatistas model[32] describes the resulting tangential velocity profile induced by an infinitesimal viscous vortex segment:

$$v_\theta = \frac{\gamma_v r}{2\pi(r_c^{2n} + r^{2n})^{(1/n)}} \tag{2.32}$$

If the vortex strength is non-dimensionalized as:

$$\bar{\gamma}_v = \frac{\gamma_v}{\Omega R^2} \tag{2.33}$$

Then the model can be expressed as:

$$\frac{v_\theta}{\Omega R} = \frac{\bar{\gamma}_v \bar{r}}{2\pi(\bar{r}_c^{2n} + \bar{r}^{2n})^{(1/n)}} \tag{2.34}$$

where $\bar{r} = r/R$ and $\bar{r}_c = r_c/R$.

The Vatistas model is a generalization of several commonly used vortex models (Figure 2.16 on the next page). For $n = 1$, this is equivalent to the Scully vortex model.[33] For $n = 2$, the model is equivalent to the Bagai-Leishman model.[34] In the limit $n \to \infty$, the Rankine vortex is described. In this dissertation, the commonly used Bagai-Leishman form with $n = 2$ is assumed, although the choice of n has little

impact on the resulting BVI noise since the slope of the tangential velocity inside the core region is similar for all values of n. The viscous vortex core does not stay a constant size, but grows as the vortex ages. One common analytical model of viscous vortex core growth is the Lamb-Oseen vortex model.[35] In non-dimensional form, this can be expressed as:

$$\bar{r}_c = \sqrt{4C_v\phi} \tag{2.35}$$

where C_v is an empircal constant.

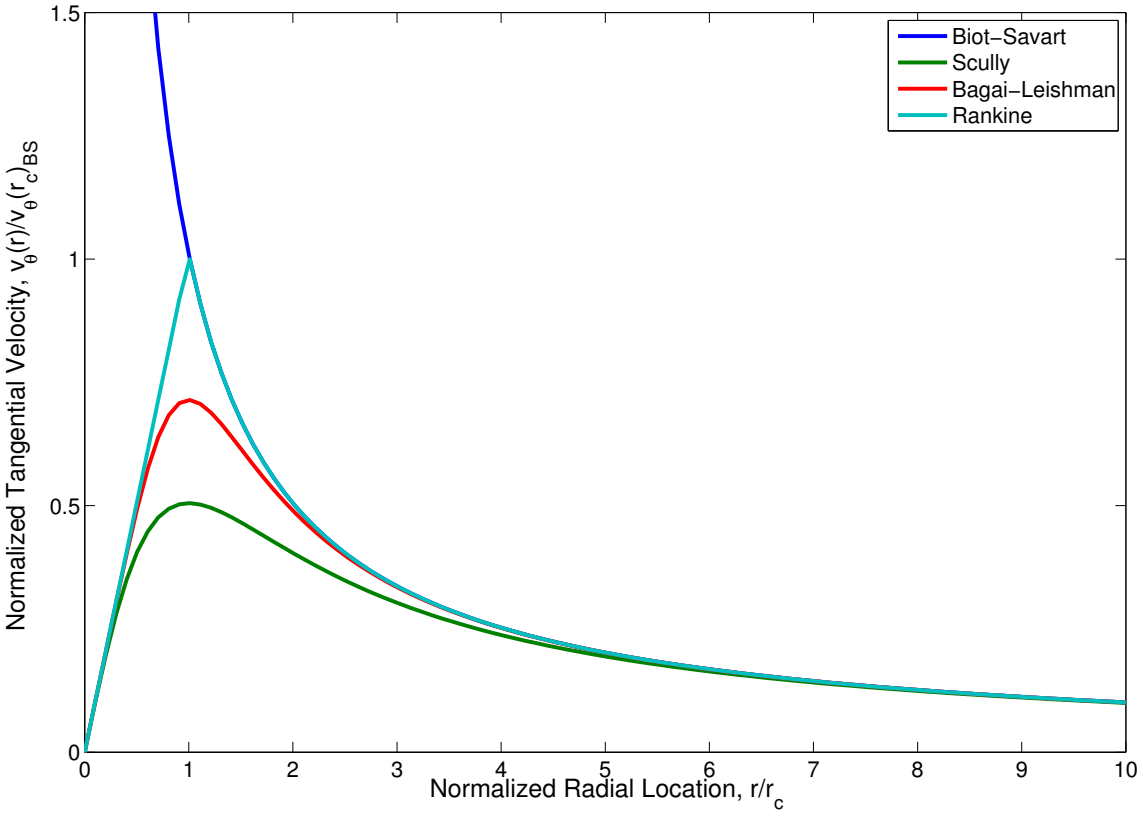

Figure 2.16: Vortex core tangential velocity profiles for several common models, normalized against Rankine core velocity.

However, the Lamb-Oseen model starts with an infinitesimal vortex core size,

which is not physically realistic. Bhagwat and Leishman[36] modified the Lamb-Oseen model to include an initial vortex core size, which more closely matches experimental measurements.

$$\bar{r}_c = \sqrt{\bar{r}_0^2 + 4C_v\phi} \tag{2.36}$$

The non-dimensional strength of the vortex is assumed to vary harmonically about the azimuth:

$$\bar{\Gamma} = \bar{\Gamma}_0 \left(\gamma_0 + \gamma_{1S} \sin\psi_v + \gamma_{1C} \cos\psi_v\right) \tag{2.37}$$

where the nominal value of the vortex strength is that produced by constant spanwise linear blade loading, again non-dimensionalized by ΩR^2:

$$\bar{\Gamma}_0 = \frac{2\pi C_T}{b} \tag{2.38}$$

Once the wake structure is fully defined, the instantaneous velocities induced on the blades as they travel about the rotor disk can be determined by summing the contributions of the trailed tip vortex segments, and from these the time-varying angles of attack of the blade sections.

Due to the relative simplicity of this wake model, it may not be suitable for all rotor configurations. The Beddoes wake model is a good choice for two-bladed rotors, but may not adequately describe the more complex wake geometry of multi-bladed rotor systems. Likewise, the single trailed tip vortex assumption is acceptable for lightly twisted rotors, but is known to be inadequate for highly twisted or flapped rotors.[37] The modeling methodology developed in this dissertation will be applied to linearly-twisted two-bladed rotors in Chapter 5 where the assumed wake model

is known to be valid. However, the assumed wake model may be inadequate to accurately characterize BVI for other rotor configurations and must be validated and refined for these configurations, if necessary.

2.2.3.4 Unsteady Aerodynamics

In the assumed wake model described in the previous section, the presence of the shed wake on the trailed wake geometry is assumed small and has been neglected. However, due to the shed wake, the effect of the unsteady velocity induced on the rotor blades by the tip vortices is not felt instantaneously and this effect should be incorporated in the BVI model. A common way to account for unsteady aerodynamic effects is through an indicial aerodynamics model. As this dissertation considers only flight conditions at low to moderate advancing tip Mach numbers, the Leishman-Beddoes 2D incompressible indicial aerodynamics model has been chosen. The Duhamel integral is evaluated over time at each blade station to determine the effective compact chord aerodynamic angle of attack, using the mid-point integration algorithm developed by Beddoes[38](Eq. 2.40) with the empirical constants (A_1,A_2,b_1,b_2) determined by Leishman.[39]

$$\alpha_e(s) = \alpha(s) - X(s) - Y(s) \tag{2.39}$$

where,

$$X(s) = X(s - \Delta s)e^{-b_1 \Delta s} + A_1 \Delta \alpha_s e^{-b_1 \Delta s/2} \tag{2.40a}$$
$$Y(s) = Y(s - \Delta s)e^{-b_2 \Delta s} + A_2 \Delta \alpha_s e^{-b_2 \Delta s/2} \tag{2.40b}$$

where s is the reduced time, i.e. the distance traveled by the airfoil in terms of semi-chords over a given time interval t:

$$s = \frac{2}{c} \int_0^t V dt \tag{2.41}$$

Given the unsteady effective angle of attack for each blade section, the section lift and drag can be readily calculated from tabulated airfoil section data, and from those values the non-dimensionalized surface pressures, $C_{p_{ij}}$. The acoustic pressure time-history can be readily calculated for any observer using Farassat Formulation 1A[40] of equation 2.14, thereby providing a complete analytical model of rotor harmonic noise generation.

2.2.4 Choice of Dependent Parameters

Altogether, the assumed loading model contains many empirical parameters that vary depending on the flight condition of the rotor as determined by the non-dimensional governing parameters of loading noise as well as the specific configuration of the rotor. Given a set of values for the unknown dependent parameters and the known independent governing parameters, the noise radiation of the helicopter is uniquely determined. However, the association between the dependent parameters and the governing parameters is not known *a priori*. The values of the dependent parameters must therefore be identified for each set of non-dimensional governing parameters based on measured data for a particular rotor configuration. Altogether, the set of dependent parameters to be identified is:

$$X = \{\, A\ B\ C\ D\ r_r\ r_0\ C_v\ \gamma_0\ \gamma_{1C}\ \gamma_{1S}\ T_0\ T_{1C}\ T_{1S}\ \cdots\ D_0\ D_{1C}\ D_{1S}\ \cdots \} \tag{2.42}$$

Chapter 3

Parameter Identification

Parameter identification is a method of building a model by determining values for a set of parameters, which are unknown *a priori*, in order to match the output of the model to measured data. Determination of the unknown parameter values requires solving an inverse problem, i.e. given the desired output for the model, determine a set of input parameters to the model. In many cases, analytical solutions to the inverse problem are not available and numerical solutions must be pursued. Numerical solutions to inverse problems iteratively run the assumed model in the forward direction for various trial parameter values until a combination is found which results in the model output closely matching the measured data. To achieve feasible solution times, this requires that the assumed model can be evaluated quickly. In addition, the assumed model should have no more degrees of freedom than are required to match the measured data—this ensures that the space of trial parameter values is not too large and also reduces the likelihood that there will be multiple distinct and incompatible solutions to the problem.

The parameter identification problem can be divided into three components. The first is the assumed analytical model of the phenomena to be modeled. The second is a quantitative measure of how closely the model output matches that measured data, termed an error metric. Lastly, an efficient method of choosing

trial parameter values so as to reduce the error metric, an optimizer, must be chosen. Altogether, these components set up the parameter identification method as an optimization problem, where the optimal values of the unknown dependent parameters are determined so as to minimize the error between the model output and measured data. A flowchart diagramming the complete method is shown in Figure 3.1.

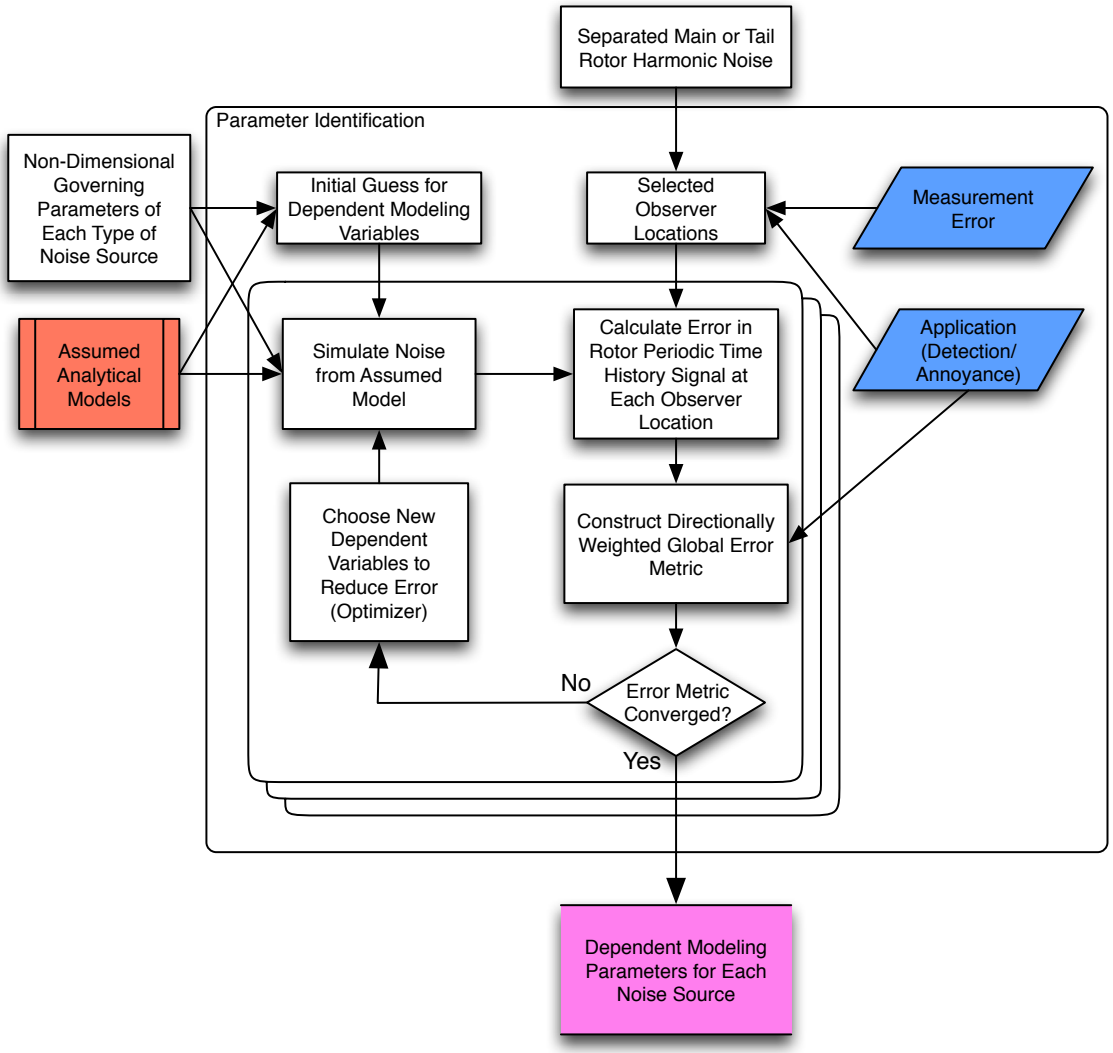

Figure 3.1: Flowchart of the parameter identification process.

The physics based modeling structure for rotor harmonic noise defined in the previous section provides the basis for the assumed model used in the parameter identification technique. The unknown parameter values to be identified are the dependent parameter values from the assumed loading model, for a given set of known non-dimensional governing parameters. The outputs of the model are the acoustic pressure time-histories produced over one rotor period at a set of observer locations surrounding and traveling through the medium with the rotor.

3.1 Error Metrics

3.1.1 Time-Domain Error Metric

The error metric describes how closely the model output matches measured data. In conjunction with the assumed physical model, this forms the objective function for the optimization problem posed by parameter identification. The error metric conveys information about the quality of the trial parameter values to the optimizer. The best choice of error metric does not necessarily have the same form as the metric that will be used to quantify the output of the identified model. The rotor acoustic models developed in this dissertation will be used to estimate ground noise contours, typically quantified using a frequency-weighted Sound Pressure Level (SPL); for example, the A-weighting is often used to model human perceptions and annoyance. However, these metrics reflect only the total energy content of the signal—there can be many acoustic signals with the same SPL but radically different waveforms, and hence physical mechanisms. In order to develop models which more

closely match the actual mechanisms of rotor harmonic noise, the error metric should include contributions of both the frequency and phase of the signal. This can be accomplished by formulating the error metric in the time domain. One common way of doing this is to use the generalized p-norm, which is an integrated measure of error over an interval of time, in this case one rotor blade passage, as shown in Figure 3.2.

$$||e||_p = \left(\int_0^T |p'_{meas}(t) - p'_X(t)|^p \, dt \right)^{\frac{1}{p}} \tag{3.1}$$

The value of p describes how the greatest error at any point is weighted against the average error over the entire time period. A value of p equal to unity is equivalent to the average error over the signal. A value of p equal to two is the RMS error of the signal. In the limit, as the value of $p \to \infty$, the norm equals the maximum error at any point in the interval.

The generalized p-norm describes how the error metric may be formulated for a single observer, however the pressure time history at one observer location is not unique and could be achieved by several distinct sets of parameter values. The uniqueness of the parameter identification solution can be improved by including additional information about the problem in the chosen error metric. Rotor harmonic noise is highly directional, so including information for several distinct observer directions in the error metric will aid in determining a single physically realistic set of dependent parameter values. (Fig. 3.3)

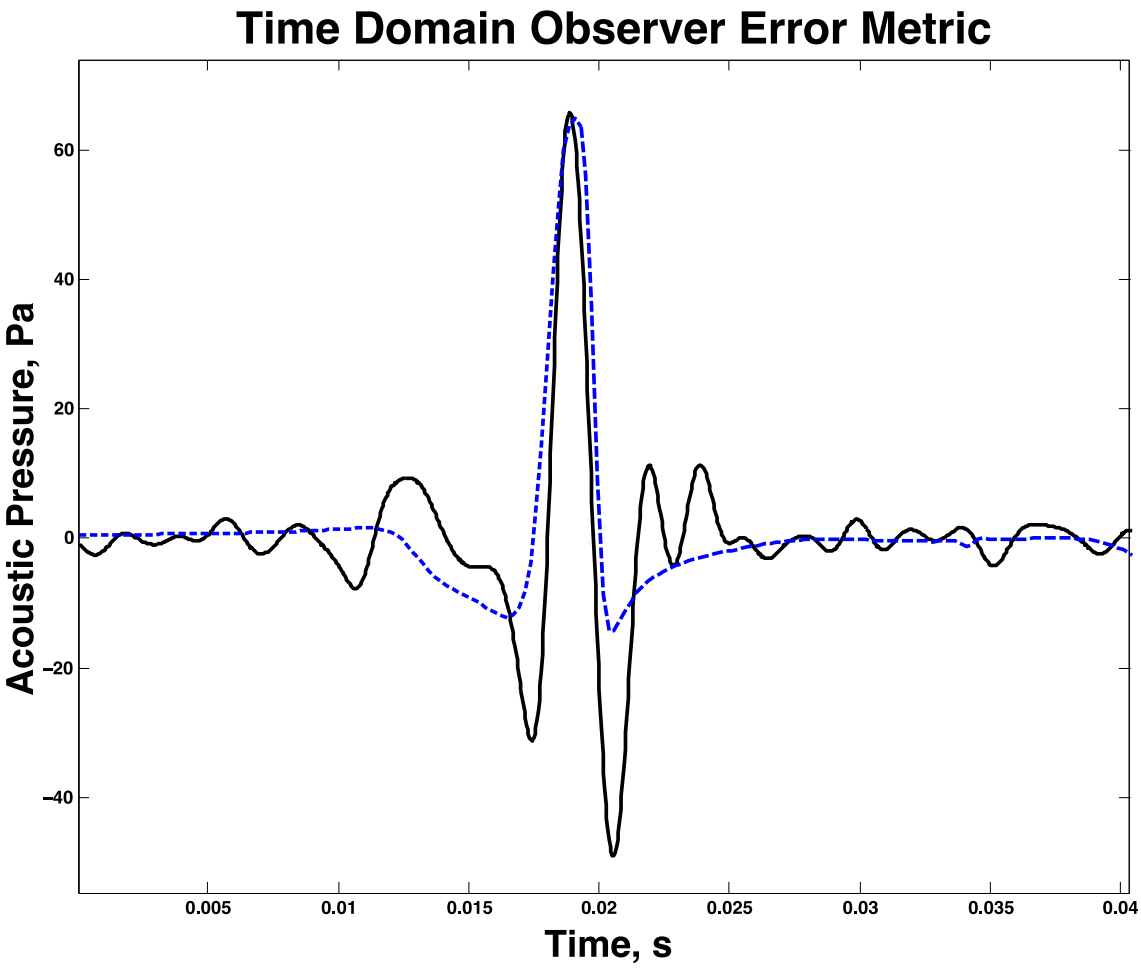

Figure 3.2: Calculation of the time domain integrated error metric. The solid black curve represents measured data, the blue dashed curve simulated data. The error metric is an integrated measure of the absolute value of the difference between the two.

3.1.2 Multi-Observer Error Metrics

An obvious way to formulate an error metric for several observer locations is to take a weighted sum of the individual time-domain error metrics for each observer location. (Eq. 3.2) For a perfect measurement and model, the choice of any non-zero weighting does not influence the solution, since all individual error metrics

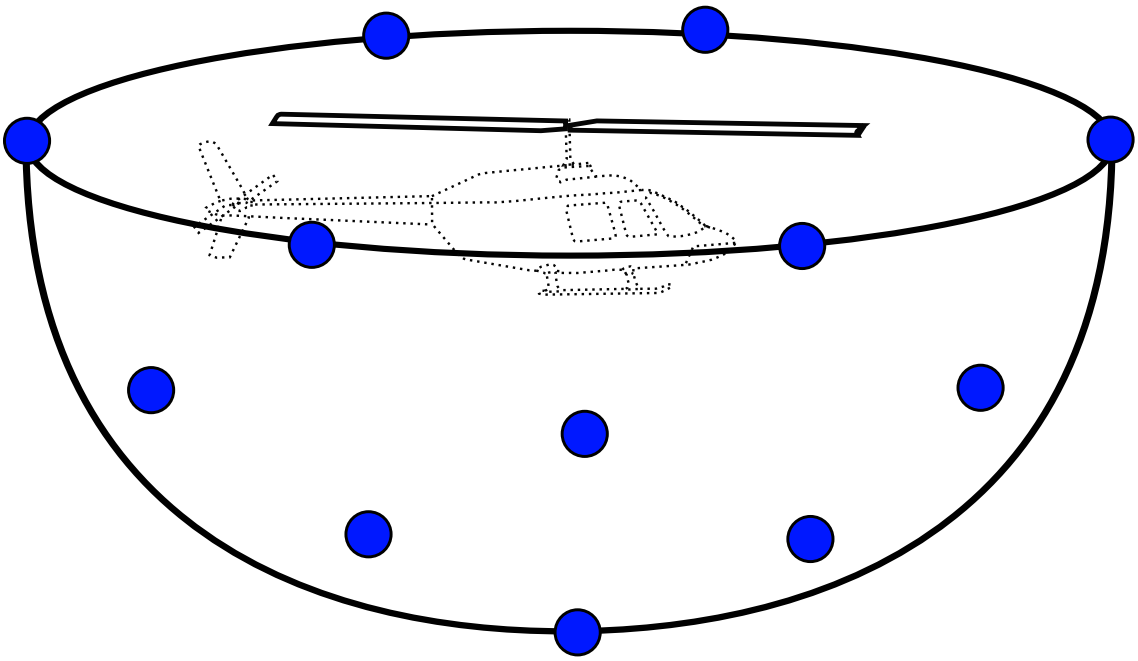

Figure 3.3: Calculation of the error metric for multiple observer locations.

can be simultaneously reduced to zero. However, with the addition of measurement noise and modeling error, it will be impossible to achieve zero error at all observers and therefore a Pareto-frontier of solutions will exist in the parameter space. The Pareto-frontier is the surface of solutions where the error cannot be reduced at any one observer without increasing it at one or more others. In this case, the choice of observer weightings will determine which directions will be more accurately modeled, and which less accurately modeled. The choice of weighting can be tailored to the intended use of the noise model—for instance, a model for long range detection may weight the in-plane observer locations more heavily than out-of-plane observer locations, vice versa for a community noise model.

$$F(X) = \sum_{k=1}^{N_{obs}} w_k ||e||_p^k \tag{3.2}$$

Another approach is to formulate the problem as a multi-objective optimization problem. In this case, instead of attempting to find the best solution for a single set of weights determined *a priori*, the optimizer attempts to define the entire Pareto-frontier, allowing the determination of observer weighting to occur after analysis. This multi-objective optimization approach requires a more expansive search through the parameter space, and hence a higher computational cost.

In addition to relative weightings of the observer locations, the number and distribution of observer locations to be included in the error metric must be determined. A sufficient number of observer locations must be chosen in distinct directions so as to discriminate the different rotor noise sources based on their directivity characteristics. However the availability and uncertainty of measurements in certain directions will also dictate the choice of observer directions included in the metric. In addition, the computational cost of evaluating the model will increase linearly with the number of observers

3.2 Optimization Methods

3.2.1 Conventional Optimization

Once the model and error metric have been determined and combined to formulate an objective function, the parameter values that minimize the objective function must be determined. An enumeration of all possible parameter values throughout the solution space would eventually find the optimal solution, but the computational cost of doing so would be inordinately high. A better approach is

to use optimization techniques to make an informed choice for each new set of trial parameters based on previous results. Traditionally, gradient-based optimization techniques are employed to minimize the objective function. These techniques start at an initial guess for the parameter values. At this point, the gradient of the objective function is calculated, indicating the direction from the trial point in which the error is reduced. If the gradient is not known analytically, the objective function will have to be evaluated at several points in the vicinity of the trial point in order to calculate the gradient by finite difference. The objective function is then evaluated several times in a direction determined by the gradient, so as to lead to a reduced value for the objective function. The set of parameter values defining this point in the parameter space become the new trial point. The process is repeated until no further progress is made in reducing the objective function value. Figure 3.4 shows the objective function (i.e. error metric) contours for a simulated set of lower harmonic data—the third harmonic thrust dimensions are shown as representative examples. This type of objective function is smooth and convex, ideally suited to conventional optimization techniques.

Figure 3.5 shows the simulated objective function contours for the model with both lower harmonic and BVI noise. These contours are shown in terms of two parameters which control the wake: the longitudinal wake skew coefficient (A) and the wake contraction coefficient (D). Unlike the lower harmonic only objective function shown in Figure 3.4, the inclusion of the wake model leads to a non-convex objective function with multiple local minima. In cases where the objective function contains numerous local minima, gradient-based methods will halt at the first local

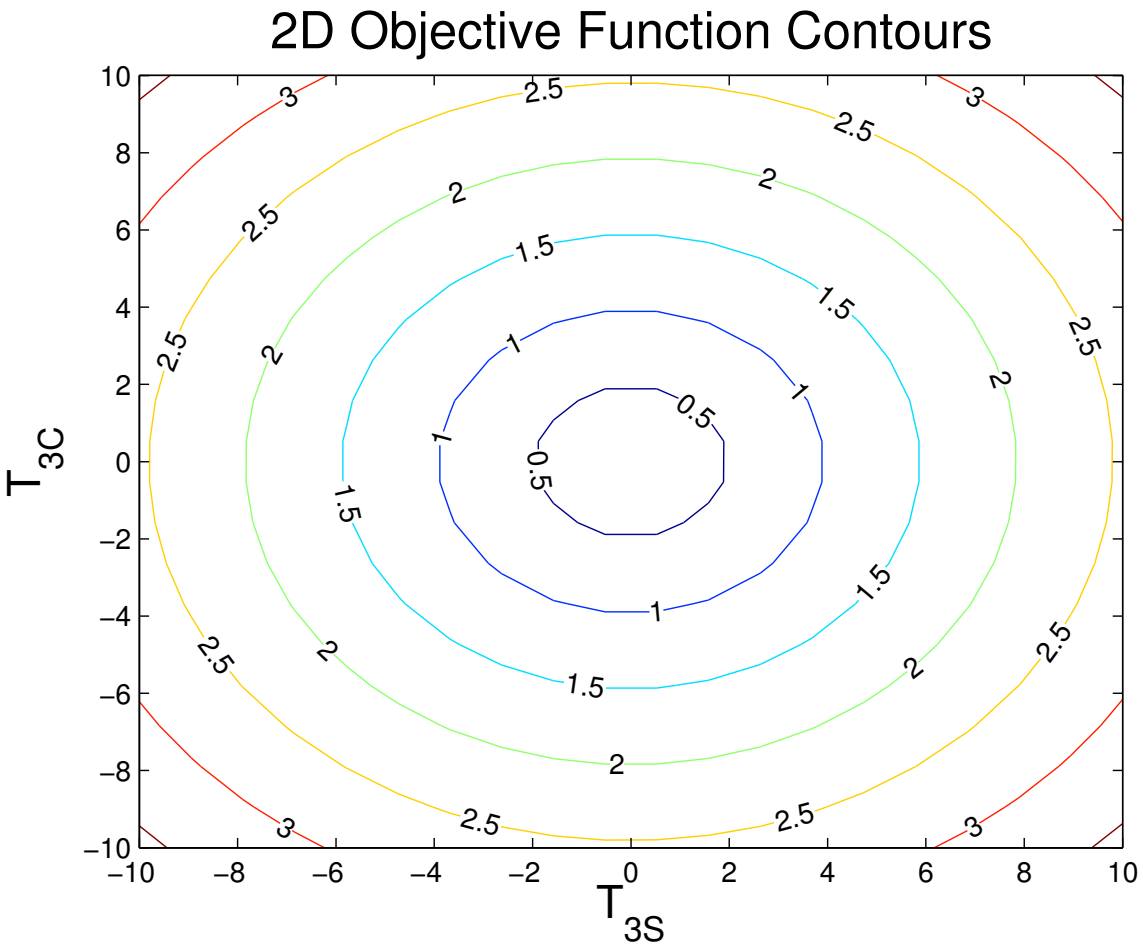

Figure 3.4: Simulated third harmonic thrust coefficient lower harmonic-only objective function contours.

minimum encountered, which may not be similar to the global optimum over the entire parameter space of the problem.

3.2.2 Global Optimization

In order to determine the global optimum of a non-convex objective function, a global optimization scheme must be employed. Stochastic methods are designed to explore the entire parameter space and identify probable global optima with a

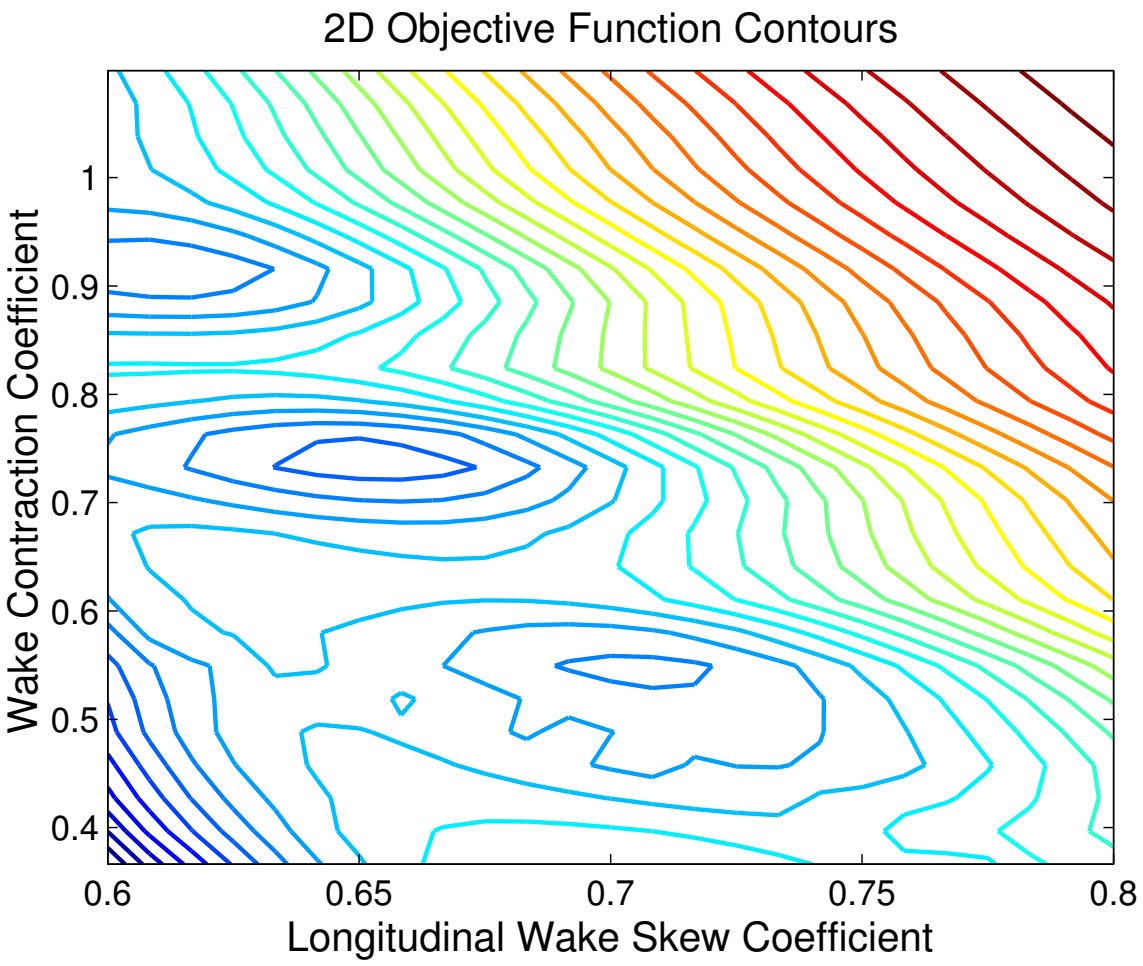

Figure 3.5: Simulated wake parameter objective function contours for lower harmonic and blade-vortex interaction noise model.

minimum number of function evaluations. Since these methods explore the entire parameter space, they are also well suited to identifying the Pareto-frontier in multi-objective optimization problems. Stochastic methods employ the statistical properties of random number distributions to ensure that the solution space is explored and that the method does not terminate in potential local minima. Common stochastic methods include genetic algorithms,[41] differential evolution,[42] and more recently, particle swarm methods.[43] Genetic algorithms are well suited to non-convex and

non-smooth problems, and are capable of identifying global optimum over a wide and varied parameter space. The genetic algorithm starts by seeding the parameter space with a population of points at randomized locations. The parameter values of each member of the population are then discretized and encoded into a binary form. The binary values of each parameter are concatenated into a single binary number representing the particle location, called a chromosome. A subset of the population is paired with other members, and a randomized portion of the chromosomes swapped to form new chromosomes. Then, random bits of the chromosome are mutated by switching bits from 0 to 1 or vice versa. The chromosomes are decoded back to parameter values, and the objective function evaluated for each. Then, the members of the population are removed through a roulette selection, with the probability of a member being removed increasing as in proportion with the associated error value of the objective function. Over successive iterations, the members of the population with the lowest error values tend to survive and share information with other members of the population. However, the chromosomes of the members of the genetic algorithm relate only indirectly to the contours of the objective function over the parameter space. This lack of a direct relation between the parameter space and the chromosome values allows the genetic algorithm to explore the entirety of the solution space in a robust manner, even in the presence of discontinuities. However, for many physical optimization problems, the objective function may be smooth over the entirety of the parameter space, and while multiple local minima may exist, they are likely confined to a small region. On such problems, the genetic algorithm spends many function evaluations exploring in fruitless directions.

The differential evolution algorithm is an adaptation of the genetic algorithm that defines each member of the population more directly by the vector of its parameter values. Parameter values are swapped between members of the population during pairing, and during mutation, the parameter values are perturbed. In this way, differential evolution can more directly exploit the shape of the objective function across the solution space, and search for optima where they seem more likely to occur. However, the amount of perturbation is governed by several user adjustable parameters. The ability of the differential evolution method to find the global optimum is very dependent on the choice of these parameters, which can be substantially different for different objective functions. Without careful tuning of these parameters, the likelihood of missing the global optimum altogether is high.

A more recent approach which has been found effective for physically-based non-convex objective functions is called Particle Swarm Optimization (PSO).[43] PSO evaluates the objective function at a number of randomly seeded particle locations in the feasible solution space. The particles are assigned velocities dictating how they travel through the solution space. At fixed intervals, the objective function is again evaluated at each particle location, and a new velocity computed for each particle. The velocity of a particle during the next iteration (v_i^{t+1}) is a randomly weighted combination of the current velocity direction (v_i^t), the direction towards the previous best set of parameters for the particle (X_{pb}^t), and the global best set of parameters discovered by any particle (X_{gb}^t). The common PSO update algorithm can be expressed simply:

$$v_i^{t+1} = a v_i^t + b_1 \mathcal{R}_1^t \left(X_{pb}^t - X_i^t \right) + b_2 \mathcal{R}_2^t \left(X_{gb}^t - X_i^t \right) \tag{3.3a}$$

$$X_i^{t+1} = X_i^t + v_i^t \tag{3.3b}$$

where $\mathcal{R}_1$ and $\mathcal{R}_2$ are random variables between 0 and 1, a is the inertia weight of the particle, and b_1 is the weight of the direction towards the historical best position of particle i, and b_2 the weight of the direction towards the best position of the entire swarm. There are several common sets of weighting terms for the PSO algorithm that are broadly applicable to a wide range of problems—in this dissertation, the weights suggested by Trelea are used.[44]

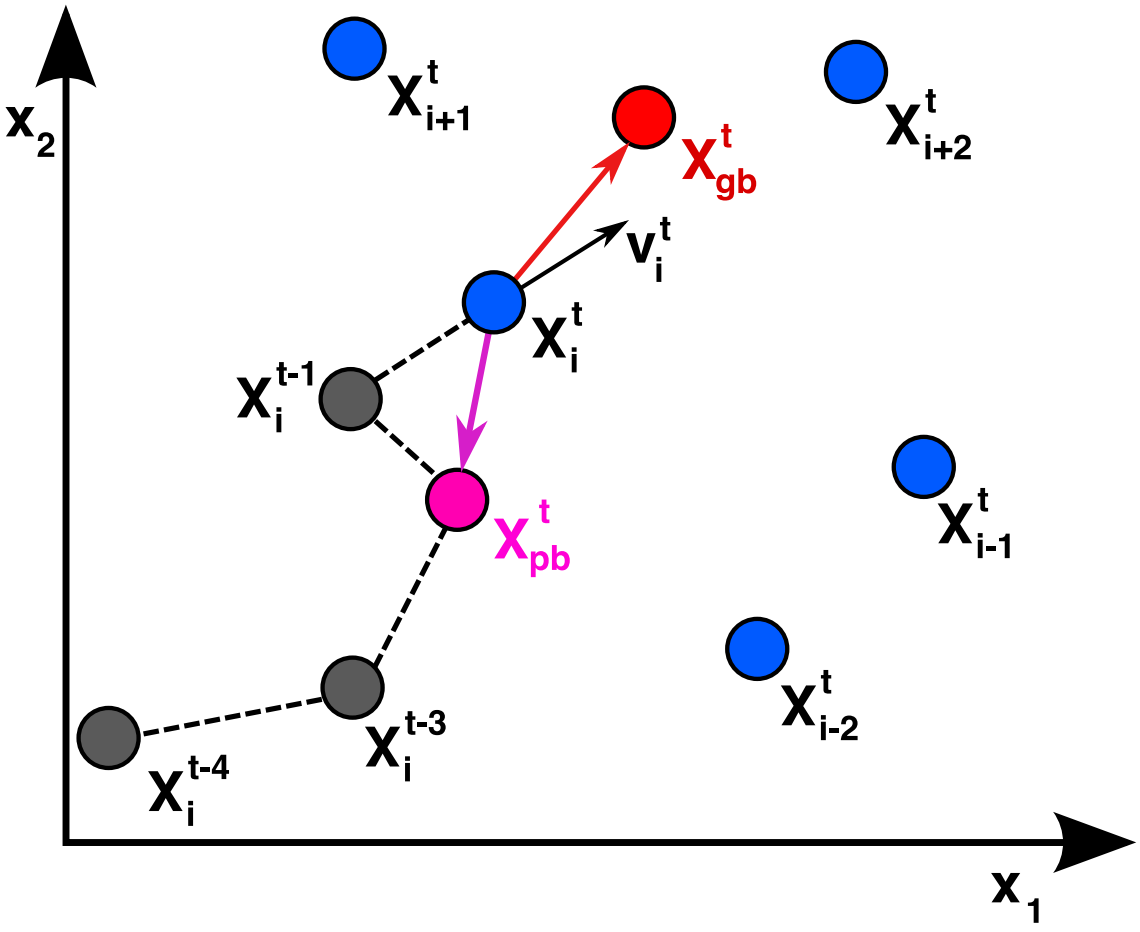

Figure 3.6: The Particle Swarm Optimization (PSO) technique.

The stochastic nature of the algorithm encourages the particles to explore the entire parameter space while the inertia term allows the particles to pass over local minima. However, the quick convergence of the standard PSO approach still makes it susceptible to premature stopping. Several extensions of the method have been proposed to improve the ability of PSO to find the global optimum. One approach employed in the PSO method used in this dissertation is the "particle reset" method.[45] When the velocity of a particle decreases below a small predetermined threshold, the particle's location is reinitialized to a random position in the space of possible solutions. This method prevents individual particles from stagnating in local minima, and ensures that the method continues to spend some time searching throughout the entire search space, even after a promising minimum has been found by the swarm.

All three global optimization methods were applied to the parameter identification problem for rotor harmonic noise using simulated data. In general, the PSO optimization consistently produced good results without much hand tuning of the optimization parameters after a relatively small number of iterations, and was selected as the optimizer for the method developed in this dissertation. However, it is likely that good performance can be achieved with any of the global optimization methods once they are adapted to this specific parameter identification problem.

Another method to improve the ability of global optimization methods, including PSO, to find the global minimum is to initialize the method so as to provide better coverage over the entire search space. The simplest way to improve the initial coverage of the search space is to increase the number of particles in the swarm, but

this increases the computational cost of the method in proportion to the size of the swarm. However, coverage can be improved without impacting the computational cost. The standard approach of seeding the method with a collection of particle locations determined using a uniform random number generator results in a very non-uniform distribution of particles over the solution space, i.e. the seeded particles tend to cluster in certain areas of the solution space and are sparsely populated in others. The uniformity can be improved by using a "quasi-random" number sequence, which defines streams of numbers which are more uniformly spread through the solution space, and yet still possess many of the statistical properties of truly random numbers. Numerous quasi-random number sequences exist—one which has been successfully applied to Monte Carlo methods[46] and stochastic optimization algorithms[47], including PSO[48], is the Sobol sequence.[49] The Sobol sequence is used in this dissertation to seed an initial population of particles numbering ten times the dimensions of the solution space. This "quasi-random" seeding allows a smaller number of particles to ensure adequate coverage of the solution space, leading to a higher likelihood that the global minimum will be correctly identified. In this dissertation, 200 "quasi-randomly" seeded particles are used to provide complete coverage over the dependent parameter space during the PSO parameter identification.

3.3 Parameter Estimation

The parameter identification technique provides the means to develop an association between a set of governing parameter values and dependent parameter

values for a single operating condition. To estimate noise for an operating condition not measured, it is necessary to determine the set of dependent parameter values that correspond to the known governing parameter values which define the operating condition.

3.3.1 Conventional Interpolation

One method is to use an interpolation method to estimate dependent parameter values based on dependent parameter values identified for other sets of governing parameter values. There are several practical interpolation approaches. The simplest method is the nearest neighbor approach, where the dependent parameter values are simply chosen to match the closest available measurement. This method is suitable when known data points are tightly spaced, and estimates only required at positions similar to measured data. Linear interpolation allows for estimates of the dependent parameter values to be made for sets of governing parameters that are farther removed from known values. There are two possible methods of performing linear interpolation on the multi-dimensional space of governing parameters. The simplest is to perform 1-D linear interpolation separately along each dimension in a predetermined order. This is similar to the approach currently utilized by RNM to interpolate the data values on acoustic hemispheres as a function of both airspeed and flight path angle. This approach ties the accuracy of the interpolation to the choice of governing parameters and the order in which the 1D interpolations occur. A better approach is to perform an N-dimensional linear interpolation, where N is the

number of governing parameter dimensions. To accomplish this process, the space of governing parameter values must be triangulated using the measured parameter sets as vertices. Then, dependent parameter values can be linearly interpolated along the hyperplane formed by the nearest set of measured value vertices. This method still has some geometrical accuracy dependence, requiring data be gathered uniformly across the governing parameter set in order to produce good results. In addition, this method cannot yield extrapolated values outside the range of measured data. In order to make the best use of measured data, a more sophisticated approximation scheme capable of extrapolation and able to yield better results with scattered data is sought.

3.3.2 Radial Basis Function Approximation

One increasingly common way to approximate unknown nonlinear functions is the Radial Basis Function (RBF) approach.[50] Any smooth function may be approximated as a linear combination of radial basis functions. Each RBF is centered at some distinct point in space. Each RBF is weighted—these weights are selected to achieve the best-known approximation of the target function. The RBF approximation can be expressed in the following form:

$$f(x) \approx \sum_{i=1}^{N} \nu_i \Phi(r(x, c_i)) \tag{3.4}$$

The radial basis functions, Φ, are weighted so as to match the dependent value at each set of independent coordinates. The argument, r, of the radial basis function is some scalar representation of the distance between the approximated point, x, and

the center of the radial basis function, c_i. In rectilinear coordinates, this distance is generally taken to be the Euclidean distance between the two points, and may be evaluated in any number of dimensions. Consequently, the value of the RBF is not dependent on direction.

There are numerous radial basis functions in common use for a range of applications. Some of the most common are Gaussian, multi-quadric, and exponential. These functions are generally chosen to exhibit some smooth, continuously decreasing, variation in value as the distance from the center increases. For interpolation problems, it is also desirable that the functions do not have a compact support, i.e. the radial basis function should have a non-zero value across the entire interpolation region. When RBF have infinite support, all RBFs extend through all data sites and interpolants. The weights of the RBF can then be determined by solving a linear system, where the vector of weights is solved for from a coefficient matrix of RBF values for each combination of center and data site location and the vector of known function values, f:

$$\begin{bmatrix} \Phi(r(x_1,c_1)) & \Phi(r(x_1,c_2)) & \dots & \Phi(r(x_1,c_N)) \\ \Phi(r(x_2,c_1)) & \Phi(r(x_2,c_2)) & \dots & \Phi(r(x_2,c_N)) \\ \vdots & \vdots & \ddots & \vdots \\ \Phi(r(x_N,c_1)) & \Phi(r(x_N,c_2)) & \dots & \Phi(r(x_N,c_N)) \end{bmatrix} \begin{bmatrix} \nu_1 \\ \nu_2 \\ \vdots \\ \nu_n \end{bmatrix} = \begin{bmatrix} f(x_1) \\ f(x_2) \\ \vdots \\ f(x_N) \end{bmatrix} \tag{3.5}$$

where, for example, the multi-quadric RBF (shown in Figure 3.7) has the form:

$$\Phi(r(x,c)) = \sqrt{1 + (\epsilon r(x,c))^2} \tag{3.6}$$

This formulation produces a function approximation which is exact at all known data points. If the RBF are chosen with compact support, some data sites may not

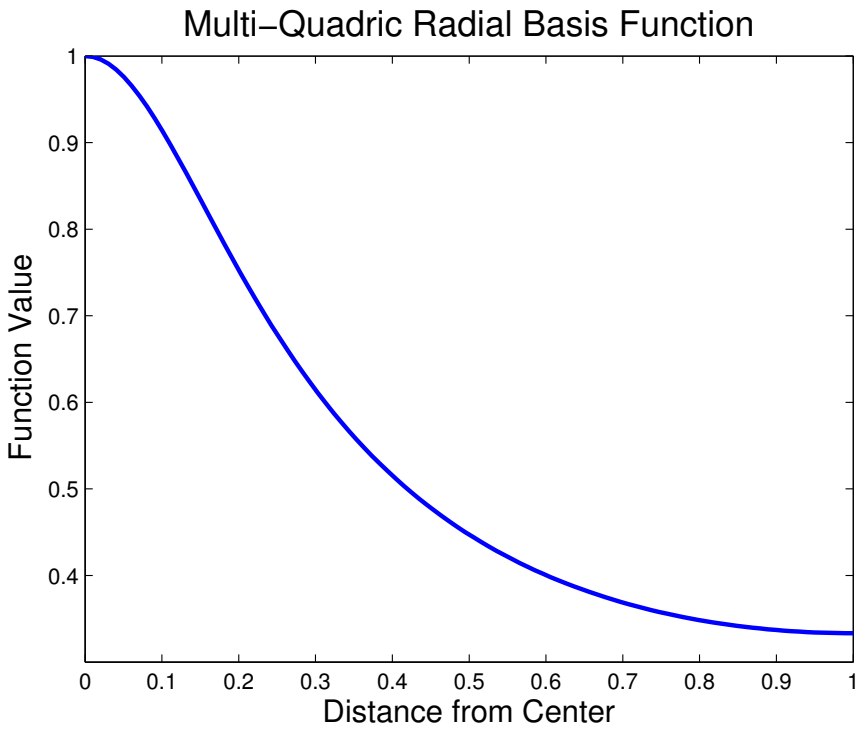

Figure 3.7: The multi-quadric Radial Basis Function (RBF).

lie within some RBF and the resulting problem may be over or under constrained. Additionally, approximation with compactly supported RBF limits the domain of the approximating function since the RBF have non-zero values over a finite region.

The centers of the radial basis functions may be chosen arbitrarily; however, for interpolation problems good results are generally achieved by collocating the RBF centers with the data site locations. This collocation ensures that each data site is strongly represented by at least one RBF. The formulation of the RBF-based approximation does not depend on the distribution or uniformity of data sites. An example of the multi-quadric RBF used to approximate the sine function using five bases is shown in Figure 3.8.

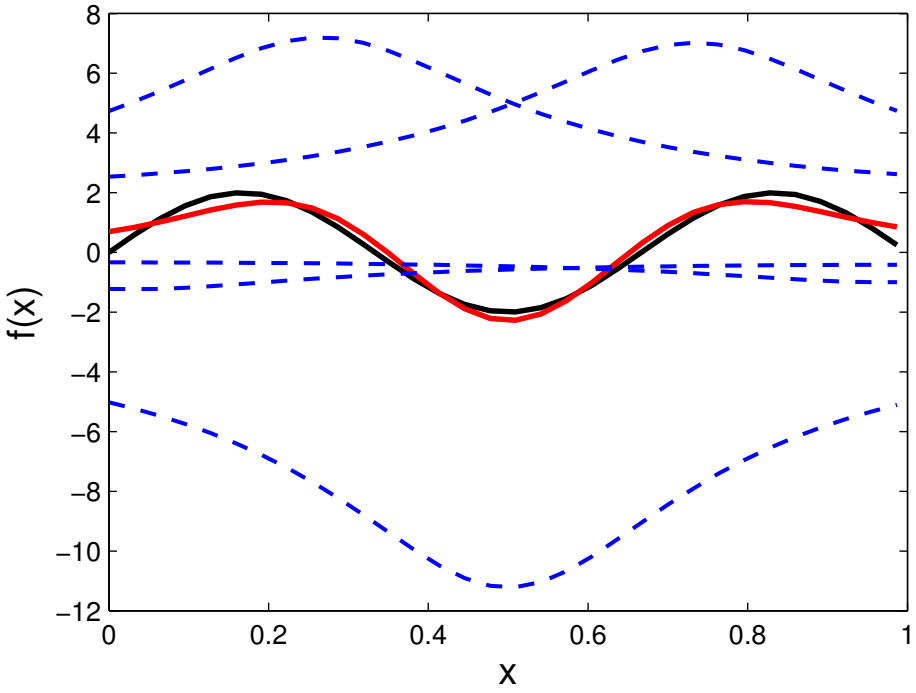

Figure 3.8: The approximation of the sine function using Radial Basis Functions (RBF). The black line is the function $\sin 2\pi x$, the dashed lines are the five RBF bases, and the red line is the RBF approximation using the superposition of the bases.

3.3.3 Neural Network Estimation

An Artificial Neural Network (ANN)[51] can be seen as a more general version of the RBF function approximation discussed in the previous section. In the context of an ANN, the basis functions are called neurons. Each neuron accepts a set of parameters as an input, and produces one output value, shown in Figure 3.9—much like a single RBF. In the RBF function approximation, the weighted sum of these outputs is taken as the overall output of the RBF approximation; this is equivalent to an ANN with a single layer of neurons, as seen in Figure 3.10. However, in a typical ANN there are multiple layers of neurons. The first layer accepts the inputs and is called the input layer. The last layer of yields the output values and is therefore called the output layer. The intermediate layers of neurons are called hidden layers—these layers accept the output of another layer as input, and likewise pass their output to another layer as inputs. Weights are determined for every input-output pair in the network, providing the ANN great flexibility in modeling nonlinear phenomena. Generally, the neurons can be described by any multi-input single-output function, although RBF are commonly used because of their utility in function approximation. A diagram of a simple ANN with two hidden layers is shown in Figure 3.11.

The process of determining the best ANN weights in order to fit the behavior of the ANN to known data is called training. There are a number of schemes in use to train ANN, most of which apply optimization techniques like those discussed in Section 3.2 in order to minimize the error between the ANN output and known training data for a given set of inputs. This error is defined as the mean sum of the

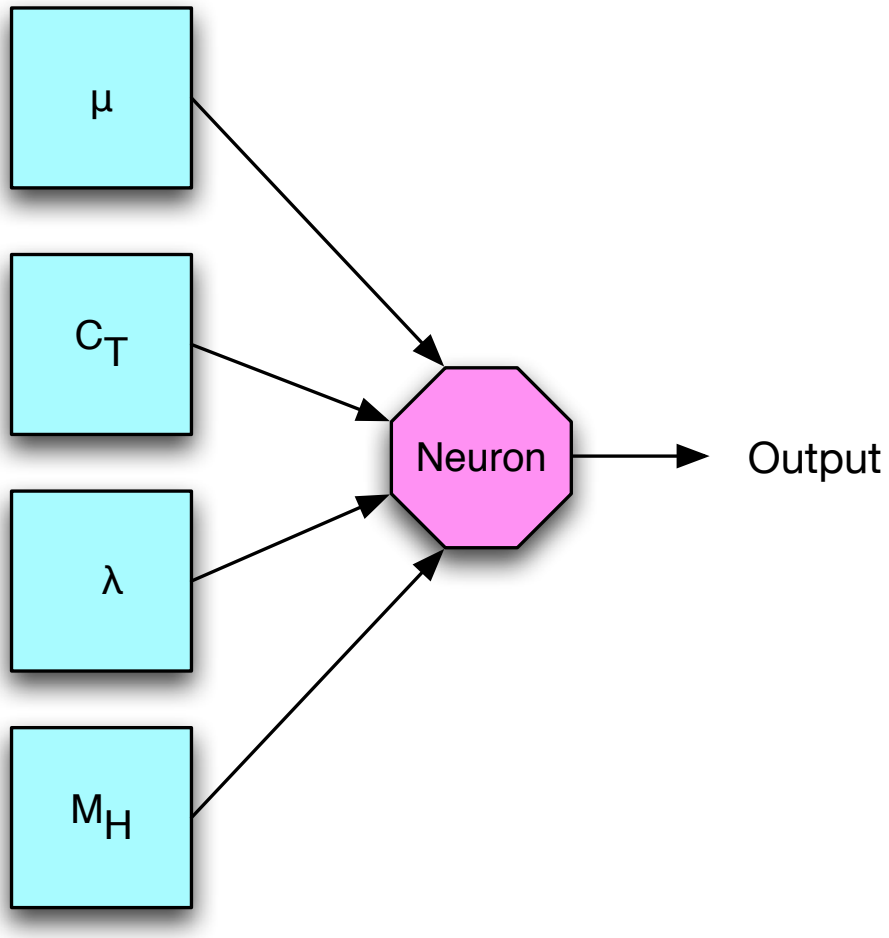

Figure 3.9: A single neuron.

squares of the error at each of the data points in the training set, i.e.:

$$F = \frac{1}{N}\sum_{i=1}^{N}(f_{ANN}(x_i) - f_{train}(x_i))^2 \tag{3.7}$$

However, due to the flexibility of ANN they are susceptible to "over-fitting", i.e. the ANN accurately reproduces the training data, but provides inaccurate results for inputs outside the set used in the initial training. The most common technique to improve the generalization of ANN to unknown data is called early stopping.[52] In this process, some randomly selected portion of the known data is withheld from

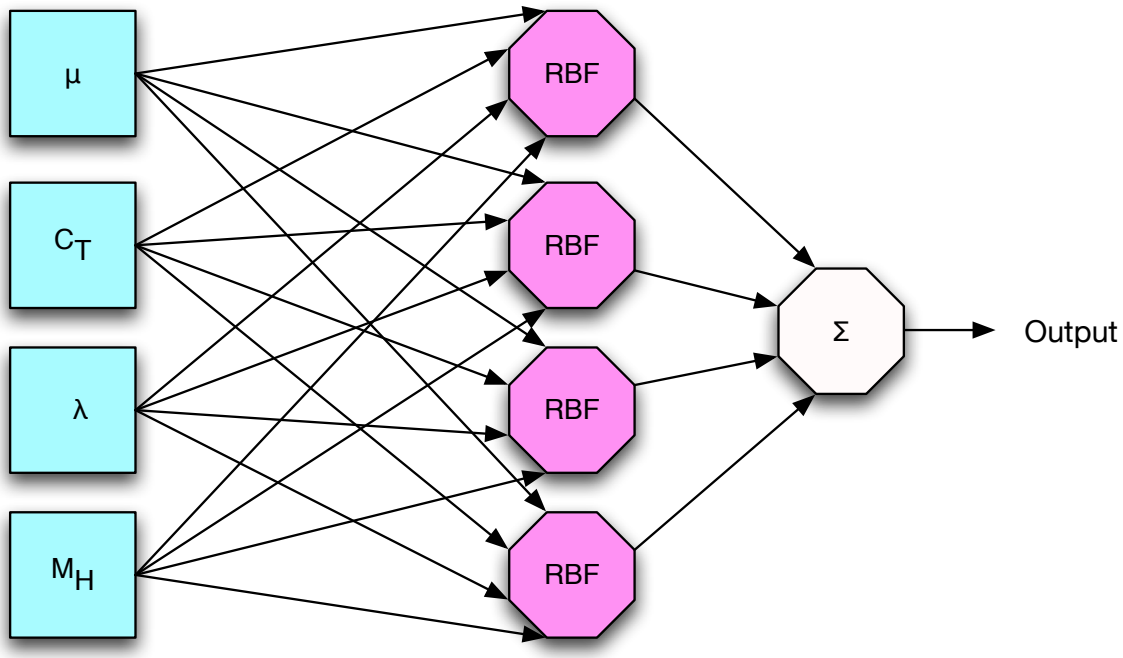

Figure 3.10: A single-layer Radial Basis Function (RBF) network.

the training set, and is called the validation set. On each iteration of the training process, the output of the ANN is compared against the validation set—initially, the error on the validation set decreases along with the error on the training set. At some point in the process, the error on the validation set begins to increase while the error on the training set continues to decrease. This indicates that over-fitting is beginning to occur, and the training process is then terminated. Early stopping is an effective technique for improving the generalization of ANN, but is not well suited to limited data sets, since some data must be set aside for validation. A different approach which results in slower training, but better generalization for smaller data sets, is called regularization. Regularization changes the metric used to assess the error of the ANN during the training process, including a term which limits the

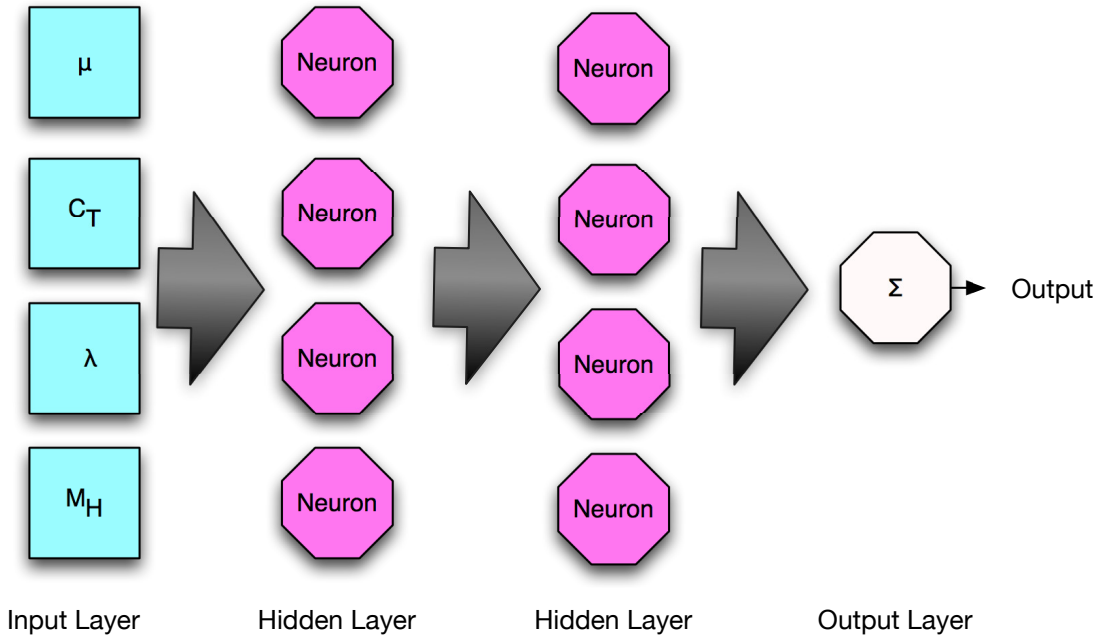

Figure 3.11: An Artificial Neural Network (ANN) network with two hidden layers. Fully connected network relations are simplified with block arrows.

magnitude of the network weights:

$$F = \beta \frac{1}{N} \sum_{i=1}^{N} (f_{ANN}(x_i) - f_{train}(x_i))^2 + (1-\beta) \frac{1}{n} \sum_{j=1}^{n} w_j^2 \tag{3.8}$$

β is called the performance ratio. Determining the optimal value of β for regularization *a priori* is difficult, but techniques exist in order to automatically adapt the performance ratio in order to ensure effective regularization. One of the most effective and commonly employed automatic regularization techniques is Bayesian regularization,[53] which uses probability theory and statistical arguments to estimate how much regularization is warranted based on the sampling of data in the training set. In this dissertation, the Bayesian regularized Levenberg-Marquardt training algorithm provided in the MATLAB® Neural Network toolbox[54] is utilized

to fit the ANN which relate the governing parameter values to the dependent parameter values discovered from the measured data using parameter identification technique described earlier in this chapter. The combination of the trained ANN and the analytical model which accepts the dependent parameters results in a complete and generalizable model of the noise radiated by a particular rotor configuration under a wide range of non-dimensionally defined operating conditions.

3.4 Model Usage

Once suitable models have been identified describing the external noise radiation of the helicopter, they can be applied to estimate noise at any specified flight condition. First, the specified flight condition must be defined in terms of the non-dimensional governing parameters of each noise source, e.g. main rotor harmonic noise, tail rotor harmonic noise. These parameters can be readily determined from the dimensional parameters defining the flight trajectory and ambient conditions to be used in the ground noise contour simulation. The non-dimensional governing parameter values are then used to select dependent parameter values for the assumed models using the parameter estimation scheme describing the mapping between governing and dependent parameters. If the multi-objective parameter identification scheme provides a Pareto frontier of possible solutions, the set of dependent parameter values can be chosen at runtime based on the type of helicopter operation performed. The noise radiated to ground based observers is then computed for each noise source using the set of governing and dependent parameters for each noise source. The

output of each noise source model is superimposed to yield a complete description of noise radiation at the desired operating state.

Chapter 4

Measurement and Data Processing

4.1 Source Noise Measurements

The simplest way to gather noise measurements from a wide range of directions for a helicopter in a steady flight condition is to utilize an array of ground-based microphones. For straight-line flight conditions, a linear array of microphones has proven effective, as is typically employed to collect data for use with RNM. As the helicopter passes over the linear array, shown in Figure 4.1, the microphones measure noise radiated from the front of the helicopter while the vehicle is ahead of the array and aft of the helicopter after it passes the array. These measurements are made across a range of lateral directivity angles by positioning a number of microphones along the ground in a line orthogonal to the flight path of the vehicle. The precise geometry of the measurement can be determined as a function of time given position tracking data from the helicopter time-synchronized with the acoustic measurement as well as the locations of the stationary microphones.

4.2 Virtual Inflight Observers

Measurements of noise on the ground are not easily comparable. The distance between the source and the observer varies with directivity angle, as well as with

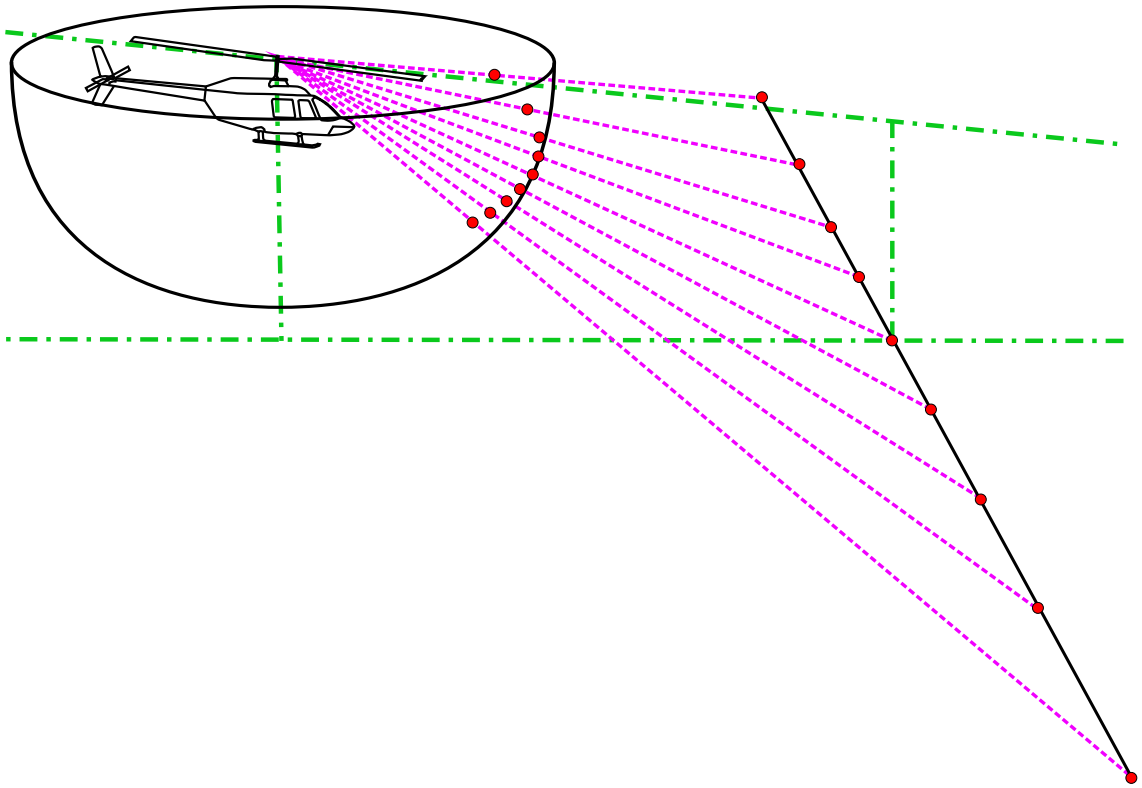

Figure 4.1: The linear microphone array used to construct acoustic hemispheres for Rotorcraft Noise Model (RNM).

changes in the trajectory of the aircraft. Differences in the propagation distance result in differences in observed noise levels due to spherical spreading and atmospheric absorption. In addition, the relative motion between the aircraft and the observers results in an apparent frequency shift in the observed acoustic signals. In order to have directly comparable sets of measurements, the measurements should be transformed to a common frame of reference.

The acoustic measurements can be transformed to a common frame of reference by introducing the concept of virtual inflight observers.[55] The virtual inflight observer makes the assumption that the helicopter can be represented as a compact

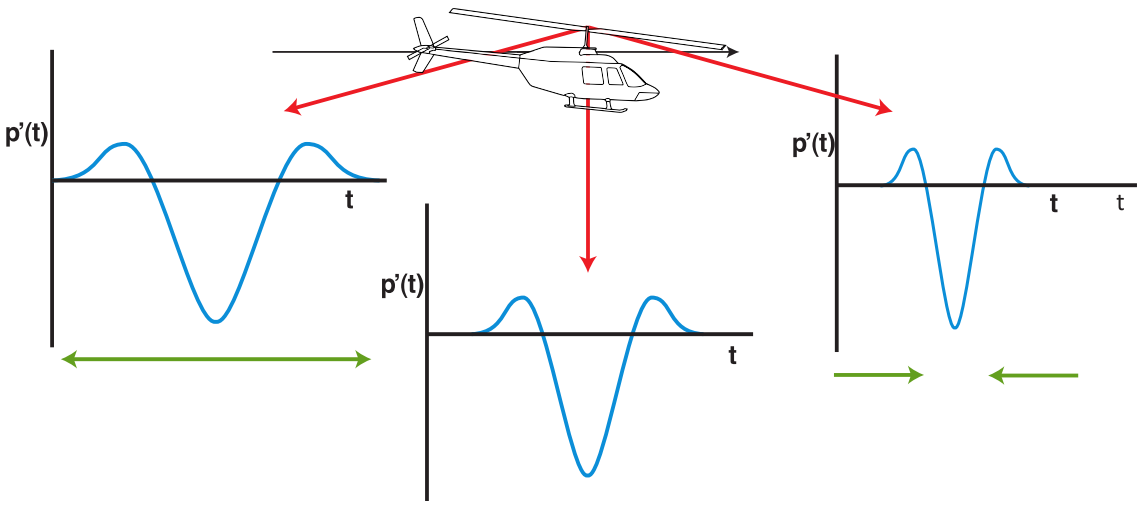

Figure 4.2: Doppler effect on acoustic pressure time histories measured by stationary observer.

noise source, with all noise from one rotor radiating from a single point on the rotor disk. The virtual inflight observer then travels through the medium with the source maintaining fixed distance from the source at all times. This is similar to a true inflight observer who is flying alongside the helicopter and analogous to measurements of a fixed source from fixed observer locations in the presence of a moving medium, e.g. acoustic measurements made in a wind tunnel. However, because the virtual inflight observer is composed from the transformation of ground-based acoustic signals, and the helicopter noise source is highly directional, the virtual inflight observers must orient themselves with respect to the helicopter noise source so as to match the corresponding directions between the noise source and the ground-based observers.

The transformation of the acoustic pressure time-history signals from from ground-based microphone measurements to those measured by the virtual inflight

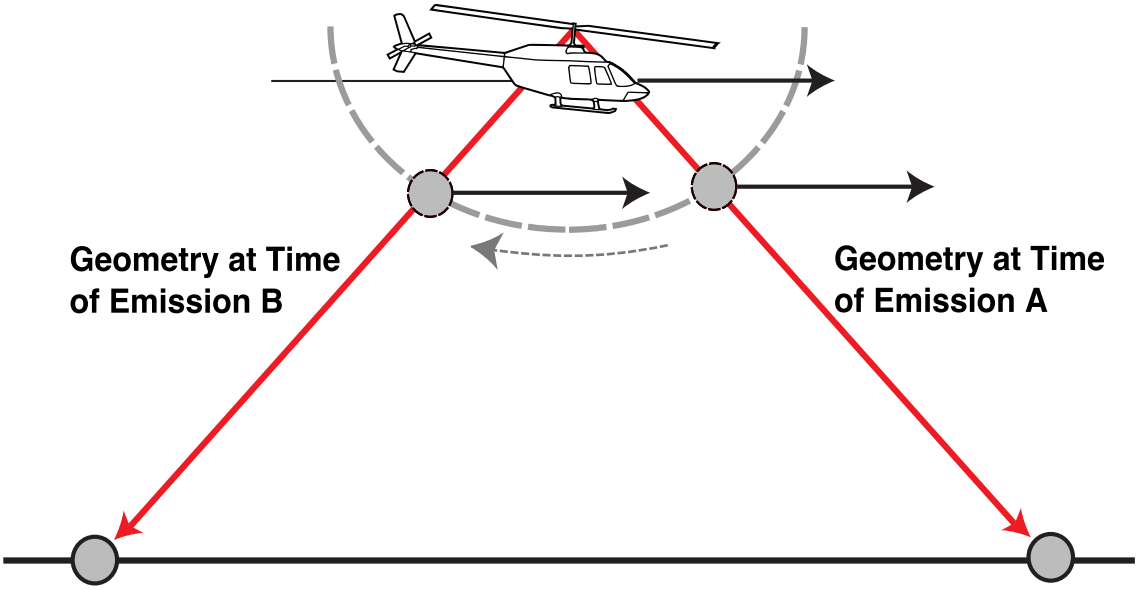

Figure 4.3: Diagram of the virtual inflight observer concept.

observers is accomplished through a time-domain process of de-Dopplerization. Unlike traditional de-Dopplerization approaches, which are formulated in the frequency domain,[56] the time-domain approach fully models how the acoustic signal deposited in the medium is perceived due to the relative motion between the source and observer. This process does not attempt to compensate for the effect of Doppler amplification, which is due to the motion of acoustic sources with respect to the medium itself. Without a complete understanding of the type, distribution, and motion of the individual sources through the medium, it is impossible to accurately model the Doppler amplification process. However, this process is fully accounted for in the physics-based analytical modeling structure described in Chapter 2, during the evaluation of the Ffowcs Williams – Hawkings equation, as an estimate of the composition of sources can be made in this case using the parameter identification

techniques of Chapter 3.

The time-domain de-Dopplerization process is a simple accounting of the retarded time equation, which describes the time delay between the emission of noise into the medium and reception from the medium by the observer.

$$t - \tau - \frac{|\vec{x} - \vec{x}_s|}{a_0} = 0 \tag{4.1}$$

where t is the time of reception, τ the time of emission, and $|\vec{x} - \vec{x}_s|$ the distance between the source and observer through the medium. The theoretical development of this transformation can be found in Appendix A.

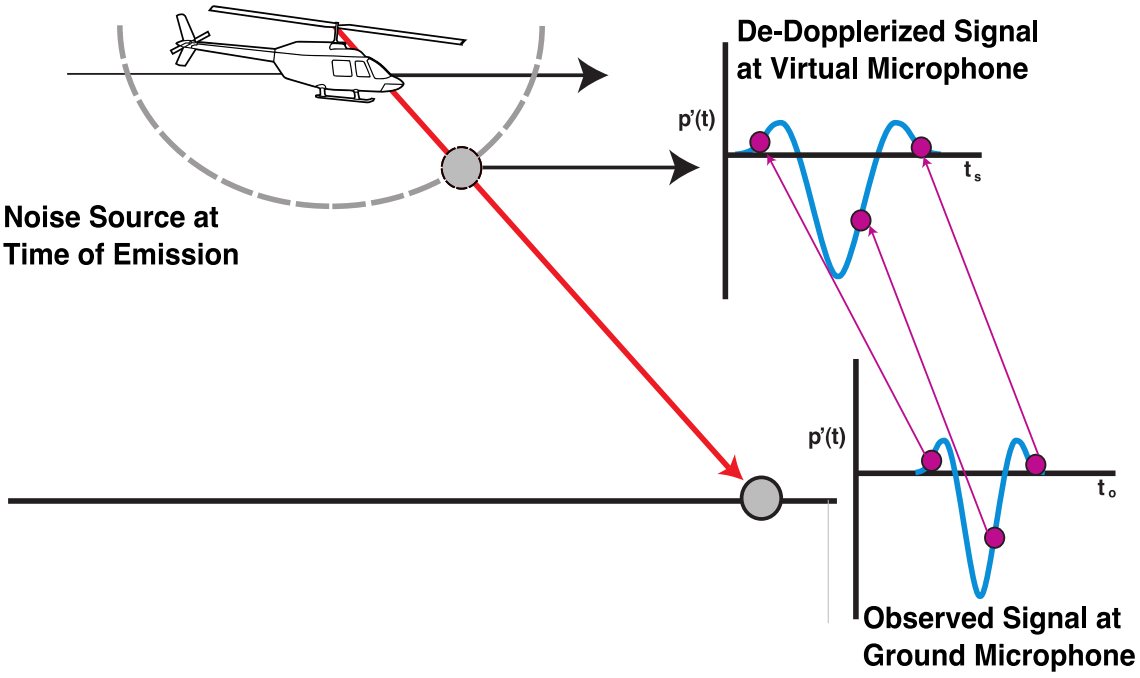

Figure 4.4: The process of time-domain de-Dopplerization.

In time-domain de-Dopplerization, this equation is evaluated continuously over the entire length of the recorded signal. This requires an accurate knowledge of the

position of the helicopter as a function of time. The process of de-Dopplerizating the pressure time-history data is as follows:

- The helicopter pressure time-history and position tracking data are discretized in time at fixed sampling rates; in general, the position tracking data is discretized at a much lower sampling rate.

- In order to provide tracking data at arbitrary time steps a continuous piecewise-defined spline is fit to the tracking data.

- For each acoustic sample, the correct time of emission, time of observation at the spherical surface, and position of the helicopter along the track are calculated. For a real trajectory, this solution is iterative but convergence is quick. The iterative solution may be initialized by assuming straight-line motion of the helicopter between known position tracking points, for which the retarded time is known exactly.

- Using the propagation distance calculated at each time-history sample, the change in amplitude due to spherical spreading may be calculated and applied for each individual pressure time-history sample. The de-Dopplerized signal observed by the "virtual inflight microphone" may now be obtained.

- The time steps between samples of the transformed signal are non-uniform. In order to calculate frequency spectra using standard techniques the signal must be resampled to a fixed time-step. This process may introduce aliasing at a lower frequency than for the untransformed signal. An increase of the initial

sampling rate by 30% has been recommended. However, the Non-Uniform Time Discrete Fourier Transform[57] can be used to calculate uniform frequency spectra without affecting the Nyquist frequency, as the average sampling frequency of the non-uniformly spaced signal does not change significantly.

The result of this process is pressure time-history signals as observed by virtual inflight microphones which slowly trace paths along the surface of a hemisphere set a fixed distance away from a point on the rotor disk, corresponding to the directions measured during the data gathering run. Assuming that the helicopter maintained a steady flight condition throughout the run, this forms a complete representation of the noise radiated by the helicopter in terms of direction, frequency, amplitude, and phase during that flight condition. However, in order to apply the parameter identification technique of Chapter 3 to these data, the contributions of the various rotor harmonic noise sources must be separated from the transformed pressure time-history signal.

4.3 Rotor Harmonic Noise Separation

A common method for separating rotor harmonic noise from measurements made in a wind tunnel is periodic ensemble averaging.[58] This method has also been applied to inflight measurements of the noise radiation of entire rotorcraft.[59] The acoustic pressure time-history signal is divided into individual rotor revolutions. Since the rotor rotational rate is not necessarily constant, data from a once per revolution sensor mounted to the rotor shaft is generally utilized to identify the actual rotor periods. Under the assumption that the acoustic state of the rotor is generally stationary from one revolution to the next, the pressure time history signals from a number of rotor revolutions are scaled to a normalized time and ensemble averaged. The averaged signal retains the component which is harmonic to the rotor, but suppresses the part of the signal which is not harmonic to the rotor. The number of rotor revolutions included in the ensemble average determines the quality of the suppression of non-harmonic noise. For wind tunnel measurements, typically on the order of 100 rotor revolutions are used to generate the separated signal.[58] The process can be applied to both the main and tail rotor to identify the contribution of each to the overall external noise radiation. Subtracting the two signals from the original measured signal produces a residual pressure time-history that includes the contribution of all non-rotor harmonic noise sources.

Having introduced the technique for transforming ground-based acoustic pressure time-history signals to those measured by virtual inflight observers, it is possible to perform periodic ensemble averaging on measured ground-noise data in order

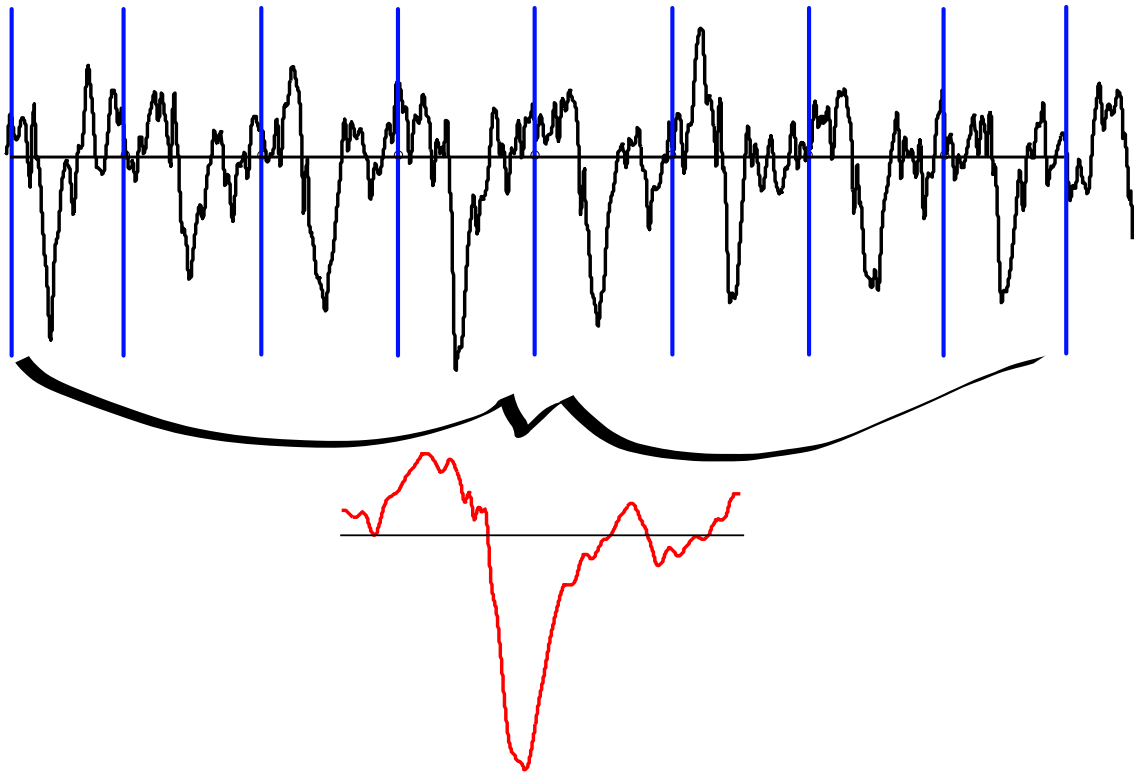

Figure 4.5: Periodic ensemble averaging of rotor noise in order to suppress the contribution of non-rotor harmonic sources.

to separate the contributions of main, tail, and non-rotor harmonic noise sources to the overall noise radiation, as would be performed in a wind tunnel.[55] The individual rotor revolutions must first be identified in the transformed signal, so as to compensate for variations in the rotor rotational speed.

For routine measurement of helicopter noise, a once per revolution sensor is not always available to provide direct measurements of the rotor periods. In this case, a virtual once per revolution sensor can be constructed from the transformed pressure time-history acoustic signals. This is accomplished by calculating a wavelet power spectrogram of the transformed signal. The continuous wavelet transform is

expressed using the following convolution:

$$U(a,t) = \int_{-\infty}^{\infty} u(t') \frac{1}{\sqrt{a}} \xi^* \left(\frac{t-t'}{a} \right) dt' \tag{4.2}$$

where a is the scale of the wavelet (inversely related to frequency), t is the time of the transform, and ξ^* is the complex conjugate of the wavelet basis function. In this dissertation, the Ricker wavelet basis function is used, as it is known to provide excellent temporal accuracy.[60] This wavelet basis is expressed as:

$$\xi(x) = \frac{1}{\sigma^3 \sqrt{2\pi}} \left(1 - \frac{x^2}{\sigma^2} \right) e^{\frac{-x^2}{2\sigma^2}} \tag{4.3}$$

where σ is a shape parameter, typically chosen about unity. The wavelet power spectrogram differs from traditional short time Fourier transform techniques in that an arbitrary frequency resolution can be employed to analyze the signal. For this application, the spectrogram is calculated at a number of wavelet scales associated with the frequencies between 90% and 110%—by picking out the maximum power over this frequency interval in time, the effect of individual blade passages can be identified, yielding the corresponding rotor period intervals. The entire rotor period identification process is shown in Figure 4.6 on the next page.

Rotor periods are collected for averaging based on angle between the propagation path from the assumed source and observer and the rotor tip-path-plane. Since the virtual observers are composed from ground-based measurements, they traverse through a range of elevation angles over time. At positions near the horizon, the rate of angular motion is small, since the ground-based microphones were far from the helicopter during the measurement. At positions underneath the helicopter, the angular rate of change of the virtual observers is more rapid, as the signal was

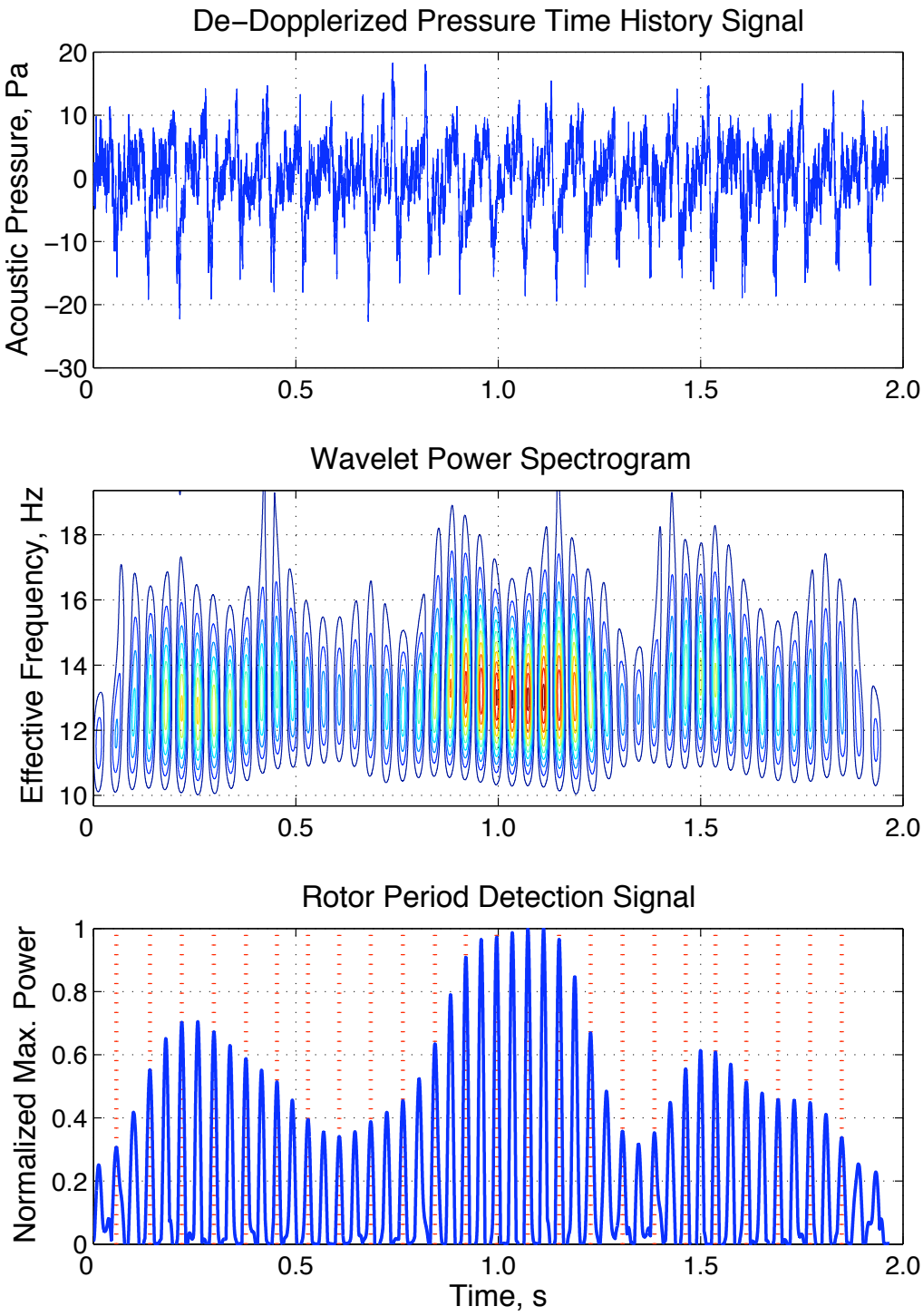

Figure 4.6: Calculation of the wavelet power spectrogram to identify rotor blade passages from the de-Dopplerized acoustic signal.

collected as the helicopter was passing directly over the ground-based microphone array. In order to correctly reflect noise radiated from a single direction, the periodic ensemble averaging process must be limited to a small angle swept by the virtual observers. Representative main and tail rotor pressure time history signals are created using periodic ensemble averaging at fixed angular increments along the paths traced by the virtual observers. Consequently, more rotor revolutions may be included in the average for virtual observers oriented towards the horizon than while underneath the helicopter. (Figure 4.7)

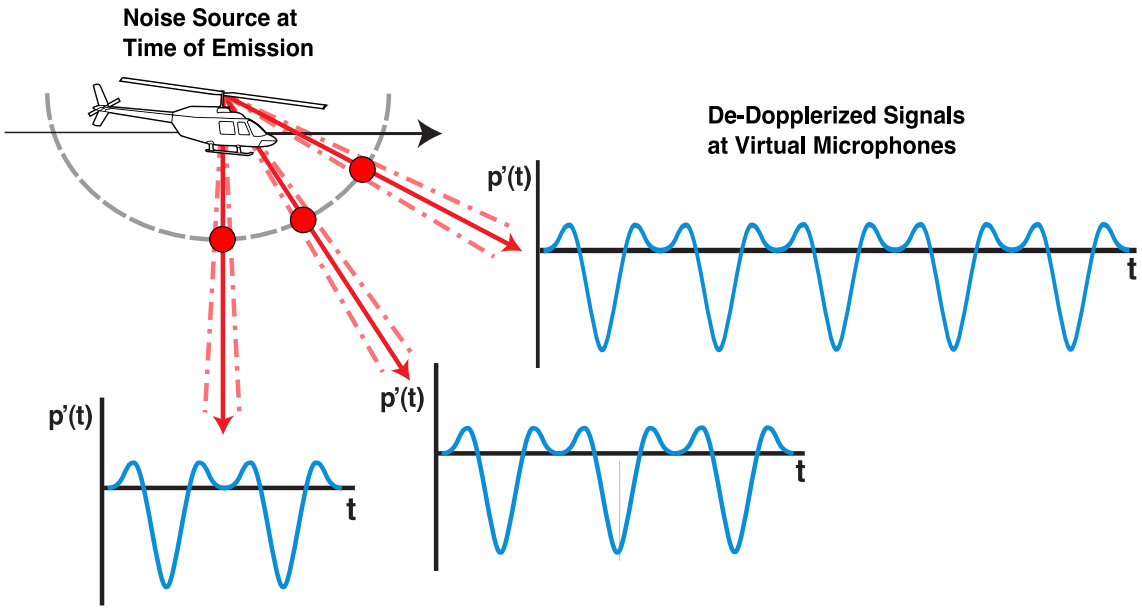

Figure 4.7: Diagram illustrating the the inclusion of rotor periods in the ensemble averaging process as a function of observation angle.

So far, the transformation process has assumed that all noise produced by the helicopter may be represented by a compact source located, for instance, at the main rotor hub. In reality, the noise is generated by a distribution of sources across the

rotor blades which vary azimuthally in strength. The assumption of a hub-centered compact source introduces an error in the phase of the acoustic pressure originating from sources away from the hub during the evaluation of the retarded time equation. For lower frequency sources, such as steady loading and thickness noise, the error in phase is relatively small. However, for impulsive noise sources like those associated with BVI, even a small change in phase can disrupt the averaging process. The error in phase is dependent on the geometry between the observer, the assumed source location, and the real source.

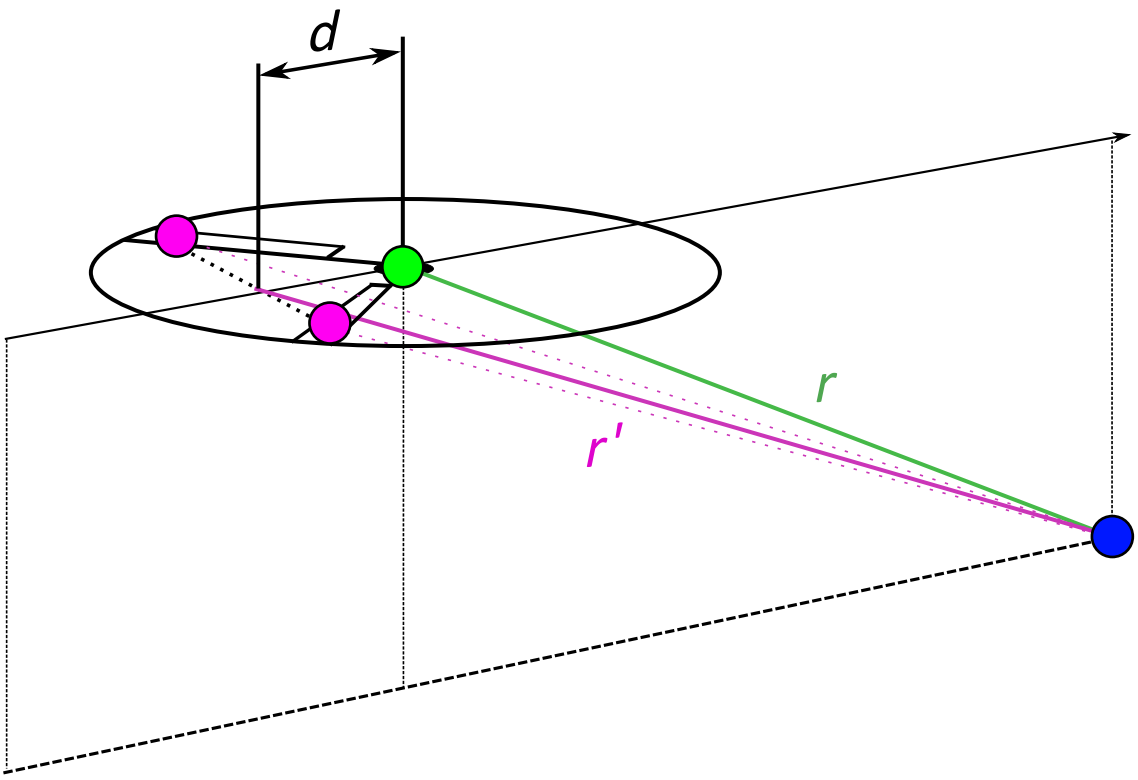

Figure 4.8: The phase error due to the compact source assumption changes with respect to observation angle.

Figure 4.8 shows the how the compact source assumption introduces a phase

error during the transformation process due to the longitudinal distance between the assumed source location and any individual real source on the rotor. When the observer lies along the line containing the assumed source location and the real source, the error in retarded time calculation will be the distance between the two divided by the speed of sound. When the observer is directly underneath the two sources, the error in the retarded time calculation will be zero, as the path lengths will be equal. If the observer is much farther from the sources than the distance between the real and assumed source, the error in retarded time may be approximated as:

$$\Delta t = \frac{d}{a_0} \cos\theta \tag{4.4}$$

where d is the longitudinal distance between the assumed and actual source location, and θ the angle between the observer and the rotor plane. Plotted against elevation angle, this results in the phase error seen in Figure 4.9 on the next page.

More significantly for the averaging process, the rate of change of the error in the retarded time calculation is highest out of the plane between the assumed source and the real source, shown in Figure 4.10 on page 92.

For the case of a real helicopter, all sources are on or near the rotor blades. Several different BVIs may occur at once, originating from different locations on the rotor disk. At the elevation angles underneath the rotor plane, the phase of the BVI pulse will shift quickly between each rotor period, eliminating the BVI pulse from the averaged signal. The error in the assumed source location is not as important in the plane of the rotor because the rate of change of phase due to error in the retarded time calculation is small. Therefore, the BVIs which radiate the most noise below the helicopter are the most sensitive to error in source location. The shifting

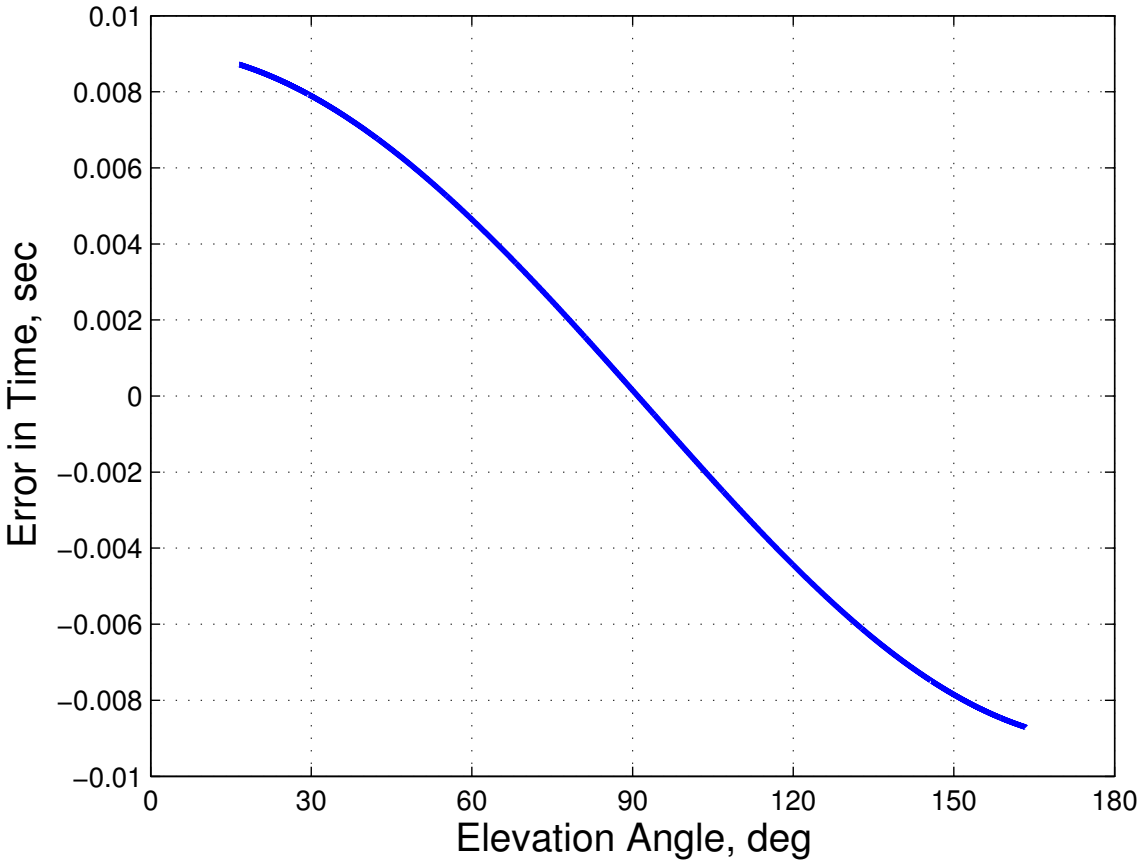

Figure 4.9: Error in time with elevation angle due to compact source assumption.

phase of such a BVI from one revolution to the next is shown in Figure 4.11.

The hemisphere could be constructed about a different assumed source location on the rotor, more representative of BVI. However, different types of BVI occur during different flight conditions, occurring at different areas on the rotor disk. For example, a parallel BVI may occur on a 2-bladed rotor at about 45° azimuth, and occurs across much of the blade simultaneously. Oblique BVIs occur across a range of azimuth, and sweep across the blade over time. Since it is difficult to predict which BVI will be dominant for a particular flight condition *a priori*, it is useful

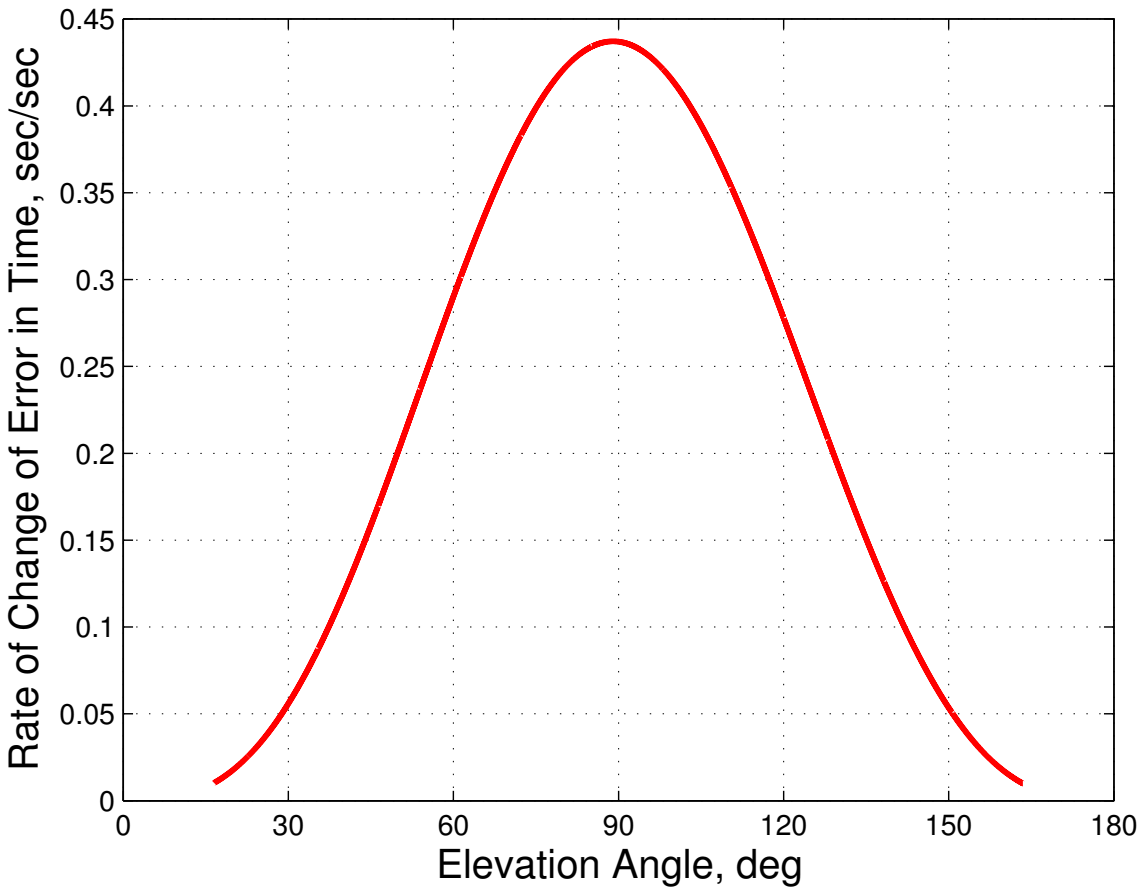

Figure 4.10: Rate of change of time error with respect to elevation angle.

to correct for the error in the phase of BVI pulses individually at each directivity angle on the surface of the acoustic hemisphere. The most prominent BVI pulses in the signals are synchronized between revolutions by adjusting the phase of each time segment used in the periodic average so as to align the peak response of the cross correlations between the signal for each rotor period and the signal of the central rotor period in time. The result is a representative rotor harmonic pressure time-history signal containing both the impulsive and lower harmonic noise radiated in the corresponding direction, shown in Figure 4.12 on page 94. This process is

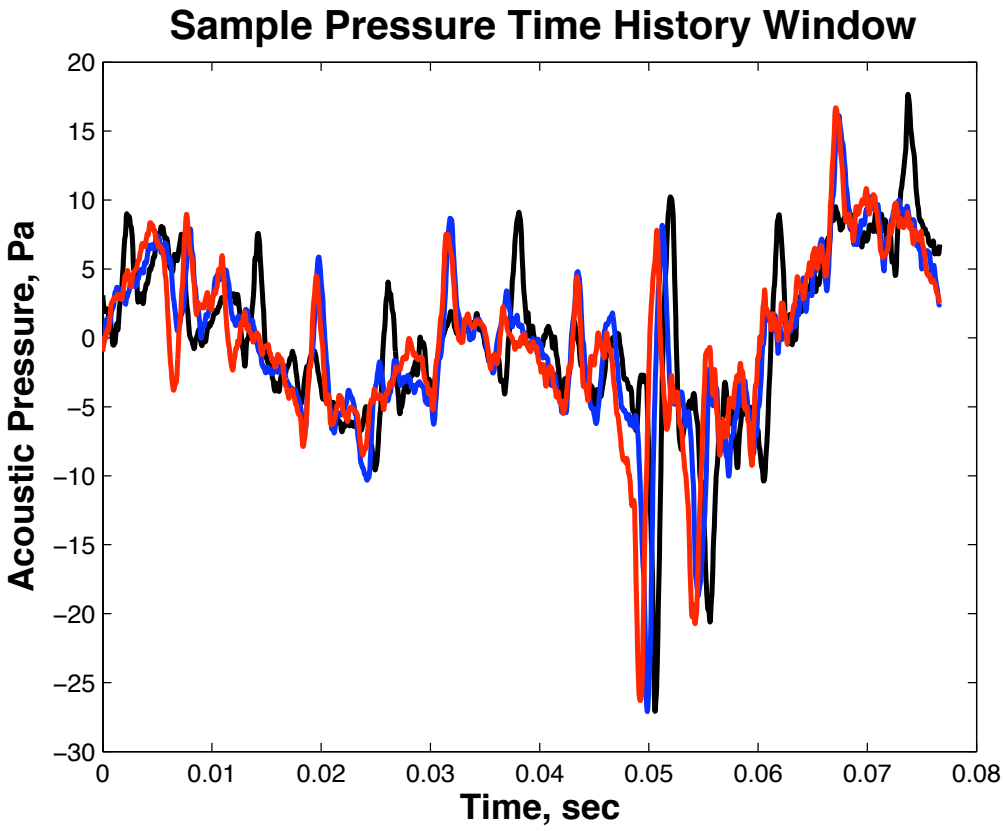

Figure 4.11: Changing time error causes impulsive BVI noise to shift in phase over successive rotor time periods.

repeated for each direction traversed by the virtual observers in order to construct a complete representation of rotor harmonic noise radiated by the helicopter. By repeating the process for both the main and tail rotor, all rotor harmonic noise sources can be characterized. Non-rotor harmonic noise is captured by subtracting the rotor harmonic noise signals for each rotor from the unaveraged virtual observer pressure time-history signals in order to yield a residual signal. This residual signal can be evaluated using standard frequency-domain techniques for generating acoustic hemispheres, since phase does not carry useful information for these noise sources.

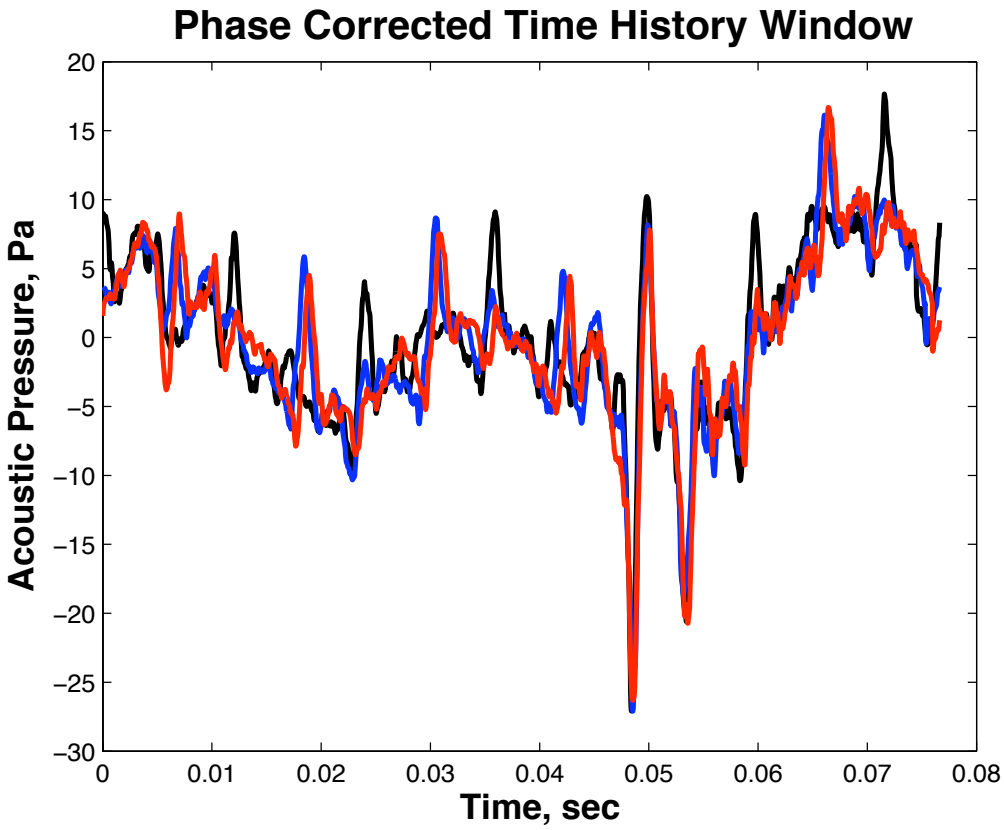

Figure 4.12: A cross-correlation can be used to adjust the phase of each rotor period so as to preserve the BVI impulse in the averaged signal.

4.4 Projection of Acoustic Hemispheres

Three-dimensional images of hemispheres are unable to show the noise levels across the entire surface of the sphere without employing multiple views. In order to display the hemisphere in its entirety on a single plot, it is necessary to project the hemisphere onto a 2D planar surface.

No 2D projection of a spherical surface can be free of distortion, as Euler proved in 1777.[61] Such a projection can either be conformal or equal-area, but never both. A conformal projection preserves the shape of features, since at each point the angles between the spherical surface coordinates are locally preserved in the flat coordinate system. However, the relative size of features will be changed globally during the transformation. An equal-area projection ensures that each region of the map will retain the same area in the flat coordinate system as it had on the spherical surface; however, the orientation of points with respect to each other within any region will be changed, distorting the shape of each feature. In order to effectively display all of the information captured by a hemisphere, some sort of projection to a flat 2D figure must be employed.

In this paper, hemispheres are displayed mapped to a 2D image using a Lambert Conformal Conic projection, developed and used commonly by cartographers to accurately display maps of polar regions.[62] The Lambert projection is perfectly conformal, but is also fairly close to being equal-area when no more than one half of a sphere is transformed at once. This is achieved by splitting the back end of the hemisphere along the 0 degree azimuth angle, and unrolling the resulting

cone to a 2D projection. (Figure 4.13) The top of the projection represents the angle directly in front of the helicopter, the split seam the angle directly behind, the right side the advancing side of the helicopter, and the left the retreating side. The center of the projection, at 90 degrees elevation, represents the bottom of the hemisphere. The radial lines thus represent the azimuth angles, and the concentric lines the elevation angles. This projection allows for an intuitive understanding of the directivity patterns of externally radiated noise.

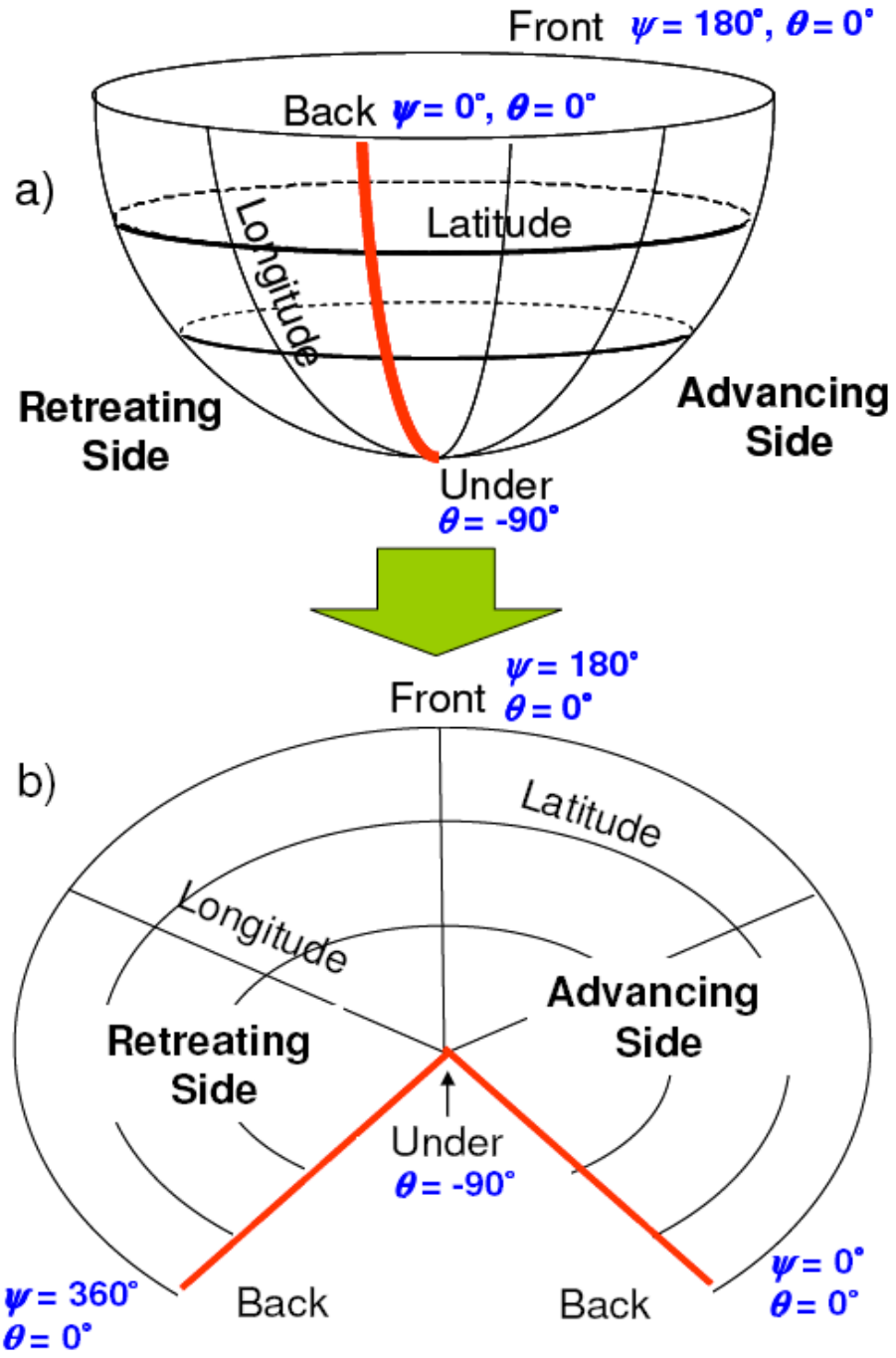

Figure 4.13: The Lambert projection of an acoustic hemisphere.

4.5 Measurement Quality

One fundamental assumption of all processes for characterizing helicopter noise from ground-based measurements is that the helicopter maintains a steady acoustic state over the measurement window, i.e. the noise radiation of the helicopter is identical from one rotor revolution to the next. In practice, this is never the case—the flight state of the helicopter is continuously changing due to atmospheric unsteadiness and pilot control corrections. It is important to ensure that the consequent variability in the acoustic state of the helicopter is within acceptable limits throughout the measurement run. Without simultaneous measurement of the helicopter at fixed observation angles, it is difficult to directly quantify the quality of the measured data. However, some indirect observations may be made to place bounds on the acoustic variability.

One simple approach is to repeat each measurement multiple times, and assess the variability of the measurement statistically. Provided that similar noise levels are measured over all directions for several repeated runs, the standard deviation in noise levels can be calculated and a level of confidence can be established in the quality of the measurements, for instance by calculating the standard deviation of the SPL at each point on the resulting acoustic hemisphere. The degree of confidence increases as more measurements are included in the analysis. However, this requires that each flight condition to be characterized must be measured many times, greatly increasing the time and expense of collecting helicopter noise data.

Another statistical method of characterizing helicopter noise is to take a moving

standard deviation of the noise levels seen by the virtual observers as they traverse the acoustic hemisphere surrounding the helicopter. With the knowledge that noise levels do not change sharply with directivity, it is assumed that sudden changes in noise levels found in the transformed signals are due to changes in the flight state of the helicopter, and can be captured by taking calculating the standard deviation over a short time window. This method provides some estimate of the variability of the acoustic state of the helicopter from a single measurement, and also indicates the quality of the measured data as a function of directivity angle. The $2N$ point moving standard deviation at point k is formulated as:

$$\sigma_k = \sqrt{\frac{1}{2N} \sum_{n=k-N}^{k+N} (x_n - \bar{x}_n)^2} \tag{4.5}$$

where $\bar{x}_n$ is the central moving average at point n.

Both of these techniques will be applied to assess the quality of the measured data in the following chapter.

Chapter 5

Applications

The data analysis and modeling methods develop in Chapters 3 and 4 can be applied not only to ground-based measurements of flying vehicles, but also to wind tunnel test data for isolated rotors. In this chapter, models are built using two sets of data for two-bladed rotors—the first is from the test of an isolated $1/7^{\text{th}}$ scale model of the AH-1 Operational Loads Survey (OLS) rotor in the German-Dutch Windtunnel (DNW).[63] The second is from the flight testing of a Bell 206B3 helicopter over Moffett Field, California.[64]

5.1 Wind Tunnel Test

The parameter identification method is first applied to acoustic measurements of several flight conditions produced from the test of the 2-bladed $1/7^{\text{th}}$ scale AH-1 Operational Loads Survey (OLS) rotor in the German–Dutch Wind Tunnel (DNW). This dataset is notable for high quality acoustic measurements over a wide range of operational conditions carefully controlled by the governing non-dimensional parameters of rotor harmonic noise sources. Nine microphones located within the wind tunnel jet, labeled 2 through 10 in Figure 5.1 on page 105, were included in the parameter identification process. Although these microphone locations are predominantly ahead of and towards the advancing side of the rotor, there is still a

R	3.14 ft
c	0.341 ft
t/c	9.71 %

Table 5.1: Geometric characteristics of the model scale OLS rotor.

sufficient variation in directivity angles to allow a single "best fit" to be identified in all cases. Using these data, the ability of the parameter identification technique to produce models correctly capturing the parametric variations of rotor noise is evaluated. The model scale OLS rotor has the geometric characteristics listed in Table 5.1.

The data collected during this test is very consistent, especially for the microphones inside of the wind tunnel jet used in this research. Figure 5.2 compares typical 100 revolution averaged and instantaneous pressure time-history measurements recorded from microphone channel #4 during the experiment. There is little difference between the instantaneous and averaged measurements, especially in terms of the impulsive BVI noise—this demonstrates the steadiness of the rotor acoustic state during the test. This steadiness is one of the major benefits of a carefully controlled wind tunnel test. The baseline operating condition is defined by the non-dimensional governing parameter values in Table 5.2.

Figures 5.3, 5.4, and 5.5 show the measured and simulated acoustic pressure time-histories for the baseline case and fitted model at in-plane, 30° and 45° out-of-

λ	0.0135
C_T	0.0054
μ	0.164
M_{HT}	0.620

Table 5.2: Non-dimensional governing parameter values for wind tunnel test cases.

plane observer locations, respectively. In general, the pressure time-histories for most observer locations are fitted by the model to within about 1 dB BVISPL; although some of the in-plane observers are fit to within 1.5 dB BVISPL. These in-plane observers capture the lower harmonic thickness noise well. In addition, the overall magnitude of the in-plane BVI noise is fairly well captured by the fitted model, but the phasing of the impulse is not in complete agreement with the measured data. The more out-of-plane observers accurately capture form of the BVI impulses in the pressure time history signal. Lower harmonic noise is well captured by the model as well, with OASPL also fit to within 1 dB (not shown) for all observers. Overall, the discrepancy between the measured and modeled pressure time-history signals is well within the natural variability of noise from one rotor revolution to the next observed in actual flight.

As an accurate analytical model of the external noise radiation of the rotor for a single flight condition has been developed, the generalization of this model to other operating conditions is now demonstrated. Using the modeling parameters

identified for the baseline condition of the model rotor estimates are made for the noise radiated at other operating conditions, as defined by variations of the non-dimensional governing parameters. These noise estimates are then compared to measured acoustic data for the OLS rotor undergoing the same parametric variations of operating condition. Figure 5.6 shows the peak-to-peak acoustic pressure for various thrust coefficients as seen at the 45° out-of-plane observer location shown for the baseline case in Figure 5.5. Both the measured and simulated data show an approximately linear trend in peak levels with variation in thrust coefficient; however, the slope of the simulated data is significantly less than that of the measured data. On closer inspection, the linear fit of the simulated model extrapolates to zero peak acoustic pressure at zero thrust, unlike the linear fit of the measured data. This indicates that some physics of the BVI noise generation process are not captured by the analytical model.

Similarly, the peak acoustic pressure trend for the measured and modeled data due to variations in advancing tip Mach number is shown in Figure 5.7. The model has a similar trend to the measured data, but over-predicts noise at lower Mach numbers and under-predicts at higher Mach numbers than the baseline case. This is because the chosen analytical model does not directly incorporate the effects of compressibility on BVI.

In order to model physics not explicitly captured in the analytical model, the dependent modeling parameters must be varied as a function of the non-dimensional governing parameters. This can be accomplished by identifying dependent parameters for several different operating conditions and then using this information to estimate

the dependent parameter values for other unmeasured operating conditions—this process is described in Section 3.3. This results in a large improvement in the accuracy of the noise models when generalized to unmeasured operating conditions. For example, Figure 5.8 shows the results of using simple linear interpolation to estimate dependent parameter values from measured data for two different different thrust coefficient values. The discrepancy between measured and modeled peak acoustic pressure values is greatly reduced over those observed when using only the dependent parameters developed from the baseline condition, as shown in Figure 5.6. Adding just one more additional set of identified parameters further improves the fit, allowing the model to match the observed trend almost exactly, as shown in Figure 5.9.

Likewise, incorporating additional measured data can also improve generalization of the model as a function of advancing tip Mach number. Figures 5.10 and 5.11 show the peak BVI acoustic pressure variation as a function of advancing tip Mach number for models incorporating data from two and three different operating conditions, respectively. Model agreement with measured data improves dramatically by incorporating just one additional set of measured data; further refinement is achieved by adding data for additional Mach number variations.

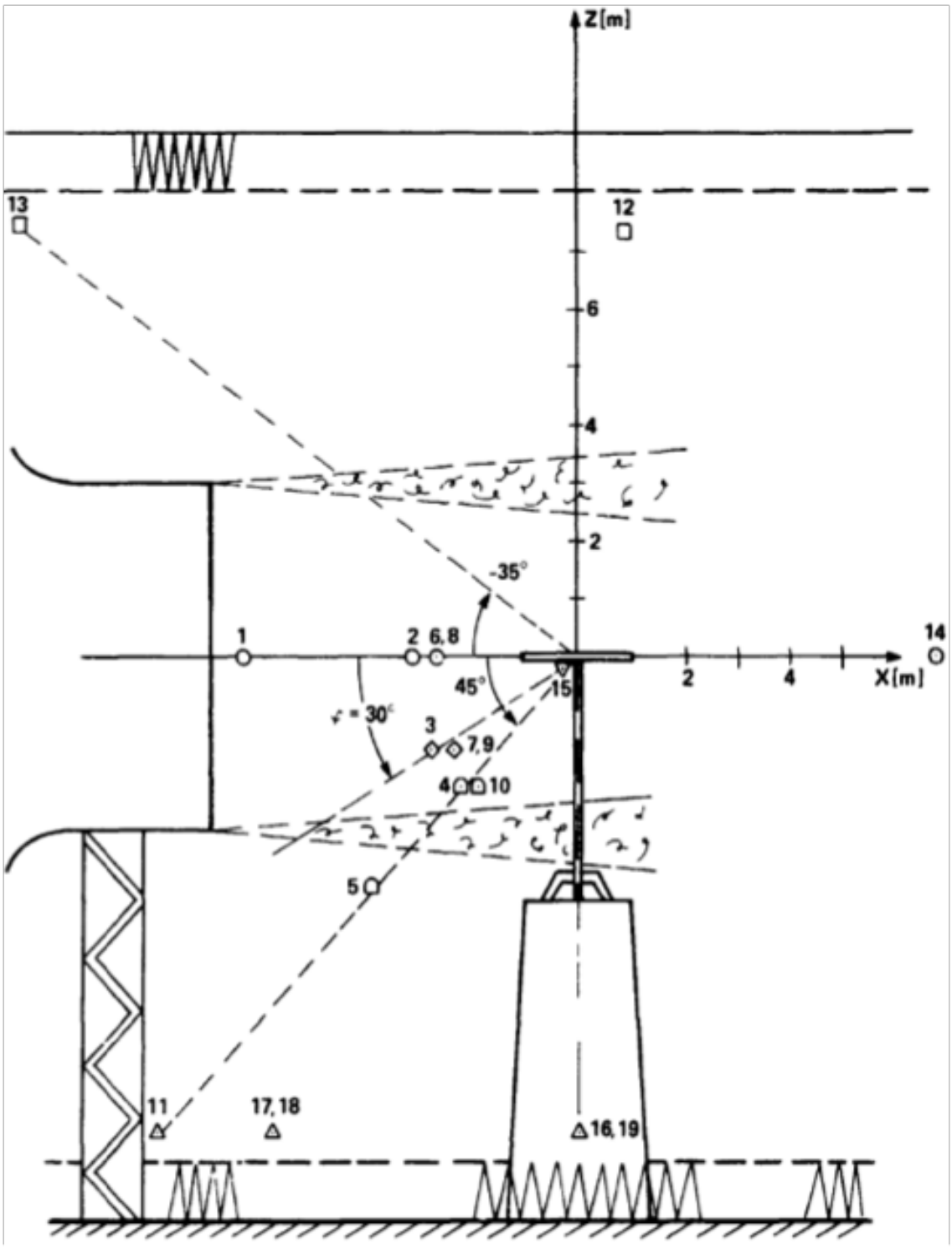

Figure 5.1: Side-view of the DNW windtunnel microphone measurement configuration for the $1/7^{\text{th}}$ scale OLS rotor.

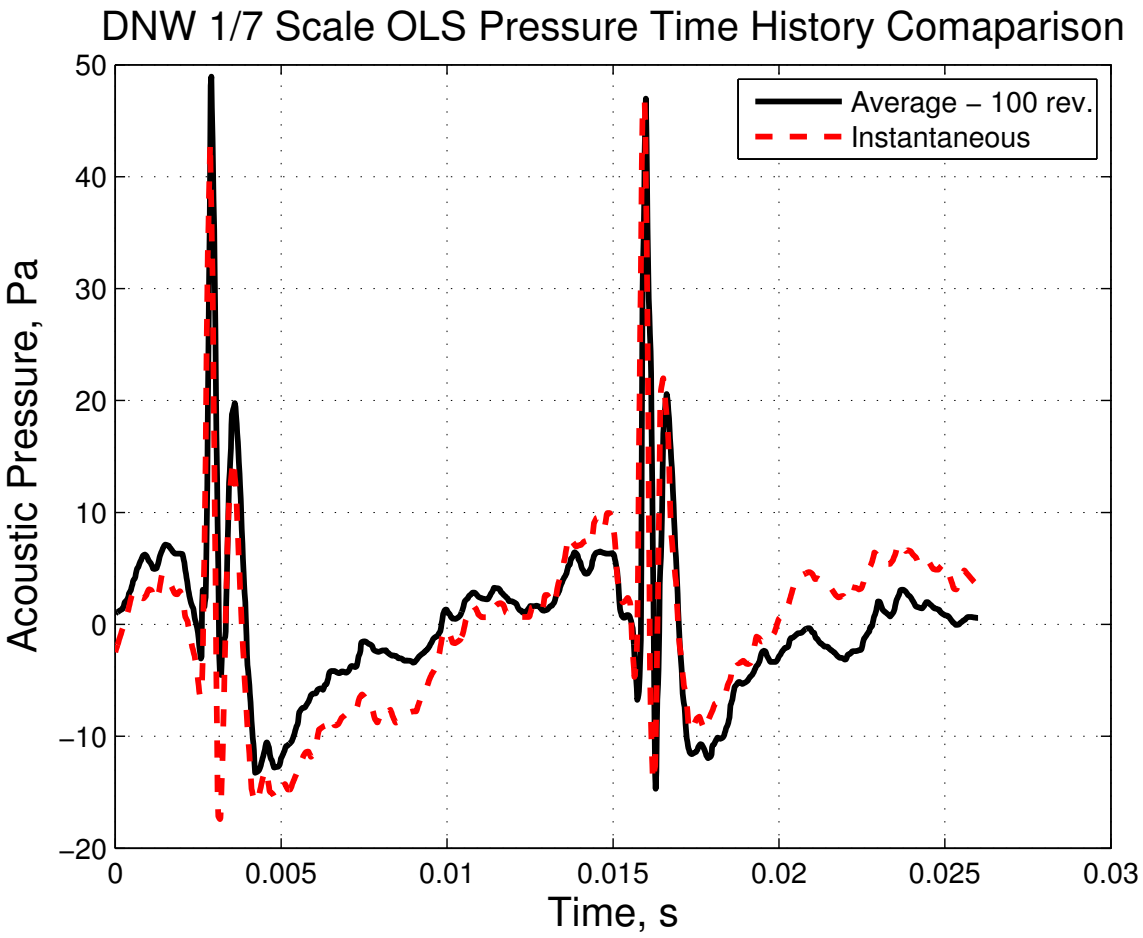

Figure 5.2: Comparison of typical averaged and instantaneous pressure time-history measurements for the DNW $1/7^{\text{th}}$ scale OLS experiment.

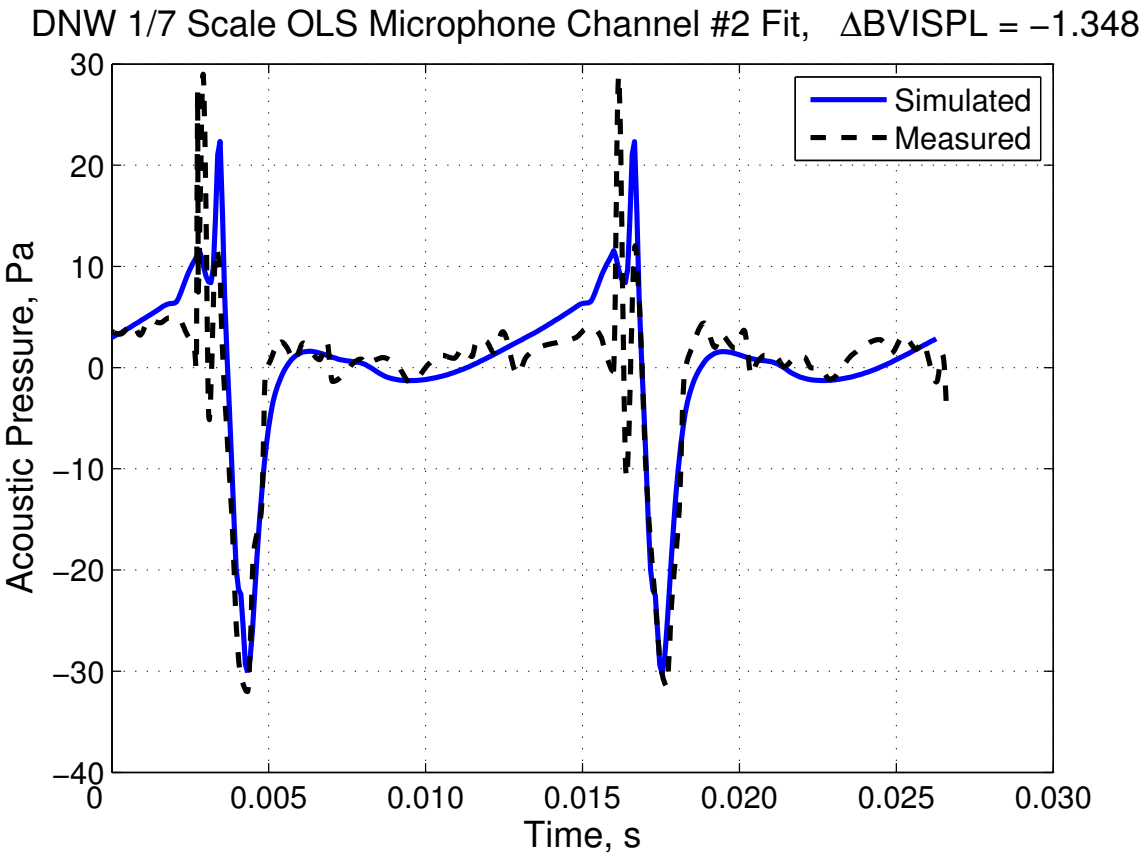

Figure 5.3: Measured and fitted-model acoustic pressure time-histories for in-plane observer location of rotor in baseline operating condition.

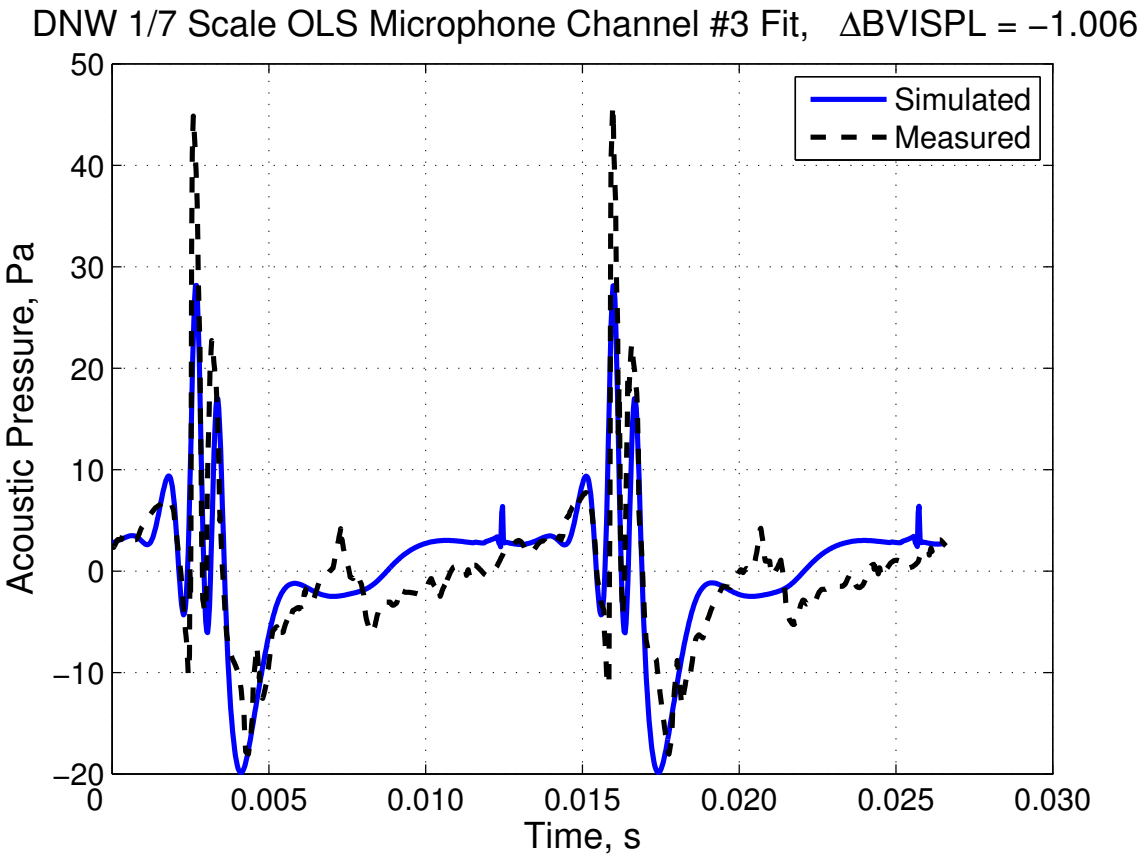

Figure 5.4: Measured and fitted-model acoustic pressure time-histories for 30° out-of-plane observer location of rotor in baseline operating condition.

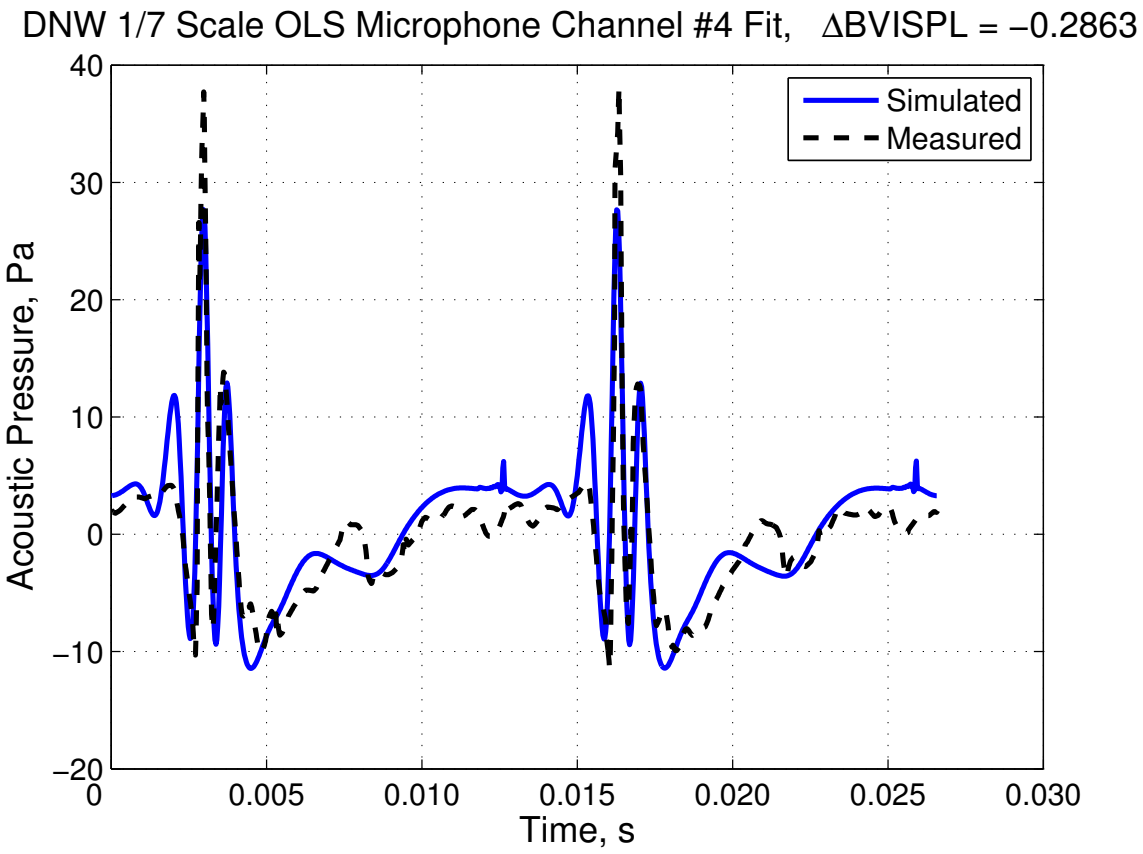

Figure 5.5: Measured and fitted-model acoustic pressure time-histories for 45° out-of-plane observer location of rotor in baseline operating condition.

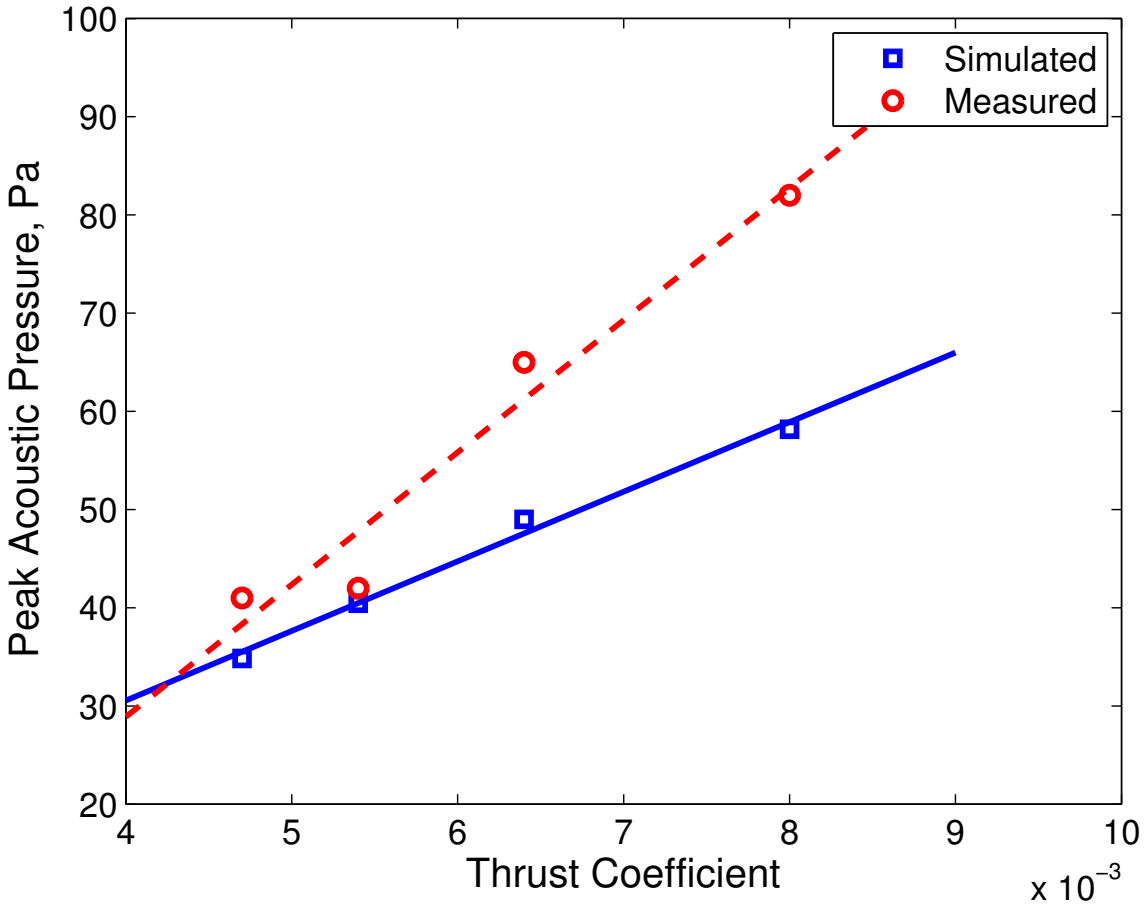

Figure 5.6: Measured and simulated variation in peak BVI acoustic pressure with thrust coefficient for the 45° out-of-plane observer. Model uses parameters developed for the baseline case.

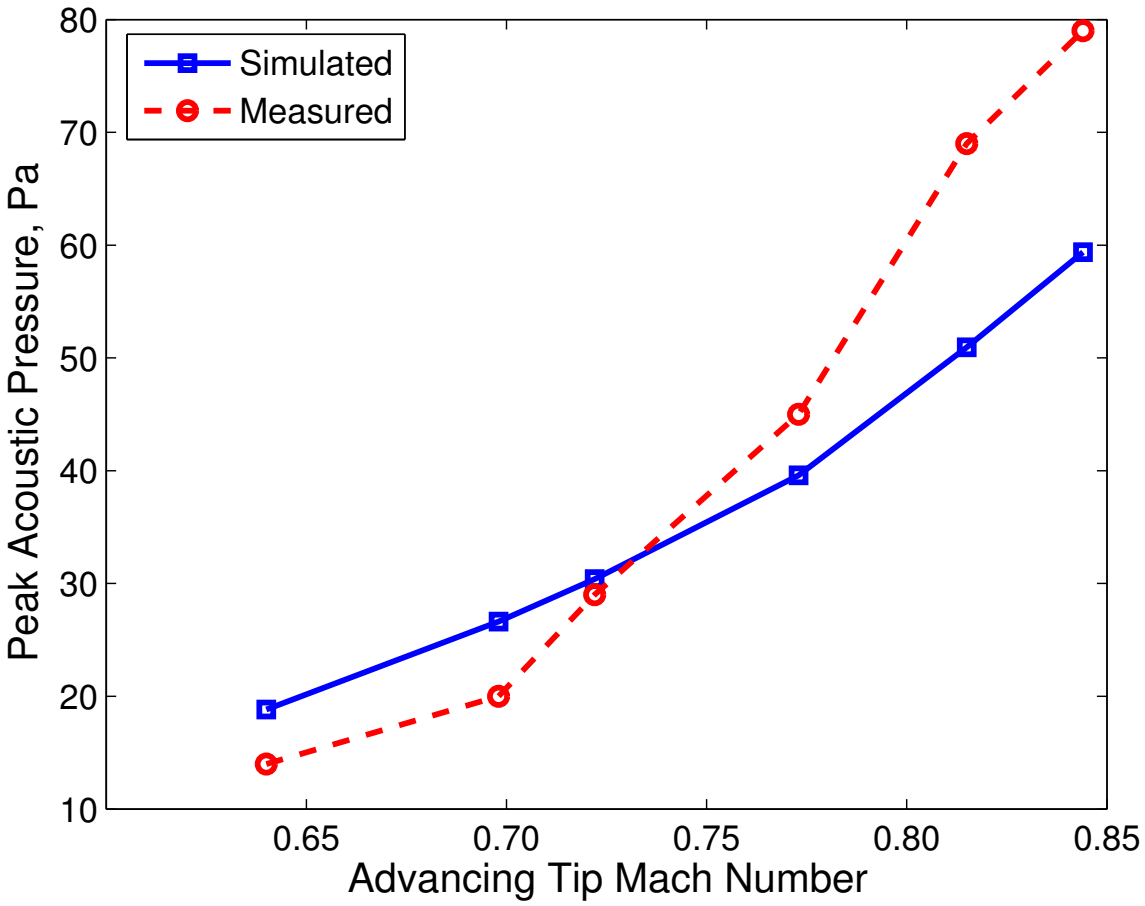

Figure 5.7: Measured and simulated variation in peak BVI acoustic pressure with advancing tip Mach number for the 45° out-of-plane observer. Model uses parameters developed for the baseline case.

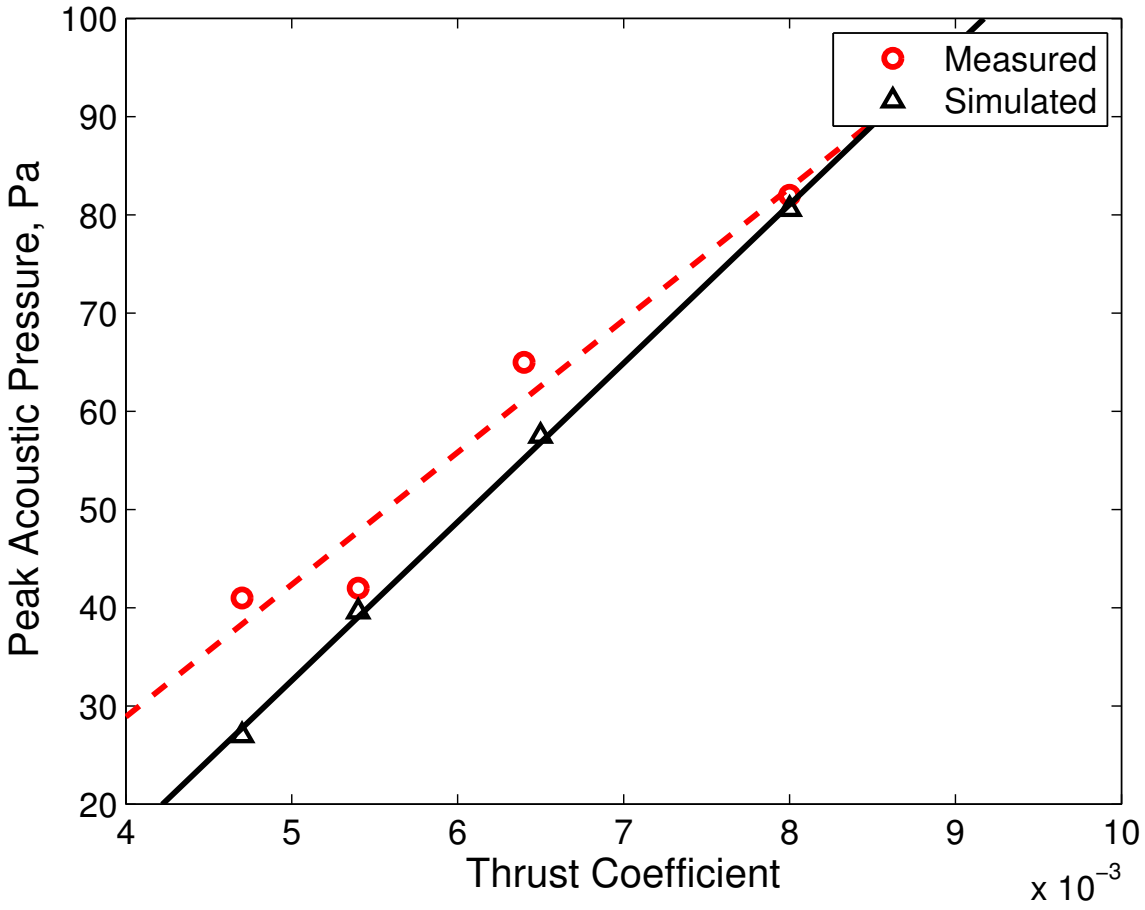

Figure 5.8: Measured and simulated variation in peak BVI acoustic pressure with thrust coefficient for the 45° out-of-plane observer. Model uses parameters developed for the baseline case and $C_T = 0.0080$.

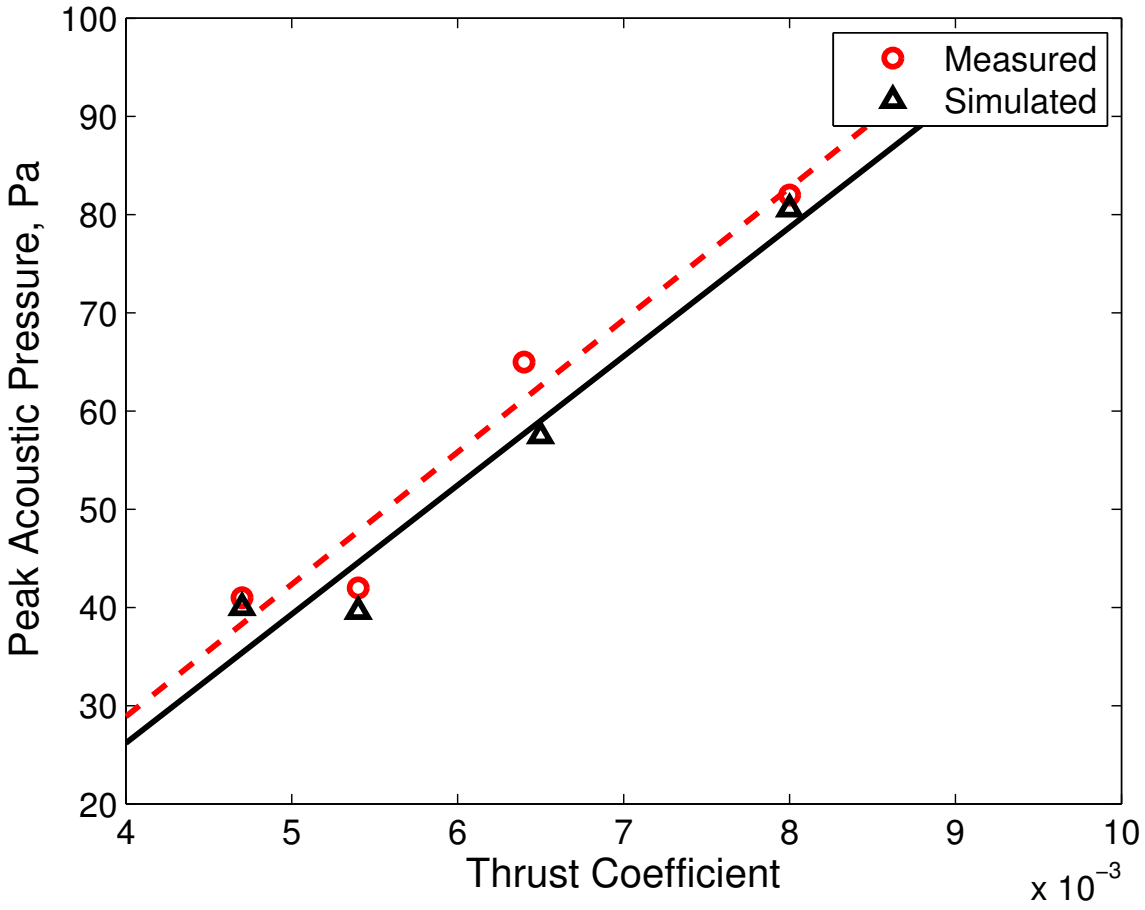

Figure 5.9: Measured and simulated variation in peak BVI acoustic pressure with thrust coefficient for the 45° out-of-plane observer. Model uses parameters developed for the baseline case, $C_T = 0.0047$ and $C_T = 0.0080$.

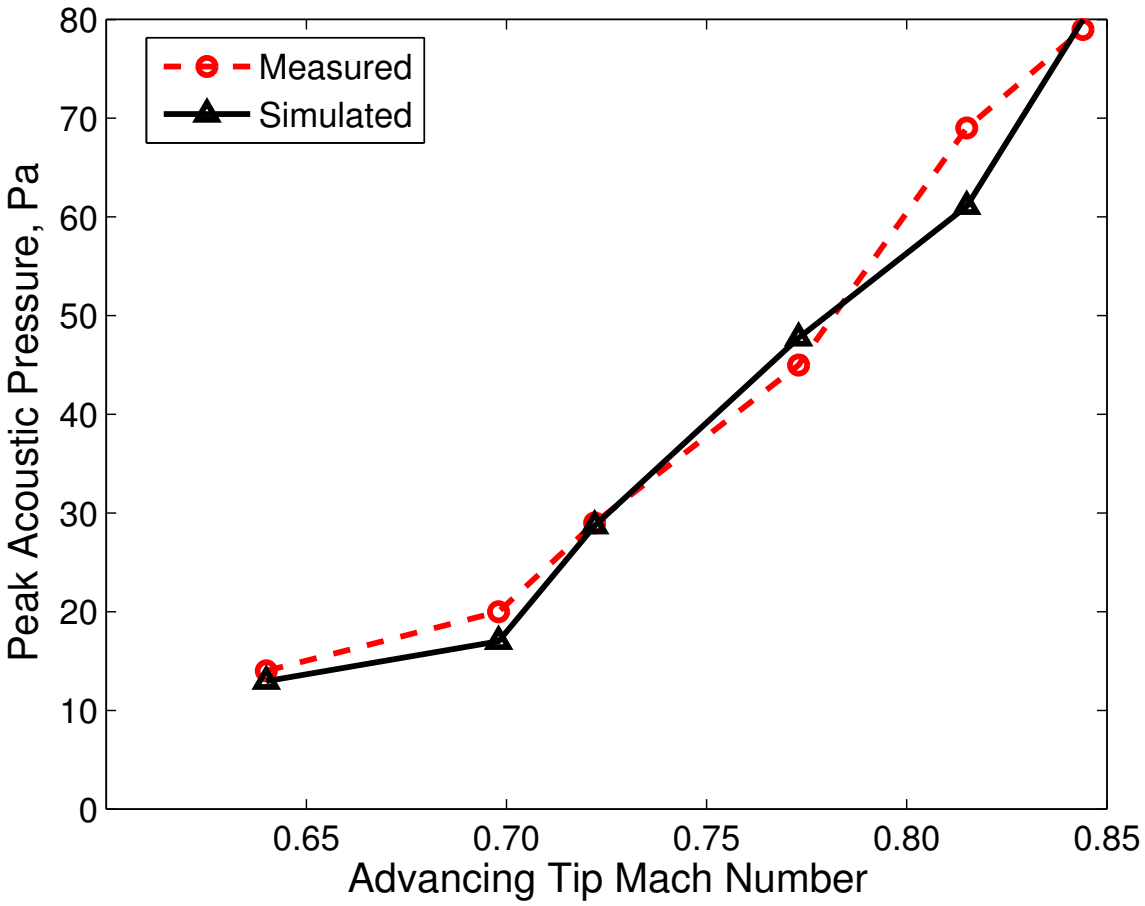

Figure 5.10: Measured and simulated variation in peak BVI acoustic pressure with advancing tip Mach number for the 45° out-of-plane observer. Model uses parameters developed for the baseline case and $M_{AT} = 0.64$.

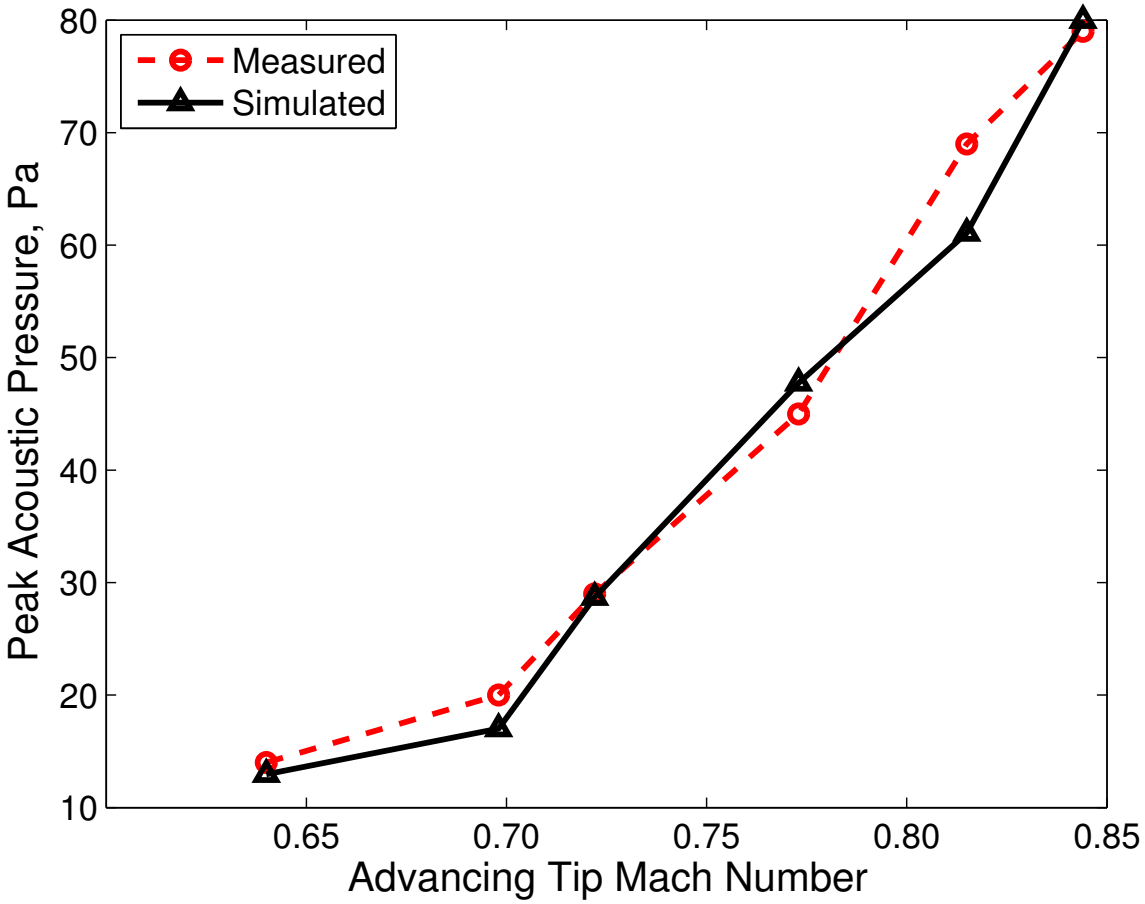

Figure 5.11: Measured and simulated variation in peak BVI acoustic pressure with advancing tip Mach number for the 45° out-of-plane observer. Model uses parameters developed for the baseline case, $M_{AT} = 0.64$ and $M_{AT} = 0.84$.

In addition to producing noise estimates at known observer locations, the models developed by this process can be used to estimate noise levels in directions which were not measured. Figure 5.12 shows the Lambert projection of the BVISPL noise level contours produced using the model for the baseline case on the surface of a hemisphere offset 30 feet from the rotor hub. In the flight condition, BVI noise is radiated ahead of and below the rotor disk. The Lambert projection is described in more detail in Section 4.4. As advance ratio increases, (Figures 5.13 through 5.15) the noise levels increase and are directed more in-plane and towards the advancing side, as has been observed in previous theoretical[65] and experimental studies of BVI.[66]

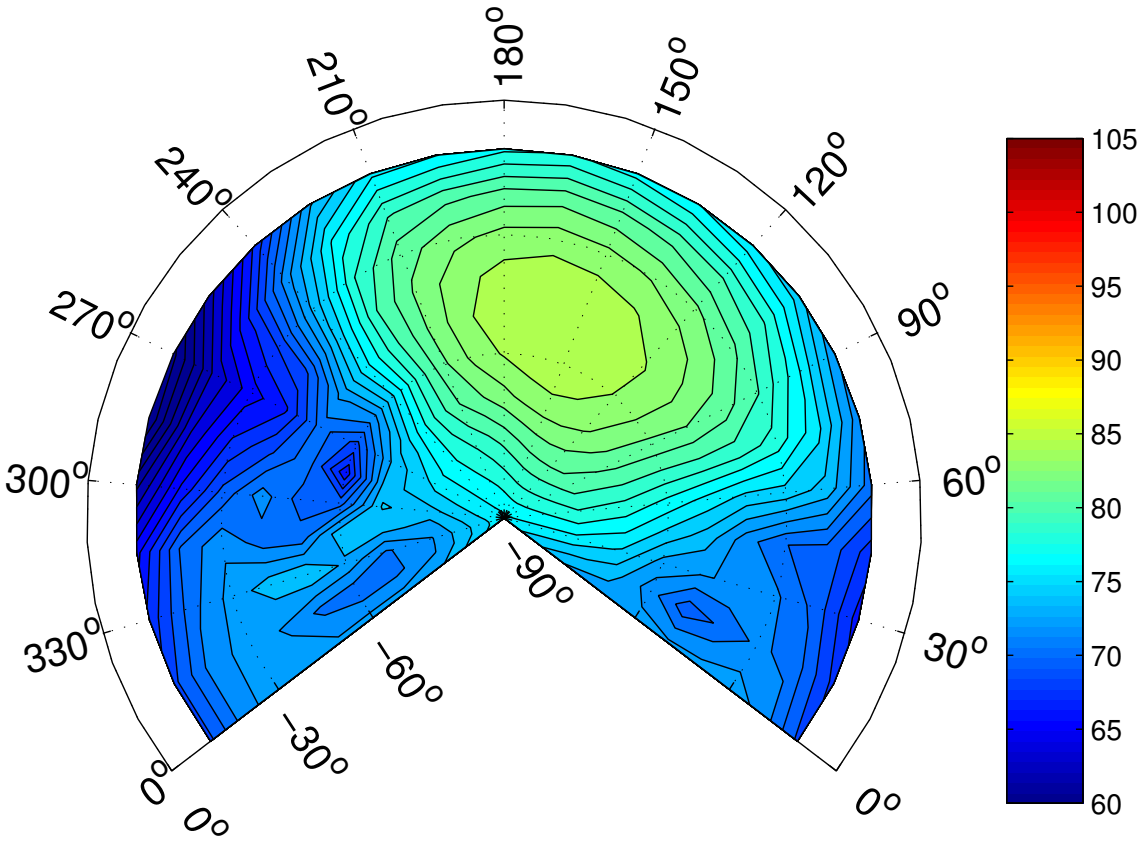

Figure 5.12: BVISPL noise level contours for the baseline case ($\mu = 0.164$).

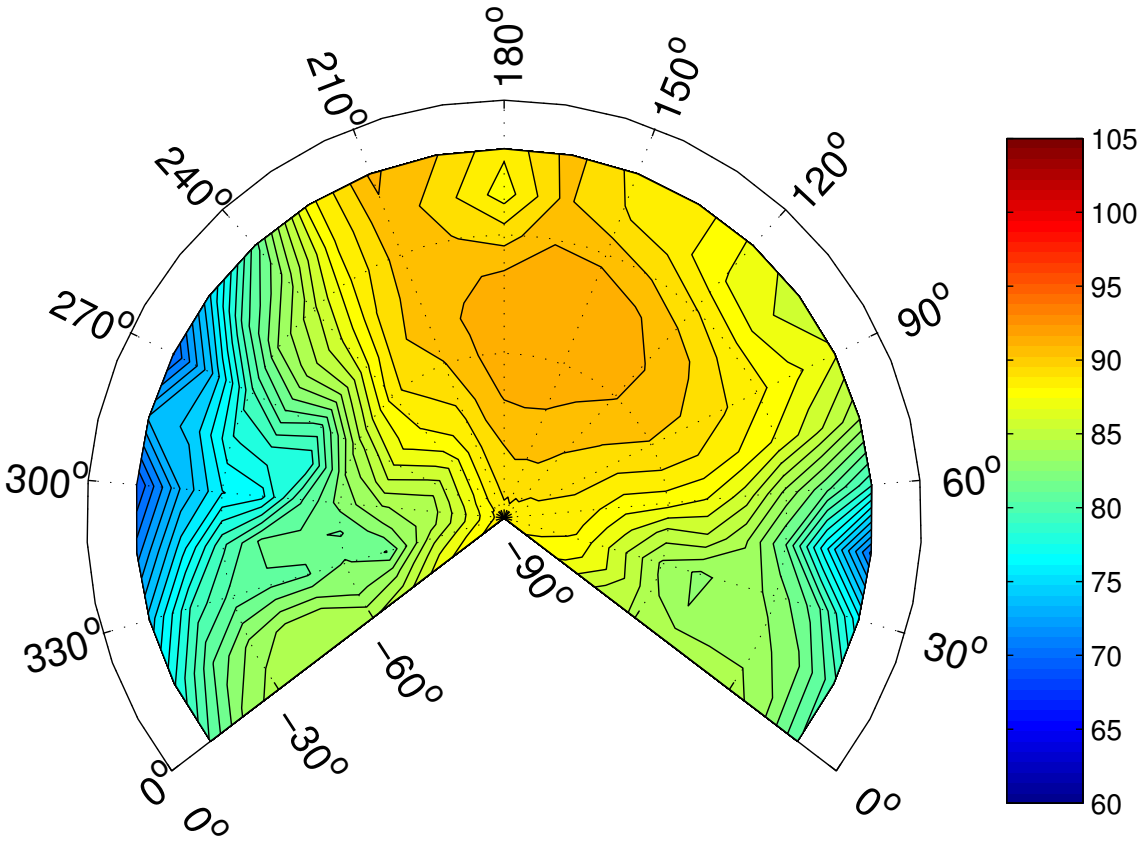

Figure 5.13: BVISPL noise level contours for $\mu = 0.194$.

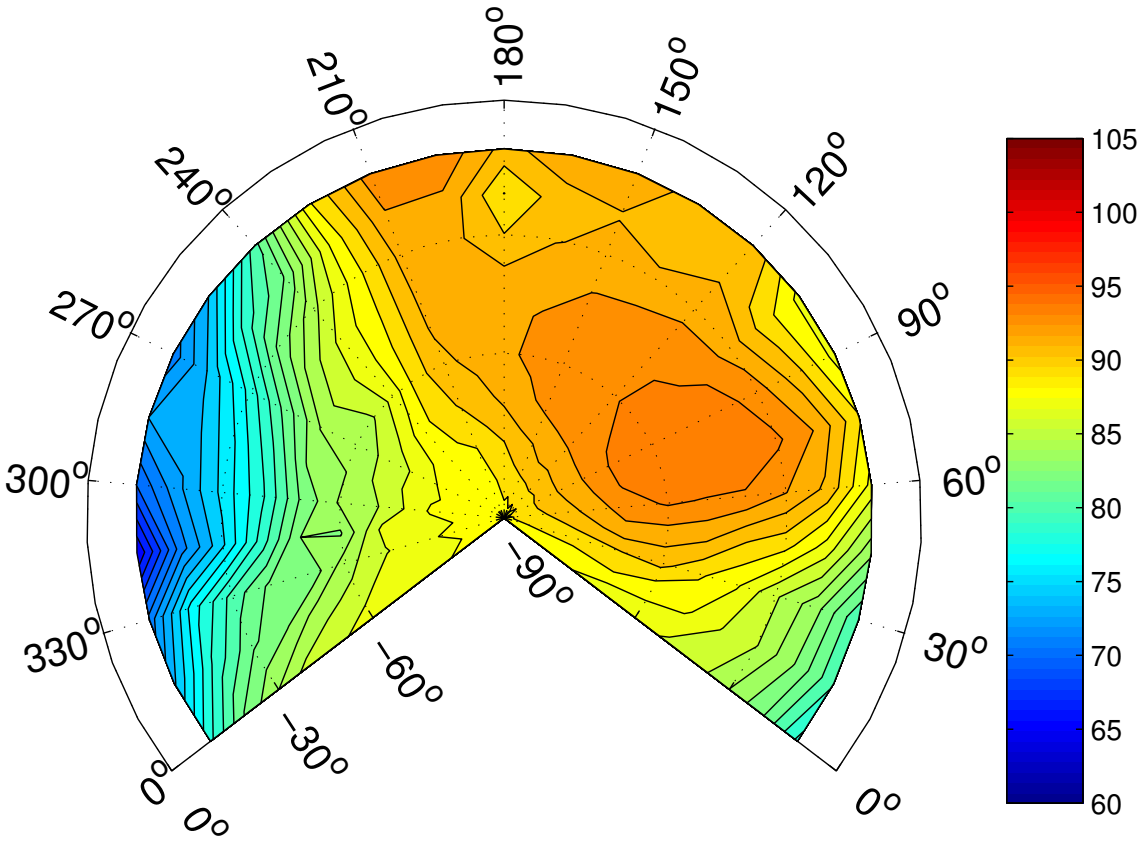

Figure 5.14: BVISPL noise level contours for $\mu = 0.224$.

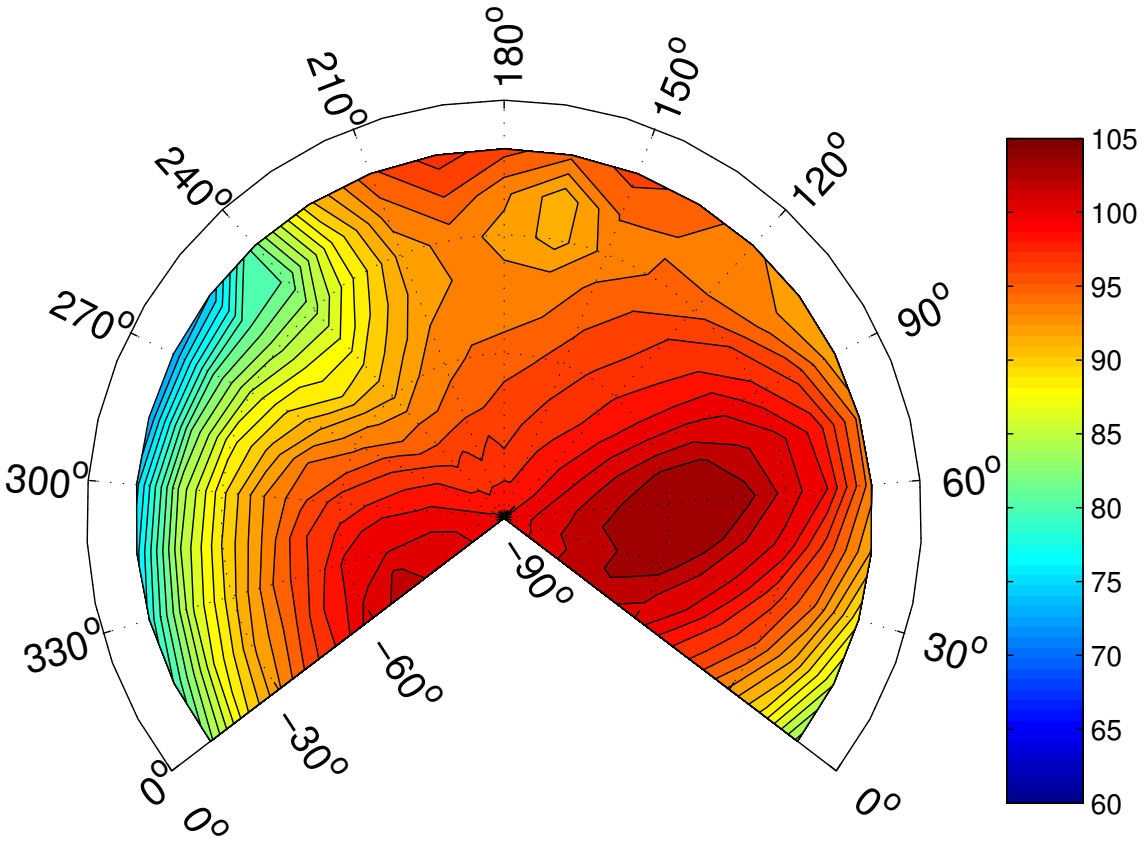

Figure 5.15: BVISPL noise level contours for $\mu = 0.270$.

5.2 Flight Test

In addition to wind tunnel data, the modeling approach is applied to measured ground noise data from the flight test of a Bell 206B3 helicopter at Moffett Field, CA, in 2006. Ground noise data were collected from a linear array of eight ground board microphones for a variety of steady and maneuvering flight conditions. In addition, the helicopter was instrumented with a unique inflight measurement array. The modeling approach developed in this dissertation is applied to this dataset to demonstrate how analytical models that relate noise to non-dimensional governing parameters may be built for full-scale helicopters. Such models are suitable for ground noise contour generation under a wide range of flight conditions. Ground noise contours for a diverse range of atmospheric and flight conditions are often required for effective mission planning and community noise abatement, yet measured ground noise data are generally available over only a limited set of operating conditions due to the significant cost of acquiring such data. Non-dimensional analytical models provide a means to generalize a limited set of measured data so that it is applicable over a wider range of conditions. In addition, the relatively simple analytical models resulting from this technique can be run in real time, which makes them suitable for inflight noise estimation. The Bell 206B3 main rotor has the geometric characteristics listed in Table 5.3.

As described in the previous section, the ground-based acoustic measurements are transformed to a reference frame analogous to wind tunnel measurements. The wavelet transform is then used to identify individual rotor revolutions from the

R	16.7 ft
c	1.10 ft
t/c	11.3%

Table 5.3: Geometric characteristics of the Bell 206B3 main rotor.

acoustic signal. The main rotor harmonic pressure time-history signals are extracted using a periodic averaging process for a number of observer directions. More rotor periods may be included in the averaging process for in-plane observers than out-of-plane observers; therefore, the more in-plane data is a better representation of the main rotor harmonic time-history signal. In addition, the dominant noise sources of the rotor do not strongly radiate directly underneath the helicopter. For these reasons, the distribution of "virtual inflight observers" included in the analysis is biased away from the underside of the helicopter and towards the dominant radiation directions. The measured signals transformed to these observers are the inputs to the parameter identification process.

The modeling process is applied to data for several steady descending flight conditions at 60 kts airspeed with approximately the same gross weight and rotor RPM for each case—in effect, a parametric variation of non-dimensional inflow which greatly affects BVI noise levels. The non-dimensional governing parameter values for this case are shown in Table 5.4.

Due to the increased variability in measured flight test data, the model does

λ	*various*
C_T	0.0033
μ	0.15
M_{HT}	0.626

Table 5.4: Non-dimensional governing parameter values for flight test cases.

not match the measured data as closely as for the wind tunnel case. However, the fit is within 1.5 dB BVISPL for all observer locations—well within the typical variations between repeated measurements of the same operating condition in flight test data. Figure 5.16 shows the unaveraged BVISPL levels for the centerline "virtual observer" at 5° increments for three different runs of the nominal 60 kts, -6° flight path angle flight condition. The condition was held fairly close to the desired test point in all three cases. In Run A, the average airspeed recorded was 61 kts. In Run B and Run C, the average airspeed was approximately 56 kts. The average flight path angle in all cases was within 0.2° of nominal. Figure 5.17 shows a plot of the standard deviation between all three runs at each observation angle. Significant deviations in measured BVISPL levels can be observed for all three cases in the range of 1.0-2.0 dB BVISPL, especially near the front of the helicopter, where the BVI noise levels are the highest. This is about the same level of repeatability observed for approach conditions in other rotorcraft flight test measurement programs.[67] Figure 5.18 shows the five-point moving standard deviation of the same "virtual observer" measurement—it can be

seen from this calculation that the largest variability in noise radiation over time time seems to occur underneath the helicopter, where retreating side BVI might contribute to the BVISPL noise levels. Of these three repeated cases, Run A was selected for modeling, due to low variability observed in the moving standard deviation and a higher "steadiness" of the condition throughout the run, as indicated by the author and the flight director from the helicopter during the run.

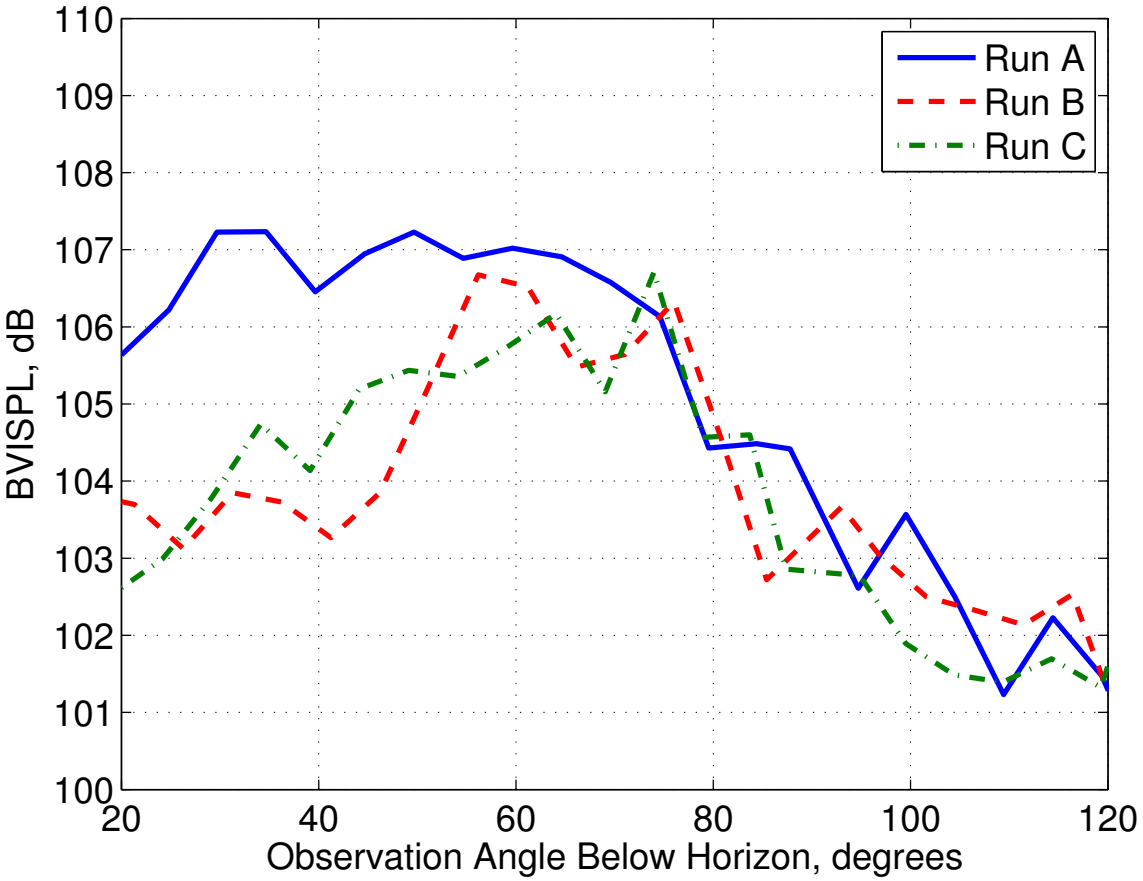

Figure 5.16: Unaveraged BVISPL at the centerline "virtual observer" during the 60kts, -6° flight condition.

Hemispheres developed by averaging and interpolating the measured main rotor harmonic noise in the BVISPL frequency range are shown for the -6° and

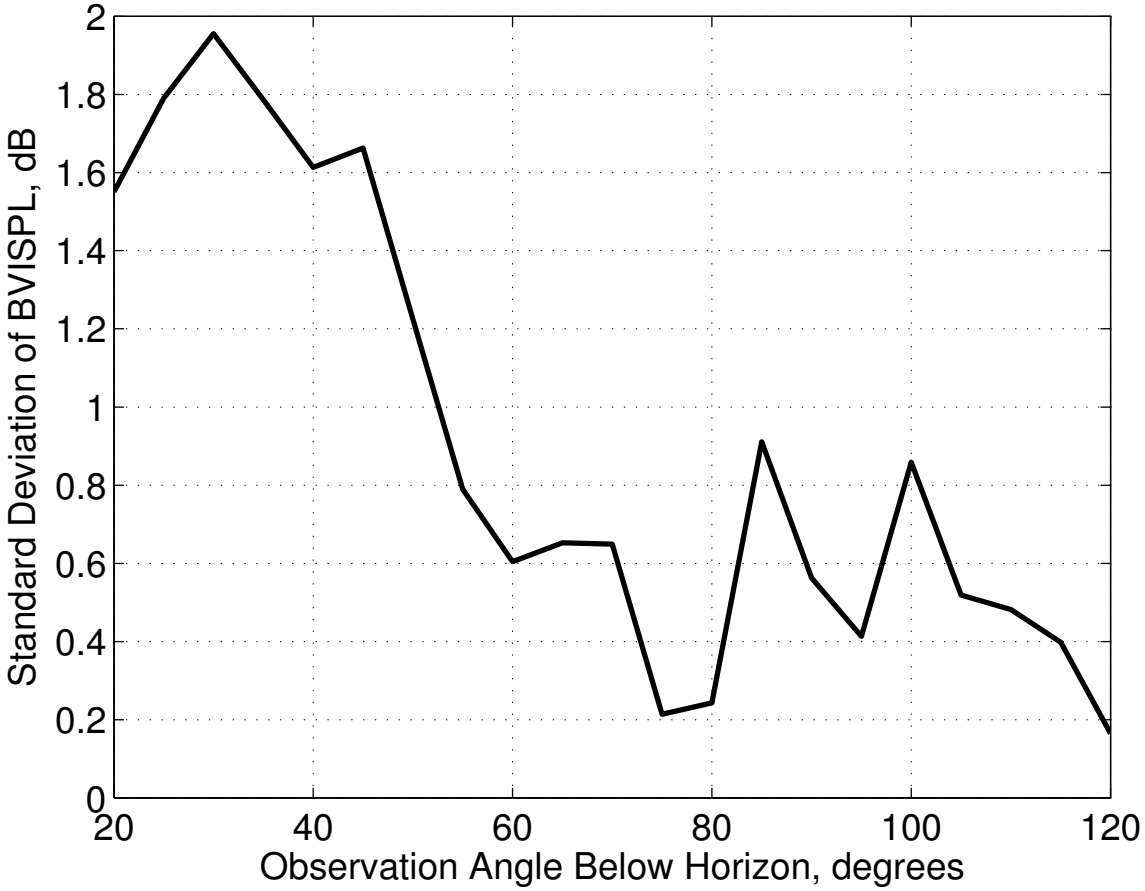

Figure 5.17: Standard deviation of BVISPL between Runs A, B, and C at the centerline "virtual observer" during the 60kts, -6° flight condition.

-7.5° flight path angle cases in Figure 5.19 and Figure 5.20, respectively. Due to the high drag of the helicopter in the experimental configuration, BVI is encountered at steeper descent angles than the "clean" configuration. In the -6° case, a strong advancing side BVI is present. In the -7.5° case, the miss distance between the rotor blades and vortices decreases further, and the magnitude of this BVI is increased; in addition, there is evidence of significant retreating side BVI noise directed beneath the helicopter. This flight condition represents the highest BVI noise levels measured in steady descending flight during the test program. The microphone measurement

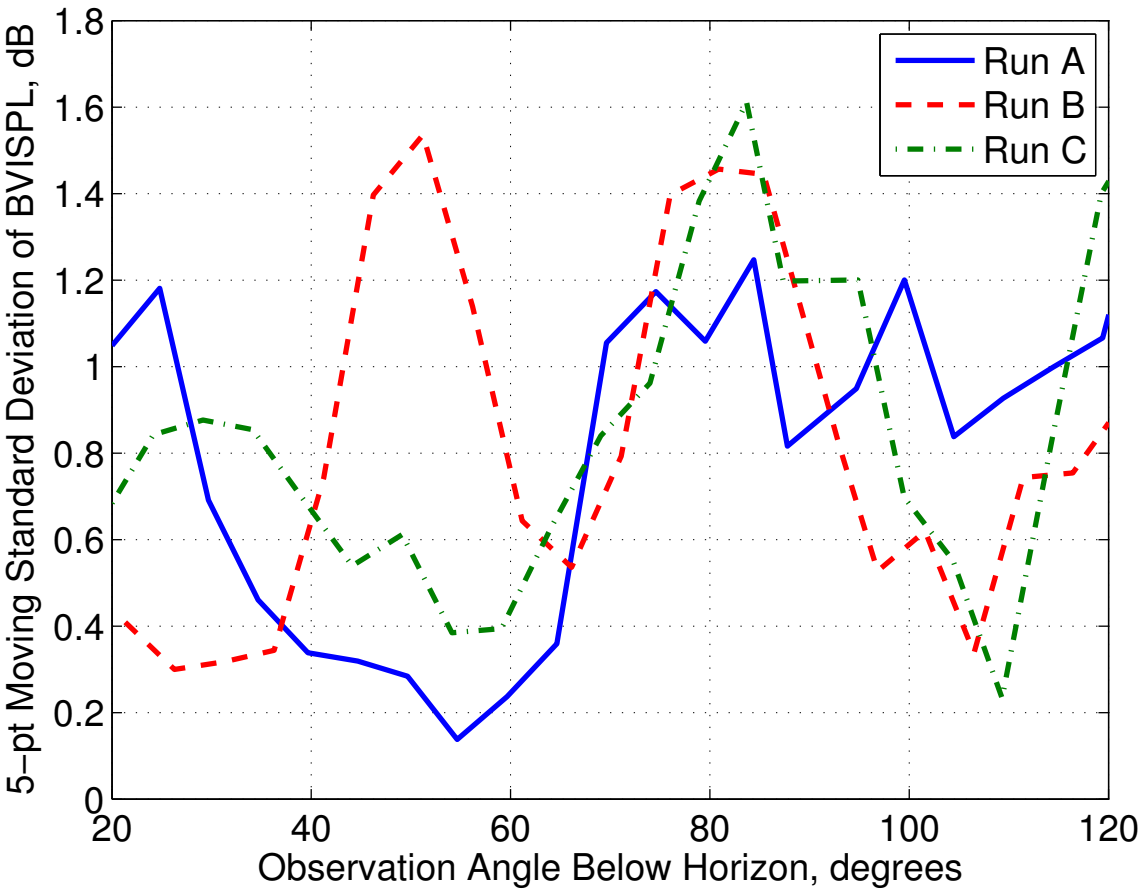

Figure 5.18: Moving standard deviation of BVISPL at the centerline "virtual observer" during the 60kts, -6° flight condition.

locations covered by the "virtual inflight array" are shown by the dotted lines on each hemisphere—estimated noise levels between these points are interpolated.

Figure 5.21 and Figure 5.22 show the simulated hemispheres generated from the assumed analytical model using the dependent parameters identified from the measured data for each case. The same general directivity trends and levels are observed in the modeled hemispheres as for the measured data, but the BVI directivity contours are much more distinct in the hemispheres generated by the analytical models. This is because the measured data must be time averaged in order to

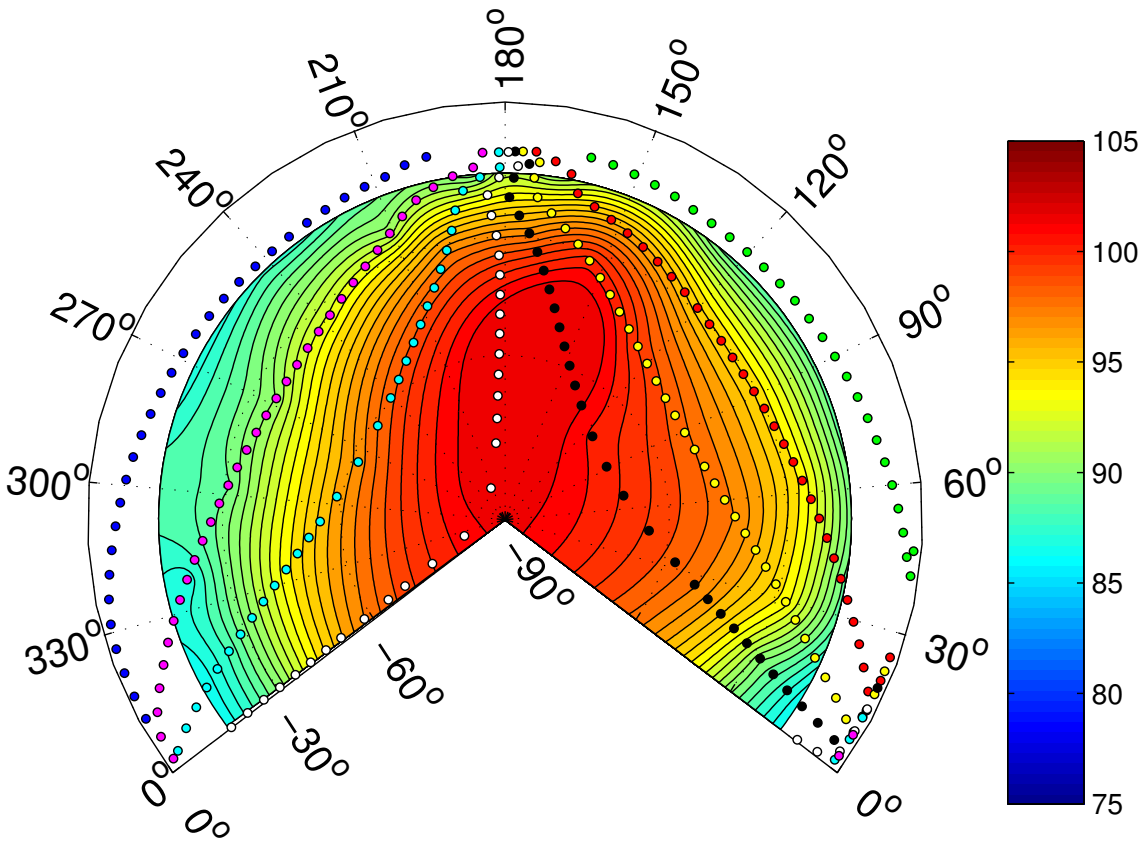

Figure 5.19: Main rotor averaged BVISPL noise level contours for -6° flight path angle condition.

compensate for variability in the flight condition during the measurement process, and then interpolated over the surface of the hemisphere in order to compensate for the relatively sparse distribution of measurements. This results in reduced accuracy on the underside of the hemisphere, where the measurement geometry changes more quickly in time and fewer periodic averages may be taken over a given angle. Conversely, the fitted analytical models estimate noise levels in regions not actually measured based on physical modeling of the noise sources. As was shown in the wind tunnel application, more accurate estimates of the noise generated by

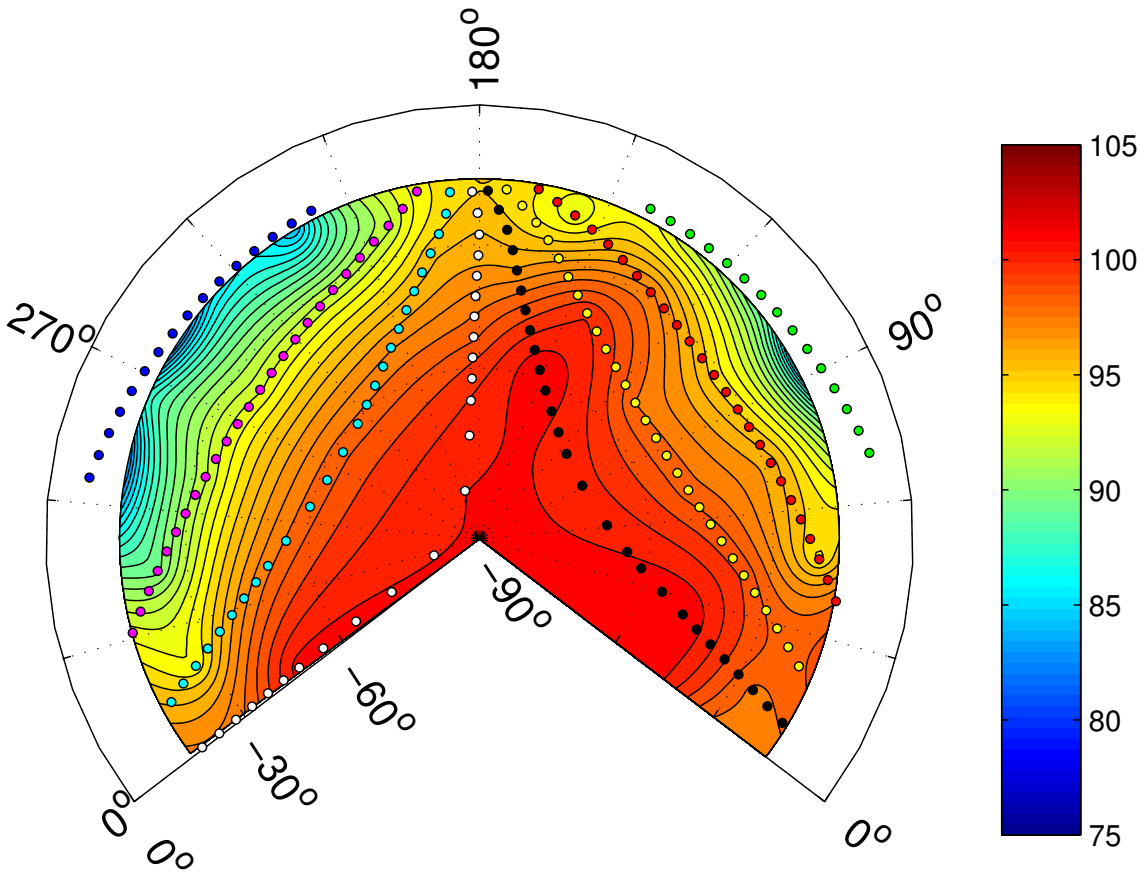

Figure 5.20: Main rotor averaged BVISPL noise level contours for -7.5° flight path angle condition.

flight conditions not measured may also be made by interpolating the dependent modeling parameters discovered by the parameter identification process with respect to the non-dimensional governing parameters that classify each flight condition. For example, the noise levels observed at the -7.5° flight condition may be estimated using the modeling parameters determined from the -3° (Figure 5.23) and -9° (Figure 5.24) flight conditions by a linear interpolation of the dependent parameters based on the change in non-dimensional inflow.

Using the standard approach of linearly interpolating SPL on an energy basis

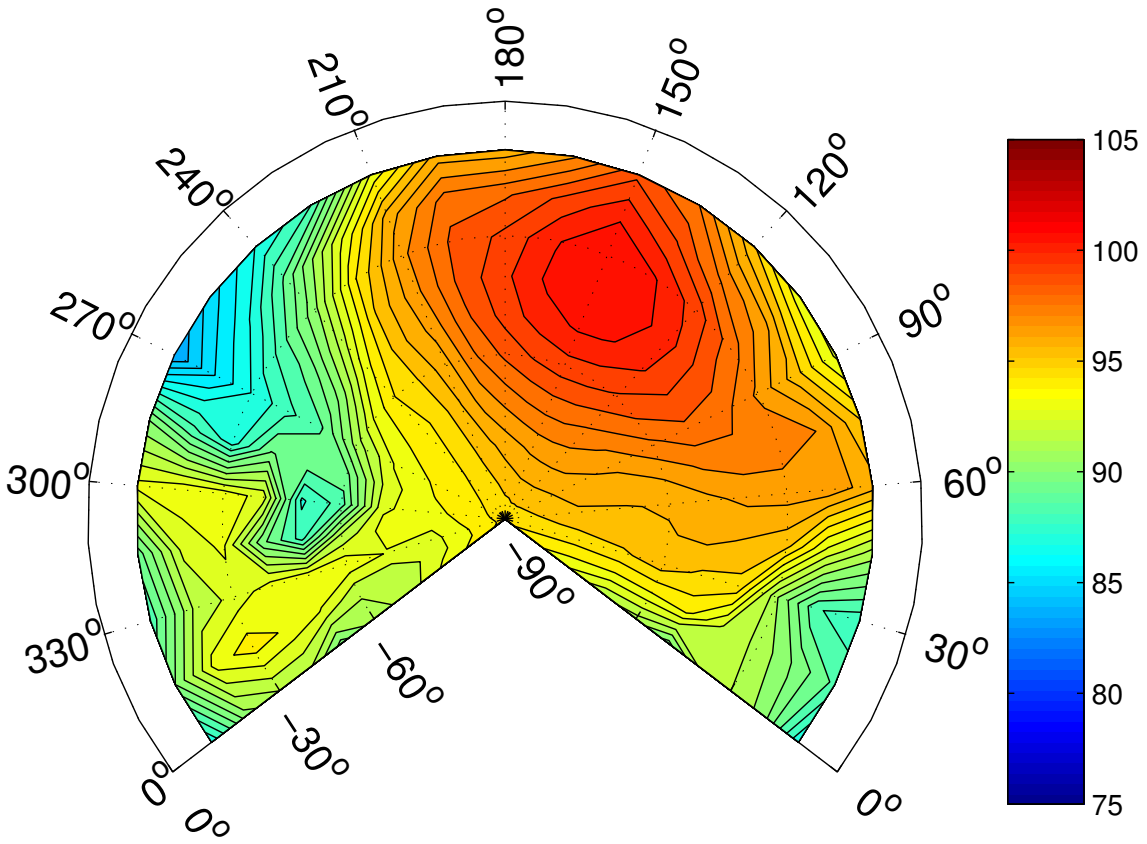

Figure 5.21: Simulated BVISPL noise level contours for -6° flight path angle condition.

(p^2_{RMS}) over the surface of the hemisphere based on the change in flight path angle (e.g. RNM[11]) results in the hemisphere shown in Figure 5.25. It is readily apparent that the estimated directivity and levels produced by this "data-driven" interpolation approach have little relation to the BVISPL contours measured for this condition, as shown in Figure 5.20. The BVI hotspot is directed farther towards the retreating side, and the maximum BVISPL on the hemisphere is 4 dB lower than measured. Without a physics-based model of BVI, the simple interpolation approach is unable to predict the occurrence of BVI noise along directivity angles where it did not occur

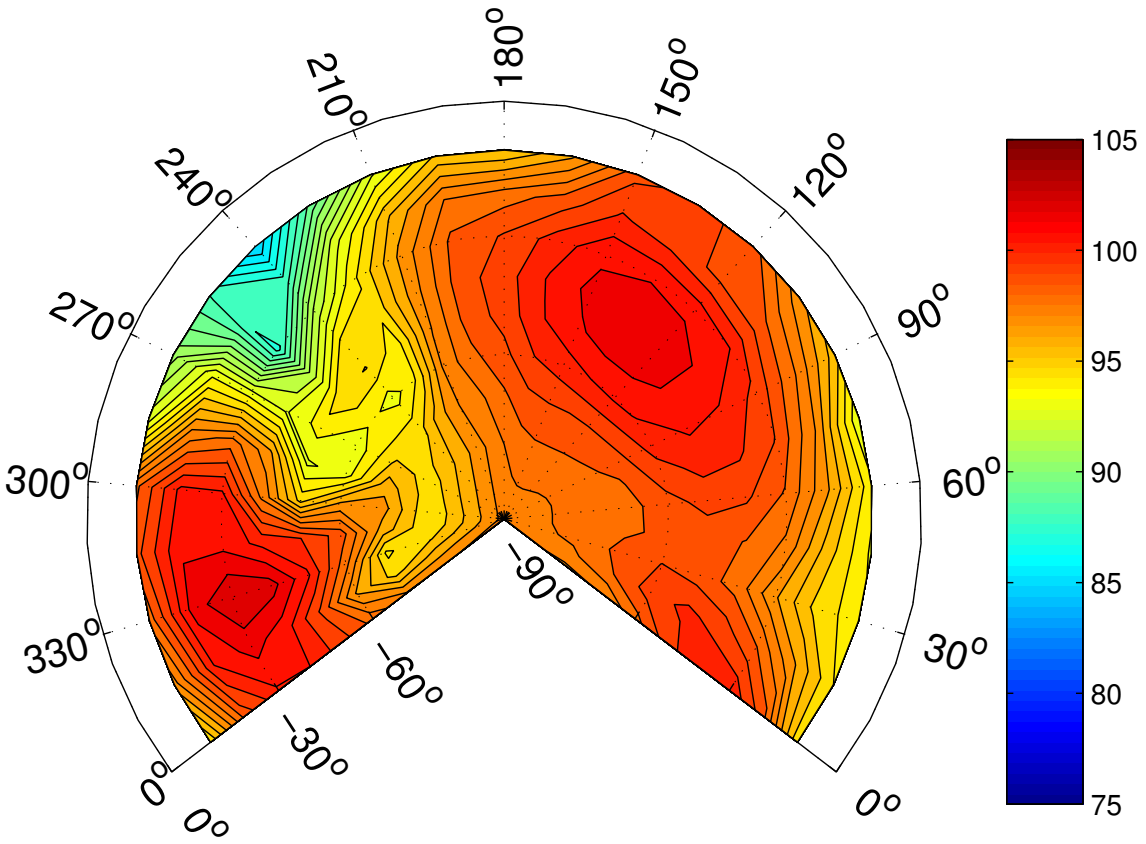

Figure 5.22: Simulated BVISPL noise level contours for -7.5° flight path angle condition.

in the measured data.

Figure 5.26 shows the estimated BVISPL hemisphere for the same condition using an interpolation of the modeling parameters input to the assumed analytical model. By using a physics-based model, directivity patterns of BVI noise can be estimated which are distinct from those observed in the measured data. The noise levels and directivity agree much more closely with the measured data. BVISPL in the BVI "hotspots" are about 1 dB lower than those measured. The analytical model also produces a more distinct directivity pattern than the hemisphere produced

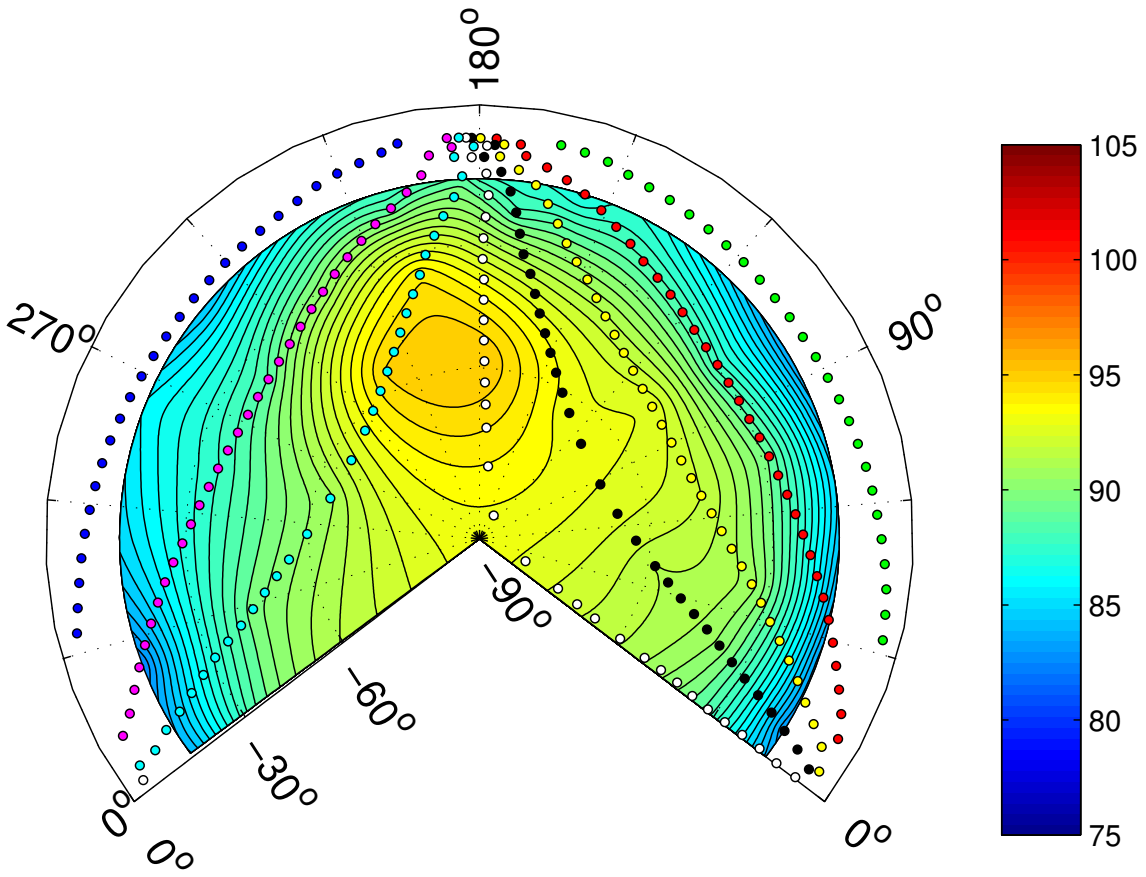

Figure 5.23: Main rotor averaged BVISPL noise level contours for -3° flight path angle condition.

directly from measurements, since the data do not need to be interpolated from sparse data across the surface of the hemisphere. The parameter identification scheme more accurately predicts noise levels and trends than simple data-driven interpolation, even for large changes in the governing parameters, where the conventional interpolation approach fails.

Likewise, the phenomenological modeling approach introduced in this dissertation can be utilized to provide more accurate extrapolation of measured data to other flight conditions than those measured. Figure 5.27 shows the results of using

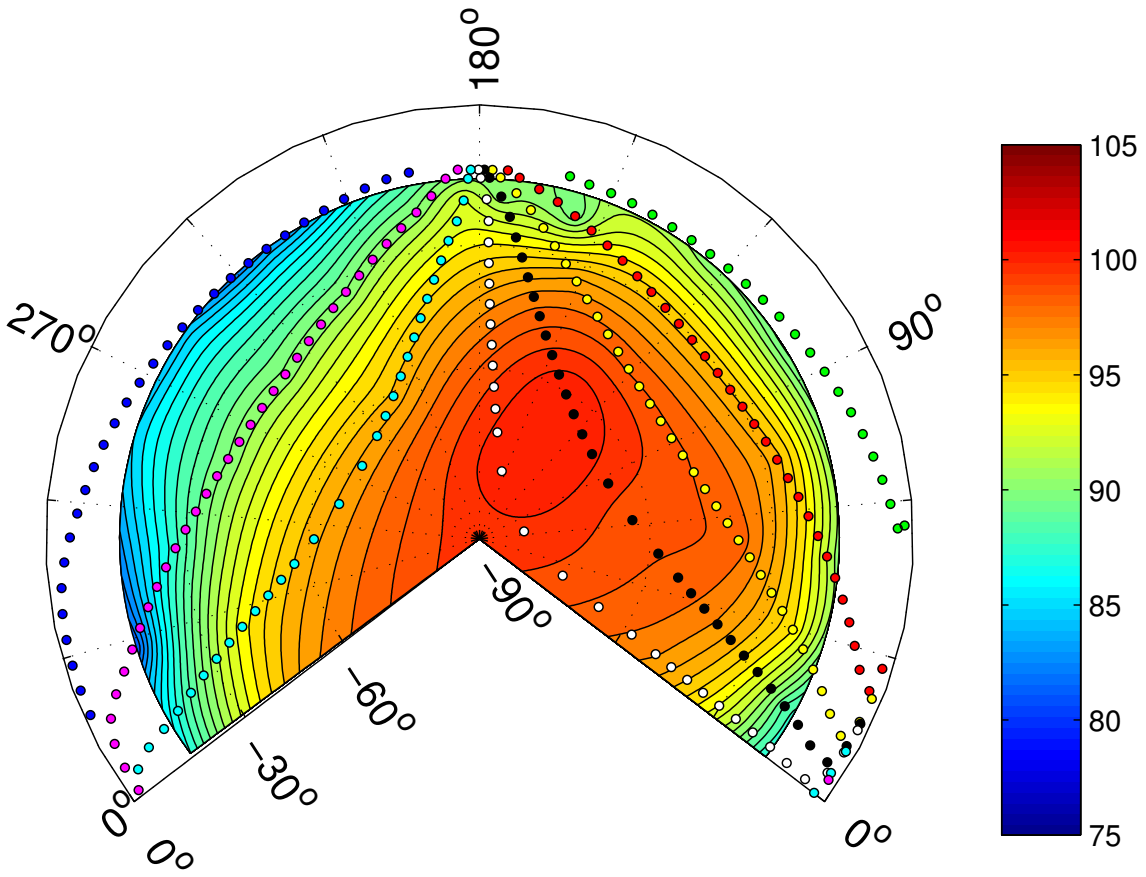

Figure 5.24: Main rotor averaged BVISPL noise level contours for -9° flight path angle condition.

the conventional "data-driven" approach to extrapolate the BVISPL contours for the -6° (Figure 5.19) and -9° (Figure 5.24) flight path angle measured and main rotor averaged acoustic hemispheres to the -3° (Figure 5.23) flight path angle flight condition. Once again, because the conventional approach lacks any information about the physical noise generation process, it is unable to accurately represent the radiated noise for conditions significantly different from the measured data—the magnitude of the estimated BVI noise is much higher than seen in the measured data, and the directivity much too far towards the advancing side.

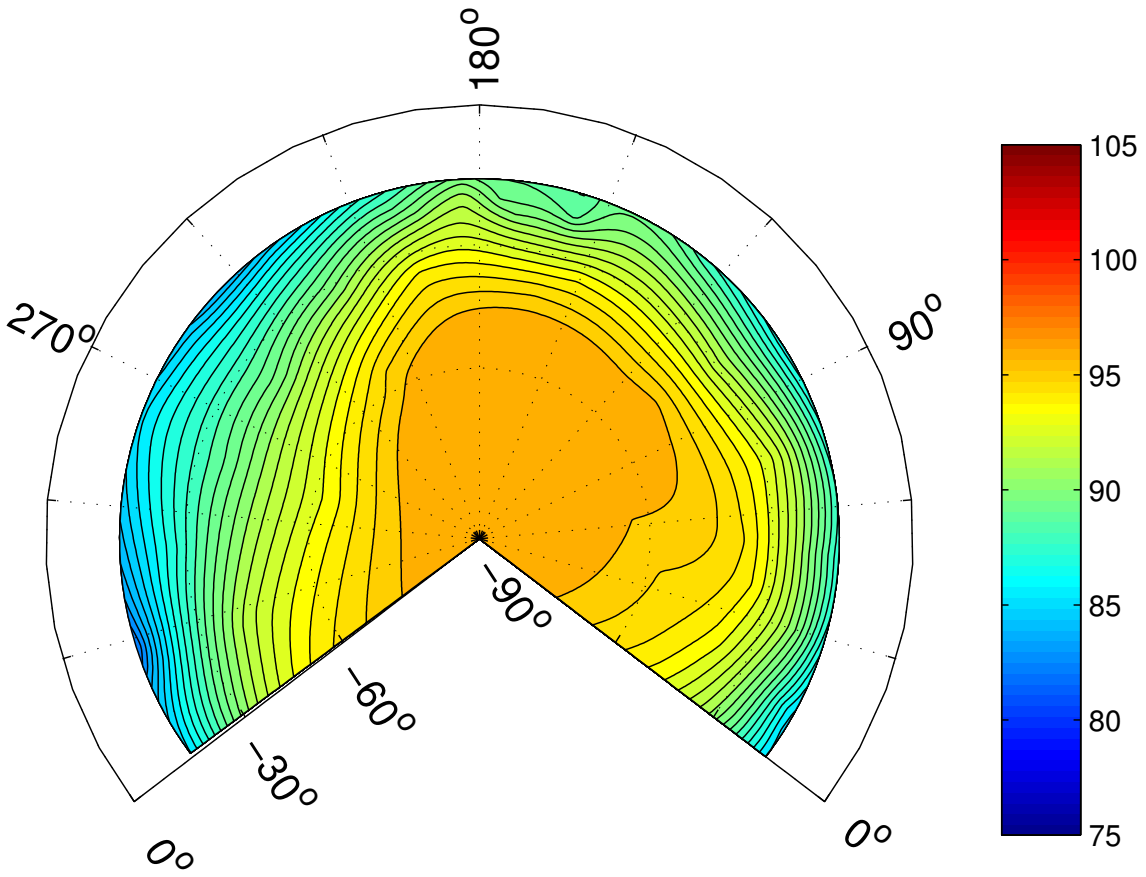

Figure 5.25: Conventional interpolation of BVISPL noise level contours for -7.5° flight path angle condition.

Figure 5.28, on the other hand, shows the results of interpolating the dependent modeling parameters and using the analytical noise model to estimate BVI noise levels at this condition. This estimate compares well with the directivity and magnitude of noise shown in Figure 5.23, predicting a single BVI "hotspot" in approximately the same direction as the measured and averaged data, with a peak level differing by about 1 dB BVISPL. In contrast to the conventional approach, the methodology introduced in this dissertation is able of producing a reasonable estimate of the noise levels at this condition by extrapolating from data collected at the -6° and -9° flight

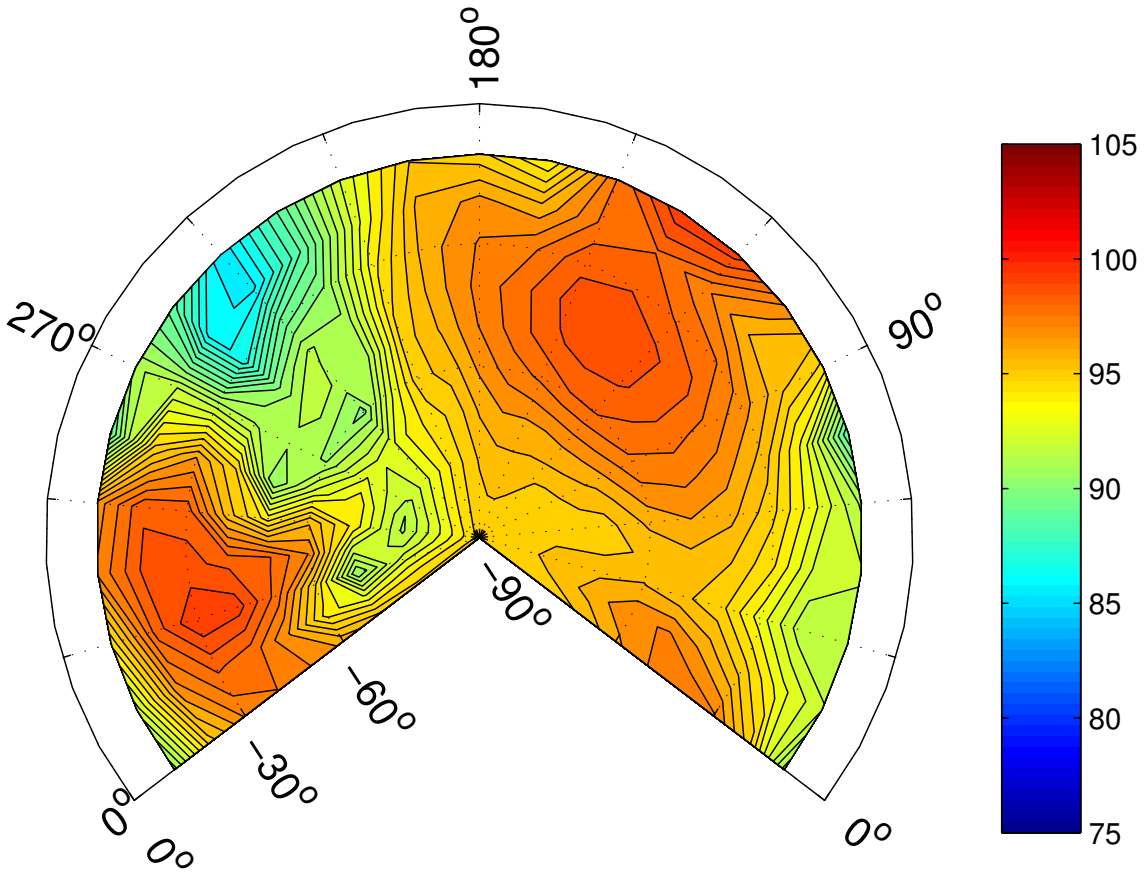

Figure 5.26: Estimated BVISPL noise level contours for -7.5° flight path angle condition.

path angle conditions.

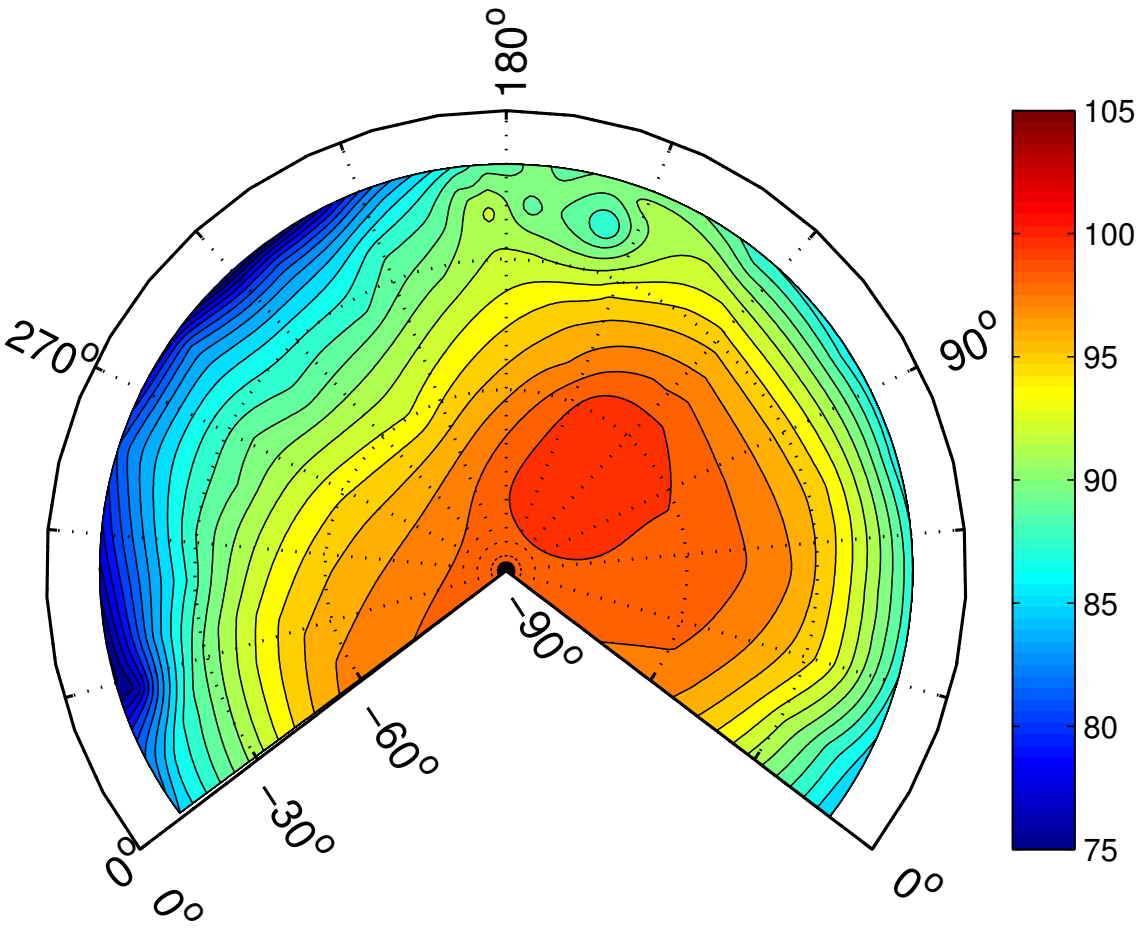

Figure 5.27: Conventional extrapolation of BVISPL noise level contours for -3° flight path angle condition.

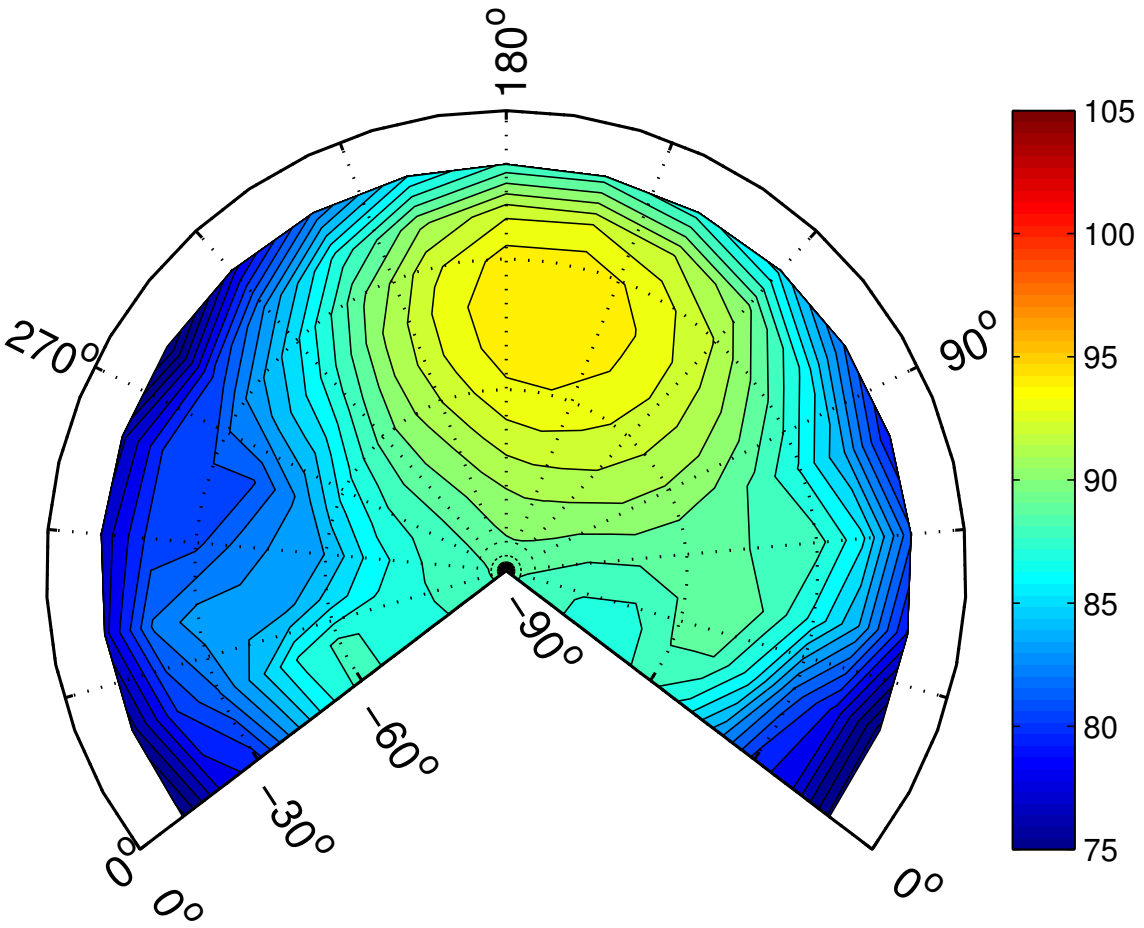

Figure 5.28: Estimated BVISPL noise level contours for -3° flight path angle condition.

5.3 Combined Wind Tunnel and Flight Test Model

The ideal set of data for the modeling approach introduced in this dissertation would consist of high quality acoustic measurements covering a wide range of operating conditions—as defined by the non-dimensional governing parameters—for the specific full-scale rotor configuration of the modeled rotorcraft. Flight test measurements of helicopter noise characterize specific rotor configurations but for practical reasons cannot be made across the entire range of ambient and flight conditions for which the helicopter may be expected to operate. Wind tunnel tests allow for carefully controlled variation of the rotor operating condition and a high measurement quality, but it is impractical to conduct full-scale wind tunnel tests for each specific rotor configuration used on production helicopters. A general-purpose rotor noise model should make use of both types of test data: wind tunnel data to capture the general parametric trends of the noise model over a wide range of operating conditions, and flight test data in order to tune the model to a similar, but specific and full-scale, rotor configuration.

5.3.1 Combined Modeling Approach

A model of the OLS wind tunnel rotor was constructed in terms of the four non-dimensional governing parameters (μ,M_H,λ,C_T) using a Bayesian regularized 20-neuron Artificial Neural Network (ANN) with two hidden layers to build a relation between the known governing parameters and identified dependent modeling parameters, as described in Section 3.3.3. The dependent modeling parameters of

the OLS rotor ANN model were then compared against the dependent modeling parameters identified for the Bell 206B3 main rotor for same non-dimensional operating conditions—the values of dependent parameters controlling the rotor wake are shown for the Bell 206B3 main rotor in Table 5.5 and for the OLS ANN derived model under the same conditions in Table 5.6. In general, there were no significant differences between the two sets of modeling parameters, with two exceptions. The initial vortex core size modeling parameter, geometrically scaled by rotor radius, $\bar{r}_0$, was significantly larger for the OLS rotor model than for the 206B3 model; it should be expected that the relative vortex core size on the OLS rotor would be larger than for the 206B3 because the difference in scale between the two rotors corresponds to a difference in Reynolds number, resulting in a difference in the non-dimensional vortex core size. However, the relative core size is an order of magnitude larger on the OLS ANN model than on the Bell 206B3 model. This difference in vortex core size is significantly larger than what would initially be expected. Figure 5.29 shows the variation of BVI noise at an observer ahead of the rotor as a function of vortex core size—from this plot it is clear that the sensitivity of BVI to vortex core size is much higher for values near those of the OLS ANN derived, but as the vortex core size decreases it's effect on BVI noise diminishes. This is because the vortex core size only has a significant effect on the BVI process when the vortex core radius is of similar or greater size than the miss-distance between the blade and tip vortex. (This is evident from Figure 2.16 of the tangential velocity induced by a viscous vortex.) Once the relevance of the vortex core parameter to BVI noise levels diminishes, the parameter identification technique of Chapter 3 tends to select a much smaller value.

The other dependent parameters do not exhibit this insensitivity over the range of allowable dependent parameter values.

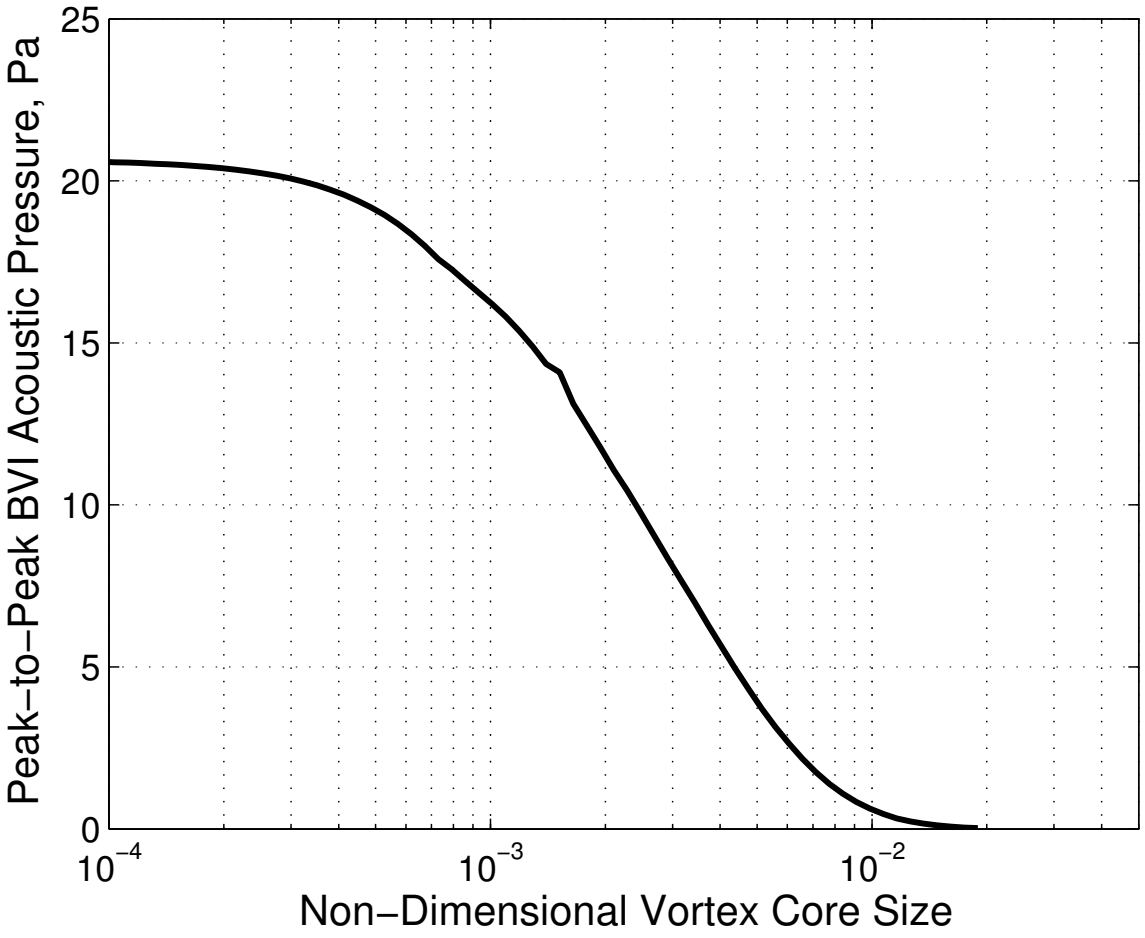

Figure 5.29: Variation of peak-to-peak BVI acoustic pressure with respect to the non-dimensional vortex core radius.

The second difference is a somewhat higher rate of wake contraction, modeled by D, for the OLS rotor model. This is a physically realistic change, as the wake is known to contract more quickly due to viscous effects for smaller scale rotors.[39] Figure 5.30 shows an estimate of the Bell 206B3 BVISPL hemisphere noise contours using a geometrically-scaled OLS ANN model for the -7.5° flight path angle case

which was previously estimated by different methods in Figures 5.20, 5.22, 5.25, and 5.26. While the directivity pattern is similar to the model built from Bell 206B3 flight test data, as shown in Figure 5.22, the magnitude of BVISPL is under predicted because of the relatively large vortex core size estimated from the OLS data. However, by adjusting the vortex core size and wake contraction parameter values in the OLS rotor ANN model to match those identified for the full-scale 206B3, a suitable full-scale model can be produced which more closely matches the measured full-scale data. The wake contraction term is adjusted by a bias factor, the best least-squares fit determined to be 0.82. As for the vortex core size, a linear least-squares fit would suggest all value be adjusted by dividing all values by a common factor of 31; although, this is an unrealistically small vortex core size. Instead, a more realistic factor of 5 was chosen. The output of this combined wind tunnel and flight test derived model is shown in Figure 5.31. The combined model compares will with the flight test derived model, as shown in Figure 5.22, in terms of both levels and directivity. The result is now a model of the full-scale helicopter which is applicable over a wide range of operating conditions, as defined by the four non-dimensional governing parameters.

γ	-3°	-6°	-7.5°	-9°
A	0.873	0.860	0.835	0.811
B	-1.153	-1.237	-1.255	-1.128
C	1.012	1.021	1.009	1.017
D	0.748	0.715	0.728	0.679
r_r	0.986	0.967	0.942	0.957
$\bar{r}_0$	2.64×10^{-4}	1.98×10^{-4}	1.32×10^{-4}	1.30×10^{-4}
C_v	8.38×10^{-5}	6.98×10^{-5}	6.34×10^{-5}	7.11×10^{-5}
γ_0	1.001	1.018	1.003	1.019
γ_C	-0.050	-0.018	-0.006	-0.031
γ_S	0.519	0.408	0.001	0.000

Table 5.5: Dependent Parameter Values for the Bell 206B3 model.

γ	-3°	-6°	-7.5°	-9°
A	0.847	0.842	0.838	0.835
B	-1.213	-1.244	-1.250	-1.255
C	1.020	1.010	1.000	1.009
D	0.849	0.835	0.838	0.728
r_r	0.971	0.956	0.947	0.942
$\bar{r}_0$	8.00×10^{-3}	6.63×10^{-3}	5.50×10^{-3}	4.59×10^{-3}
C_v	6.34×10^{-5}	6.13×10^{-5}	6.30×10^{-5}	6.34×10^{-5}
γ_0	1.020	1.004	1.003	1.003
γ_C	-0.030	-0.011	-0.005	-0.006
γ_S	0.522	0.341	0.016	0.001

Table 5.6: Dependent Parameter Values for the OLS ANN model.

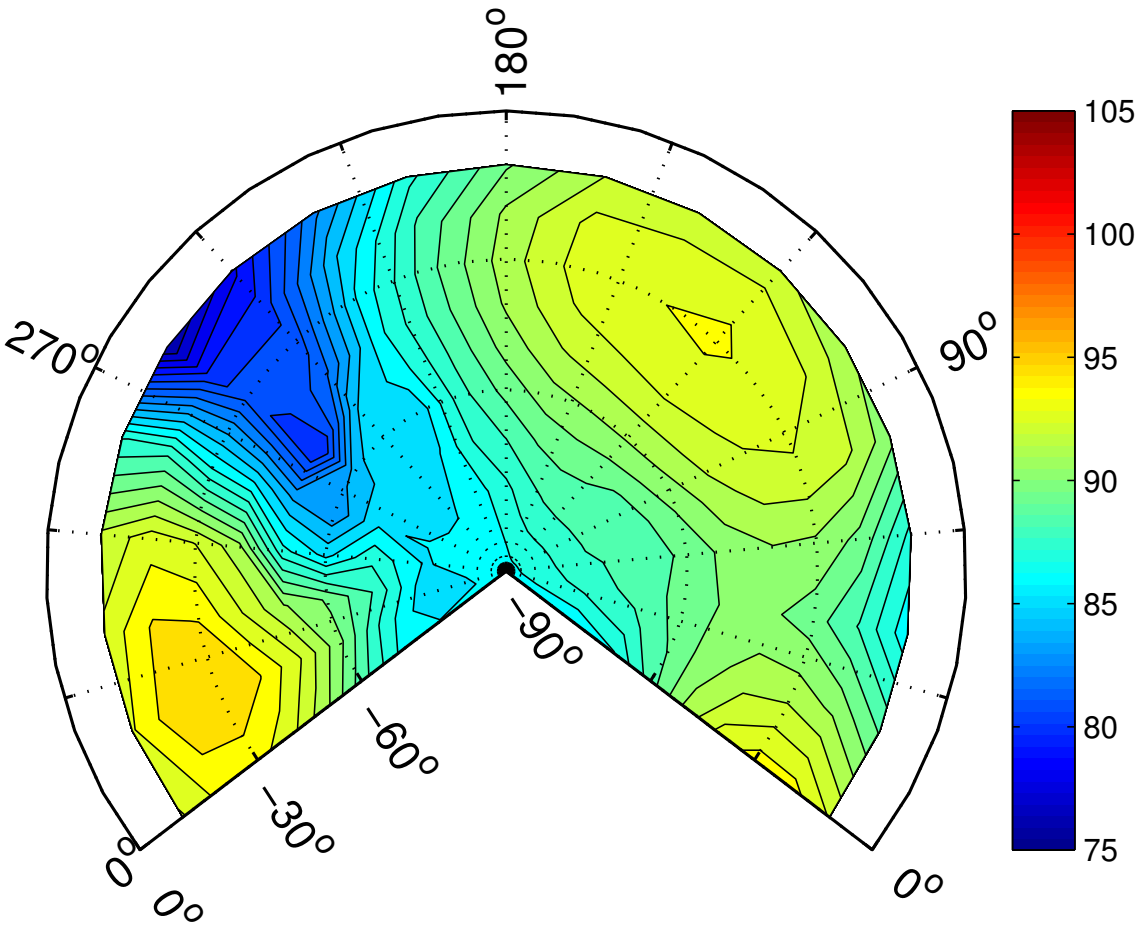

Figure 5.30: Geometrically-scaled OLS model BVISPL hemisphere estimate for Bell 206B3 -7.5° flight path angle condition, as in Figure 5.22.

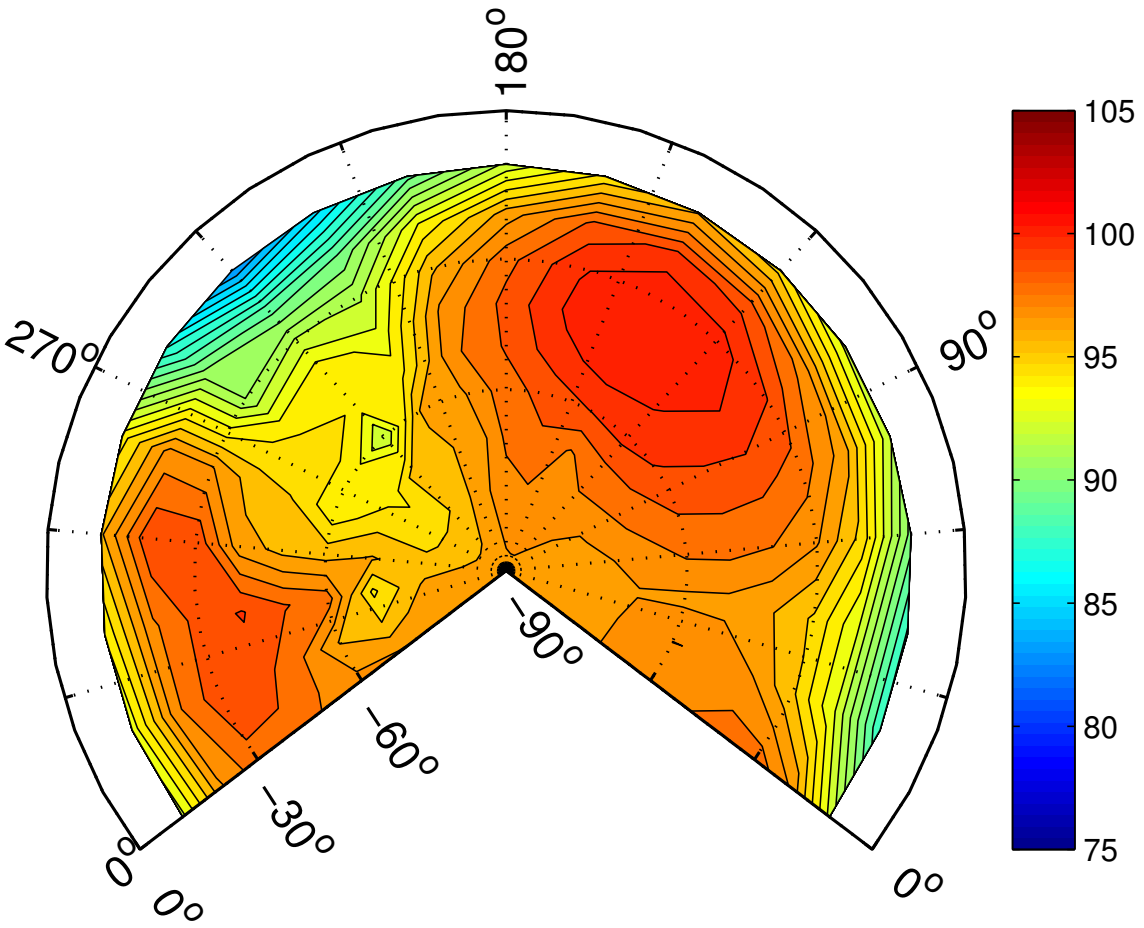

Figure 5.31: Combined Bell 206 – OLS model BVISPL hemisphere estimate for Bell 206B3 -7.5° flight path angle condition, as in Figure 5.22.

5.3.2 Modeling the Effects of Ambient Conditions

Existing empirical helicopter noise models—currently used in mission planning tools—are couched in a limited set of dimensional performance parameters, commonly airspeed and flight path angle. These models do not take into account the effect that changes in ambient conditions have on the physical process of noise generation. In this dissertation, phenomenological models are built in term of non-dimensional governing parameters. Non-dimensionalization of noise models allows them to be generalized to different operating conditions.

Figure 5.32 illustrates how these non-dimensional parameters can vary with ambient conditions for a flight condition defined by a constant set of dimensional indicated parameters—in this example a Bell 206B3 operating at a -7.5° flight path angle and 60 kts indicated airspeed at a variety of altitudes with ambient temperature and density varying as specified by the International Standard Atmosphere (ISA) model.[68] Each of the four non-dimensional governing parameters influences the noise generation process in a different way. The effect of the individual parameter variations due to changes in altitude is investigated in detail in Appendix B.

These variations in the non-dimensional governing parameter values can result in a significant change in the rotor acoustic state with variation in altitude. This effect is not accounted for in any of the empirical rotor noise modeling methods currently in use, all of which are developed on the basis of dimensional performance parameters. The effect of a change in ambient conditions can not be easily predicted using simple empirical corrections, since the effects of changes in the non-dimensional

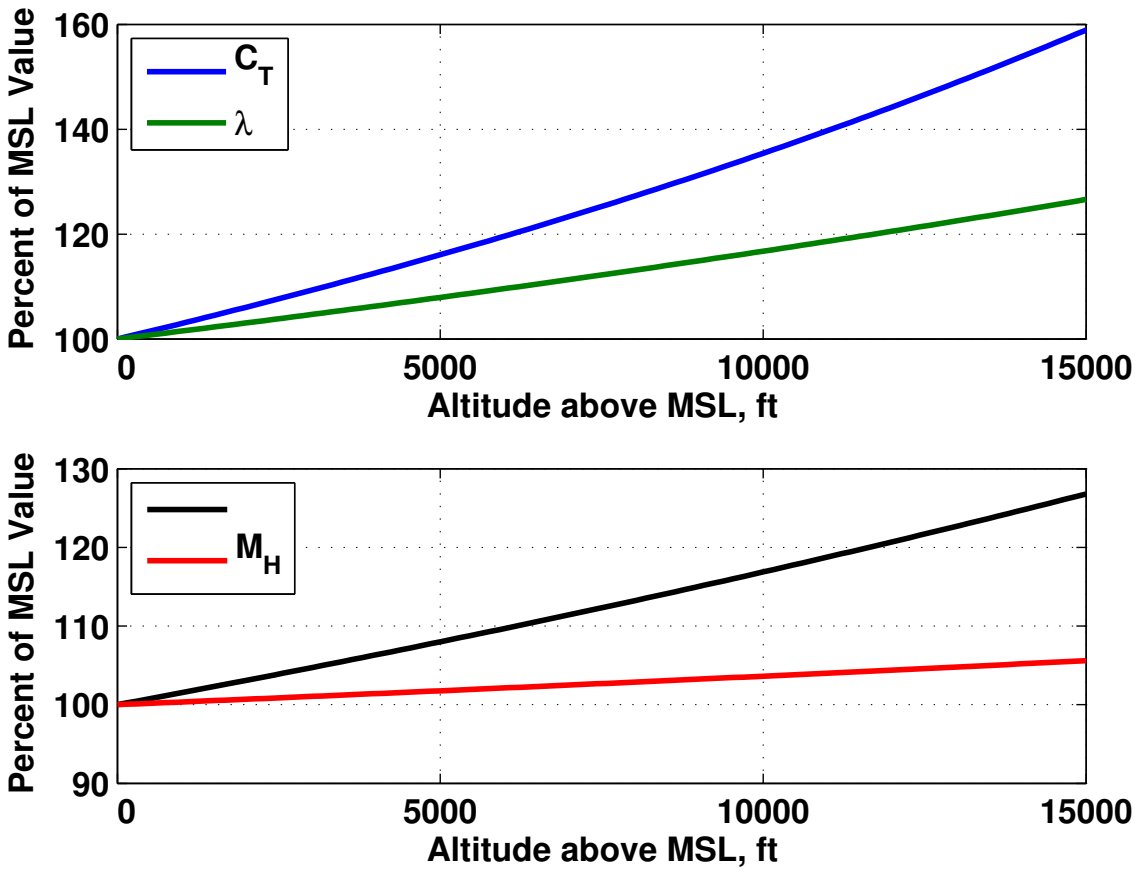

Figure 5.32: An example of the variation in non-dimensional governing parameters with altitude.

governing parameters due to ambient conditions can be complementary or conflicting and depend on the specific flight condition of the measured data, as demonstrated in Appendix B. For this particular case, the BVISPL noise level contours incorporating the changes in all non-dimensional parameter variations with altitude are plotted in Figures 5.33 and 5.34 for the 7500 ft and 15000 ft ISA cases, respectively. As altitude increases, BVI noise levels are shown to increase. Moreover, the directivity of the radiated noise is shown to shift dramatically, in the case from the retreating side towards the advancing side of the rotor.

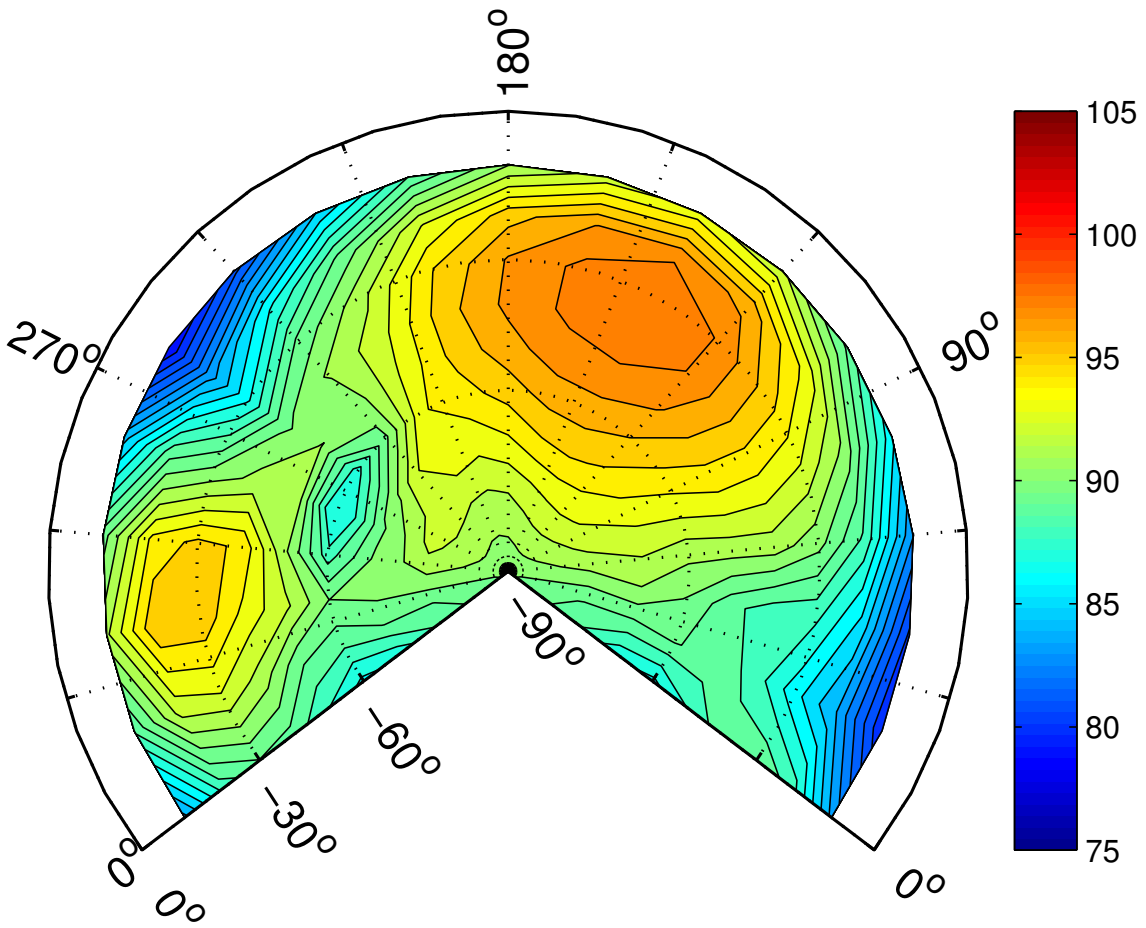

Figure 5.33: Combined Bell 206 – OLS model BVISPL hemisphere estimate for Bell 206B3 -7.5° flight path angle condition at 7500 ft ISA altitude.

In addition to plots of the directivity and magnitude of BVI noise, the change in the noise generation process with changes in the ambient conditions can be seen by examining the acoustic pressure time-histories at several observers for the ambient conditions associated with the sea level, 7500 ft and 15000 ft altitudes. The three selected observer locations are superimposed on the sea level BVISPL hemisphere plot (shown previously in Figure 5.31) in Figure 5.35. Figures 5.36, 5.37 and 5.38 show these pressure time-histories for the observers ahead of, toward the advancing side

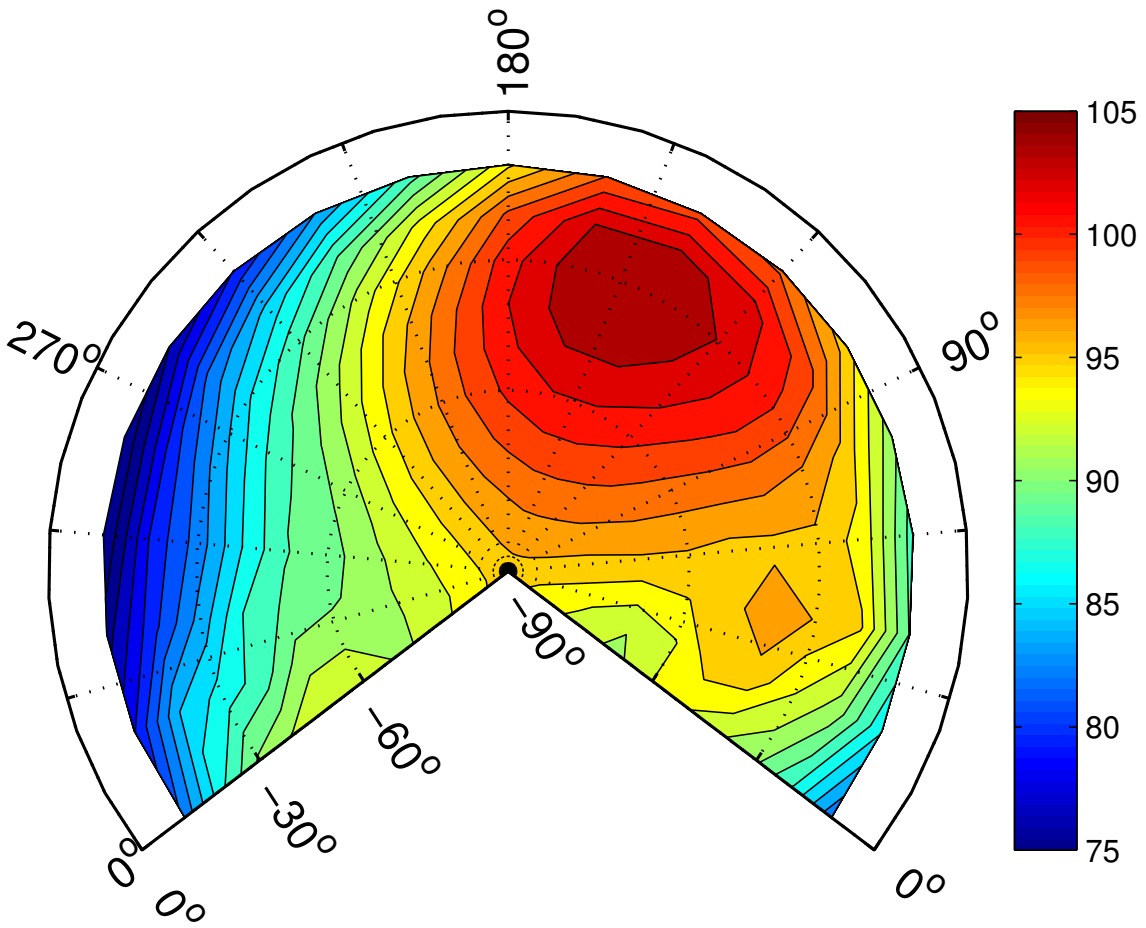

Figure 5.34: Combined Bell 206 – OLS model BVISPL hemisphere estimate for Bell 206B3 -7.5° flight path angle condition at 15000 ft ISA altitude.

of, and toward the retreating side of the rotor, respectively. For all three observers, significant changes in the pressure time-history signal are observed. The phasing of the BVI change with altitude in addition to the relative magnitude of the individual BVI pulses. For instance, Figure 5.36 shows two distinct BVI pulses at sea level, but as altitude increases the magnitude of the first BVI pulse decreases while the magnitude of the second BVI pulse increases. A similar trend is seen in Figure 5.37 for the advancing side observer. For the retreating side observer, a retreating side (i.e.

negative) BVI pulse is seen at sea level, but weakens rapidly with altitude—at 15000 ft, a small advancing side BVI pulse can be seen by this observer. This changes in acoustic pressure time-history with altitude may affect the subjective "character" of the BVI noise in ways not captured by the BVISPL metric.

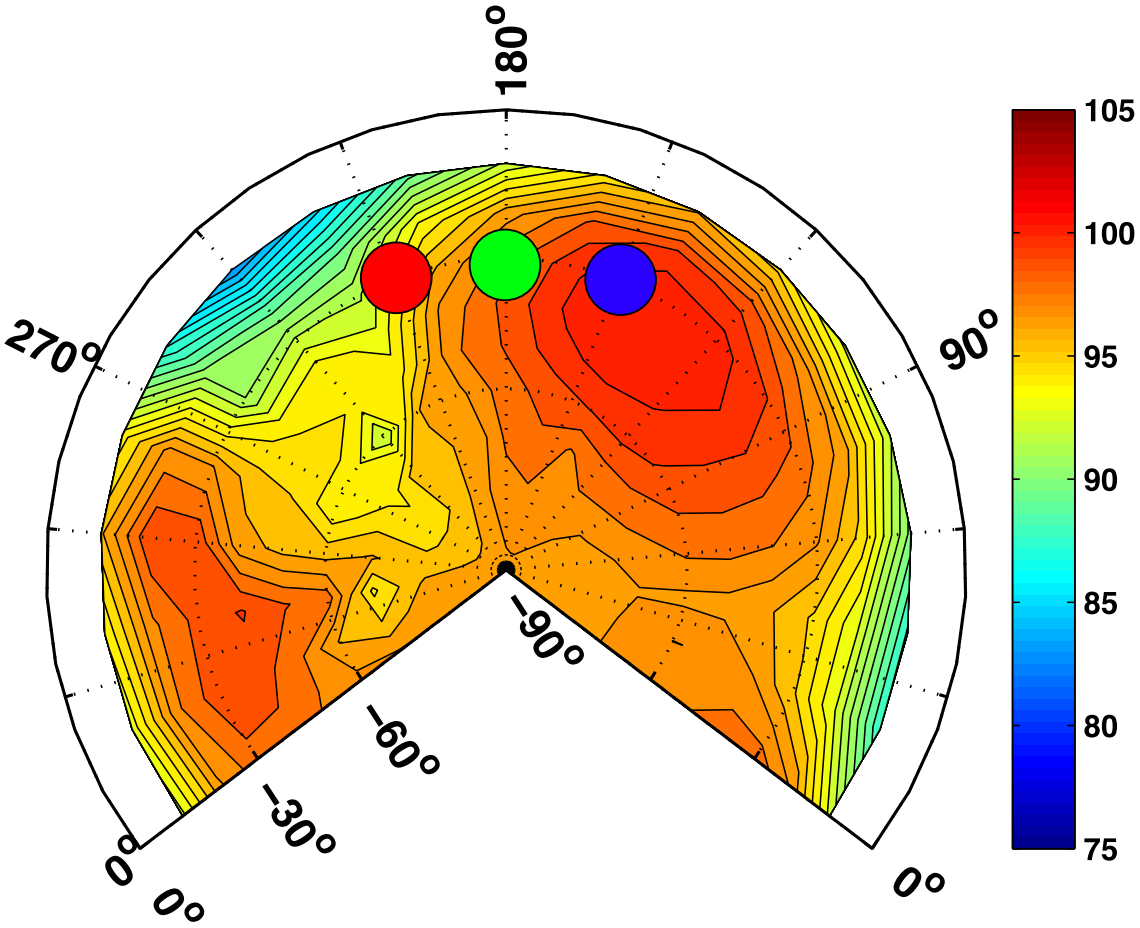

Figure 5.35: Directions of observers ahead of (green), toward the advancing side of (blue), and toward the retreating side of the rotor, superimposed on the sea level hemisphere previously shown in Figure 5.31.

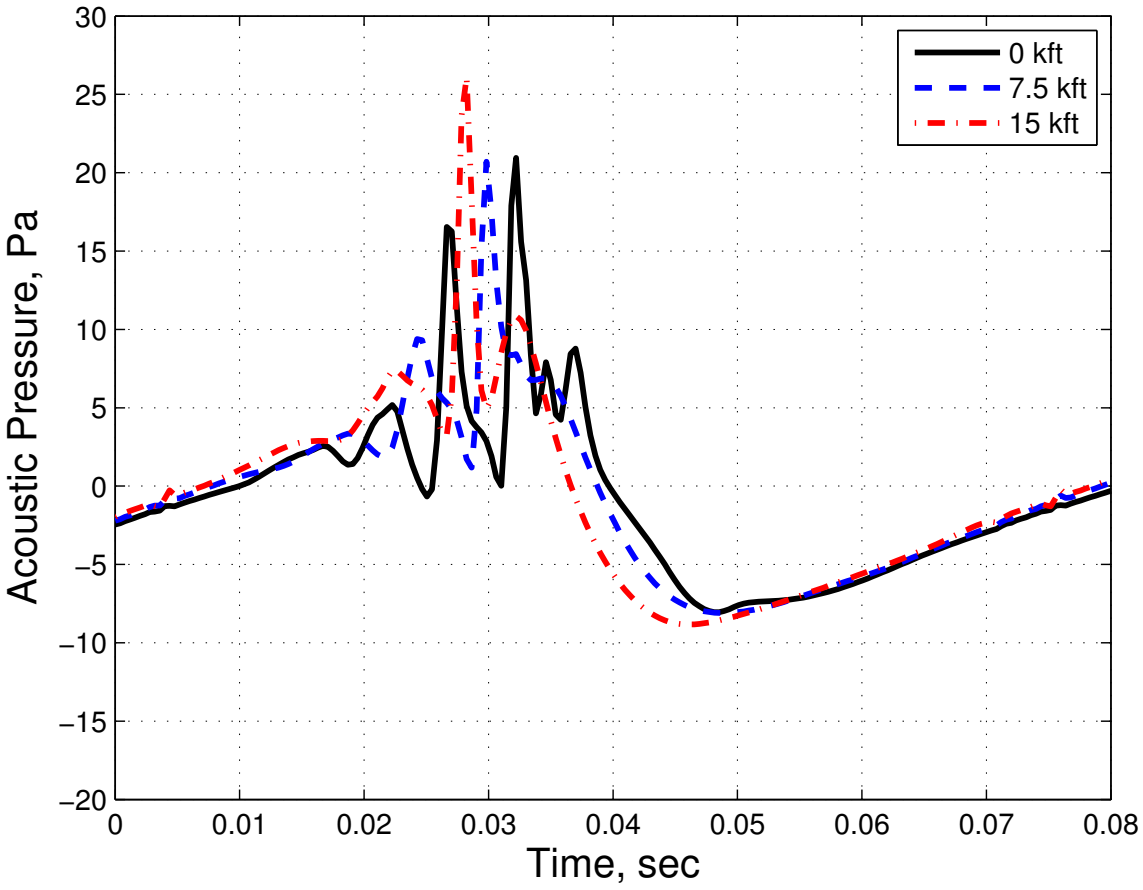

Figure 5.36: Variation with altitude of the acoustic pressure time-history signals of one blade passage for an observer directly ahead of and 30° below the rotor.

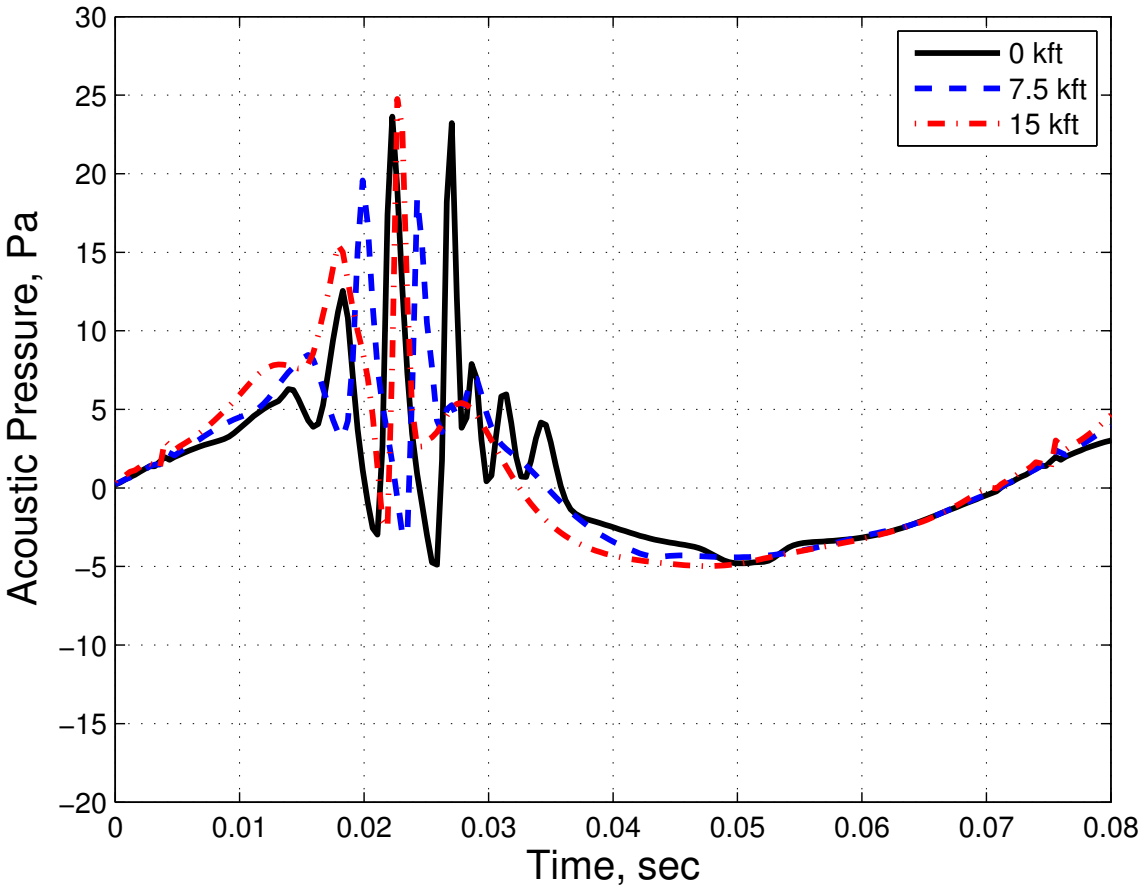

Figure 5.37: Variation with altitude of the acoustic pressure time-history signals of one blade passage for an observer 30° towards the advancing side of and 30° below the rotor.

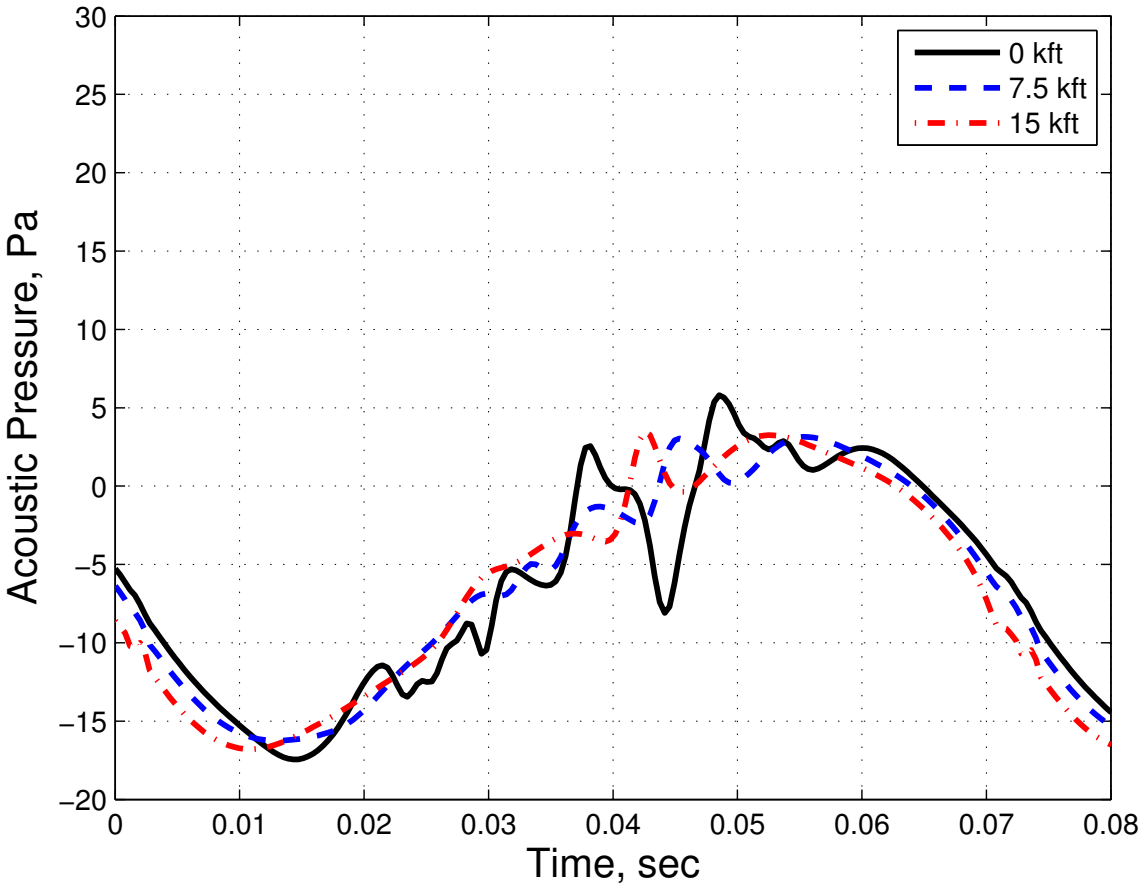

Figure 5.38: Variation with altitude of the acoustic pressure time-history signals of one blade passage for an observer 30° towards the retreating side of and 30° below the rotor.

The non-dimensional phenomenological models built using the methodology introduced in this dissertation offer a new way of estimating the changes in noise due to changes in the ambient condition. This is increasingly important as mission planning tools are being employed to estimate noise in environments considerably different from those where noise measurements are typically made. For example, while a military helicopter may be characterized at sea level conditions the noise models are likely to be used in hot and high conditions. Likewise, civilian helicopters regularly operate in all sorts of environmental extremes—for example, in the Grand Canyon national park alone, terrain elevations range from 2500 ft to 8000 ft above sea level, with temperatures ranging between 0°F and 100°F.[69] Helicopter sightseeing operations are severely constrained by noise limits within national parks; the current practice of neglecting atmospheric effects on the helicopter noise sources is likely to have led to significantly erroneous estimates of the type and number of helicopter operations allowed for compliance with existing regulations.[70]

Chapter 6

Conclusions

This dissertation introduces a new non-dimensional and phenomenological methodology for developing analytical rotorcraft noise source models using measured acoustic data. In contrast, existing empirical noise source models are developed in terms of dimensional flight performance parameters, such as airspeed and rate of sink, and do not incorporate physical knowledge of the individual rotor noise generation mechanisms. In this new methodology, noise models are individually constructed for the major helicopter noise sources by applying parameter identification techniques to adapt assumed aeroacoustic models to measured data. The principal advantage of this new methodology is that it greatly enhances the applicability of measured rotorcraft acoustic data. This new methodology is unique in that:

- *Each of the major helicopter noise sources is considered independently*

  Multiple noise sources contribute to the external noise radiation of helicopters, each with its own mechanisms and governing parameters. In this dissertation, the dominant rotor harmonic noise sources (i.e. main rotor and tail rotor harmonic noise) are separated from the measured data so that separate models can be developed for each. In addition, the rotor harmonic noise sources are further separated into lower harmonic loading, thickness, and blade-vortex interaction impulsive mechanisms. Although this dissertation focuses on main

rotor harmonic noise sources, especially BVI, the technique is equally applicable to tail rotor harmonic noise sources.

- *Noise models are developed in terms of non-dimensional governing parameters*

  By developing models in a non-dimensional form, they can be generalized to a wide range of equivalent dimensionally defined operating conditions. This concept greatly extends the applicability of the noise models; for instance, by applying the previously developed Q-SAM principle,[13][19] noise models generated from steady straight-line flight data can be utilized in order to model the noise radiated by gradually accelerating or turning helicopters.

- *Models are built within an assumed analytical framework which incorporates physical knowledge of the noise generation processes*

  Physically-realistic analytical models are tuned to each of the major noise sources using parameter identification techniques. Since physical knowledge is incorporated into the modeling framework, the generated noise models can be more accurately interpolated or extrapolated to predict noise in radiation directions and at operating conditions for which measured data is not available. This phenomenological modeling approach is a significant advancement over the "data-driven" approaches used by existing empirical helicopter source noise modeling methods.

- *Models can be constructed using data from both wind tunnel and flight test measurements, allowing further extrapolation of the flight test data*

  Both wind tunnel and flight test measurements of rotor noise have distinct ad-

vantages and disadvantages. Wind tunnel noise measurements can be conducted over a wide range of operating conditions with a high degree of consistency and repeatability of acoustic measurements, but full-scale measurements of helicopter rotors are very costly for small vehicles and impossible for large ones. Flight test measurements can be conducted for any rotorcraft, but the practical range of operating conditions is limited and the flight and acoustic state of the helicopter much more variable. In this dissertation, a new method of relating flight test data to wind tunnel data is developed, based on the concept of a "virtual inflight observer." This allows the same analytical modeling framework to be utilized for both wind tunnel and flight test da ta. Moreover, this dissertation introduces a method of combining models built from high-quality model-scale wind tunnel measurements with models built from lower-quality full-scale flight test measurements of a helicopter with a similar rotor to produce a single model which is generalizable to a wide range of operating conditions, but still applicable to the full-scale vehicle.

The new methodology developed in this dissertation was applied to measured wind tunnel and flight test data of two-bladed rotors. Using these data, the following capabilities were demonstrated:

- *Accuracy of existing methods retained*

  The models constructed were accurate to within the variability of the measured flight test data used by existing methods. Moreover, due to the assumed analytical structure of the modeling method, the error introduced in noise radiated

in directions underneath the rotor by conventional hemisphere averaging and interpolating schemes is limited. Lastly, by extending the applicability of high quality wind tunnel data to full-scale rotors, the negative effects of the inherent acoustic variability of helicopter flight on the modeling process can be reduced.

- *Noise estimates made in directions not measured*

  Due to the assumed analytical form of the noise source models, noise can be estimated in directions not measured directly during testing, as was demonstrated using a model built from wind tunnel measurements. This capability is especially important when generalizing straight-line flight models to steady turning flight, where the helicopter will be banked, and noise radiated above the rotor during straight-line flight will now be radiated towards the ground. For practical reasons, conventional flight test measurements utilize ground-based microphones, making measurements of noise at or above the plane of the rotor impractical.

- *Noise estimates made at flight conditions not measured*

  The noise models produced using the methodology introduced in this dissertation are more easily interpolated or extrapolated to flight conditions not included in the measured data set. Wind tunnel data was used to show that a limited set of test data can be used to produce noise models applicable across a wide range of flight conditions defined by non-dimensional governing parameter variations. A more limited set of flight test data was then utilized to demonstrate the improved generalizability of the modeling approach introduced

in this dissertation over conventional empirical modeling methods: the model constructed using the methodology developed in this dissertation was able to produce accurate estimates of noise at flight conditions far away from the data used for modeling where the conventional approach produces inaccurate results.

- *Noise estimates made at ambient conditions not measured*

  Existing empirical models neglect the impact of ambient conditions on the noise generation process. Using a model constructed from wind tunnel and flight test data, the effect of changes in ambient conditions on the noise generation process is demonstrated, and found to be significant throughout a practical range of helicopter operating environments. Since existing empirical models lump all rotor noise sources together and are couched in terms of dimensional performance parameters, they are incapable of correcting models for differences between the ambient conditions of the measurement and the operating environment. In contrast, the non-dimensional phenomenological models developed in this dissertation are readily adapted to provide noise estimates for different ambient conditions than those measured.

The new modeling methodology presented in this dissertation represents a significant advancement over the state-of-the-art in empirical rotorcraft noise source modeling. The applicability of measured helicopter noise data is greatly extended to a wide range of operating conditions while maintaining practical data collection requirements. The methodology introduced in this dissertation is applicable to

all types of rotorcraft and can be easily extended with higher fidelity modeling schemes for increased accuracy and generalizability as computational resources permit. With some additional work, described in Chapter 7, these models will be ready for routine use in mission planning tools. In addition, the techniques developed in this dissertation have application to other uses of rotorcraft external noise modeling.

Chapter 7

Future Work

7.1 Remaining work for Mission Planning Tool Development

The modeling methodology developed in this dissertation is suitable for developing helicopter noise source models for mission-planning tools; however, some work remains before a complete modeling tool can be developed which is suitable for routine use. The specific development tasks necessary to accomplish this goal are:

- *The incorporation additional physical knowledge into analytical lower harmonic noise source models*

  In this dissertation, very simple models were developed for the lower harmonic noise sources of the rotor. For thickness noise, the pressure time history was predicted directly from the monopole displacement term in the Ffowcs Williams – Hawkings equation, however it is known that this formulation under-predicts the apparent magnitude of thickness noise seen in measurements, especially at higher tip Mach numbers—this is probably because the monopole thickness noise formulation only includes the contribution of the airfoil surface itself to the displacement of the medium, and neglects off-surface aerodynamic phenomena, such as the airfoil boundary layer and separated flow downstream of the blade section. The thickness noise model used in this dissertation should be expanded to include adjustable physics-based dependent parameters, much like the other

noise sources modeled in this dissertation. For example, one approach might be to allow the mass sinks used to model the fluid displacement caused by the airfoil aft of the point of maximum thickness to be redistributed past the trailing edge to represent separated flow.

Likewise, lower harmonic loads were determined by assuming a simple spanwise triangular distribution of lower harmonic loads, and then using the parameter identification technique to determine the first few harmonics of the variation of this assumed load distribution by rotor azimuth. The advantage of directly specifying the lower harmonic loads in this fashion is that the blade motion (e.g. flapping, feathering) and full rotor trim do not need to be calculated in order to determine the blade loads necessary to reproduce the measured lower harmonic loading noise. However, because this approach does not incorporate much physical modeling of the lower harmonic airloads, the resulting lower harmonic loading noise models are not as amenable to accurate generalization to other operating conditions as the BVI noise model. A more powerful extension of the model could be developed which predicts lower harmonic airloads using the induced velocities determined from the wake model, incorporates a simple articulated rigid blade motion model, and determines the control input necessary to trim the rotor for each flight condition. This process would increase the computational costs of model evaluation, but this may be partially offset during the parameter identification process by a reduction in the number of dependent parameters needed to define the rotor state. Additional

refinements to the models might be made to account for the effects of active rotor control (e.g. higher harmonic twist/pitch control, trailing edge flaps, split flaps) on lower harmonic noise. These extensions would be particularly useful for designing helicopter operations to avoid detection, which is generally set by the lower frequency components of rotor harmonic noise.

- *The development of a systematic approach for addressing the secondary non-rotor harmonic noise sources*

  The approach introduced in this dissertation is valid for the dominant rotor harmonic noise sources, both main and tail rotor, but neglects other rotorcraft noise sources which can contribute to the overall external noise radiation under some flight conditions or rotor configurations. The rotor harmonic noise separation technique developed in Section 4.3 allow the non-rotor-harmonic noise sources to be isolated. The contributions of these noise sources could be stored directly as an acoustic hemisphere, as in existing empirical methods, but the correct set of non-dimensional governing parameters for these noise sources should be identified to ensure that the measured noise is correctly generalized. Alternatively, a frequency-domain parameter identification approach might be developed for rotor broadband noise sources and engine noise predicted for a given operating condition from existing empirical models.[71] In either case, further development is required. In addition, main rotor – tail rotor interactions may result in significant external noise radiation for some rotor configurations and flight conditions; while this noise source is not harmonic with either the

main rotor or tail rotor, it is deterministic and might be modeled in a similar way as main rotor BVI noise. However, a method of isolating the contribution of main rotor – tail rotor interactions to the non-rotor-harmonic noise signal must be developed.

- *Validation of modeling method for multi-bladed rotor systems*

  The measured data used in this dissertation are for two-bladed rotor systems. In concept, the analytical models developed in this dissertation are applicable to multi-bladed rotor systems. The non-dimensionalization arguments and the analytical acoustic model are well established for rotors with any number of blades. However, the addition of rotor blades leads to a more complicated wake structure which may not be adequately captured by the assumed Beddoes-derived wake model. The methodology of this dissertation should be validated against multi-bladed rotor data, and the assumed wake model refined, if necessary, for accurate BVI noise modeling.

- *Validation of extrapolation of full-scale helicopter noise models to other ambient conditions than those measured*

  This dissertation shows the potential of using non-dimensional phenomenological noise models to estimate the changes in noise levels due to changes in ambient conditions. These results must be validated against measured flight test data for a helicopter operated in different ambient conditions. No suitable data set exists at this time, so a new flight test program must be developed and executed to this end.

- *Validation of the extrapolation of full-scale helicopter noise models to other flight conditions, such as steady turns*

  Existing modeling methods are valid only for steady straight-line flight conditions. The new physics-based and non-dimensional modeling method developed in this dissertation is immediately applicable to slowly maneuvering flight conditions and provides a framework for future extensions to the modeling of noise during transient maneuvers. The Quasi-Static Acoustic Mapping (Q-SAM) method,[13] described in Section 2.2.2.2, uses momentum theory arguments to make an acoustic equivalence between moderate accelerations or decelerations and flight path angle. The Q-SAM method was later extended by the author to steady-turning flight conditions,[24] allowing acoustic equivalences to be made for slowly maneuvering conditions terms of bank angle, acceleration, and flight path angle. However, under these conditions, the thrust of helicopter rotor can no longer be assumed to always equal the weight of the vehicle, and measuring the noise radiated by helicopters under these conditions is difficult. In addition, the Q-SAM method makes equivalencies based on the factors that control main rotor harmonic noise only—under some flight conditions the tail rotor governing parameters may vary independently of those for the tail rotor (e.g. tail rotor thrust and inflow may change during a turn). For these flight conditions where there are also significant levels of tail rotor noise, this main rotor based "equivalence" may lead to erroneous results. While the effect of acceleration on BVI noise has been well established, only preliminary testing of noise levels in steady turning flight has been conducted.[72] The extrapolation

of noise models to steady turning flight conditions must be more fully validated.

- *Adapt modeling method to address non-steady flight conditions, including transient maneuvers*

  For quickly maneuvering flight conditions, the quasi-static assumption of Q-SAM may no longer hold, and additional parameters, such as non-dimensional roll and pitch rates, should also be considered in any model. However, the method developed in this dissertation may provide a framework from which to develop models suitable to more rapidly maneuvering flight conditions. The physics-based quasi-static models built using this method may be useful in defining initial conditions for an aeroacoustic model with a time-varying wake suitable for estimating the effects of transient maneuvers. Further refinement could be achieved by applying parameter identification techniques to a limited set of data for transient flight conditions.

7.2 Other Uses

In addition to developing noise models for mission-planning purposes, the methodology developed in this dissertation could be adapted to other useful purposes.

7.2.1 Generalization of Theoretical Noise Models

In addition to accepting inputs from wind tunnel and flight test data, the modeling methodology developed in this dissertation could be utilized to construct lower-fidelity analytical models from the output of higher-fidelity theoretical models

of helicopter external noise radiation, for example combined computational fluid dynamics – computational structural dynamics models.[73][74] The development of accurate state-of-the-art theoretical models of helicopter noise for any given rotor configuration and operating condition is time consuming, but such theoretical models offer the only means of predicting the acoustic characteristics of new rotorcraft before they are constructed. Developing theoretical noise models across a wide range of operating conditions for a new rotor configuration is impractical; however, the modeling methods developed in this dissertation could be used to generalize a limited set of theoretical noise models to a much wide range of operating conditions at a much lower computational cost. This could be useful in assessing the impact of rotor design changes on community and military noise metrics.

7.2.2 Real-Time Noise Estimation

Although the parameter identification process is time consuming, the resulting analytical models are lightweight and can yield estimates of external noise radiation in real time. Since these models are generalizable to a wide range of flight conditions and have no limitations in terms of directivity, they can be used to estimate noise in real time for arbitrary helicopter trajectories and observer locations without *a priori* knowledge of the helicopter operation. This would allow a helicopter pilot to more easily avoid noise sensitive areas, alert him to potential detection by adversaries, and provide immediate corrective feedback for maintaining a low noise flight state.

7.2.3 Far-Field Acoustic State Estimation

In addition to providing a useful tool for pilots, real-time noise estimation could be extended to "close the loop" on active noise control systems. Previous research into active noise control for helicopters has either utilized manual sweeps of the control variables or closed-loop feedback control utilizing microphones located on the helicopter body itself.[75] Open loop control is not ideal for real world noise control systems, since even small changes in the rotor operating condition can lead to large changes in noise radiation, such that any pre-programmed active noise control inputs are unlikely to work well under actual flight conditions. On the other hand, existing closed-loop approaches are wholly unsuitable as it is well known that noise measured on the vehicle does not correlate with external noise radiation in any direct fashion. The framework developed in this dissertation, however, offers a method of estimating the acoustic state of the helicopter in all directions. The analytical framework developed in this research might be extended to higher-harmonic control inputs—at least with respect to the lower-harmonic noise sources—allowing far-field noise predictions to be made. In addition, the phenomenological models developed in this work are applicable to both near- and far-field noise and might be used to relate inflight noise measurements to the overall acoustic state of the vehicle.

7.2.4 Time-Domain Receiver Modeling

Although most receiver models in current use are based on frequency-domain relations, there is recent research which indicates that these models may be inadequate

for representing human aural detection, identification, or annoyance in response to helicopter noise.[6] Increased interest in non-linear models of human hearing means that helicopter noise models which are capable of representing external noise radiation in the time-domain may soon be required. Unlike any helicopter noise models in current use, the modeling framework developed in this dissertation is capable of providing this data.

7.2.5 Electronic Detection and Classification

While it is still inconclusive whether the human ear can perceive phase information, it is readily apparent that electronic devices can. The models developed using the method in this dissertation could be used to train electronic detection equipment to recognize helicopters in a wide range of operating conditions and directions. In addition, using this method to extend the size of the training set will increase the accuracy and robustness of electronic acoustic detection and classification equipment.

Appendix A

Theoretical Development of the Virtual Observer

This Appendix describes the theoretical basis of the virtual inflight observer concept, previously developed by the author[55] and introduced in Section 4.2 of this dissertation.

When a helicopter is in steady-state flight, it is creating harmonic noise that is associated with and necessary for powered flight. The resulting acoustic waves are propagated in the medium (air) and constitute the harmonic noise radiation of the helicopter. Motion of the helicopter has an effect on how the waves are deposited in the medium. Motion of the observer does not influence the sound field produced by the source, but does affect the acoustic pressure time-history as it is measured at the observer's location. The mechanism of the Doppler effect due to motion of both source and observer is described in this section, using the general equations for a sound source in motion.[76]

A.1 Theory

The general equation for the acoustic pressure observed at location $\vec{x}$ due to an acoustic source of strength q is given in Equation A.1.

$$p'(\vec{x},t) = \int \frac{q(\vec{y},\tau)}{4\pi|\vec{x}-\vec{y}|} d^3\vec{y} \tag{A.1}$$

Where t is the time the acoustic pressure is observed at $\vec{x}$ and τ is the associated time at the source.

If the source is assumed to occupy a single point in space, $\vec{x}_s$, it may be expressed as follows:

$$q(\vec{y},\tau) = Q(\tau)\delta(\vec{y} - \vec{x}_s(\tau)) \tag{A.2}$$

Substituting into Equation A.1:

$$p'(\vec{x},t) = \int_{-\infty}^{t}\int_{V} \frac{Q(\tau)\delta(\vec{y} - \vec{x}_s(\tau))}{4\pi|\vec{x} - \vec{y}|} d^3\vec{y}d\tau \tag{A.3}$$

By evaluating the point source at the single time of emission associated with the time of observation, the following expression is obtained using the retarded time equation:

$$p'(\vec{x},t) = \int_{-\infty}^{t}\int_{V} \frac{Q(\tau)\delta(\vec{y} - \vec{x}_s(\tau))}{4\pi|\vec{x} - \vec{y}|}\delta(t - \tau - \frac{|\vec{x} - \vec{y}|}{a_0}) d^3\vec{y}d\tau \tag{A.4}$$

Resolving the integral in space over the compact source:

$$p'(\vec{x},t) = \int_{-\infty}^{\infty} \frac{Q(\tau)\delta(t - \tau - \frac{|\vec{x} - \vec{x}_s(\tau)|}{a_0})}{4\pi|\vec{x} - \vec{x}_s(\tau)|} d\tau \tag{A.5}$$

A useful property of δ-functions is given in Equation A.6.

$$\int_{-\infty}^{\infty} f(\tau)\delta(g(\tau))d\tau = \left[\frac{f(\tau)}{|\frac{dg}{d\tau}|}\right]_{\tau=\tau^*} \tag{A.6}$$

τ^* is the root of $g(\tau)$ - in this case, the retarded time equation.

$$g(\tau^*) = t - \tau^* - \frac{|\vec{x} - \vec{x}_s|}{a_0} = 0 \tag{A.7}$$

Carrying out the differentiation of the denominator, the result is dependent on the Mach number of the source *with respect to the medium* along the radiation direction between the source and observer.

$$\left|\frac{dg}{d\tau}\right| = \left|-1 + \frac{x_i - x_{si}}{|\vec{x} - \vec{x}_s|}\frac{1}{a_0}\frac{dx_{si}}{d\tau}\right| = |1 - M_r| \tag{A.8}$$

Substituting Equations A.6 and A.8 into Equation A.5 results in the equation for the acoustic pressure generated by a moving point source. The point source is amplified by the Doppler amplification factor $|1 - M_r|$.

$$p'(\vec{x}, t) = \frac{Q(\tau^*)}{4\pi|\vec{x} - \vec{x}_s(\tau^*)|}\frac{1}{|1 - M_r|} \tag{A.9}$$

For a source traveling along direction x_1 at a constant speed U, the correct emission time τ^* can be calculated directly from a quadratic equation from the geometry shown in Figure A.1. Taking the subsonic root yields Equation A.10.

$$\tau^* = t - \frac{M(x_1 - Ut)}{a_0(1 - M^2)} - \frac{\sqrt{(x_1 - Ut)^2 + (1 - M^2)(x_2^2 + x_3^2)}}{a_0(1 - M^2)} \tag{A.10}$$

By substituting Equation A.10 into Equation A.9, the acoustic pressure generated by the moving source in the medium may be calculated for any point $\vec{x}$ at any time t. Motion of the observer is accounted for by defining the location of the observer within the medium, $\vec{x}$, as a function of observer time, t. It is this relation between source time, τ^*, and observer time, t, which causes the well known Doppler frequency shift by expanding or contracting the acoustic pressure time-history emitted by the source in time, as seen by the observer. (Figure A.2)

The classical frequency-domain expression for the Doppler frequency shift may be obtained from the retarded time expression given by Equation A.10. For example,

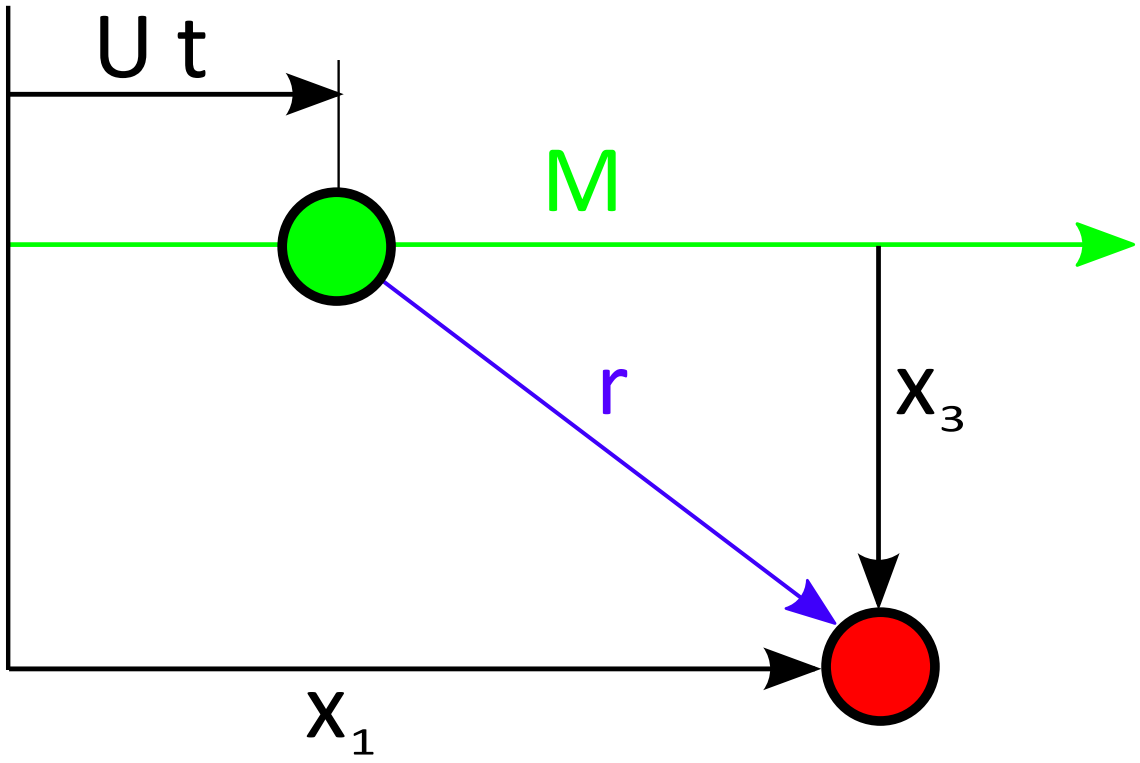

Figure A.1: Equation A.10 geometry, source (green) and observer (red).

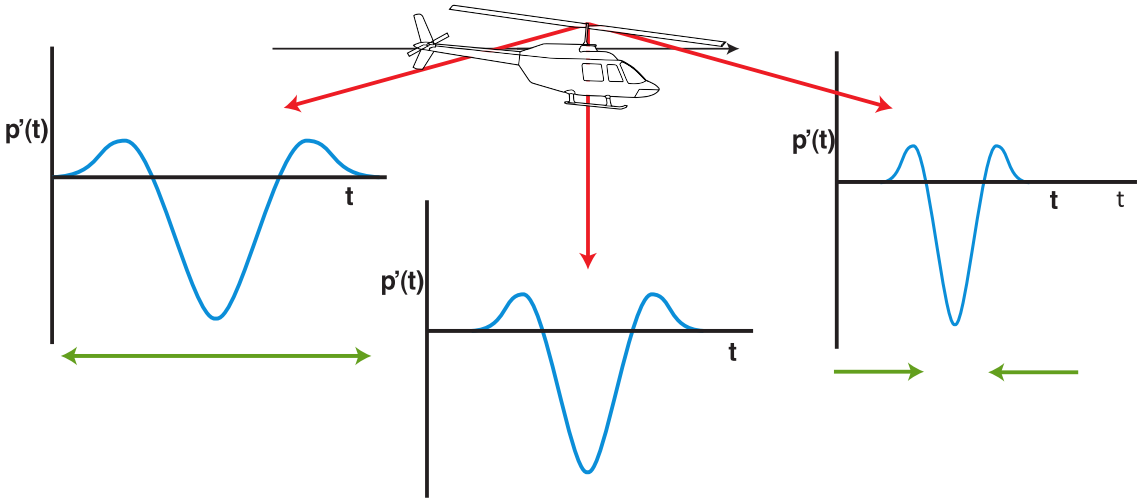

Figure A.2: Time dilation of pressure time-history signal of a moving source as seen by a stationary observer.

consider a simple harmonic source, as described by Equation A.11. Let the source move at speed U in the same direction as the observer, moving at speed X as shown in Figure A.3.

$$Q(\tau^*) = \sin(\omega\tau^*) \tag{A.11}$$

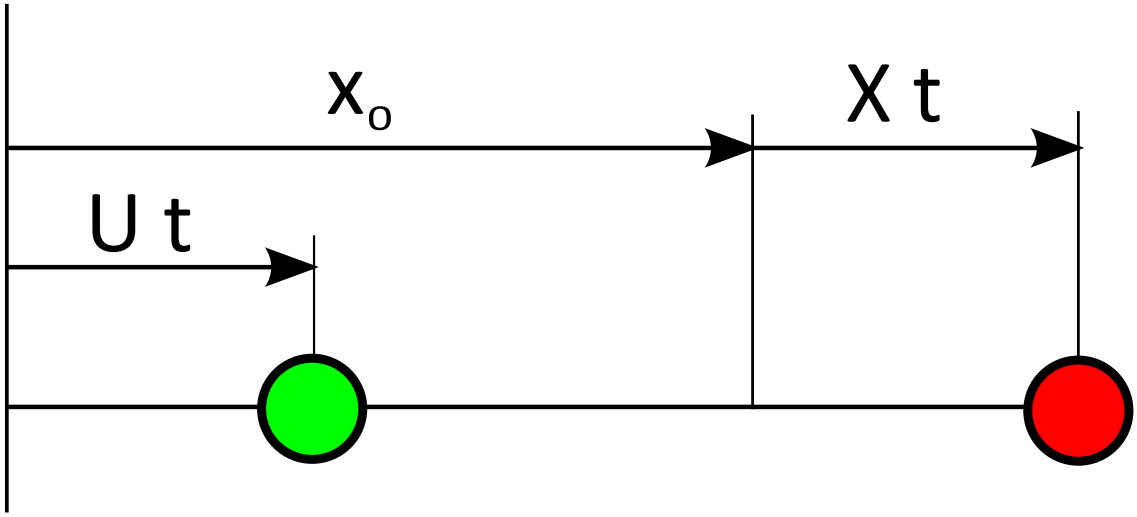

Figure A.3: Simple 1-D geometry example, source (green) and observer (red).

Using Equation A.10 the apparent frequency seen by the observer can be readily determined. Applying the source and observer geometry shown in Figure A.3 to Equation A.11 yields,

$$\begin{aligned} \tau^* &= t - \frac{M(Xt + x_0 - Ut) - \sqrt{(Xt + x_0 - Ut)^2}}{a_0(1 - M^2)} \\ &= t - \frac{M_o t + x_0 - Mt}{(1 - M)} = \frac{1 - M_o}{1 - M} t + \frac{x_0}{a_0(1 - M)} \end{aligned} \tag{A.12}$$

Substituting Equation A.12 into A.11 yields the well known frequency-domain expression for the change in observed frequency due to the motions of the source

and observer.

$$\begin{aligned} Q(t) &= \sin(\omega \frac{1 - M_o}{1 - M} t + \omega \frac{x_0}{a_0(1 - M)}) \\ &= \sin(\omega' t + \Delta\phi) \end{aligned} \tag{A.13}$$

where

$$\omega' = \frac{1 - M_o}{1 - M} \omega$$

However, when the direction of propagation does not lie along the direction of motion of both the source and the observer, the change in apparent frequency is no longer constant in time. Instead, the Mach numbers of the source and observer as measured along the direction of propagation vary over time yielding a time-varying change in the apparent frequency. This effect is fully accounted for in Equation A.10, which is valid for any motion of the observer relative to the moving source.

A.2 Sample Calculation

The case of a moving point source with strength varying harmonically, as described in Equation A.11, is considered for three observer geometries. The source motion is similar to that of a helicopter during a level flight flyover, and is described in Table A.1. The observer geometry is described in Table A.2. The first observer geometry is that of a typical ground-based microphone, stationary with the medium. The second is an air-based observer which travels a fixed distance away from the source, but sweeps along the same elevation angles covered by the ground-based observer during the flyover. The third observer also travels with the source, but

maintains a constant elevation angle as well a distance, analogous to a stationary wind tunnel or inflight measurement. The ground- and air-based observer geometries are shown in Figure A.4 and are evaluated using Equation A.10. The wind tunnel geometry is similar to the air-based geometry, except that observer travels with the source at a fixed angle such that the relative velocity between the observer and source is exactly zero. As such, the signals observed by the air-based and wind tunnel observers are nearly identical.

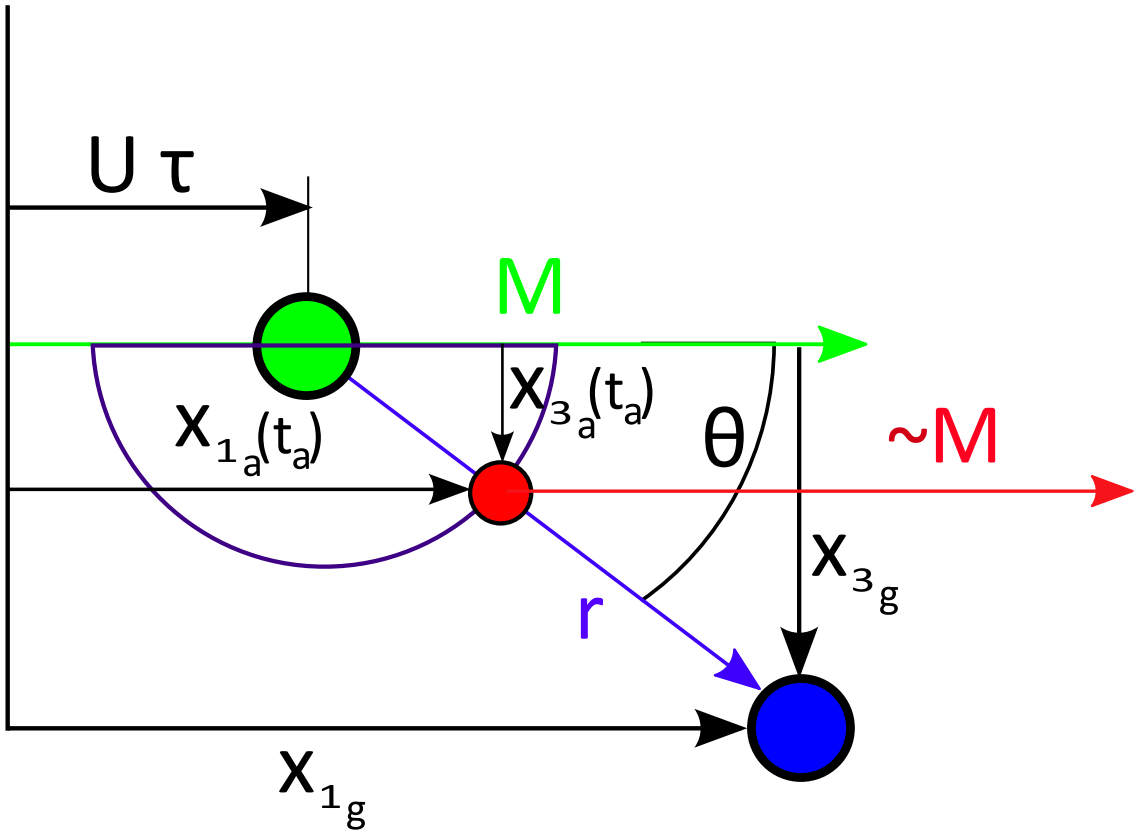

Figure A.4: Ground- (blue) and air- (red) based observer geometries, as evaluated by Equation A.10.

Figure A.5 shows the resulting pressure time-history for the 15 Hz source at all

U	170	ft/s
a_0	1100	ft/s
R	30	ft
ω	15 & 150	Hz
f_s	20	kHz

Table A.1: Example calculation source motion parameters.

	Ground	Air-Based	Wind Tunnel
x_1	1000 ft	$Ut + R\cos(\theta_g)$	$Ut + R\cos(\pi/4)$
x_2	0	0	0
x_3	492 ft	$-R\sin(\theta_g)$	$R\sin(\pi/4)$

Table A.2: Example calculation observer geometries, where θ_g is the elevation angle of the ground based observer, i.e. $\tan(\theta_g) = x_{3g}/x_{1g}$

three observers for the first 0.2 seconds of the simulated flyover. Amplitudes of all three signals are approximately equal, however due to the continuously decreasing time delay between the moving source and the stationary ground observer, the signal observed on the ground is compressed in the time domain.

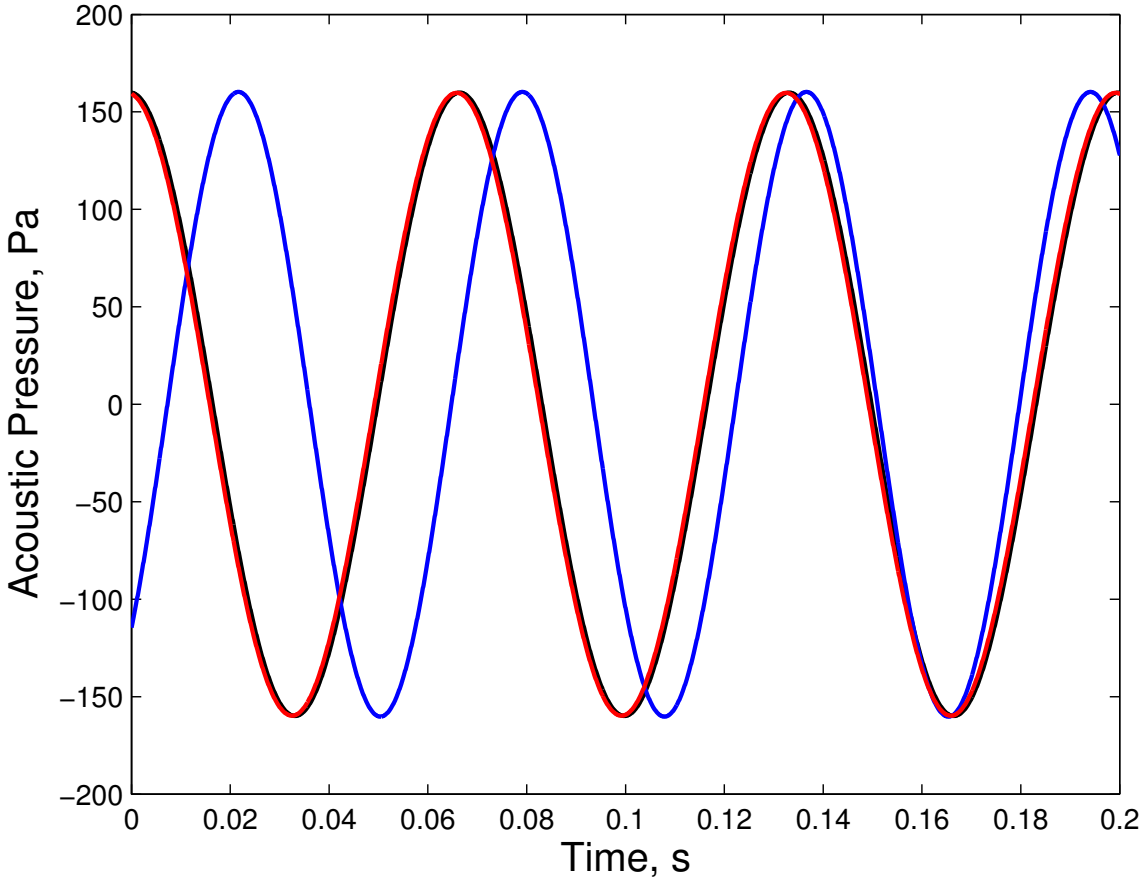

Figure A.5: Pressure time-history of 15Hz signal observed by: ground (blue), inflight (red), wind tunnel (black).

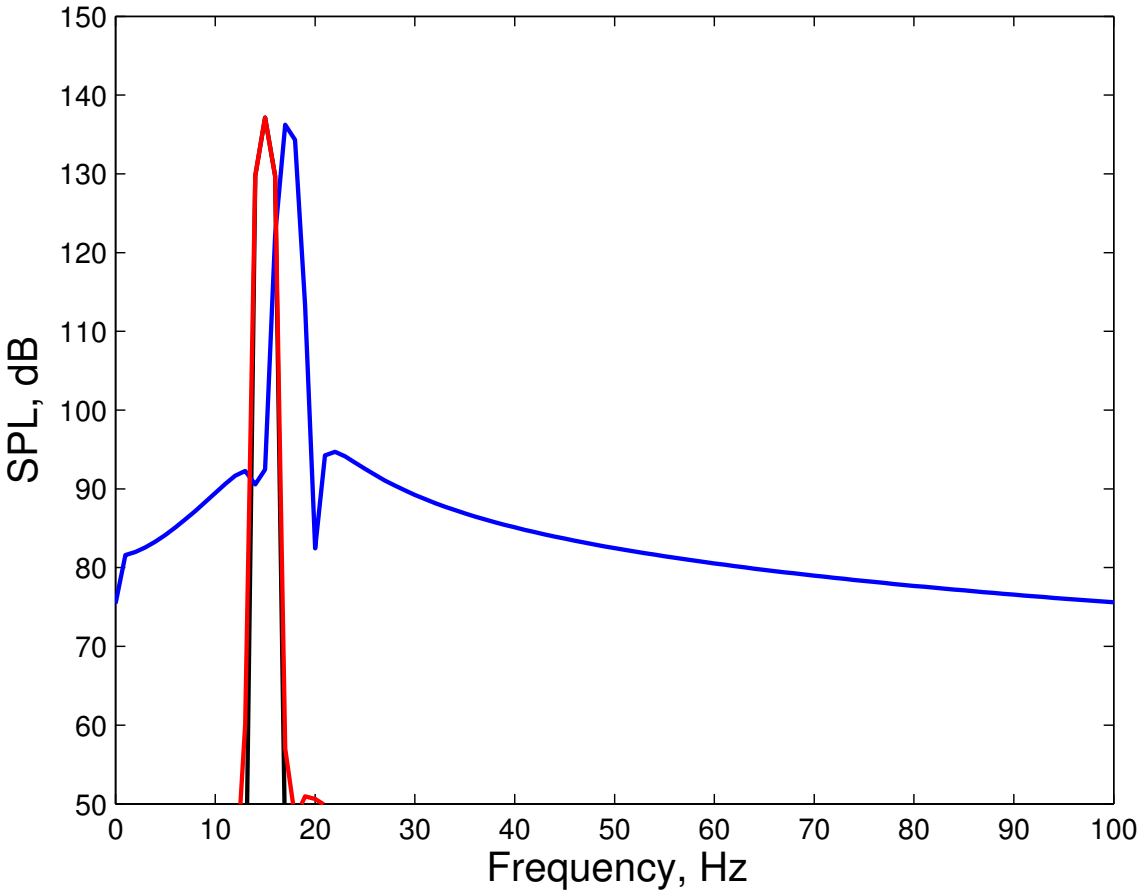

Figure A.6: Frequency spectra of first second of 15Hz signal observed by: ground (blue), inflight (red), wind tunnel (black).

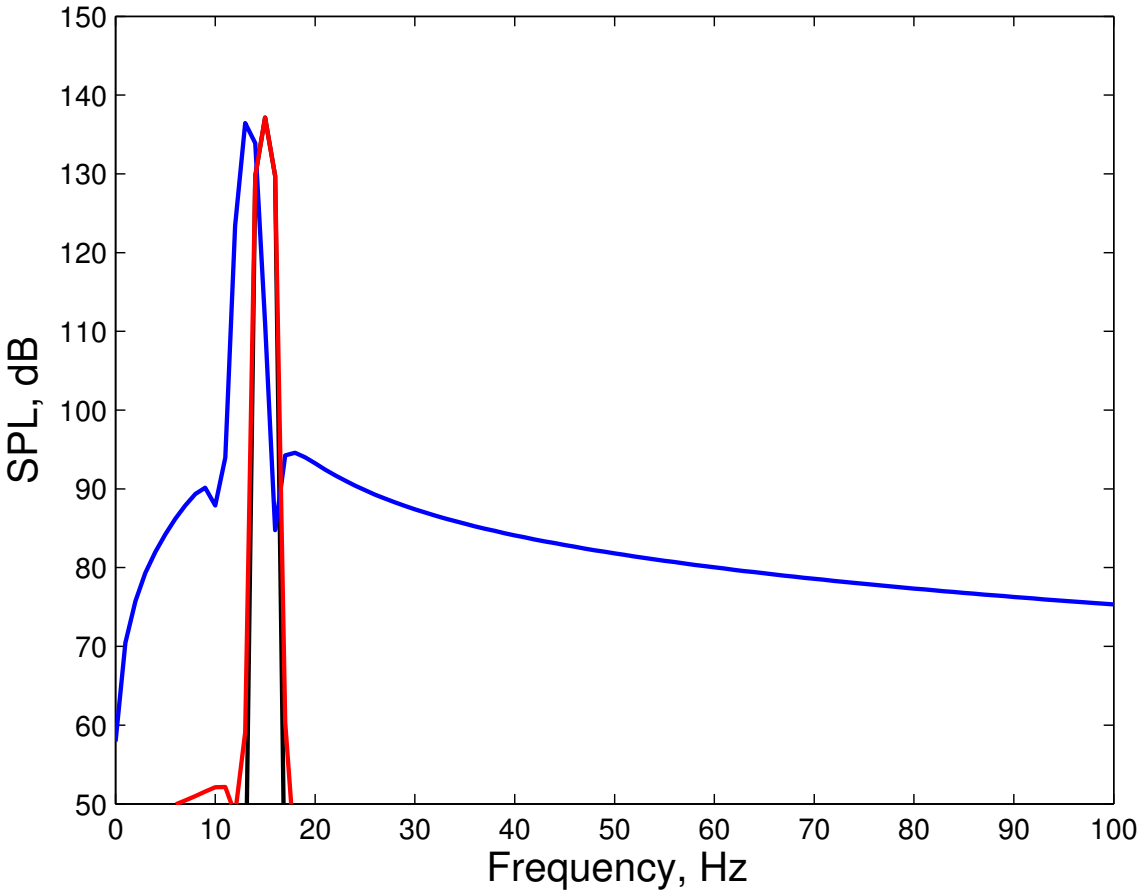

Figure A.7: Frequency spectra of last second of 15Hz signal observed by: ground (blue), inflight (red), wind tunnel (black).

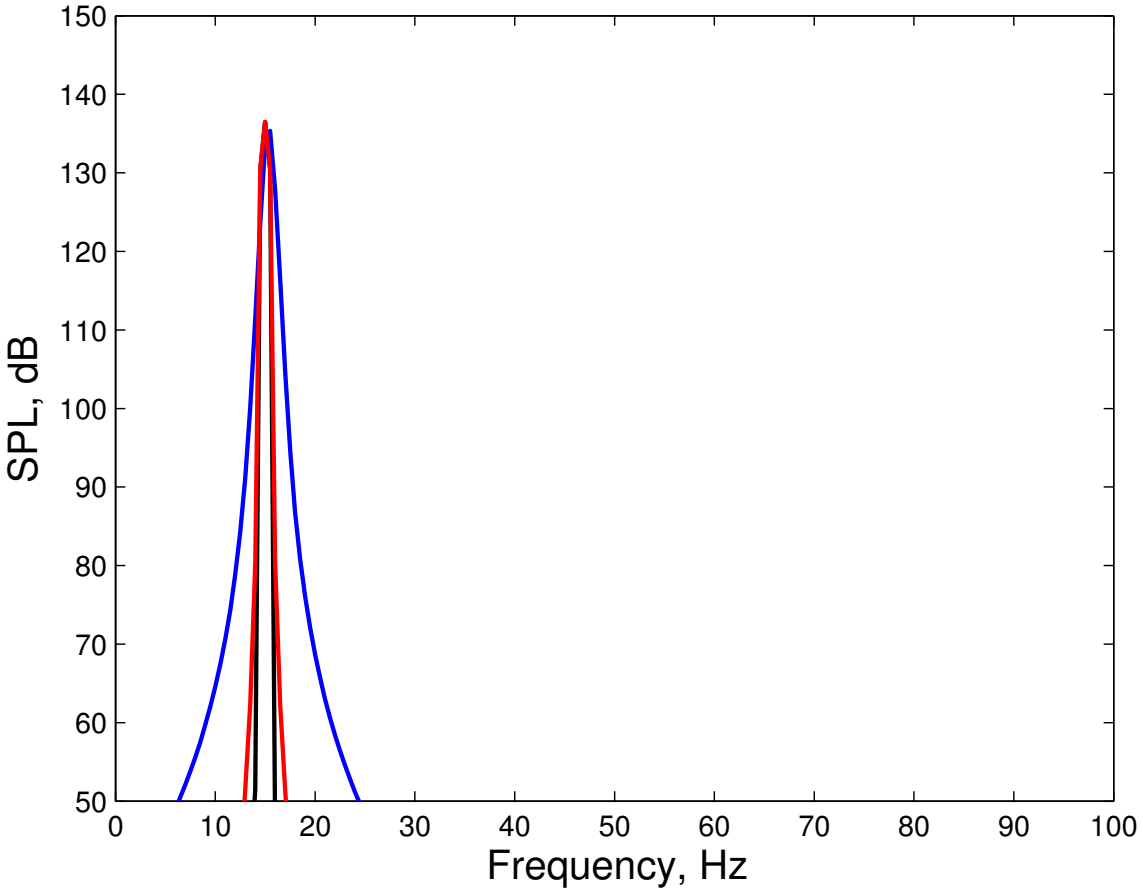

Figure A.8: Frequency spectra of middle second of 15Hz signal observed by: ground (blue), inflight (red), wind tunnel (black).

Figures A.6, A.7, and A.8 show the frequency spectra of the signals as observed during the first, last, and middle second of the flyover, respectively. During the first second of the flyover, the source is approaching the ground-based observer. During the middle second of the flyover, the source passes overhead the ground-based observer. During the last second the source travels away from the ground-based observer. The frequency spectra are calculated using a Hann window over one second of data, in order to reduce spectral leakage. The air-based signal appears as a steady 15Hz tone in all three spectra, as does the wind tunnel signal. However, the peak value of the ground-based signal is shifted in frequency, increasing as the source moves towards the observer and decreasing as the source moves away. More importantly, the frequency spectra for the ground-based signal is "smeared" across a broader range of frequencies, because the time-delay between source and observer varies throughout the one second frequency spectra window. The "smearing" is most severe when the source passes directly overhead, since the rate of change of the directivity angle (i.e. slew rate) is highest. "Smearing" of the inflight spectra is minimal due to the slight motion between the source and observer. As expected, no "smearing" is observed for the stationary wind tunnel observer, producing a frequency spectra nearly identical to that seen by the air-based observer.

Figures A.9, A.10, and A.11 show the same frequency spectra for the 150 Hz source. A greater shift in frequency content is observed.

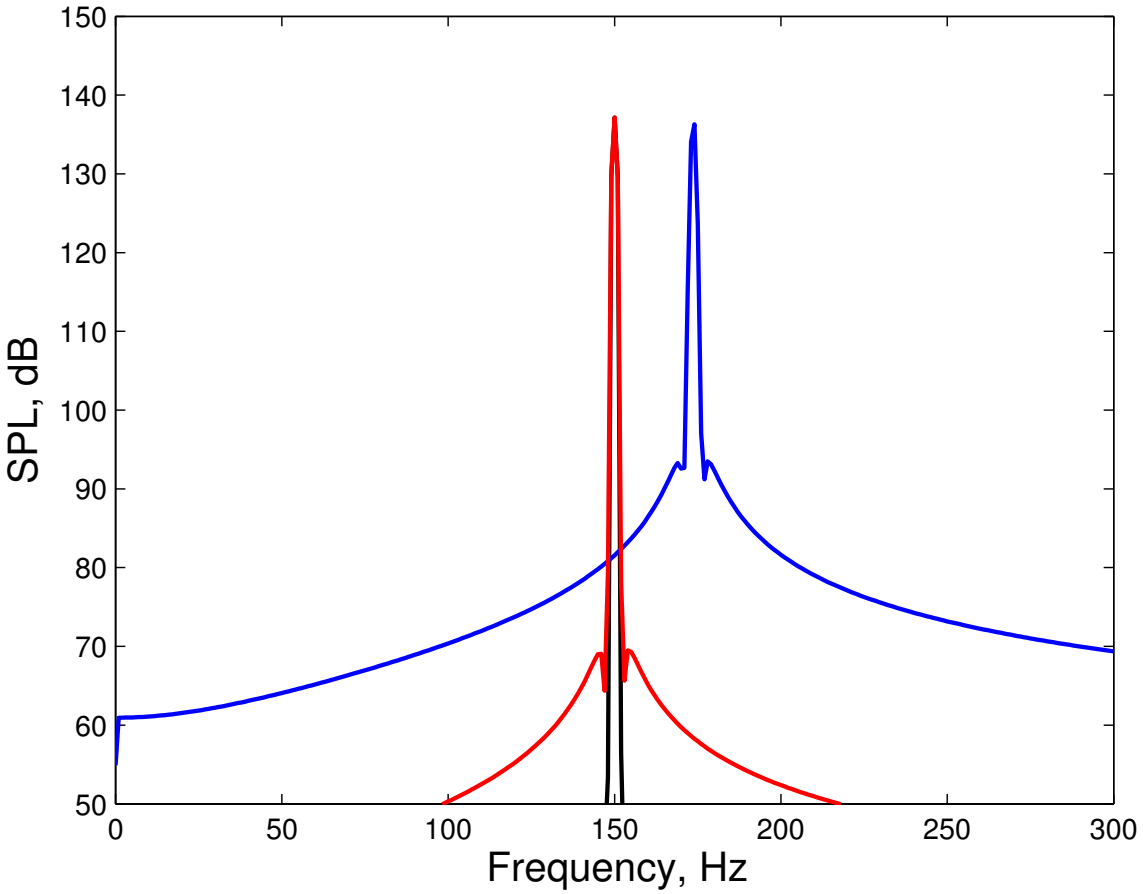

Figure A.9: Frequency spectra of first second of 150Hz signal observed by: ground (blue), inflight (red), wind tunnel (black).

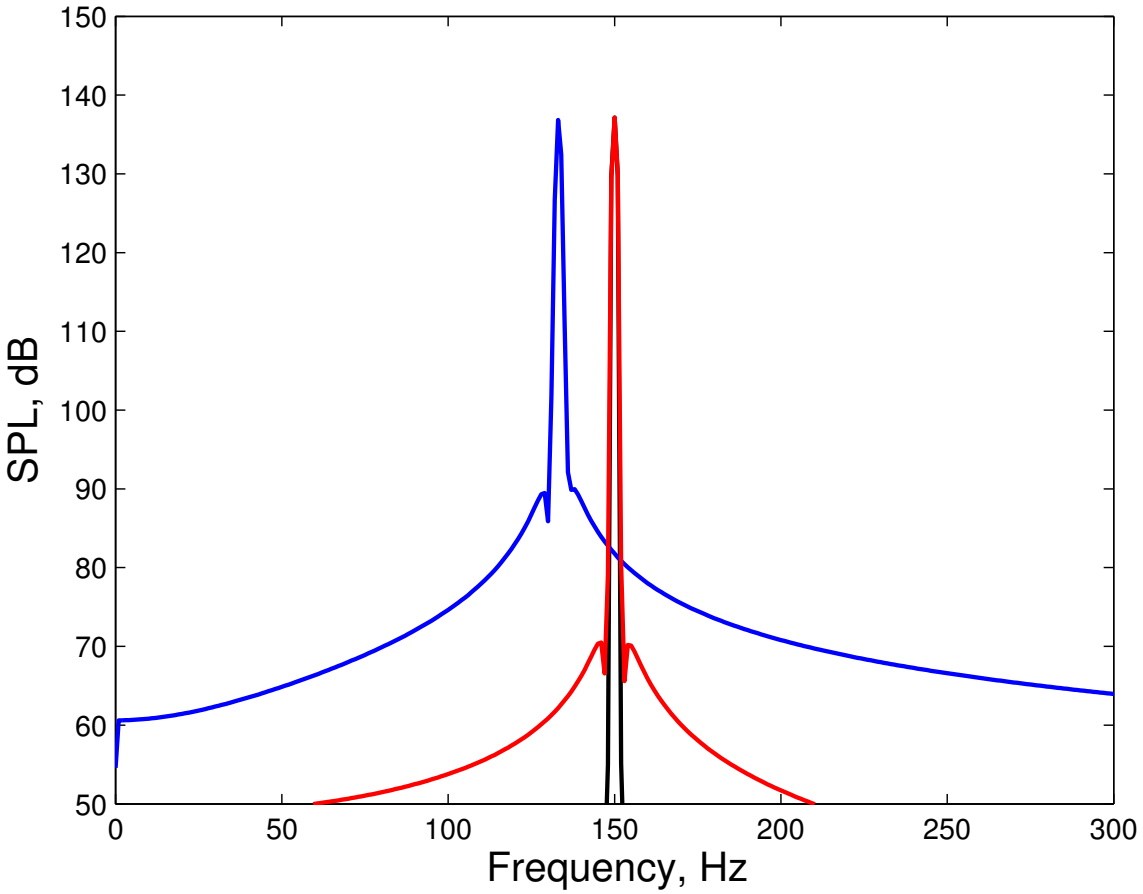

Figure A.10: Frequency spectra of last second of 150Hz signal observed by: ground (blue), inflight (red), wind tunnel (black).

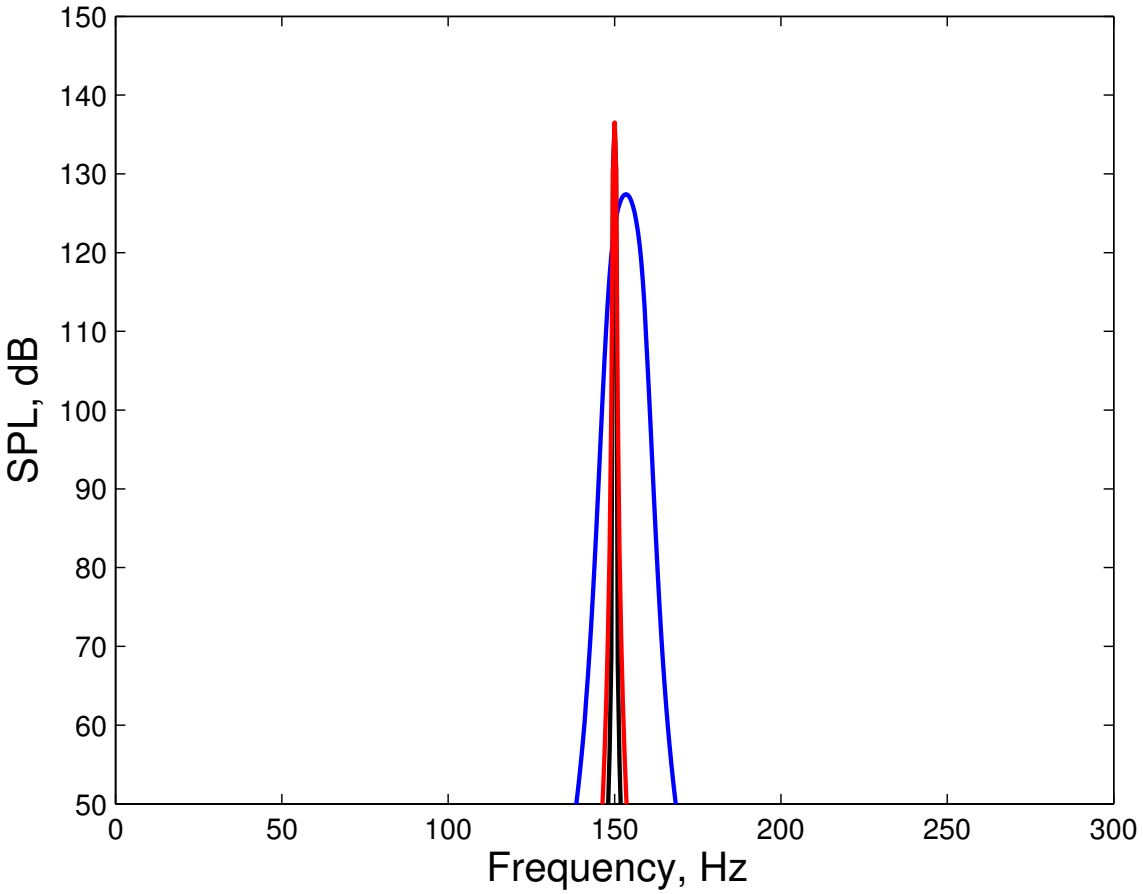

Figure A.11: Frequency spectra of middle second of 150Hz signal observed by: ground (blue), inflight (red), wind tunnel (black).

The case of a square pulse source is also analyzed. The pressure time-history observed for a square pulse source with a 10% duty cycle activated at 15 Hz is shown in Figure A.12. Again, the observed signal is compressed or expanded in time due to the change in retarded time, but the pulse shape is not distorted.

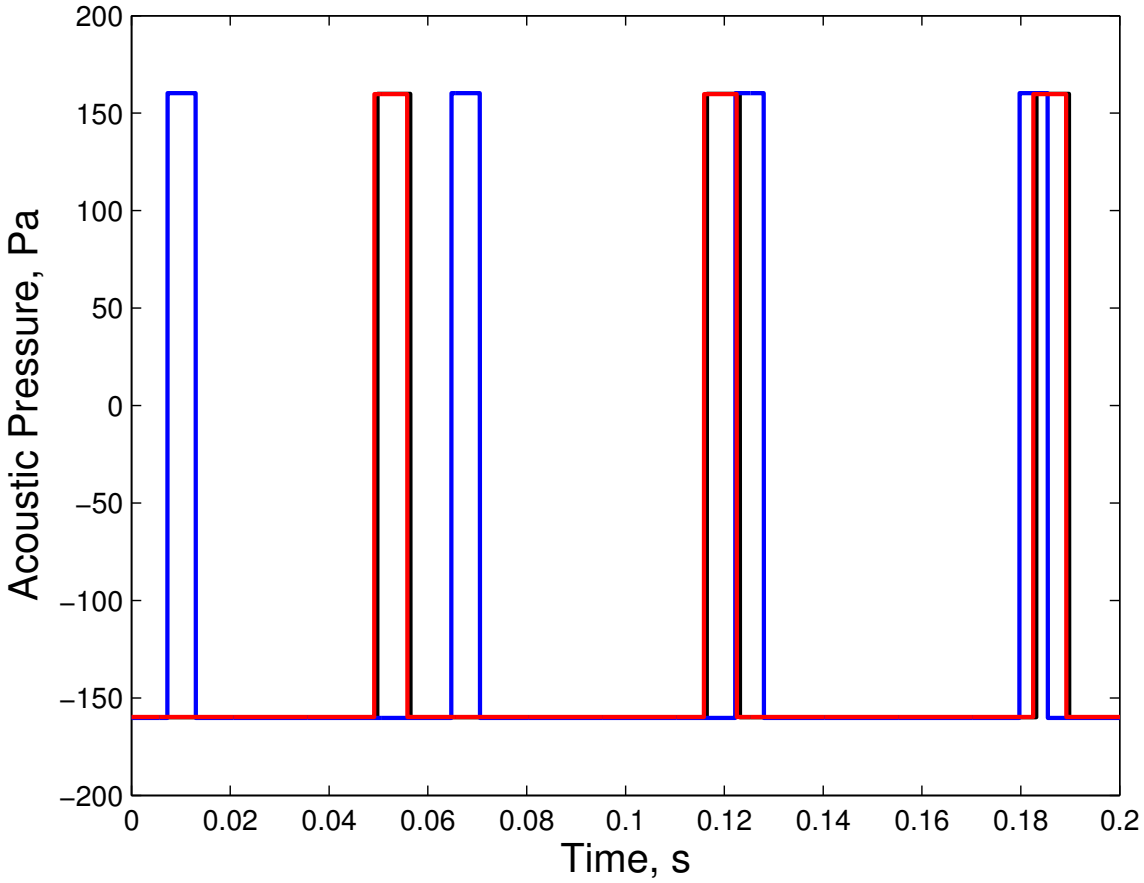

Figure A.12: Pressure time-history of square pulse signal observed by: ground (blue), inflight (red), wind tunnel (black).

Figures A.13, A.14, and A.15 show the first, last, and middle second frequency spectra for the square pulse source. The effect of frequency "smearing" masks the clear 15 Hz harmonic peaks produced by the square pulse for the ground-based observer, especially for the middle second where the source is flying directly over the

observer and the geometry between the source and observer changes most rapidly. The tonal content of the source remains distinct for the inflight observer throughout the simulated flyover and is nearly identical to that observed in the wind tunnel case.

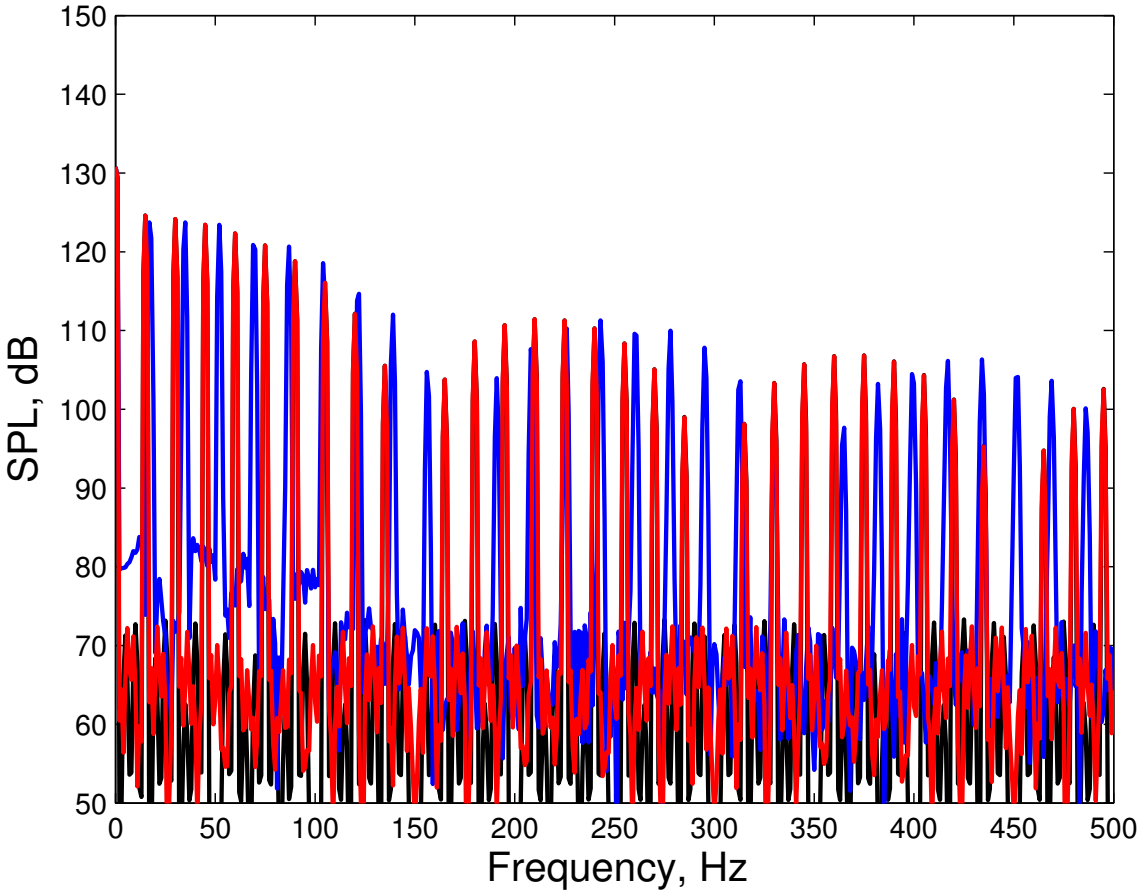

Figure A.13: Frequency spectra of first second of square pulse signal observed by: ground (blue), inflight (red), wind tunnel (black).

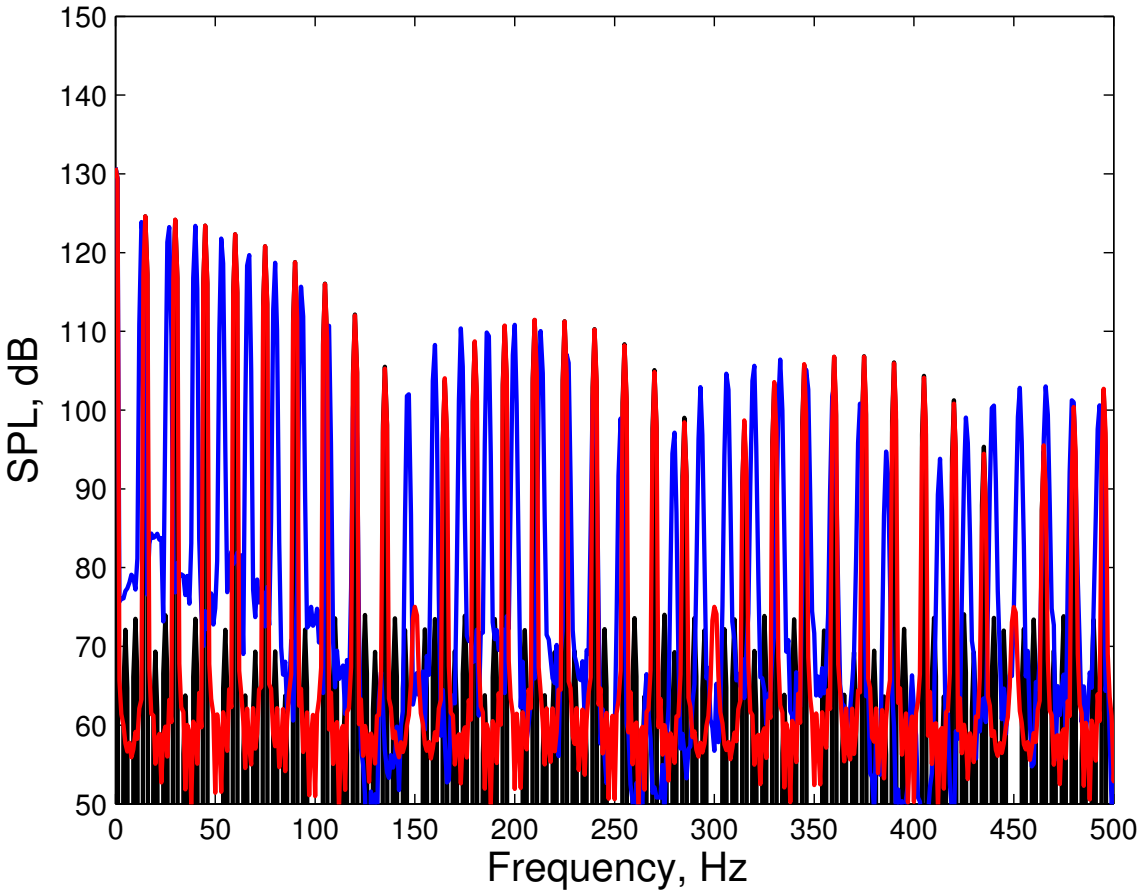

Figure A.14: Frequency spectra of last second of square pulse signal observed by: ground (blue), inflight (red), wind tunnel (black).

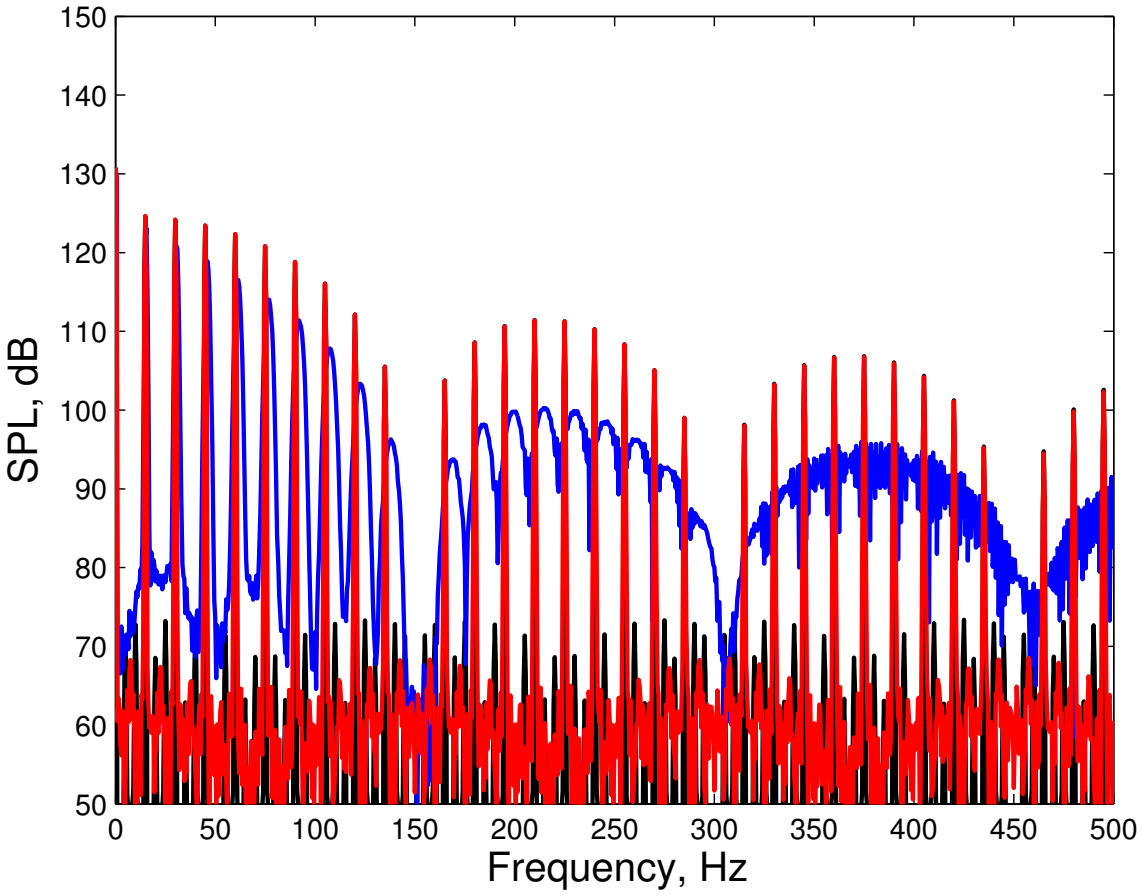

Figure A.15: Frequency spectra of middle second of square pulse signal observed by: ground (blue), inflight (red), wind tunnel (black).

The "smearing" of the frequency of the source due to the Doppler effect is clearly evident in all of the ground-based measurements, and is especially disruptive for cases with impulsive harmonic noise sources—a dominant type of rotorcraft noise—where the various tonal frequency contributions may "smear" together. On the other hand, the difference between the virtual inflight and wind tunnel observers is negligible for typical helicopter flight test geometries.

For this single noise source, all observers are subject to the same Doppler amplification, since this is determined by the Mach number of the source with respect to the medium. Regardless, for typical helicopter flight speeds, ($M < 0.2$) the effect of Doppler amplification due to the velocity of the helicopter through the medium is negligible. For example, for $M = 0.2$ ($\sim$130 kts at sea level) the maximum possible Doppler amplification due to overall helicopter motion is only 0.35 dB. However, rotor noise sources are moving with respect to the vehicle at much higher Mach numbers than the motion of the vehicle with respect to the medium; therefore, Doppler amplification can not be fully accounted for by considering all external noise radiation as originating from a single noise source affixed to the vehicle. This has not been accounted for in previous attempts at de-Dopplerization of rotorcraft noise sources[77][78] which have attempted to "correct" for Doppler amplification due to the motion of the vehicle as a whole, treating the rotorcraft as though it were a fixed-wing aircraft. Instead, the individual rotor noise source must be treated independently, as described in Section 2.2.

Appendix B

Effects of Isolated Governing Parameter Variations due to Altitude

In this Appendix, the contribution of each of the four non-dimensional governing parameters to variations in helicopter external noise radiation with changes in altitude is independently assessed, using the combined Bell 206 – OLS model, flight condition and ambient condition variation from Section 5.3.2. Each of the governing parameter variations, shown previously in Figure 5.32, has a different effect on the magnitude and directivity of BVI noise.

The thrust coefficient increases as density decreases with altitude. The thrust coefficient has a direct effect on the strength of the tip vortices trailed by the rotor blades, and hence an effect on the strength of BVI noise. Using the combined Bell 206 – OLS ANN model developed in Section 5.3.1, the effect of thrust on BVI noise can be estimated in isolation. Figure B.1 shows the corresponding increase in BVI noise levels when the thrust coefficient is raised in isolation to its value at 7500 ft ISA altitude. Figure B.2 shows the further increase in BVI noise levels due to an increase in thrust coefficient to the 15000 ft value. Recall that the baseline sea level -7.5° case was shown for the combined Bell 206 – OLS model in Figure 5.31.

In order to maintain the same indicated airspeed, dynamic pressure must be held constant. Since density decreases with altitude, true airspeed must be increased to maintain the same dynamic pressure. This corresponds to an increase in rotor

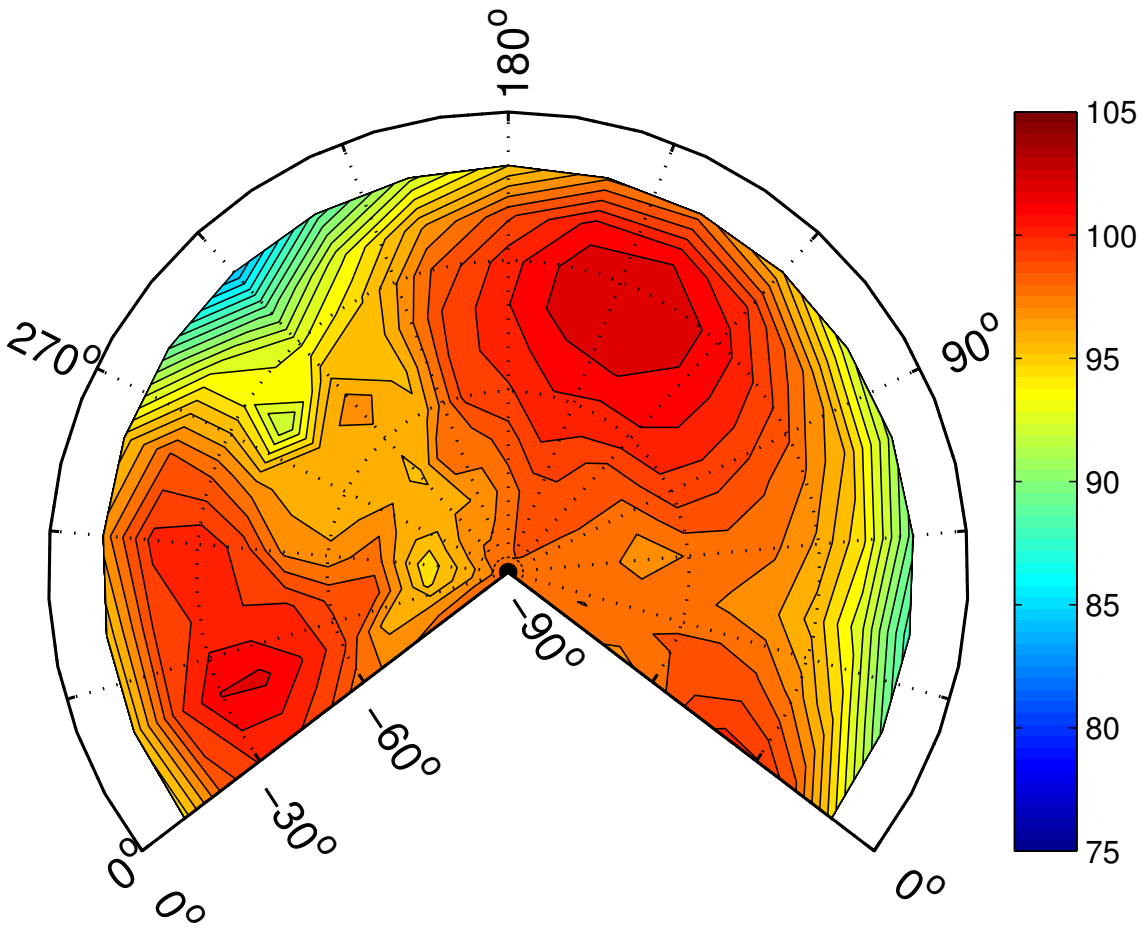

Figure B.1: Combined Bell 206 – OLS model BVISPL hemisphere estimate for Bell 206B3 -7.5° flight path angle condition with thrust coefficient at 7500 ft.

advance ratio with altitude. The advance ratio controls the epicyclodial structure of the rotor wake, influencing both the strength and directivity of BVI noise. The advance ratio also has a secondary effect on the lateral inflow distribution, which affects the relative miss-distance of advancing versus retreating side BVI. The effect of changes in advance ratio on noise can be seen in isolation by estimating the noise levels using the combined Bell 206 – OLS ANN model. The BVISPL noise contours are plotted for the 7500 ft and 15000 ft advance ratios in Figures B.3 and B.4,

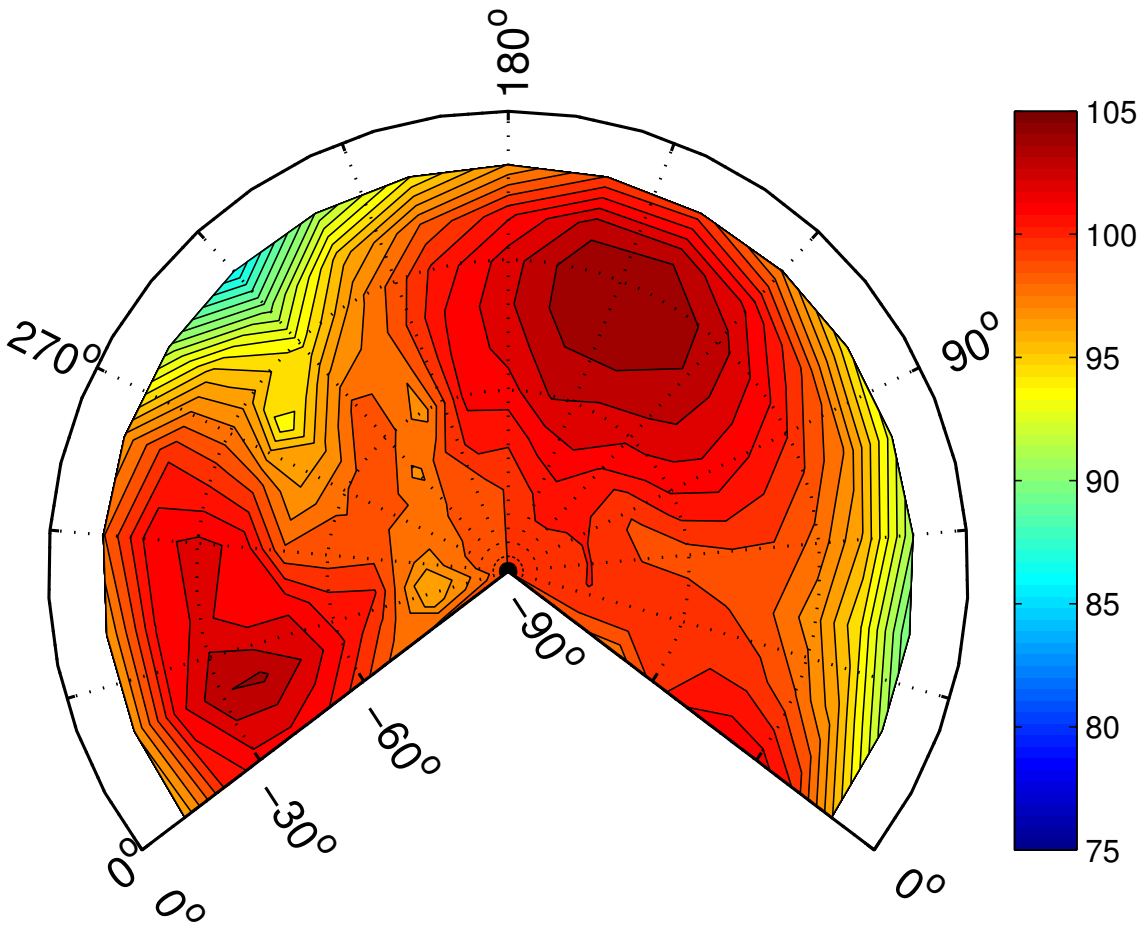

Figure B.2: Combined Bell 206 – OLS model BVISPL hemisphere estimate for Bell 206B3 -7.5° flight path angle condition with thrust coefficient at 15000 ft.

respectively. The change in levels and directivity with increasing advance ratio is readily apparent.

Since dynamic pressure is held constant for constant indicated airspeed, to first order the longitudinal trim of the helicopter (i.e. tip-path-plane angle of attack) remains unchanged with altitude. However, as altitude increases and air density decreases, the induced inflow through the rotor must increase in order to produce sufficient thrust to maintain a steady flight condition. Overall, this results in an

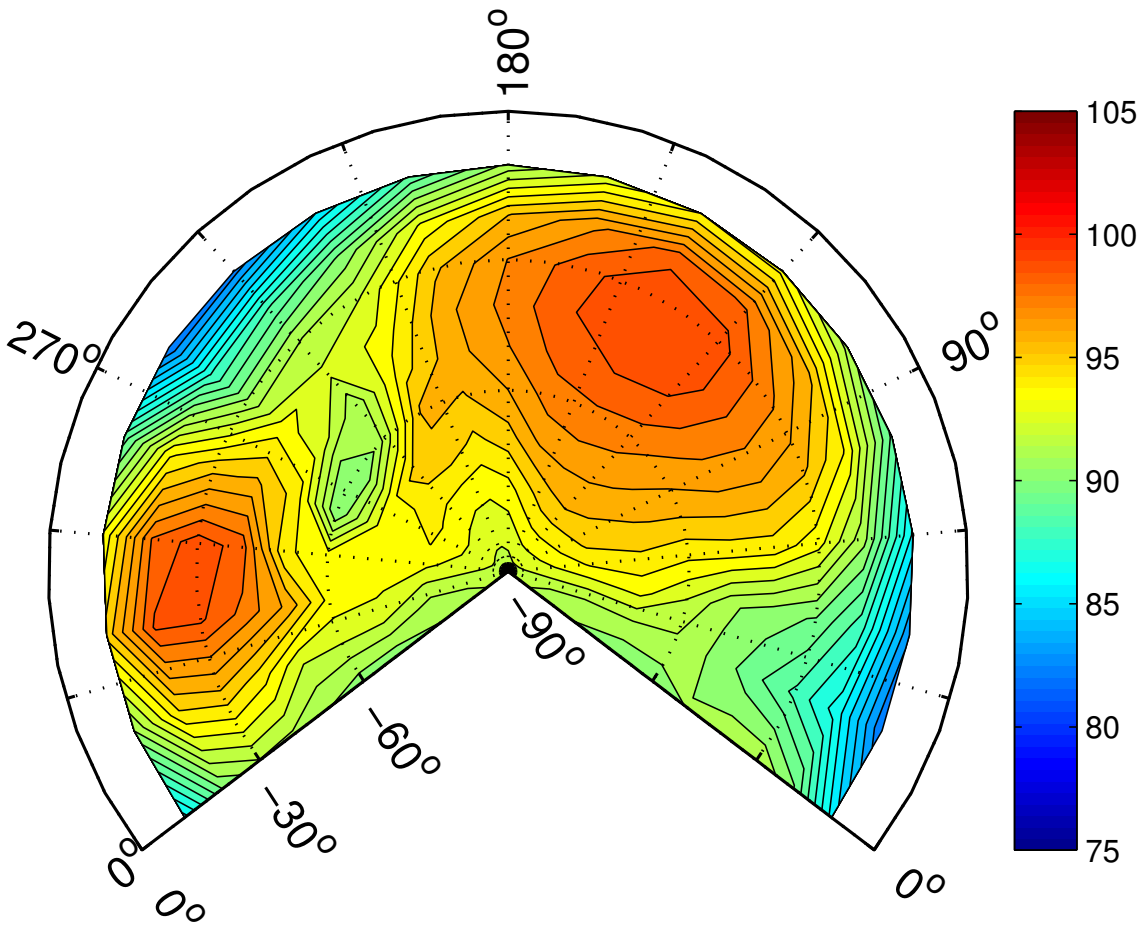

Figure B.3: Combined Bell 206 – OLS model BVISPL hemisphere estimate for Bell 206B3 -7.5° flight path angle condition with advance ratio at 7500 ft.

increase in the mean inflow ratio—for flight conditions where the wake is below the rotor, such as the baseline -7.5° flight path angle case, this results in an increase in the miss-distance and a decrease in BVI noise levels. This is illustrated in Figures B.5 and B.6 for the 7500 ft and 15000 ft ISA altitudes, respectively. However, if the wake were above the rotor for the baseline case, an increase in inflow would result in a decrease in miss-distance and hence an increase in BVI noise.

Lastly, due to the decrease in ambient temperature with altitude, the speed of

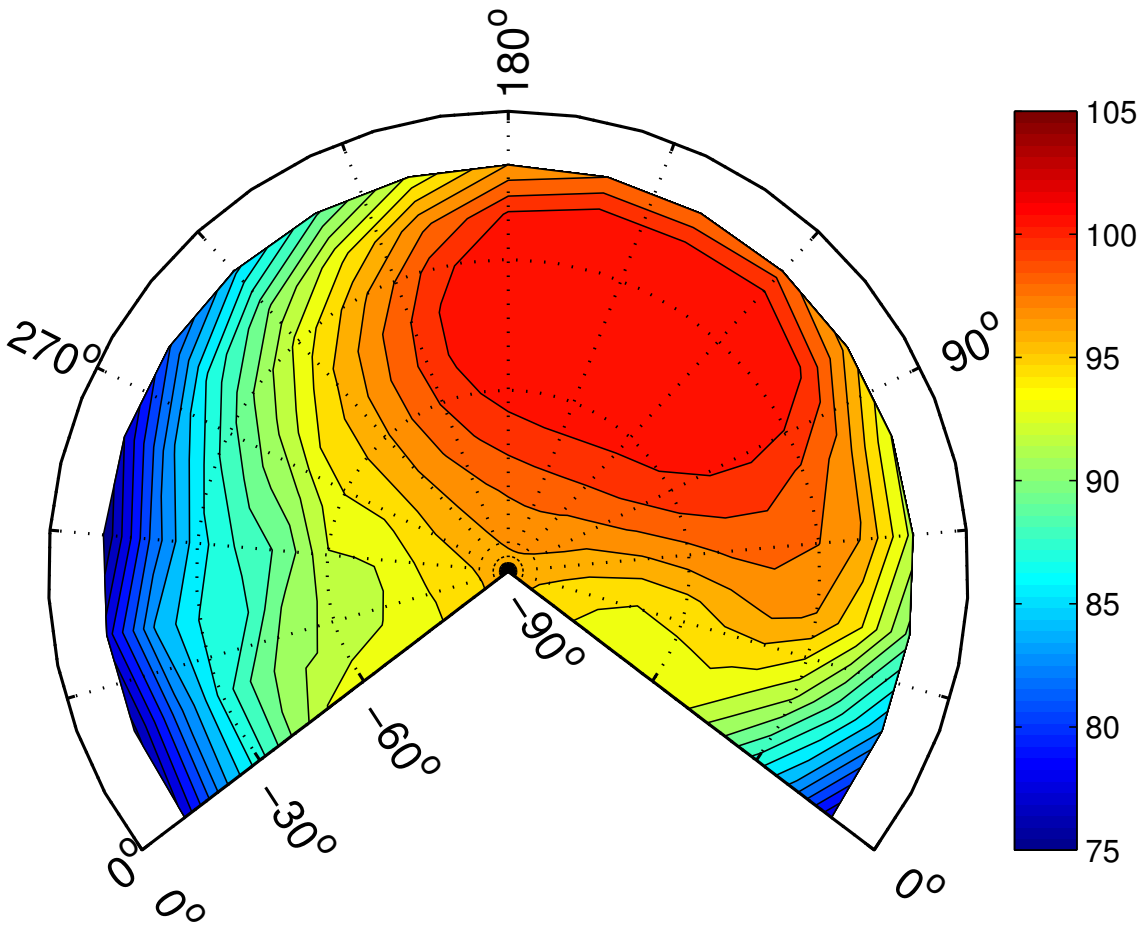

Figure B.4: Combined Bell 206 – OLS model BVISPL hemisphere estimate for Bell 206B3 -7.5° flight path angle condition with advance ratio at 15000 ft.

sound decreases, leading to an increase in the rotor tip Mach number. An increase in rotor hover tip Mach number results in an increase in radiated noise of all sorts, including BVI@. The sensitivity of noise to changes in tip Mach number increases as tip Mach number increases. The Bell 206B3 has a relatively low hover tip speed ($\approx$ 700 ft/s); for helicopters with higher tip speeds, even greater changes in noise levels with rotor tip Mach number can be expected, especially at high forward flight speeds where the advancing tip Mach number enters the transonic regime. The

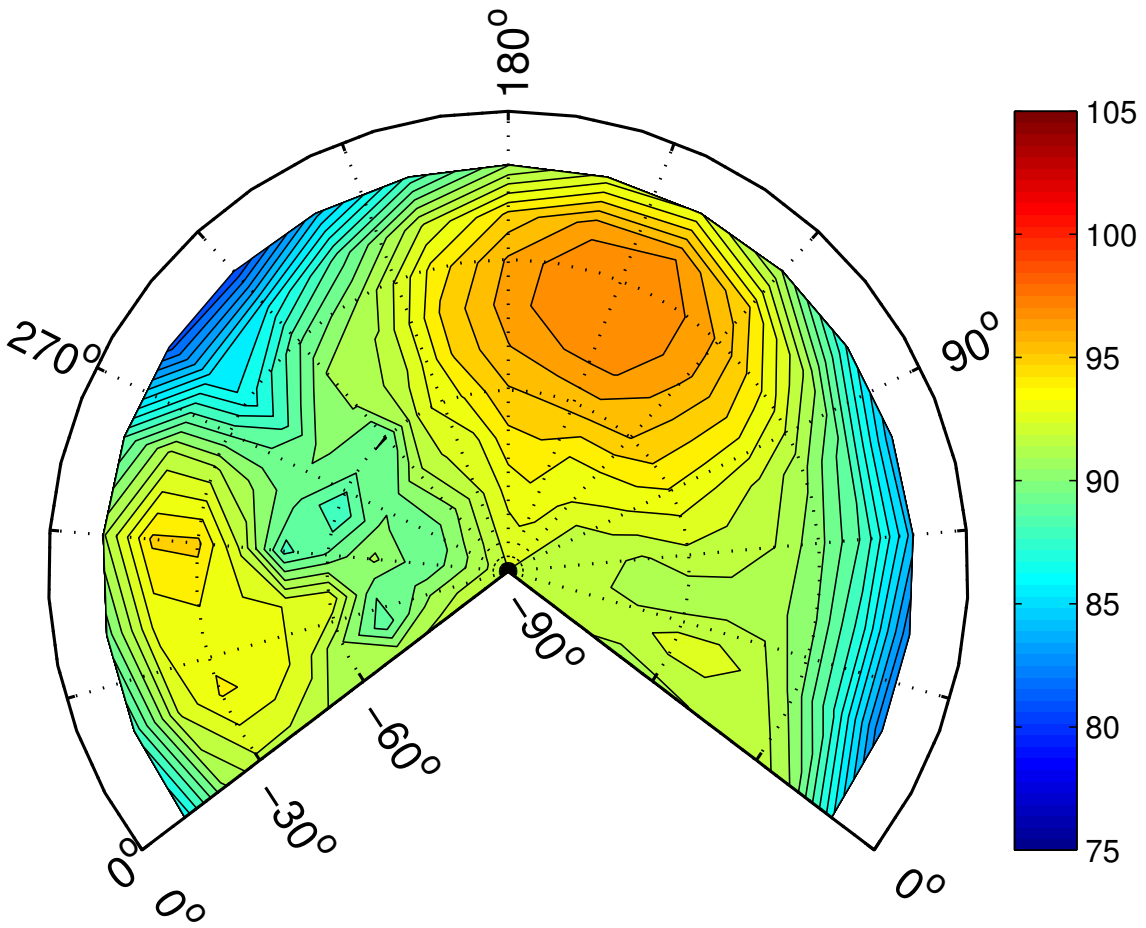

Figure B.5: Combined Bell 206 – OLS model BVISPL hemisphere estimate for Bell 206B3 -7.5° flight path angle condition with inflow ratio at 7500 ft.

change in noise levels is shown in Figures B.7 and B.8 for the 7500 ft and 15000 ft ISA altitudes, respectively.

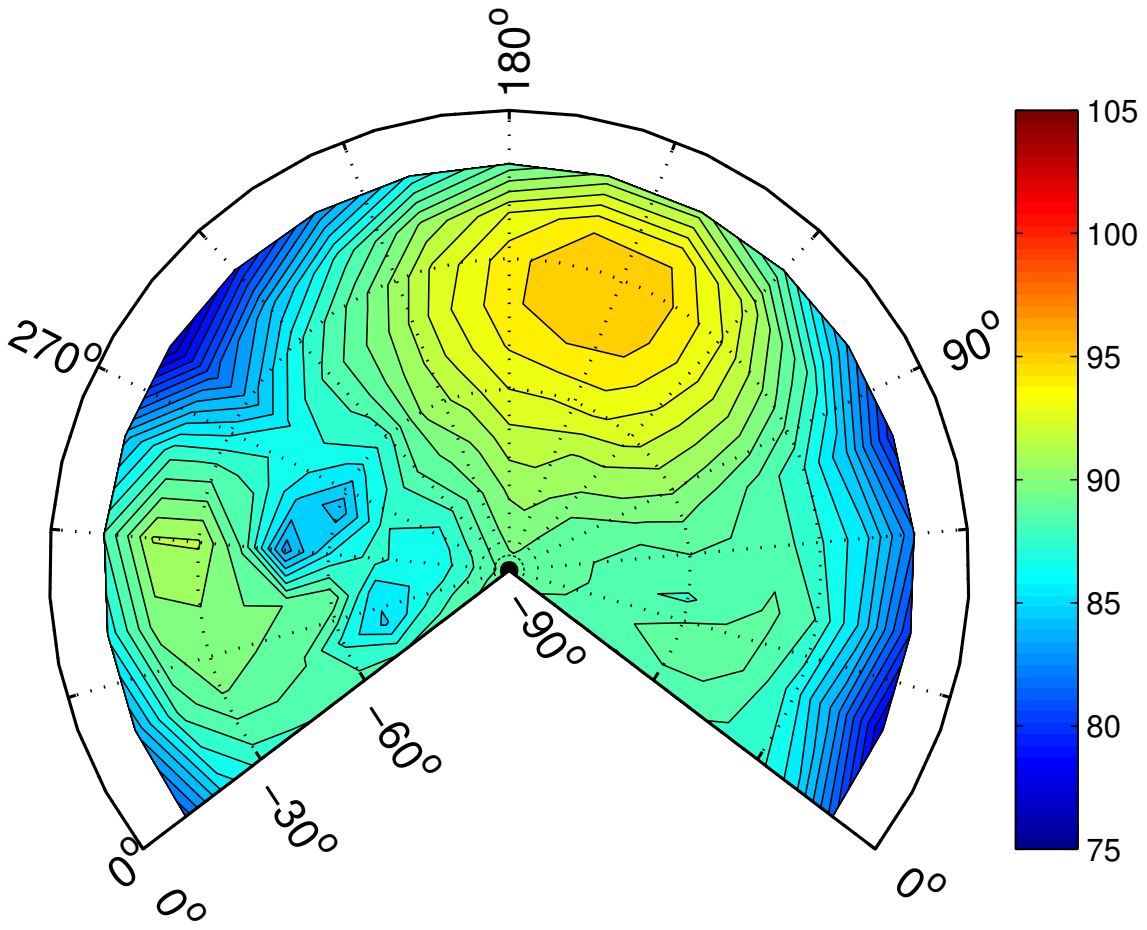

Figure B.6: Combined Bell 206 – OLS model BVISPL hemisphere estimate for Bell 206B3 -7.5° flight path angle condition with inflow ratio at 15000 ft.

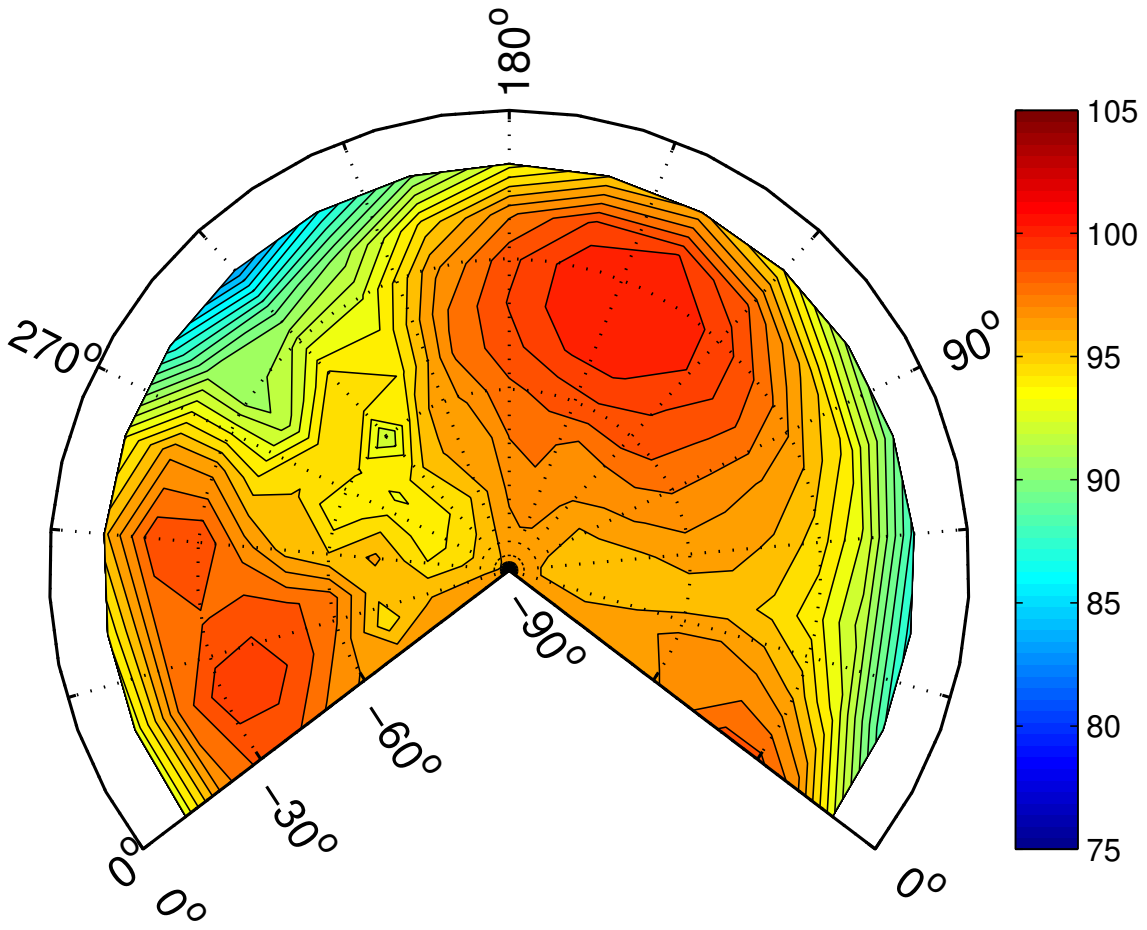

Figure B.7: Combined Bell 206 – OLS model BVISPL hemisphere estimate for Bell 206B3 -7.5° flight path angle condition with hover tip Mach number at 7500 ft.

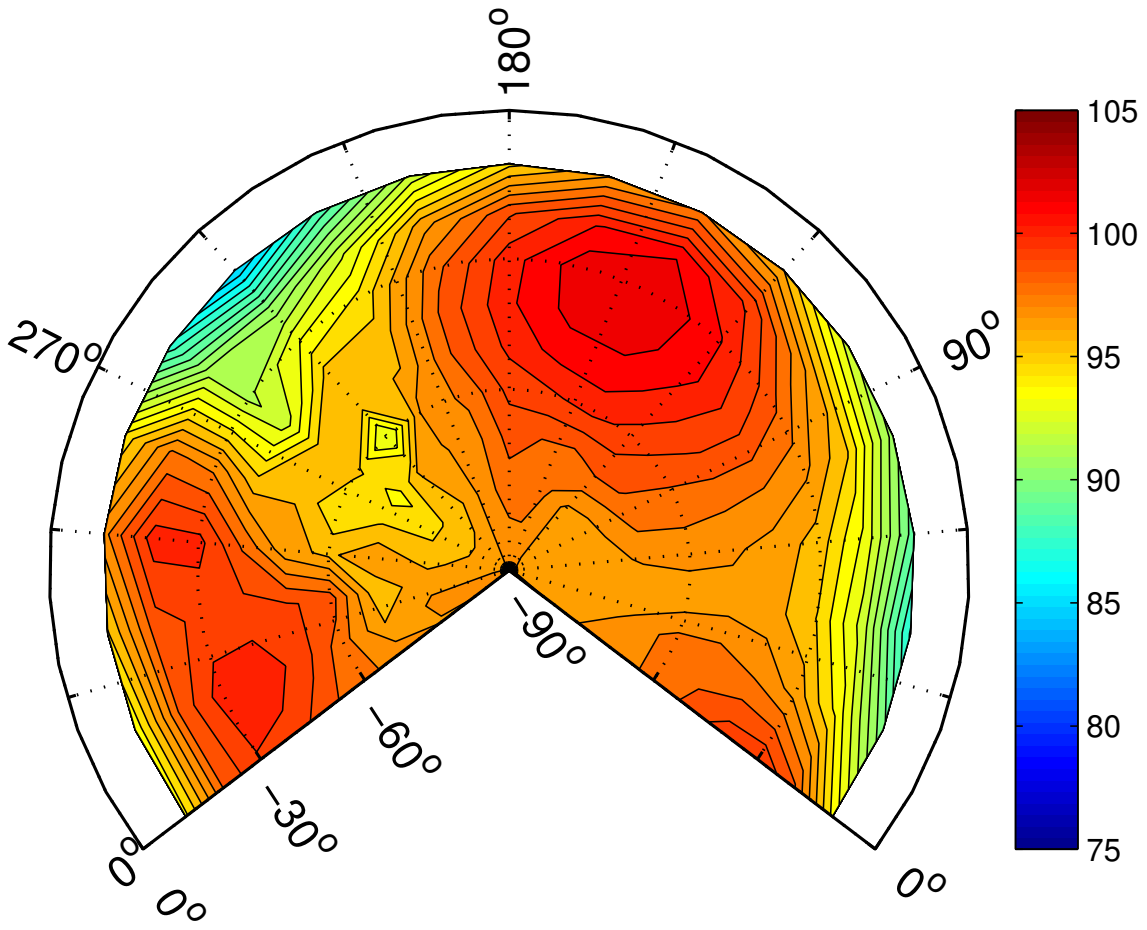

Figure B.8: Combined Bell 206 – OLS model BVISPL hemisphere estimate for Bell 206B3 -7.5° flight path angle condition with hover tip Mach number at 15000 ft.

References

[1] F. H. Schmitz and B. W.-C. Sim, "Radiation and directionality characteristics of helicopter blade-vortex interaction noise," *Journal of the American Helicopter Society*, vol. 48, no. 4, pp. 253–269, 2003.

[2] E. W. Jacobs, R. D. Prillwitz, R. T. N. Chen, W. S. Hindson, and O. L. Santa Maria, "The development and flight test demonstration of noise abatement approach procedures for the Sikorsky S-76," in *AHS Technical Specialists' Meeting for Rotorcraft Acoustics and Aerodynamics*, (Williamsburg, VA), October 1997.

[3] G. Gopalan, M. Xue, E. Atkins, and F. H. Schmitz, "Longitudinal-plane simultaneous non-interfering approach trajectory design for noise minimization," in *American Helicopter Society 59th Annual Forum*, (Phoenix, AZ), May 2003.

[4] R. W. Browne, R. M. Munt, C. R. Simpson, and T. Williams, "Prediction of helicopter noise contours for land use planning," in *10th AIAA/CEAS Aeroacoustics Conference*, 2004.

[5] A. W. Mueller, C. D. Smith, and P. Lemasurier, "Improvement of the predicted aural detection code ICHIN (I Can Hear It Now)," in *Proceedings of the 1993 National Conference on Noise Control Engineering*, (Williamsburg, VA), May 1993.

[6] E. W. Large and A. E. Tretakis, "Tonality and nonlinear resonance," *Annals of the New York Academy of Sciences*, vol. 1060, pp. 53–56, 2005.

[7] G. G. Fleming and E. J. Rickley, "Heliport Noise Model, HNM. version 2.2 (user's guide)," tech. rep., Federal Aviation Administration, February 1994.

[8] T. L. Connor, "Integrated Noise Model-the Federal Aviation Administration's computer program for predicting noise exposure around an airport," *Inter-noise 80: Noise control for the 80's*, Jan 1980.

[9] C. Roof, A. Hansen, G. Fleming, T. Thrasher, A. Nguyen, C. Hall, E. Dinges, R. Bea, F. Grandu, B. Kim, S. Usdrowski, and P. Hollingsworth, "Aviation Environmenal Design Tool (AEDT) system architecture," Tech. Rep. AEDT-AD-01, Federal Aviation Administration, January 2007.

[10] D. Forsyth and J. Gulding, "Review of Integrated Noise Model (INM) equations and processes," Tech. Rep. CR-2003-212414, NASA, May 2003.

[11] D. A. Conner and J. A. Page, "A tool for low noise procedures design and community noise impact assessment: The Rotorcraft Noise Model (RNM)," in *Heli Japan*, pp. 11–13, Heli Japan, 2002.

[12] M. J. Lucas and M. A. Marcolini, "Rotorcraft Noise Model," in *AHS Technical Specialists' Meeting for Rotorcraft Acoustics and Aerodynamics*, (Williamsburg, VA), October 1997.

[13] G. Gopalan, *Quasi-Static Acoustic Mapping of Helicopter Blade-Vortex Interaction Noise*. PhD thesis, University of Maryland, 2004.

[14] M. Gervais, V. Gareton, A. Dummel, and R. Heger, "Validation of EC130 and EC135 environmental impact assessment using HELENA," in *American Helicopter Society 66th Annual Forum*, (Phoenix, AZ), May 2010.

[15] F. Guntzer, P. Spiegel, and M. Lummer, "Genetic optimizations of EC-135 noise avatement flight procedures using and aeroacoustic database," in *35th European Rotorcraft Forum*, (Hamburg, Germany), September 2009.

[16] F. H. Schmitz, "Rotor noise," in *Aeroacoustics of Flight Vehicles: Theory and Practice* (H. H. Hubbard, ed.), vol. 1, pp. 65–145, Acoustical Society of America, 1 ed., 1995.

[17] F. H. Schmitz and Y. H. Yu, "Helicopter impulsive noise: theoretical and experimental status," *Journal of Sound and Vibration*, vol. 109, pp. 361–422, January 1986.

[18] F. H. Schmitz, D. A. Boxwell, and C. R. Vause, "Highspeed helicopter impulsive noise," *Journal of the American Helicopter Society*, vol. 22, pp. 28–36, January 1977.

[19] F. H. Schmitz, "Reduction of Blade-Vortex Interaction (BVI) noise through X-force control," *Journal of the American Helicopter Society*, vol. 43, pp. 14–24, January 1998.

[20] D. C. Sargent, "In-flight array measurements of tail rotor harmonic noise," Master's thesis, University of Maryland, Jan 2008.

[21] T. F. Brooks, D. S. Pope, and M. A. Marcolini, "Airfoil self-noise and prediction," Tech. Rep. RP1218, NASA, 1989.

[22] J. E. Ffowcs Williams and D. L. Hawkings, "Sound generation by turbulence and surfaces in arbitrary motion," *Transactions for the Royal Society of London*, vol. 264, pp. 321–342, May 1969.

[23] D. A. Boxwell, F. H. Schmitz, W. R. Splettstoesser, and K. J. Schultz, "Model helicopter rotor high-speed impulsive noise: Measured acoustics and blade pressures," Tech. Rep. TM 85850, NASA, September 1983.

[24] E. Greenwood, "A physics-based approach to characterizing helicopter external noise radiation from ground-based noise measurements," Master's thesis, University of Maryland, Jan 2008.

[25] T. A. Egolf and A. J. Landgrebe, "Helicopter rotor wake geometry and its influence in forward flight. Volume 1: Generalized wake geometry and wake effect on rotor airloads and performance," Tech. Rep. CR 3726, NASA, October 1983.

[26] T. S. Beddoes, "A wake model for high resolution airloads," in *International Conference on Rotorcraft Basic Research*, (Research Triangle Park, NC), February 1985.

[27] H. Glauert, "On the horizontal flight of a helicopter," Tech. Rep. RM 1157, ARC, 1928.

[28] A. Gessow and G. C. Myers, *Aerodynamics of the helicopter*. New York: The Macmillan Company, 1 ed., 1952.

[29] B. G. van der Wall, "The effect of HHC on the vortex convection in the wake of a helicopter rotor," *Aerospace Science and Technology*, vol. 4, no. 5, pp. 321–336, 2000.

[30] J. M. Drees, "A theory of airflow through rotors and its application to some helicopter problems," *Journal of Helicopter Association of Great Britain*, vol. 3, no. 2, 1949.

[31] A. J. Landgrebe, "The wake geometry of a hovering helicopter rotor and its influence on rotor performance," *Journal of the American Helicopter Society*, vol. 17, no. 4, 1972.

[32] G. H. Vatistas, V. Kozel, and W. C. Mih, "A simpler model for concentrated vortices," *Experiments in Fluids*, vol. 11, no. 1, pp. 73–76, 1991.

[33] M. Scully, "Computation of helicopter rotor wake geometry and its influence on rotor harmonic airloads," Tech. Rep. ASRL 178-1, Massachusetts Institute of Technology, 1975.

[34] L. A. Young, "Vortex core size in the rotor near wake," Tech. Rep. TM-2003-212275, NASA, 2003.

[35] H. Lamb, *Hydrodynamics*. Cambridge, UK: Cambridge University Press, 1932.

[36] M. J. Bhagwat and J. G. Leishman, "Generalized viscous vortex core models for application to free-vortex wake and aeroacoustic calculations," in *58th Annual Forum of the American Helicopter Society*, (Montreal, Canada), June 2002.

[37] C. L. Burley, T. F. Brooks, B. D. Charles, and M. McCluer, "TiltRotor Aeroacoustic Code (TRAC) prediction assessment and initial comparisons with tram test data," in *25th European Rotorcraft Forum*, (Rome, Italy), September 1999.

[38] T. S. Beddoes, "Practical computation of unsteady lift," *Vertica*, vol. 8, no. 1, 1984.

[39] J. G. Leishman, *Principles of Helicopter Aerodynamics*. New York: Cambridge University Press, 2 ed., 2006.

[40] F. Farassat, "Derivation of formulations 1 and 1A of Farassat," Tech. Rep. TM-2007-214853, NASA, 2007.

[41] K. Deb, A. Pratap, S. Agarwal, and T. Meyarivan, "A fast and elitist multiobjective genetic algorithm: NSGA-II," *IEEE Transactions on Evolutionary Computation*, vol. 6, pp. 182 –197, Apr. 2002.

[42] R. Storn and K. Price, "Differential evolution – a simple and efficient heuristic for global optimization over continuous spaces," *Journal of Global Optimization*, vol. 11, no. 4, pp. 341–359, 1997.

[43] Kennedy, J. and Eberhart, R., "Particle swarm optimization," in *IEEE International Conference on Neural Networks*, vol. 4, pp. 1942–1948, August 1995.

[44] I. C. Trelea, "The particle swarm optimization algorithm: convergence analysis and parameter selection," *Information Processing Letters*, vol. 85, no. 6, pp. 317 – 325, 2003.

[45] K. Tatsumi, T. Yukami, and T. Tanino, "Restarting multi-type particle swarm optimization using an adaptive selection of particle type," in *IEEE International Conference on Systems, Man and Cybernetics*, pp. 923 –928, October 2009.

[46] B. Feil, S. Kucherenko, and N. Shah, "Comparison of monte carlo and quasi monte carlo sampling methods in high dimensional model representation," in *First International Conference on Advances in System Simulation*, pp. 12 –17, September 2009.

[47] H. Maaranen, K. Miettinen, and M. Mkel, "Quasi-random initial population for genetic algorithms," *Computers and Mathematics with Applications*, vol. 47, no. 12, pp. 1885 – 1895, 2004.

[48] P. Wannakarn, S. Khamsawang, S. Pothiya, and S. Jiriwibhakorn, "Optimal power flow problem solved by using distributed Sobol particle swarm optimization," in *International Conference on Electrical Engineering/Electronics Computer Telecommunications and Information Technology (ECTI-CON)*, pp. 445 –449, May 2010.

[49] I. M. Sobol, "On quasi-monte carlo integrations," *Mathematics and Computers in Simulation*, vol. 47, no. 2-5, pp. 103 – 112, 1998.

[50] J. Park and I. W. Sandberg, "Universal approximation using radial-basis-function networks," *Neural Computation*, vol. 3, no. 2, pp. 246–257, 1991.

[51] R. D. Reed and R. J. Marks, *Neural Smithing: Supervised Learning in Feedforward Artificial Neural Networks*. Cambridge, MA, USA: MIT Press, 1998.

[52] R. Caruana, S. Lawrence, and L. Giles, "Overfitting in neural nets: backpropagation, conjugate gradient, and early stopping," in *Advances in Neural Information Processing Systems* (T. K. Leen, T. G. Dietterich, and V. Tresp, eds.), vol. 13, pp. 402–408, Massachusetts Institute of Technology, 2001.

[53] D. J. C. MacKay, "A practical bayesian framework for backpropagation networks," *Neural Computation*, vol. 4, no. 3, pp. 448–472, 1992.

[54] H. Demuth and M. Beale, *Neural network toolbox user's guide*. The MathWorks, Inc, 7 ed., 2010.

[55] E. Greenwood and F. H. Schmitz, "Separation of main and tail rotor noise ground-based acoustic measurements using time-domain de-dopplerization," in *35th European Rotorcraft Forum*, (Hamburg, Germany), September 2009.

[56] G. Howell, A. Bradley, M. McCormick, and J. Brown, "De-dopplerization and acoustic imaging of aircraft flyover noise measurements," *Journal of Sound and Vibration*, vol. 105, no. 1, pp. 151 – 167, 1986.

[57] D. Bland, T. Laakso, and A. Tarczynski, "Analysis of algorithms for nonuniform-time discrete fourier transform," in *IEEE International Symposium on Circuits and Systems*, vol. 2, pp. 453 –456 vol.2, May 1996.

[58] F. H. Schmitz, D. A. Boxwell, S. Léwy, and C. Dahan, "Model- to full-scale comparisons of helicopter blade-vortex interaction noise," *Journal of the American Helicopter Society*, vol. 29, no. 2, pp. 16–25, 1984.

[59] F. H. Schmitz and D. A. Boxwell, "In-flight far-field measurement of helicopter impulsive noise," *Journal of the American Helicopter Society*, vol. 21, no. 4, pp. 2–16, 1976.

[60] J. Liu, Y. Wu, D. Han, and X. Li, "Time-frequency decomposition based on ricker wavelet," *SEG Technical Program Expanded Abstracts*, vol. 23, no. 1, pp. 1937–1940, 2004.

[61] J. P. Snyder, *Flattening the Earth: Two Thousand Years of Map Projections*. University of Chicago Press, 1993.

[62] J. P. Snyder, "Map projections: A working manual," Tech. Rep. PP1395, USGS, 1982.

[63] D. A. Boxwell, F. H. Schmitz, W. R. Splettstoesser, and K. J. Schultz, "Helicopter model rotor-blade vortex interaction impulsive noise: Scalability and parametric variations," *Journal of the American Helicopter Society*, vol. 32, no. 1, pp. 3–12, 1987.

[64] F. H. Schmitz, E. Greenwood, R. D. Sickenberger, G. Gopalan, B. W.-C. Sim, D. A. Conner, E. Moralez, and W. Decker, "Measurement and characterization of helicopter noise in steady-state and maneuvering flight," in *American Helicopter Society 63rd Annual Forum*, (Virginia Beach, VA), May 2007.

[65] F. H. Schmitz and B. W.-C. Sim, "Acoustic phasing, directionality and amplification effects of helicopter blade-vortex interactions," *Journal of the American Helicopter Society*, vol. 46, no. 4, pp. 273–282, 2001.

[66] W. R. Splettstoesser, G. Niesl, F. Cenedese, F. Nitti, and D. G. Papanikas, "Experimental results of the european helinoise aeroacoustic rotor test," *Journal of the American Helicopter Society*, vol. 40, no. 2, pp. 3–14, 1995.

[67] D. A. Conner, M. A. Marcolini, B. D. Edwards, and J. T. Brieger, "Xv-15 tiltrotor low noise terminal area operations," in *Proceedings of the American Helicopter Society 53rd Annual Forum*, pp. 1–11, 1997.

[68] International Organization for Standardization, "Standard atmosphere," Tech. Rep. 2533:1975, ISO, 1975.

[69] C. A. Stockwell, G. C. Bateman, and J. Berger, "Conflicts in national parks: A case study of helicopters and bighorn sheep time budgets at the grand canyon," *Biological Conservation*, vol. 56, no. 3, pp. 317 – 328, 1991.

[70] G. G. Fleming, K. J. Plotkin, C. J. Roof, B. J. Ikelheimer, and D. A. Senzig, "Assessment of tools for modeling aircraft noise in the national parks," tech. rep., FICAN, March 2005.

[71] K. B. Kontos, B. A. Janardan, R. E. Kraft, P. R. Gliebe, and U. States., "Improved nasa-anopp noise prediction computer code for advanced subsonic propulsion systems [microform]," Tech. Rep. CR 202309, NASA, 1996.

[72] E. Greenwood, F. H. Schmitz, and G. Gopalan, "Helicopter external noise radiation in turning flight: Theory and experiment," in *American Helicopter Society 63rd Annual Forum*, (Virginia Beach, VA), May 2007.

[73] D. D. Boyd, "HART-II acoustic predictions using a coupled CFD/CSD method," in *American Helicopter Society 65th Annual Forum*, (Grapevine, TX), May 2009.

[74] B. W. Sim, M. A. Potsdam, D. A. Conner, and M. E. Watts, "Direct CFD predictions of low frequency sound generated by a helicopter main rotor," in *American Helicopter Society 66th Annual Forum*, (Phoenix, AZ), May 2010.

[75] D. Patt, L. Liu, and P. P. Friedmann, "Simultaneous vibration and noise reduction in rotorcraft using aeroelastic simulation," *Journal of the American Helicopter Society*, vol. 51, no. 2, pp. 127–140, 2006.

[76] P. M. Morse and K. U. Ingard, *Theoretical acoustics*. Princeton University Press, 1 ed., 1968.

[77] A. S. Babkin, "Signal restoration of non-stationary acoustic signals in the time domain," Tech. Rep. CR-181627, NASA, April 1988.

[78] J. J. Kelly and M. R. Wilson, "De-dopplerization of aircraft acoustic signals," *Journal of Aircraft*, vol. 32, pp. 1012–1017, September 1986.